Parameterization of Lattice-Based Tumor Models from Data.

Nick Jagiella

Parameterization of Lattice-Based Tumor Models from Data.

THÈSE DE DOCTORAT

Présentée par

Nick Jagiella

pour obtenir le grade de

DOCTEUR DE
L' UNIVERSITÉ PIERRE ET MARIE CURIE - Paris VI

Spécialité : Mathématiques Appliquées

Soutenue publiquement le 21 Septembre 2012 devant le jury composé de :

Dirk Drasdo	Directeur de thèse
Luigi Preziosi	Rapporteur
Francois Graner	Rapporteur
Benoit Perthame	Examinateur
Mark Chaplain	Examinateur
Irene Vignon-Clementel	Examinateur

Après avis favorables des rapporteurs : Luigi Preziosi et Francois Graner

Thèse préparée au sein de l'équipe-projet BANG
Centre de Recherche INRIA Paris-Rocquencourt
Domaine de Voluceau, BP 105
78153 Le Chesnay CEDEX

Resumé

Dans le but d'établir un modèle prédictif pour la croissance tumorale in-vivo et la thérapie, le modèle multi-échelle doit être élaboré et calibré par étape et de façon individuelle pour chaque type de cellule ciblé et pour différents environnements (in-vitro et in-vivo).

Nous présenterons, en tant que preuve de concept et à partir de différentes sources de données, les étapes de la construction et de la paramétrisation du modèle de la croissance avasculaire des lignées de cellules EMT6/Ro et SK-MES-1.

Dans une première étape, un modèle multi-échelle à base d'agents a été construit et validé avec des données provenant de la littérature sur les sphéroïdes multicellulaires de carcinomes mammaires de souris EMT6/Ro. Pour cette lignée de cellules, il a pu prédire que la cinétique de croissance est contrôlée par une combinaison de contraintes spatiales et de limitation des nutriments. Il a été trouvé que l'ATP est la ressource critique que les cellules essayent de garder constante en permutant d'un métabolisme aérobique à anaérobique et ce pour de larges plages de concentrations d'oxygène et de glucose. La saturation de la croissance a été observé uniquement dans le cas de faibles concentrations d'oxygène et de glucose ce que le modèle a pu expliqué par une migration guidée par l'adhésion de cellule à cellule.

Dans une seconde étape, le modèle a été adapté à la lignée cellulaire SK-MES-1. Nous avons calibré la cinétique de croissance qualitativement en analysant des images de cryosections de sphéroïdes marquées pour l'apoptose et la prolifération et quantitativement en la comparant des courbes de croissance. Au delà de l'ATP, le lactate a été identifié comme contrôlant la taille du noyau nécrotique.

Pour rendre compte de la situation in-vivo, nous proposons une extension du modèle qui prend en compte un réseau de vaisseaux sanguins et le phénomène de l'angiogenèse associé. Afin de paramétrer les propriétés des vaisseaux fonctionnels et dans le but de valider les lois de l'angiogenèse, nous menons à partir d'images de perfusion d'agents de contraste une étude de sensibilité aux paramètres.

Dans un premier temps, nous résolvons le problème direct de la perfusion des agents de contraste dans un réseau de vaisseaux perméables ou non. Ensuite, nous résolvons le problème inverse rigoureusement et, grâce à des comparaisons directes entre les paramètres originaux et ceux récupérés, nous étudions la capacité de prédiction du modèle dans différents cas.

Abstract

In order to establish a predictive model for in-vivo tumor growth and therapy, a multi-scale model has to be set-up and calibrated individually in a stepwise process to a targeted cell type and different environments (*in-vitro* and *in-vivo*).

As a proof of principle we will present the process chain of model construction and parametrization from different data sources for the avascular growth of the EMT6/Ro and the SK-MES-1 cell line. In a first step, a multiscale and individual-based model has been built up and validated with EMT6/Ro mouse mammary carcinoma multi-cellular cell spheroid data from literature. For this cell line it predicted the growth kinetics to be controlled by a combination of spatial restrains and nutrient limitation. ATP was found to be the critical resource which the cells try to keep constant over a wide range of oxygen and glucose medium concentrations by switching between aerobic and anaerobic metabolism. Only if both, oxygen and glucose are very limiting saturation was observed which the model could explain by cell-cell-adhesion-driven migration. In a second step, the model was adapted to the SK-MES-1 cell line. The growth kinetics was calibrated quantitatively in comparison with growth curves and qualitatively by image analysis of spheroid cryosections stained for apoptosis and proliferation. Beside ATP, lactate was identified to control the size of the necrotic core.

For the transition to the *in-vivo* situation, we propose a model extension introducing a blood vessel network and angiogenesis. In order to parametrize the functional vessel properties and to validate angiogenesis rules, we study the parameter inference from contrast enhanced perfusion images. As a benchmark, we first solve the direct problem of contrast agent perfusion along a network of either permeable or non-permeable vessels. Then by voxel-wisely solving the inverse problem and direct comparison between recovered and original parameter maps we study its predictive efficiency for different cases.

Contents

Introduction

Chapter 1

Introduction

This chapter aims at giving a summary of the motivations of this work: what is cancer? How can mathematical models help to study cancer? How can such complex models be parametrized with specific data? In the following, we will give a brief background on the biology of cancer, treatment strategies and experimental investigation methods of special interest for this thesis. In the next section, a coarse overview of recent models addressing cancer in its avascular and angiogenic stages will be given. An overview of the research conducted in this thesis will then be presented. Finally, we will close with an outline of the manuscript.

Contents

1.1 Motivation

Cancer is a leading cause of death worldwide, accounting for 7.6 million deaths (around 13% of all deaths) in 2008. With almost 20% (1.37 million deaths) lung cancer is the most common cause of cancer-related death in men and women [http://www.who.int].

Computer simulations can help to guide experiments and identify (or exclude) the microscopic mechanisms leading to phenomena on the tissue scale typically observed in cancerous tissues: uncontrolled cell growth, hyper-nutrition/hypoxia, the creation of necrotic areas, blood vessel remodeling/angiogenesis and the formation of metastasis.

Multi-scale models in particular are excellent tools to combine the findings from very different data sources (in-vitro tumor spheroids, in-vivo animal models and patient data) on different scales (molecular, cellular, tissue etc.) and, thus, allow us to relate and extrapolate their insights between one another. Once a model is parametrized, it can make predictions and be the basis for developing and optimizing new cancer therapies and treatment strategies.

Below a more detailed introduction into cancer, models of cancer and multi-scale models is given before an overview about this thesis is presented.

1.2 Background on Cancer

1.2.1 Carcinogenesis

Cancer arises from a series of mutations that are manifested in phenotypic changes of both the cells and the local tissue structure. The process of a healthy cell turning into a malignant cancer is in general referred to as *carcinogenesis*. It was shown that more than one mutation is required before a normal cell will transform into a cancer cell [FV90].

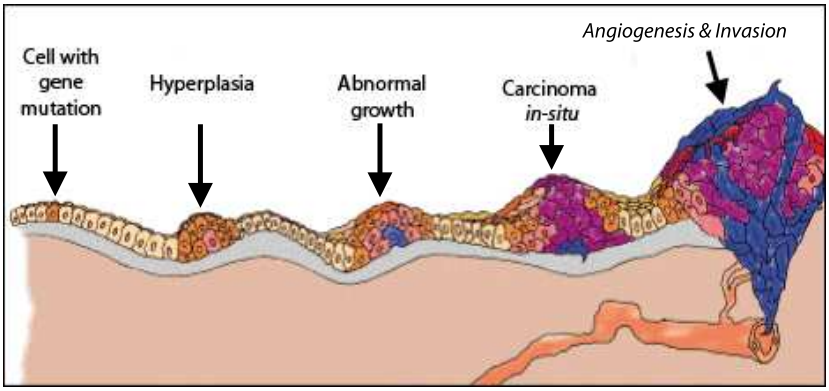

Figure 1.1: Carcinogenesis. Schematic of the evolution from an healthy cell to a malignant and invasive cancer. Image modified from [http://science.education.nih.gov]

Figure 1.1 shows the typically observed evolution of a cancer. At the stage of neoplasia or *in-situ* tumor, a pre-state on the path to invasive cancer, cells divide out of control but still form a compact colony well separated from its environment. The transition from an in-situ tumor to invasive cancer is marked by a number of steps. This includes angiogenesis, the formation of new blood vessels to supply the growing tumor with oxygen and nutrients, and detachment of cells from the tumor that subsequently invade the tissue and the blood vessels to be transported into distant organs where they can lead to the formation of secondary tumors, so called metastases [DJRC+10].

1.2.2 "Hallmarks" of Cancer

Hanahan and Weinberg [HW00, HW11] believe that the capabilities all cancer (or malignant tumor) cells acquire during *carcinogenesis* can be characterized by eight common traits ("hallmarks") (see figure 1.2):

(1) The acquisition of *self-sufficiency in growth signals* and (2) the *loss of sensitivity to anti-growth signals* leads to uncontrolled growth. (3) The acquired *resistance to cell death* (i.e. apoptosis) allows cells to grow despite genetic errors and external anti-growth signals. (4) The *loss of senescence* leads to limitless replicative potential (immortality). (5) The active recruitment of new vessel via *angiogenesis* allows

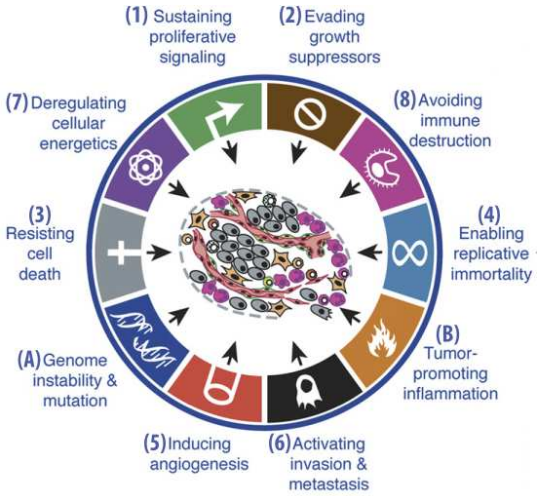

Figure 1.2: Hallmarks of cancer (1-8) and enabling characteristics (A-B). Image modified from [HW11]

the tumor to grow beyond the limitations of passive nutrient diffusion. (6) Acquisition of ability to *invade neighboring tissues or blood vessels* and to create *metastases* at distant sites, the defining property of invasive carcinoma. (7) *Deregulation of cellular energetics* limits the metabolism to glycolysis even under aerobic conditions. (8) *Avoiding immune destruction.*

Thereby, the genetic alterations leading to a particular capability as well as the order in which these capabilities are acquired might be quite variable across different cancer types.

1.2.3 Treatments

Several cancer treatments target some of the above described "hallmarks":

Chemotherapy Chemotherapeutic drugs exploit the fact that cancer cells have an increased proliferative activity (Hallmarks 1 & 2). They affect cell division or DNA synthesis and function, which in general stops cell division and leads to cell death [TC08]. Chemotherapy is a very widely used anti-cancer therapy (without and after surgery). Nevertheless, it has multiple side-effects, e.g. patients dramatically lose body mass, and get a weakened immune-system due to chemotherapeutic drugs killing healthy cells in proliferation as well.

Radiotherapy Radiation therapy works by damaging the DNA of cancerous cells. This DNA damage is caused by one of two types of energy, photon or charged particle. As cancer cells have a diminished ability to repair sub-lethal damage (Hallmark 3), single-strand DNA damage is passed on through cell division. Consequently, damage to the cancer cells' DNA accumulates, causing them to die or reproduce more slowly.

Anti-angiogenic therapies Folkman first made the hypothesis that tumor growth is angiogenesis-dependent and that inhibition of angiogenesis could be therapeutic [Fol71] (Hallmark 5). While VEGF (vascular endothelium growth factor) neutralization can initially limit tumor proliferation due to its anti-angiogenic effect, it can also result in transient vascular normalization with improved oxygenation and perfusion [Jai05], favoring drug delivery. In the last 35 years, it has been estimated that > 200 companies have worked and are still working in the area of angiogenesis and several of the compounds that modulate angiogenesis are currently being evaluated in clinical trials [Rib10]. Nevertheless, their efficiency stays very questionable: Clinical responses of anti-angiogenic therapies have been found to be transitory and can even lead to an increase of invasiveness and metastasis [ELCM$^+$09]. For critical reviews on this subject see ref. [BH08, Rib10, EK11].

1.2.4 Biological Tumor Models & Clinical Investigation

Tumors are studied with different biological models.

In early development, tumors grow up to 1-2mm in diameter, nourished by nutrients and oxygen of the existing vasculature. This phase is often called the *avascular growth* (neoplastic and in-situ tumor stage, see figure 1.1); many aspects of this growth phase are extensively studied in-vitro by growing multi-cellular tumor spheroids (MCTS). MCTS show a similar establishment of pathophysiological gradients and the concentric arrangement of heterogeneous cell populations (see figure 1.3(b)) as found in avascular tumor nodules, micro-metastases or inter-capillary micro-regions of solid in vivo tumors. Multi-Cellular Tumor Spheroids (MCTSs) can be cultivated in large batch cultures, e.g. in hanging drops or microarrays (see figure 1.3(a)). A recent review on MCTS can be found in [HMD+10].

On the other hand, the effect of vascularization, angiogenesis as well as anti-angiogenic drugs require an *in-vivo* model. As preclinical models, mouse xenografts became a very popular tool to mimic cancer growth and tumor-induced vessel remodeling by transplanting human cancer cells under the skin of mice. In general, a genetically manipulated mouse, called the nude mouse (see figure 1.4), is used which as consequence of a mutation is lacking a thymus[1]. This is expressed by missing body hair and a reduced number of T cells making nude mice a good host system for human tumor cells as their immune system is not rejecting them. Its use for experimental and clinical investigations of human tumor cells are discussed e.g. in [JB78, JB82].

For preclinical (e.g. xenografts, see above) and clinical (patient) studies of new treatments or treatment efficiency, non-invasive methods are used to examine tumor progression and drug effects on tumor vascularization (in case of angiogenic treatment). This allows a temporal monitoring without harming the body. Examples are ultrasound (US), magnet-resonance imaging (MRI) or computer tomography (CT). In most cases they are used in combination with contrast agents which are injected into the blood stream in order to enhance the visibility of blood vessels. Contrast-Enhanced Ultrasound (CE-US) for example uses air-filled micro-bubbles which, due to their echogenicity[2] different to tissue, create a large contrast between vessels and tissue and allow the quantification of blood vessel volume (see figure 1.4) [PHL+08]. More advanced techniques of *dynamic enhancement* even allow to quantify dynamic properties as blood flow (for DCE-US see e.g. [LCC+11]) and vessel permeability (for DCE-MRI see e.g. [BSP+91, TK91, BBH+99, TBB+99, BKL+04, BZKG09]) by the evaluation of temporal sequences of images.

[1] The thymus "educates" T-lymphocytes (T cells), which are critical cells of the adaptive immune system.

[2] Echogenicity is the ability to bounce an echo.

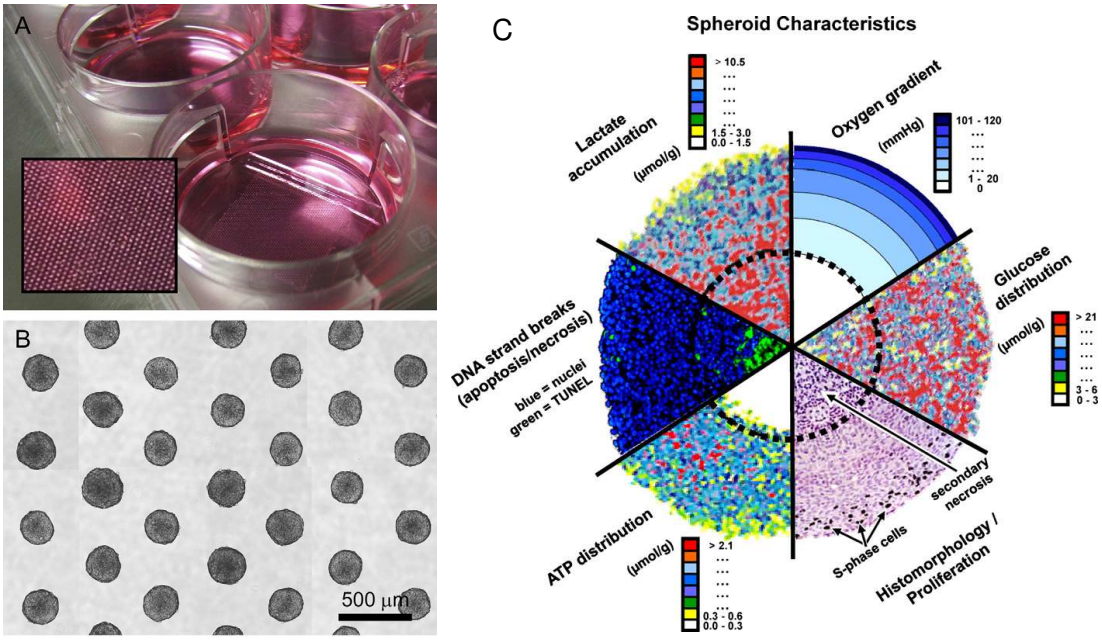

Figure 1.3: An individual microarray can be accommodated within each of the wells of a standard 6-well tissue culture plate for the scalable production of over 10,000 spheroids (A). Microscopy image compilation of uniformly sized human HT29 colon carcinoma spheroids cultivated on the perforated thin film polydimethylsiloxane (PDMS) micropattern (B). Combination of analytical images of spheroid median sections studied with different technologies: autoradiography, the tunnel assay, bioluminescence imaging, and probing with oxygen micro-electrodes. Together these measurements enable the concentric arrangement of cell proliferation, viability and the micro-milieu in large spheroids to be understood (C). Ref. [HMD+10]

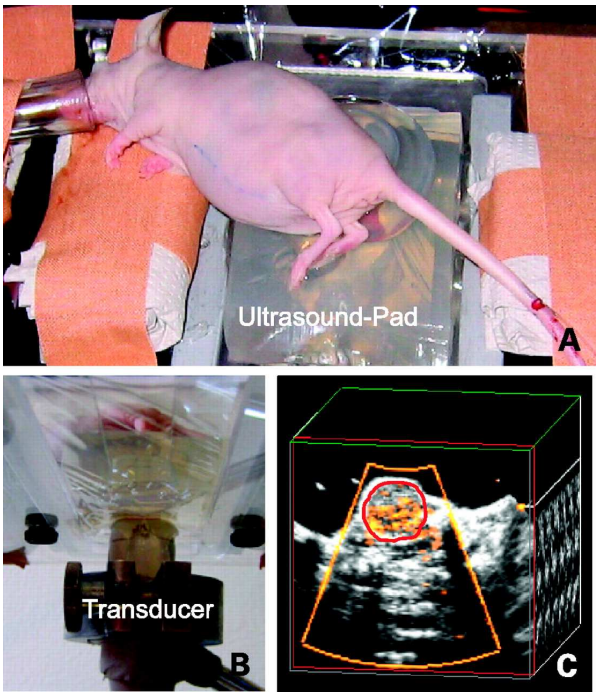

Figure 1.4: SPAQ-based molecular imaging. (*A*) A nude mouse (tumor implanted s.c. on the right hind leg) is placed on an ultrasound pad. (*B*) The ultrasound transducer is fixed below the navigable table that can be moved in micrometer increments. (*C*) During the ultrasound scan (mechanical index = 1.6), the targeted micro-bubbles disintegrate and emit detectable signals (yellow dots; red, region of interest). The two-dimensional ultrasound images are reconstructed to a three-dimensional dataset that is analyzed quantitatively by an automatic video densitometry system as to the color pixel density within the region of interest. Ref. [PHL+08]

1.3 Background on Modeling Tumor Growth

There are mainly three types of approaches for which representative recent references are given: (1) continuum models (Partial Differential Equations (PDEs) in time and space) where the density of the different components evolves in time and space (see e.g. [WLFC08, PT09, BRJ+09]), (2) agent-based models that describe each entity individually (for example, at the cellular level how tumor and endothelial cells grow, divide, move and die).

1.3.1 Multi-Scale Models for Cell Dynamics

The different approaches have also been combined in hybrid or multi-scale models. Examples include agent-based models for cells and continuum models [SMH05, JPGCF05, ABM05, DH05, DHB07, KSO07, WBR08, RCDCA08, RCCAD09] or simplified assumed profiles [BR06, LR06] for diffusion of oxygen, nutrients and/or growth factors or inhibitors. Note that in [KSO07] the different tumor zones were represented with either agent-based models or continuum models.

1.3.2 Multi-Scale Models of Vascularization

The effect of vasculature is explored with a given network [ABM05] or includes angiogenesis and remodeling [BR06, LR06, MMA+09, OAMB09], angiogenesis being by itself an active subject of modeling (see e.g. [MAC06, MWO04, CM09, SGZ+09, PBC+11]).

1.3.3 Problem: Parametrization

Despite the large variety of models, the quantitative parametrization stays a difficult task. Problems are the large number of parameters and the lack of validation of underlying mechanisms. Many models are fitted to the growth dynamics of the cell population (e.g. [SMH05, JPGCF05]) without verifying that the mechanisms leading to certain growth curves and cellular arrangements correspond to experimental findings (see figure 1.3(b)). E.g. the transition from the exponential to a linear radius growth phase can be due to contact-inhibition or nutrient-limitation.

Especially challenging is the parametrization of models mimicking angiogenesis. The spatial and functional organization of the vessel structure spans over many scales ($\mu m - cm$). The dynamic properties (pressure, flow, shear, etc.) depend on the topology (vessel radii, branching, etc.) and vice-versa. In order to get the topological information of the vascular trees down to the capillary scales (e.g. histology) one loses information about the dynamic properties and the possibility to monitor their changes within the course of time as the host has to be sacrificed. Non-invasive acquisition strategies, on the other hand, suffer from coarse resolutions not reaching the micro-vessel scales (figure 1.4).

1.4 Research Overview

1.4.1 Funding Project and Objectives

This thesis was defined in the scope of a research network and grant project on lung cancer (LUNGSYS) funded by the German ministry of education and research (BMBF).

In this project, the motivation to study lung cancer was, that lung cancer is the most lethal cancer world wide. Due to late diagnosis in the majority of the cases, only few patients undergo surgery. Instead, they are often treated by systematic chemotherapy which as a side-effect causes anemia[3]. To compensate for anemia, chemotherapy is often combined with the administration of Recombinant Human Erythropoietin (rHuEPO) which is a growth factor that controls the red blood cell production.

In clinics it has been observed, that the administration of rHuEPO to patients might in some cases promote the propagation of lung cancer. One reason could be the over expression of EPO-receptor discovered in many cancer cells, especially the Non-Small-Cell Lung Carcinoma (NSCLC), or EPO-specific effects on endothelial cells promoting angiogenesis (see fig. 1.5). But overall, the reasons remain unclear.

The LUNGSYS project addresses the question of how EPO influences tumor growth during chemotherapy, by a system biology approach. The idea is to systematically analyze tumor cells on different scales (intra-cellular, cellular and tissue scale) in different systems (in-vitro monolayers and spheroids, in-vivo xenograft models and patient) and combining their insights in a multi-scale model to gain a better understanding of the interactions on and between the different scales.

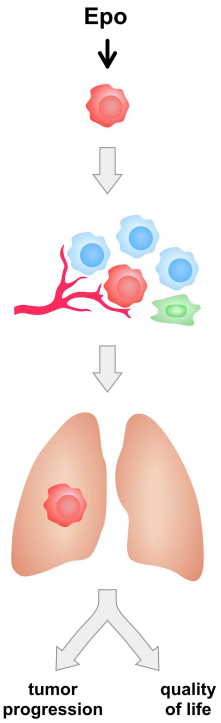

Figure 1.5: EPO effect on tumor progression. [LUNGSYS proposal]

1.4.2 Scientific Questions Addressed in this Thesis

Tumor Growth as a Complex Multi-Scale Process

The growth of tumors *in-vivo* is a complex process, which is largely influenced by many different factors:

[3] Anemia (or anaemia) is a decrease in number of red blood cells (RBCs) or less than the normal quantity of hemoglobin in the blood.

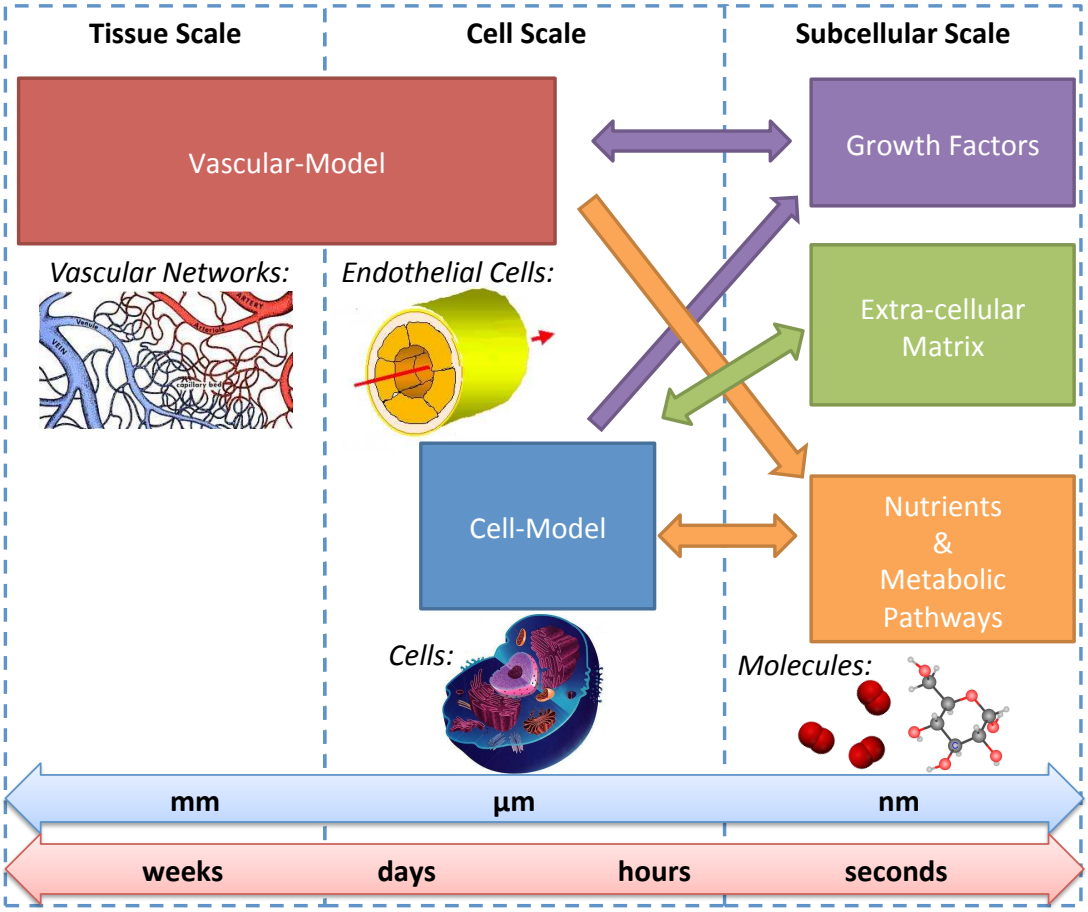

Figure 1.6: Components and relations between them involved in tumorigenesis or cancerogenesis spanning over different time and space scales. Pictograms depict the biological or biochemical compounds and the boxes their modeled counterparts. Otherwise there were also signal transduction pathways, gene regulation networks etc.

1. *Cell Type:* Every tumor cell type can show different growth, death and even migratory behaviors. Depending on the individual genetic, and thus phenotypic alterations, tumor cells might respond differently to growth or survival promoting (e.g. growth factors, nutriment supply, etc.) or - often resist - inhibiting (e.g. contact-inhibition, nutrient-limitation, intoxication by metabolites and scattered remainings of necrotic cells) conditions and signals.

2. *Environment:* the tumor cell population is embedded in a healthy tissue consisting of other cells (e.g. tissue dependent cells, endothelial cells, macrophages etc.). Those represent a physical constraint to an expanding tumor cell population and furthermore - as the tumor cells themselves - have a fundamental impact on the chemical environment (concentration gradients throughout the tissue). Cells communicate with their surrounding via the secretion and reception of signaling molecules (e.g. under-oxygenated cells spread Vascular Endothelial Growth Factor (VEGF) which stimulates endothelial cells to grow and form new blood vessels). The vascularization supplies nutrients and oxygen to the tissue (and tumor) which is essential for cell survival and replication. Cells, on the other hand, consume those nutrients and secrete metabolites which - especially under anaerobe conditions - can harm other cells if not eliminated.

The spatio-temporal evolution of a tumor (see *carcinogenesis* in section 1.2.1, figure 1.1), i.e. the speed and the pattern of expansion into the healthy tissue and the spatial arrangement of cell phenotypes within the tumor (proliferating, quiescent and necrotic cells), emerges directly from the *interplay* of all those factors on different spatial and temporal scales (see figure 1.6).

Role of Mathematical Models

Biological experiments are the main tool to identify possible dependencies by systematically altering some of the (possible) factors, but cannot entirely explain the underlying mechanisms linking those factors. Here mathematical models become very useful: hypotheses on biological mechanisms made from experimental observations can be tested *in-silico* and tested by direct comparison between the experimental and simulation outcomes. Mathematical and computational models give formalized interpretations of the biological processes that lead to the experimental observations. This allows to (1) integrate findings of different experimental setups (*in-vitro*: suspended cell culture, mono-layer and spheroid, *in-vivo*: xenografts) or patient and (2) to predict how tumor progression changes under different conditions. A fundamental difference between tumors and multi-cellular tumor spheroids is the embedding tissue, vascularization and the tumor-induced angiogenesis. We ask the question of how vascularization and angiogenesis influence the growth of tumors, and vice-versa.

1.4.3 Strategy & Methods

To pursue the questions asked above, a tumor growth model framework was created in a step-wise process, increasing the complexity of the model gradually. For each new component (cells, molecules and blood vessels) we studied how to parametrize the corresponding model module and how to couple it to the rest of the model from experimental data of comparable complexity. The parametrization process called several times for enrichments of the model: proposal of mechanisms (chapters 3 & 4) to better capture experimental spheroid data (chapters 2) and in the study of perfusion imaging, building of a much more complex vascular network (chapter 6) than in the initial vascularized tumor model (chapter 5). For a summary see figure 1.7.

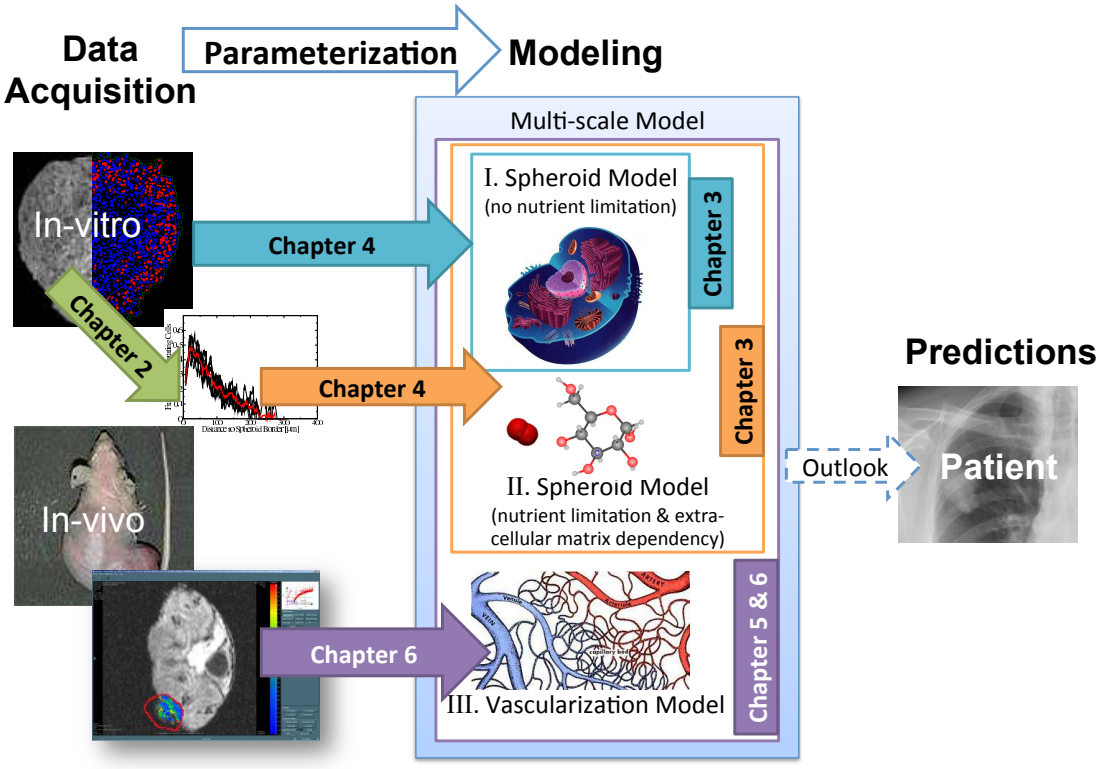

Figure 1.7: Process chain of modeling and parametrization as a step-wise process performed in this thesis.

Part I: Model Framework for Avascular Tumor Growth

The first part of this thesis focuses on the construction of a model framework that mimics avascular tumor growth and its parameterization from data of a specific cell type. As avascular tumors show strong similarities with MCTSs (see section 1.2.4) in terms of concentric organization (proliferating rim, quiescent rim and necrotic core) and temporal evolution (exponential growth, linear radius growth and saturation), MCTSs were chosen as the biological reference model for comparison and parameterization.

First a model framework was built mainly based on data from literature considering all relevant spatial scales and components, i.e. cells (section 3.2) and molecules (section 3.3), as experimental data were not available at that time. Here spheroid data on EMT6/Ro cells were chosen for parameterization as they are a very well studied cell line.

In a second step, experiments with spheroids of the lung cancer cell line SK-MES-1 were performed by our experimental partners from funding project LUNGSYS, Dr. Benedikt Müller and Prof. Margareta Müller from the DKFZ (German Cancer Research Center), Heidelberg, Germany (section 2.1), and the acquired data were analyzed (section 2.3) to parametrize and extend the model for this cell line (section 4.2).

Cell Model (Chapter 3)

Cells were previously modeled following different approaches. As already stated in section 1.3 two types of models have been proposed in the literature: individual-based and continuum models. As this thesis aimed at identifying the cell-based mechanisms leading to phenomena at the tissue scale, cells were represented as individual objects permitting individual state, decisions and behavior. In addition this type of model explicitly represents the different processes that can be a basis for phenomenological advection-reaction-diffusion continuum models. Here one further distinguishes between lattice-based (cells populating a fix or dynamic lattice) and off-lattice models. While off-lattice models position cells in a continuum space, in lattice based approaches cells populate a static or dynamically changing underlying lattice. Consequently for the first one the cell movement and size can be represented completely continuously in time and space: they are driven by forces which act on each cell by the environment and cell-cell-interactions. In contrast, lattice-based models represent the cellular dynamics by defined rules which represent the result of these underlying biophysical forces. However, off-lattice models suffer from large computational costs. Besides they cannot easily be up-scaled to scales ($>1\text{mm}^3$) necessary to study certain tumor-related phenomena at the tissue scale. This is for example necessary to model in-vivo vascularized tumor growth, which a predictive treatment-relevant tumor model should aim at. The temporal dynamics of lattice-based models can be calculated stochastically e.g. by minimizing

an energy functional such as the Hamiltonian in the cellular Potts model, or by solving the master equation. In the first approach the probabilities to accept a certain system change are based on an Hamiltonian that includes adhesion energies, and volume and surface area constraints. Cells occupy many lattice sites, and thus can have various cell shapes. On the other hand such a high resolution combined with the fact that many system changes are refused, limits the total number of simulated cells due to computational costs. Thus a master equation approach was chosen here to describe the systems spatio-temporal evolution taking into account the characteristic time distributions of the biological processes (cell growth, division, migration and death). The master equation can be solved analytically only for very simple systems. Here the stochastic simulation algorithm proposed by [Gil77] solves it numerically.

The model proposed in this thesis is an extension of the model described in [RBH$^+$09]. Cells occupy exactly one lattice site. Cells can migrate to neighboring free lattice sites by free migration or with a bias among all free neighboring sites. Cells can divide if there is a free site with a maximal distance of proliferation length ΔL. If a division takes place, then first all cells are shifted along the shortest path from the dividing cell to the closest free site, and then a new daughter cell occupies the newly freed site.

As an extension a more general approach for the cell decision between division and quiescence was chosen. As it was shown by the radial profiles extracted from the experimental spheroid cryo-sections, the transition from high proliferation activity in the outer rim to quiescence in the inner part of the spheroids is much smoother than a step function. The model was extended by a generic function of the distance of a certain cell to the closest free space to determine the probability of its re-entrance into the cell cycle, e.g. Heavy side function, Hill function or exponential decay. Furthermore, the list of processes was extended by necrosis (of viable cells) and lysis (of necrotic cells) processes linking the cellular and the nutrient models. Furthermore, cell growth was included as a sub-event of the cell cycle. Cells will thus double their volume at a defined moment of the cell cycle by occupying a second lattice site. Migration can be either free or biased by adhesion or the local gradient of a morphogen.

Molecular Model (Chapter 3 & 4)

As molecules are much smaller than cells, a continuum approximation was chosen to represent them at the cell scale. Glucose, oxygen, lactate and morphogen are modeled by time-varying reaction-diffusion partial differential equations. The extra-cellular matrix evolves locally with ordinary differential equations.

The nutrient-related parameters derive from experiments neglecting the influence of contact-inhibition. The consumption rates of glucose and oxygen were fitted to measurements made for single cells in a suspension culture exposed to different nutrimental

conditions [FS85].

Parametrizing the Cell Model (Chapter 4)

The purely cell-dependent parameters (e.g. cell cycle time, shape and thickness of proliferating rim) are derived from the comparison with biological experiments where nutrient-limitation could be neglected. For the EMT6/Ro cell line the cell parameters were estimated from growth curves of spheroids growing in suspension with 16.5 mM glucose and 0.28 mM oxygen, and for the SK-MES-1 cell line from growth curves and quantified concentric arrangements of spheroids growing in suspension with 25mM glucose and 0.28 mM oxygen (assuming physiologically relevant conditions around 3-15 mM and 0.05-0.2 mM [Buc11]). The growth rate was fitted from the exponential growth phase (i.e. all cells are dividing) of the number of cells per spheroid in time. The (apparent) thickness of the proliferating rim was fitted from the geometric growth phase (i.e. when the spheroid radius is linear function of time).

Coupling of Cell and Molecular Models (Chapter 4)

The coupling of nutrients and the cellular phenotype (proliferating, quiescent, apoptotic) could not be directly addressed as no data on the relation between the concentration and the induced change in cell phenotype was directly accessible. Because of the stochastic behavior of the (cell) model an automated parameter estimation could not be applied. Initial trials with methods like gradient decent, which evaluate the gradient of a defined fitness function (e.g. mean squares between experimentally and numerically obtained growth curves and radial profiles) in the parameter space to estimate the optimal path towards a set of best fitting parameters, failed. The problem is that the fluctuations between single simulations lead either to non-reliable gradients, and thus to a random walk-like behavior in the parameter space, or to reliable gradients, but non reasonable computation times by increasing the number of single simulations for the average behavior. Instead a systematic sensitivity analysis was performed to study the influence of each parameter on the system behavior to estimate the possible ranges.

Part II: Vascular Tumor Modeling & Parametrization

The second part of this thesis investigates the influence of vascularization and tumor progression via a multi-scale model integrating a vascular network (and rules for remodeling and angiogenesis), and the possibility to infer the functional and architectural vessel properties from perfusion data.

Vascular Model (Chapters 5 & 6)

The vascularization can be modeled in many ways representing blood vessels as the density of endothelial cells in a continuum approach or as discrete objects. As we are interested in the spatio-temporal interaction of blood vessels with the cells as well as the dynamical properties (blood flow, pressure and shear stress), the vasculature was chosen to be represented by a vessel graph consisting of vessel nodes and vessel segments similar to that in [WR10]. The functional properties of the vessels, flow (segments) and pressure (nodes), are described by Poiseuille's law and linked by algebraic relations. In order to solve the system, boundary conditions must be given (i.e. pressure at the entrance and exit of the vessel network) as well as the architectural properties of the vascularization (length, radius). Blood viscosity is assumed to be a function of the radius [PSG+94].

Angiogenesis (Chapter 5)

To study the interplay between vascularization and tumor progression, the vascular model was coupled to the avascular tumor growth model.

As the domain size is limited to 1mm^3 blood vessels were assumed to be mainly capillaries. They have the same dimension as cells and populate the same underlying unstructured lattice. Besides, they serve as the only source of glucose and nutrients to the system. On the other hand, cells which are hypo-nourished produce VEGF. VEGF is modeled by a reaction-diffusion equation.

Vessel remodeling and angiogenesis rules are inspired by the model defined in ref. [BR06]: if the local VEGF concentration is large enough, blood vessels sprout or dilate with a certain probability. Vessels collapse with a certain probability if the oxygen concentration and flow, or shear stress are too low.

Starting with an initial network with a typical cell-capillary distance of a healthy tissue, the influence of the angiogenic switch on tumor progression was studied and compared to tumors growing in a static vessel network or without nutrient-limitation.

Parameterization of Vascular Model (Chapter 6)

The vasculature is a complex structure where functional (flow, pressure, leakiness), architectural (vessel radii) as well as topological (network topology) properties are all inter-related. Thus it is insufficient to just look at the histological information of tumor vascularization as the topological and functional aspect are missing. The three-dimensional reconstruction of vascular trees from non-invasive Magnet Resonance Imaging (MRI) or Computer Tomography (CT) can give a good insight into the topology, but is limited to the larger vessels due to the image resolution. Micro-CT gives

a much higher resolution but this data acquisition method is invasive and often requires for resolution purposes, the sacrifice of the host organism (e.g. xeno-graft) as for histology, and thus is not able to monitor long term changes of the same tumor vasculature.

A promising tools in diagnosis are Dynamic Constrast Enhanced-Magnetic Resonance Imaging (DCE-MRI), Dynamic Constrast Enhanced-Computer Tomography (DCE-CT), and more recently Dynamic Constrast Enhanced-Ultrasonography (DCE-US), which estimate functional and architectural vessel properties from a temporal sequence of perfusion images. The images show the intensity of an injected Contrast Agent (CA) transported along the vessels, in some case diffusing into the interstitial space and that finally gets washed out. Many simplified non-spatial models mimicking the perfusion of CA have been proposed to infer in each region of interest the functional and structural vessel properties via an inverse procedure. But little is known about how the accuracy of these models.

We propose to develop virtual vascularizations where all properties are known by construction to first simulate the perfusion of a CA as a direct problem. This process leads to in-silico perfusion images. In a second step those perfusion images are used to evaluate the accuracy of the two-compartment model proposed by Brix et al.[BKL+04].

For this purpose a stand-alone vascularization is created on a regular lattice. Starting from predefined arterial and venous root nodes a completely random network of arterial and venous vessel trees is grown. Then by applying the algorithm proposed by Goedde and Kurz [GK01], the capillary shear stress is homogenized among the whole vessel network by iteratively collapsing capillaries with low shear stress and randomly regrow the vascular trees. Between iterations the vessel radii are calculated via a power law of all vessel segment radii at a branch. The exponents for arterial and venous vessels are chosen by comparing the resulting average vessel properties for different vessel sizes with experimental data.

The tumor it-self was not explicitly modeled, but its typical vascularization (see Chapter 5) is constructed by different rules inside regions defined as tumor or necrotic core: (1) different vessel collapse and regrow probabilities, (2) vessels of arterial and venous trees are connected by a number of parallel capillaries to account for a higher micro-vessel density, and (3) vessels are more permeable to CA.

Preliminary work was performed on assessing the inverse procedure first on simple topologies and then on healthy and diseased vascularizations. The direct problem of CA perfusion is calculated by a transport equation within the vascular compartment and a diffusion equation within the interstitial space compartment (i.e. extra-vascular and extra-cellular space). Both compartments are coupled by an exchange term for the diffusion across the membrane. For purely intra-vascular CAs only the intra-vascular transport was solved numerically using the explicit Upwind scheme. The blood vessel segments were refined in order to reduce numerical diffusion. For extra-cellular agents

the full system was solved by an implicit scheme in 2D and 3D and by explicit Lax-Wendroff for the transport term in 1D without vessel refinement. Then the perfusion images created by the direct problem were used for the inverse problem. Here, for each voxel the non-spatial Brix II model [BKL+04] was fitted to the CA concentration by using the Levenberg-Marquardt algorithm.

1.4.4 Main Contributions

Work Presented in this Thesis

It could be shown that a hybrid-multi-scale model can be parametrized such that it explains the growth curves (spheroid volume and number of viable cells as functions of the time) of EMT6/Ro MCTS cultivated under four different nutrimental conditions varying glucose and oxygen concentrations. The model-components were parametrized directly from data of the same cell type: the nutrient-independent cell behavior from the growth curves of EMT6/Ro spheroid experiments [FS86] during the exponential (cell cycle time τ) and geometric growth phase (proliferation length ΔL and cell size), and the nutrient-related parameters from measurements of the glucose and oxygen consumption rates in suspended EMT6/Ro cell culture of varying glucose and oxygen concentrations [FS85]. The proposed model was able to explain all three growth phases - exponential, and geometric growth phase as well as saturation of radius growth - by a mix of mechanical contact-inhibition, ATP-limited cell growth and survival and an adhesion-driven cell migration. ATP is proposed to be a direct outcome of the consumed glucose and oxygen assuming that cells maximize the amount of ATP produced from given glucose and oxygen. This allows cells to automatically and smoothly switch between aerobic and anaerobic metabolisms. Furthermore, two ATP thresholds are proposed as criteria for cell growth and survival. The estimation of both threshold values for fitting the oxygen-limited case gives a good prediction for the glucose-limited case as well, and vice-versa. For the low glucose and oxygen condition, saturation of spheroid radius expansion was explained by a homeostasis of cell division in the periphery and central necrosis, and could only be established by proposing the following mechanism: an adhesion-driven migration, which as a result keeps the spheroids at a fixed size.

For another cell line, the SK-MES-1 cells, we established a process chain of designing experiments, quantitative image analysis and model parametrization. Beside the growth curves of spheroids, the radial profiles of proliferating and necrotic nuclei fraction as well as the density of Extra-Cellular Matrix (ECM) was used for the fitting procedure. It could be shown that the cells decision between proliferation or quiescence is not deterministic, i.e. cells divide with probability 1 if there is free space within a distance ΔL, else they are quiescent, but rather probabilistic with a probability to reenter the cell cycle after a cell division which exponentially decreases with the distance to the

closest free space. While the first leads to a compact proliferating rim, only the second shows an agreement with the smoothly decreasing proliferative activity toward the spheroid centers found by quantitative image analysis. Even if both approaches can lead to comparable spheroid expansion speeds for conditions where nutrient-limitation is neglectable, the predictive value of the model increases using the correct proliferation profiles as nutrient-limitation modifies those profiles only at a certain depth. Furthermore, a correlation of low ECM density and a drop of proliferative activity at the outermost spheroid border could be explained by a model extension by ECM which is produced by cells and necessary for cell cycle re-entrance. The model was able to explain the growth curves (radius as function of time) and radial profiles (proliferating and necrotic nuclei fraction, and ECM-density as function of the distance to the spheroid border) during exponential and geometric growth phases of SK-MES-1 spheroids cultured under two nutrimental conditions. The simultaneous fit of growth curve and radial profiles was reached only, if - beside low ATP - a high lactate concentration induced cells to become necrotic. Lactate is a direct side-product of the proposed metabolic model.

For the transition to the in-vivo situation, a model extension was proposed to integrate vascularization, vascular remodeling and angiogenesis. Blood vessels populate the same unstructured lattice as the tumor cells and thus can physically interact with each other. The model incorporates components on the sub-cellular (oxygen, glucose and VEGF), cellular (tumor and endothelial cells) and tissue scale (endothelial cells form vascular network) that are all coupled together. The environment is three-dimensional and permits to simulate a tissue cube of 1mm^3 ($= 10^6$ cells) in reasonable time (30days = 1day to compute[4]). The solver for the partial differential equations is parallelized.

In addition, we aimed at estimating the vascularization model parameters (architecture and function) from non-invasively acquired dynamic contrast-enhanced perfusion images which up to now is a purely diagnostic tool. To this aim, we proposed an extended spatial in-silico tumor vascularization to simulate the perfusion of a virtual contrast-agent. The resulting virtual perfusion images can serve as a direct benchmark to evaluate the predictive value of simplified non-spatial inverse methods that are typically used in radiology. Such a method could also serve to estimate angiogenesis parameters.

These contributions have been leading to one published book chapter and two publications in preparation (on the avascular and perfusion imaging topics respectively).

Additional Work not further Described in this Thesis

The three following paragraphs summarize projects that are not further described in this manuscript because they represent satellite contributions to the main PhD work.

[4] on an HP Z800 Workstation, Intel Quad-Core 3GHz, 32GBytes RAM

Upscaling: the current models for avascular tumor growth and angiogenesis are limited by there individual cell-based nature to a maximal population size of a few mm^3. To reach the centimeter scale the possibility of coarse-graining the cell and molecular components of the model was studied. Here, we pursued (a) a purely coarse-grained approach (one lattice site contains up to N cells) and (b) a hybrid approach using a lattice which dynamically changes its resolution locally adapted to the need of accuracy (see section 7.3).

Downscaling: in order to reach a sub-cellular resolution which e.g. permits the consideration of different cell shapes and sizes, cells are associated to several lattice sites.

Bioreactors: the growth of epithelial cells in bioreactors was simulated with the same model for the purpose of optimizing the production of influenza vaccine. Epithelial cells are a very fast growing cell type and thus ideal to create in a short time a large host population to be infected by a chosen strand of influenza virus. Then the host population serves as a biological factory of large amount of viruses which in inactivated form or whose extracted hull proteins serve as the final vaccine. As epithelial cells grow only attached to surfaces, the growth media in the bioreactors are enriched with small microcarrier beads. The choice of culture conditions as the size and number of the microcarriers, the inoculation number of cells into the medium, etc. was subject of investigation to optimize the total gain of host cells in limited time. A publication is in preparation.

1.5 Outline of Thesis

The thesis is organized in four parts containing this brief summary of the subject, the Avascular Tumor Spheroid Modeling (*Part I*: 2. image processing and analysis, 3. avascular model and 4. parametrization), Tumor Vascularization (*Part II*: 5. angiogenesis tumor modeling, 6. parametrization from perfusion images), and some closing conclusions and discussions on the implications and perspectives of this work.

1.5.1 Part I: Avascular Tumors - Modeling & Parameterization

The goal of *Part I* is to successively set up a multi-scale model (chapter 3) incorporating different sources of information: literature data, experimental measurements and the outcome of image analyzing tools treated in chapter 2. Then based on the comparison between the in-silico results and the experimental observations we study the different spatio-temporal growth phenomena of growing tumor spheroids to identify (or exclude) the mechanisms leading to the experimental observations described above (chapter 4).

1.5.2 Part II: Vascularization - Modeling & Parameter Inference

In *Part II*, the avascular tumor model proposed in chapter 3 is extended to blood vessels (as a certain type of cells), their function (hemodynamics, nutrient providers) and interactions with the other model components (angiogenesis and remodeling) in chapter 5. How to parametrize the vascular compound of the model by better understanding contrast-agent perfusion images is elaborated in chapter 6.

Part I

Modelling Avascular Tumor Spheroids

Chapter 2

Data Acquisition from Histological Spheroid Images via an Image Processing Chain

In this chapter, we will introduce and apply some image processing techniques to images of stained cryosections of tumor spheroids. We will extract quantitative information of the *extra-cellular matrix density*, the *cell size*, the *proliferative activity* and *mortality* as a function of depth (or distance to the outer spheroid border) which in the following chapter will serve as input for the model parameterization.

Contents

2.1 Tumor Spheroids Cultivation & Data Acquisition

In the following subsections, you will find a summary of how the multi-cellular spheroid of SK-MES-1 cells were cultivated under different nutrimental conditions, and how the temporal growth curves and immunofluorescence images were acquired from the spheroids scarified at different moments of the experiments [MM]. The Experiments as well as the image acquisition was performed by Dr. Benedikt Müller and Prof. Margareta Müller from the DKFZ (German Cancer Research Center), Heidelberg, Germany.

2.1.1 Cell Culture

NSCLC cell line SK-MES-1 used in this study was obtained from ATCC (Manassas, VA, USA) and cultivated in a humidity controlled incubator at 37°C and 5% CO_2 in 150cm^2 tissue culture dishes (TPP) in DMEM (Dulbecco's modified Eagle's medium, LONZA, Verviers, Belgium) supplemented with 10% FCS (fetal calf serum, Southern America, GIBCO, Germany) and 1% Penicillin/Streptomycin (Biochrom AG, Berlin, Germany). Cells were used between passages 10 and 30 and passaged at a split ratio of 1:4 to 1:6. Cultures were routinely tested for mycoplasma contamination as described by Stacey and Doyle 1997 and always found to be negative. Additional medium for the test cultures was DMEM w/o Glucose (GIBCO, Germany) supplemented with 10%FCS and 1mM Glucose (Carl Roth GmbH, Germany), and DMEM with 1,0 g/L glucose w/o L-Glutamine (LONZA, Verviers, Belgium) supplemented with 10% FCS and 25mM L-Glutamin (SIGMA, Germany). Additionally, cells were kept in a humidity controlled incubator at 37°C and 5% CO_2 and either normal normal atmospheric 20% O_2 (corresponding to 0,28mM) or 5% O_2 (corresponding to 0,07mM).

Solutions

2% Methocel solution was prepared by stirring 6g Methylcellulose (SIGMA, Germany) in 250ml propagation medium at 60°C for 20min. Then a further 250ml of medium were added and stirred at 4°C over night. The solution was aliquotted in 50ml Falcon tubes, centrifuged two times for 99min at 4000 rpm to concentrate long Methylcellulose-Fibers at the bottom of the tube. Tubes were then stored upright at 4°C.

2% Agar-Solution was prepared by solving 5g bacterial grade Agar (GIBCO, Germany) in 250ml of H20. This solution was autoclaved and then kept at 60°C until 24 well-Plates were coated.

Spheroid generation and cultivation

For the generation of spheroids with defined size and cell number, a hanging drop assay was employed. Here cells were first trypsinized, counted, then centrifuged and

resuspended in propagation medium with 20% Methocel-Solution. Drops of 20μl of this cell suspension were pipetted on the lid of a 150cm^2-culture dish, which was subsequently carefully inverted back onto the dish. In this approach, all suspended cells in the resulting hanging drop contribute to the formation of a single spheroid. After 48h in the hanging drop the spheroids were transferred on 24 well plates, by carefully pipetting with a cut 200ml pipette tip, with one spheroid in one ml of respective medium per well. The wells were pre-coated with 250μl of 2% agar each to prevent attachment of spheroids. Medium was changed once a week. Four different glucose/oxygen conditions were employed: I: 1mM Glucose / 0,28 mM O_2, II: 5 mM Glucose / 0,28 mM O_2, III: 25mM Glucose / 0,28 mM O_2 and IV: 25 mM Glucose / 0,07 mM O_2 (see table 2.1(a)). Spheroids were cultivated over a period of over 48 days.

2.1.2 Spheroid Growth Curves

Growth of spheroids was monitored by acquisition of bright field images through an Olympus IX-70 microscope fitted with an AxioCam Erc5s camera (Zeiss, Germany) twice a week. The projected area of spheroids was determined using ImageJ, software version 1.43u. Mean areas and standard deviations were calculated using Microsoft Excel. At least 4 Spheroids were evaluated per time point and condition.

2.1.3 Cryosectioning and Immunofluorescence Staining

Spheroids were taken out at specified time points, embedded in TissueTek®(SAKURA Finetek, Netherlands) cryo-medium, frozen over liquid nitrogen and processed for cryostat sectioning. Cryosections of 6-8 μm thickness were mounted on slides, air dried and then fixed with 4% PFA for 20 min at RT, washed in PBS for 30 min at RT, permeabilized with ice cold 0,1% TritonX-100 / 0,1% sodium citrate for 2min on ice. To stain for apoptotic cells we employed the In Situ Cell Death Detection Kit (No. 12 156 792 910 Roche Applied Science) according to the manufacturer's protocol. Staining for proliferating cells and ECM component Collagen IV was performed with anti human Ki67, mouse monoclonal (No. M7240 DakoCytomation, Glostrup, Denmark) and anti Collagen IV, rabbit polyclonal (No. 10760, Progen, Heidelberg, Germany) antibody in 12% BSA respectively. Secondary antibodies used were anti mouse, donkey, Cy3 (No. 715-166-151, Dianova, Hamburg, Germany) and anti rabbit, goat, Alexa 488 (No. A-11034 Molecular Probes USA/NL) in 12% BSA. In both cases, nuclei were stained with Bisbenzimide H 33258 (SERVA, Heidelberg, Germany) in 12%BSA. Sections were examined and photographed using a Leica DM RBE (Leica, Germany) microscope fitted with epifluorescence optics.

Table 2.1: Culture and imaging information.

(a) Culture conditions

Condition	[G]	$[O_2]$
I	1 mM	0.28 mM
II	5 mM	0.28 mM
III	25 mM	0.28 mM
IV	25 mM	0.07 mM

(b) Cryosectioning & IF imageing

Timepoint
T1 = 5days
T2 = 10days
T3 = 17days
T4 = 24days
T5 = 34days
T6 = 46days

(c) Supplementary Information

Observation	Value	Reference
nucleus diameter	$d_{nucleus} = 10\mu m$	Estimation from images
cycle time	$\tau = 20 - 24h$	[MM]
cryosection depth	$h_{slice} = 6 - 8\mu m$	[MM]
image resolution	$pixel = 1.03\mu m^2$	[MM]

2.2 Applied Image Processing Techniques

The images acquired (see section 2.1) are raw data. They consist in a set of pixels with position $(x, y) \in \mathbb{N}^2$ and color intensities for the three color channels red, green and blue defined by

$$\begin{aligned} I^{channel}(x, y) &\in [0, 1] \\ I^{channel} &: \mathbb{N}^2 \to \mathbb{R} \end{aligned} \tag{2.1}$$

where $channel \in \{red, green, blue\}$.

In the following, some image processing tools are introduced which will be used to preprocess the raw images (e.g. to reduce noise) and to identify, or *segment*, objects (e.g. *cell nuclei*) which will be the subject of quantitative analysis in section 2.3.

2.2.1 Smoothing & Noise Reduction

In order to reduce noise as well as to smooth the image (necessary for the later segmentation algorithm, see section 2.2.2), a number of different linear and non-linear filters can be applied.

Linear Time-Invariant (LTI) Filters

Filters are operators which transform an continuous input signal (in our case the image data) $i(x, y)$ into an impulse response $i^*(x, y)$. For LTI-filters the impulse answer is usually calculated by convolution with a filter function $k(x, y)$ given as

$$\begin{aligned} i^*(x,y) &= (i \star k)(x,y) \\ &= \iint i(x+x', y+y')k(x', y')\mathrm{d}x'\mathrm{d}y'. \end{aligned} \tag{2.2}$$

As the pixel information is discrete, the filters can be reduced to filter matrices or filter kernels of a defined size $n \times n$, corresponding to the area (or window of pixels) affected by the filter and in the following referred to as the *kernel region*. Then

$$\begin{aligned} I^*[x,y] &= (I \star K)[x,y] \\ &= \sum_{i=0}^{n-1}\sum_{j=0}^{n-1} I[x+i-a, y+j-a]K[i,j], \end{aligned} \tag{2.3}$$

where $a = (n-1)/2$.

- *Mean filters* basically average locally among all pixels within the kernel region. The kernel of size 3×3 looks like the following.

$$K_{mean}^{3\times 3} = \begin{bmatrix} \frac{1}{9} & \frac{1}{9} & \frac{1}{9} \\ \frac{1}{9} & \frac{1}{9} & \frac{1}{9} \\ \frac{1}{9} & \frac{1}{9} & \frac{1}{9} \end{bmatrix} \tag{2.4}$$

- *Gauss filters* modify the input signal by convolution with a Gaussian function.

$$g(x, y, \sigma) = \frac{1}{2\pi\sigma^2} e^{-\frac{x^2+y^2}{2\sigma^2}} \tag{2.5}$$

  The corresponding kernel can be obtained by

$$K_{gauss,\sigma}^{n\times n} = \left(g\left(i-a, j-a, \sigma\right)\right)_{0\le i<n, 0\le j<n}, \tag{2.6}$$

  where $a = (n-1)/2$.

  Instead of an expensive 2d-convolution a one-dimensional gauss kernel can be applied in two passes for each dimension.

$$K_{gauss,\sigma}^{n} = \left(g\left(i-a, \sigma\right)\right)_{0\le i<n}, \tag{2.7}$$

  where $a = (n-1)/2$ and $g(x, \sigma) = \frac{1}{2\pi\sigma^2} e^{-\frac{x^2}{2\sigma^2}}$.

  This reduces the computational complexity from $O(n^2m^2)$ to $O(2nm^2)$, m being the number of pixels of the image.

Non-linear Filters

- *Median Filter* is very widely used in digital image processing because, under certain conditions, it preserves edges[1] while removing noise. The impulse response for each input pixel is the median of neighboring entries within a certain 'window' of size $n \times n$.

- *Dilation Filter* is a morphological operator for probing and expanding the shapes contained in the input image. It application is emphasize shapes or to remove "holes" within shapes. Its impulse response is defined by

$$I'[x,y] = \max_{\substack{|x-x'|\leq a \\ |y-y'|\leq a}} \{I[x',y']\} \tag{2.8}$$

  where $a = (n-1)/2$ for a kernel size of $n \times n$.

- *Erosion Filter* is a morphological operator doing exactly the opposite of the *Dilation Filter*. It reduces shapes in size. Usually it is used to remove small objects from an image. Its impulse response is defined by

$$I'[x,y] = min_{\substack{|x-x'|\leq a \\ |y-y'|\leq a}} \{I[x',y']\} \tag{2.9}$$

  where $a = (n-1)/2$ for a kernel size of $n \times n$.

Figure 2.1 shows the results of smoothing the blue color channel of an image section via a *median filter* (kernel size 9×9) and an *Gaussian filter* ($\sigma = 2.5$). For both filters we can see a much smoother intensity landscape compared to the original image. Nevertheless, the median filter conserves better the original features of the landscape than the Gaussian filter. Thus, in the following we will use the *median filter* for image smoothing.

2.2.2 Watershed Algorithm

The *watershed algorithm* is a segmentation algorithm[2] separating an image into different regions using the concept of *watersheds*. It was first proposed by [BL79] and later enhanced by a fast algorithm presented in [VS91].

[1] *Edge-preserving smoothing* is an image processing technique that smoothes away textures whilst retaining sharp edges.

[2] Segmentation is the process of partitioning a digital image into multiple segments (sets of pixels, also known as superpixels). The goal of segmentation is to simplify and/or change the representation of an image into something that is more meaningful and easier to analyze.

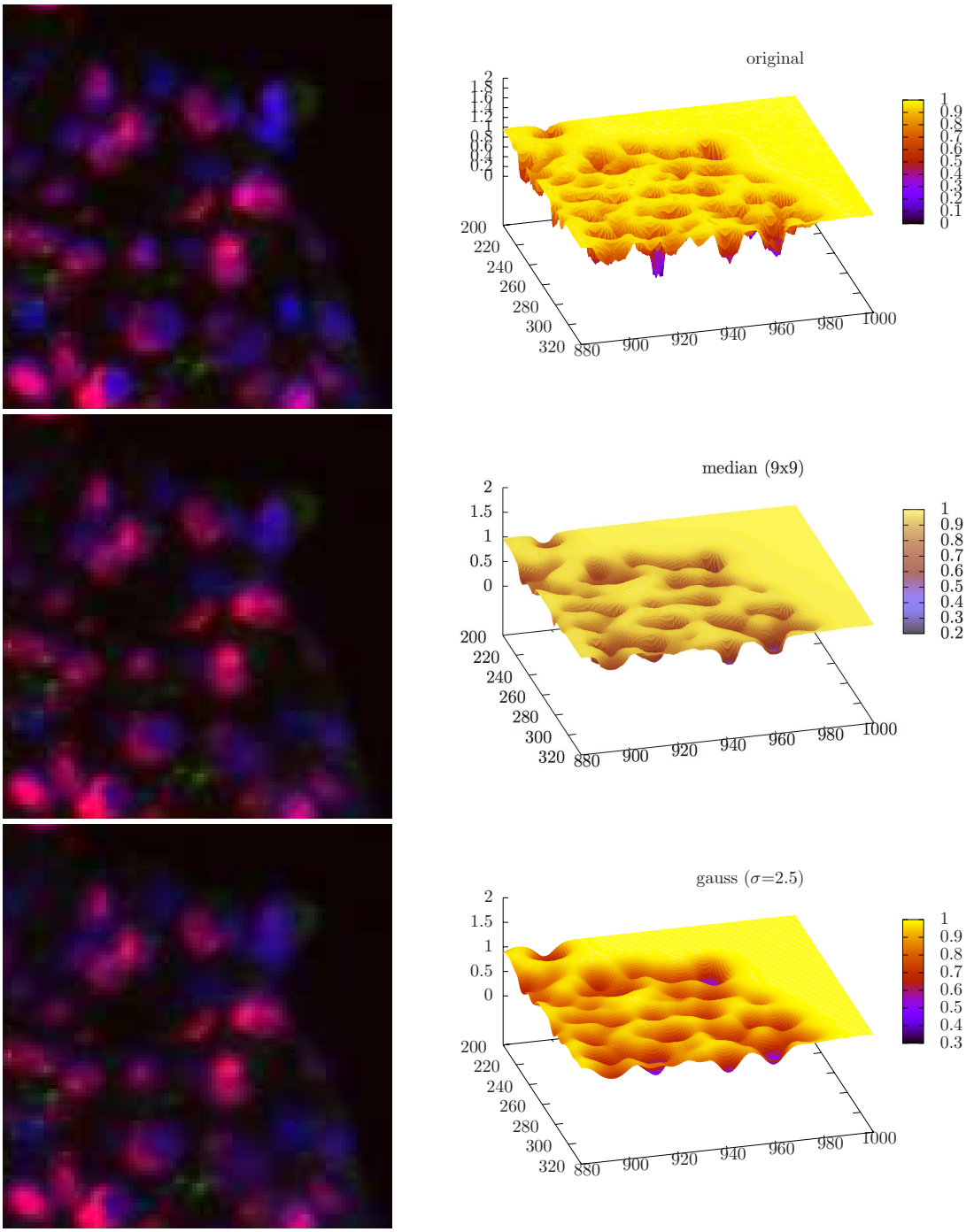

Figure 2.1: Image smoothing. The original image (*top*) was smoothed by two different filters: median filter (*center*) and Gaussian filter (*bottom*). The smoothed images (*left*) are visualized as landscapes of the inverted blue color channel intensities, $1 - I^{blue}$ (*right*).

What is a watershed? A watershed is the area of land (or landscape) that drains to a particular point along a stream (see figure 2.2(a)). The line dividing different of such areas is called *watershed line*. The areas they divide are called *catchment basins*.

Algorithm The idea of the algorithm is to treat the images as landscapes, where the color intensities $I[x, y]$ corresponds to the amplitude. The landscape representation of three example images are shown in figure 2.1. The local minima of the landscape are the minima of the corresponding *catchment basins* (see figure 2.2(b)). To detect the exact shapes of those basins, the landscape is successively "flooded" and pixels of the current altitude will be associated to the basin of the neighboring pixels (already associated to a basin). If two basins touch each other they will create a *watershed line* between each other and locally stop expanding. The algorithm either stops at a chosen maximum altitude (color intensity), or when none of the basins can expand anymore.

As each local minimum is giving rise to one *catchment basin*, it is important to smooth the images before the segmentation in order to avoid an over-segmentation [3].

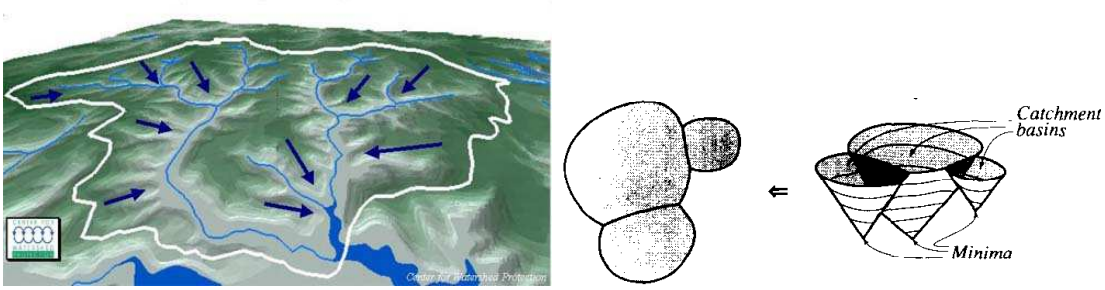

(a) Watershed in Landscape. (b) Creating Watersheds in Images.

Figure 2.2: Watersheds in landscapes and images. (a)Areas of land that drain to a particular point along a stream are called water sheds [Lab]. (b) The area associated to local minima of color intensities in an image can be estimated by the same concept [VS91].

2.3 Results of Image Processing and Image Analysis

In this section, at first the cell nuclei, the spheroid lumen and the spheroid border are extracted from the images. Then in a second step some quantitative analysis will be performed.

[3] A key problem in segmentation is that of splitting up into too few (under-segmentation) or too many regions (over-segmentation).

2.3.1 Nuclei Segmentation

The cell nuclei were stained with HOECHST staining (*blue color channel*, see figure 2.3). In order to segment the single nuclei, the images were smoothed by a series of four median filters with kernel size 3×3 (see section 2.2.1) as a preprocessing step. In the following, the watershed algorithm (see section 2.2.2) was applied to the inverted blue color channel, $1-I[x,y]^{blue}$, for pixels above a certain threshold, $I[x,y]^{blue} > I^{HOECHST}$ (see table 2.2). The threshold avoids the segmentation of the whole image, focusing only on regions clearly stained by HOECHST and thus associated with the cellular nuclei.

Figure 2.3(b) shows the result of the nuclei segmentation of figure 2.3(a). The red and blue areas are the detected nuclei.

2.3.2 Spheroid Lumen & Border

The base for estimating the spheroids borders are the cell nuclei (in section 2.3.1). By applying a series of dilation filters (see equation 2.8) will give a coarse approximation of the cell shapes around the nuclei. Finally, the empty spaces (necrotic areas) in the center of the spheroids are removed by hole-filling algorithms (e.g. by flood filling).

Figure 2.3(b) shows the estimated spheroid lumen around the cell nuclei in *green* color for an example picture (see figure 2.3(a)). The spheroid border is assumed to be the interface between the *green* (lumen) and the *black* (background) area(s).

2.3.3 Radial Profiles, Binning & Averaging

As the spatial arrangement of cell phenotypes and ECM density can be assumed to be concentric, the following sections will focus on extracting the statistical information as radial profiles. As figure 2.3(a) shows, the spheroids are not completely spherical, but slightly elongated and with irregular surfaces. To account for this, all statistics will be extracted as a function of distance to the spheroid border, defined by Δ_b, instead as a function of distance to the center of mass. For the estimation of the radial profiles *binning* is used. I.e. Δ_b is divided into small intervals $\Delta_{b,i}$, so-called *bins*, of $1\mu m$ length (image resolution: pice $= 0.98\mu m^2$). Then each nuclei who has at least one pixel whose distance to the closest border pixel is $\Delta_b \in [\Delta_{b,i}, \Delta_{b,i+1})$ will enter into the statistics of *bin* i. Then the statistical information in bin i or interval $[\Delta_{b,i}, \Delta_{b,i+1})$ is the average of all nuclei concerned. The average curves created from the radial profiles of single images are average values of the corresponding bins with the same index.

2.3.4 Nuclei Density & Cell Diameter

The local cell density can be estimated by the relation *number of nuclei per area*. Its inverse is the *area per nucleus*. Approximating the 2D cell shapes by a Voronoi diagram

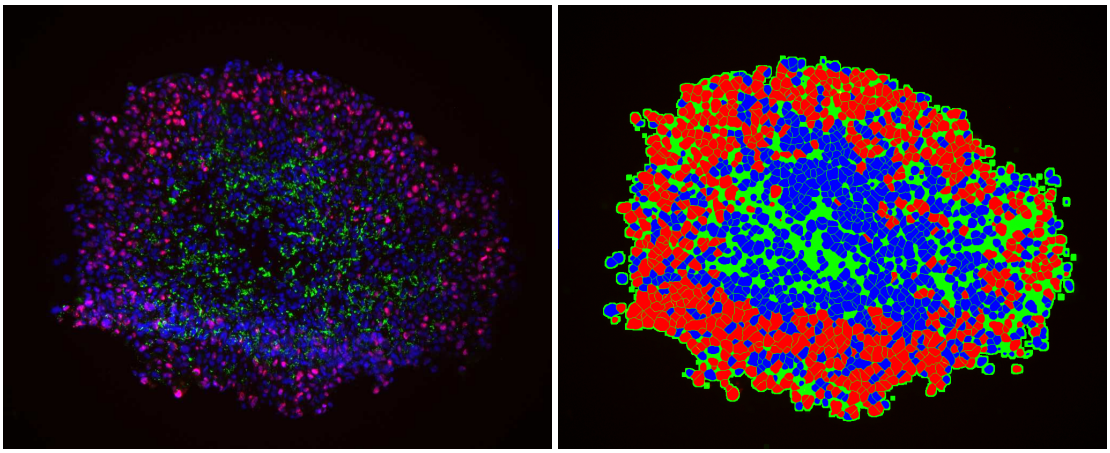

(a) Original Image (b) Segmented Image

Figure 2.3: Cell nuclei segmentation and spheroid lumen estimation. (a) The micrographs show a cryosection of a spheroid stained with HOECHST (*red*), Ki67 (*blue*) and ColIV (*green*). (b) The cell nuclei where segmented from the blue color channel (section 2.3.1) and differentiated between Ki67 positive (*red*) and negative (*blue*) nuclei by means of the red channel (section 2.3.5). The spheroid lumen (*green*) is approximated by inflated nuclei (section 2.3.2). For a more detailed view see figure 2.9.

of the segmented cell nuclei[4] (segmentation in section 2.3.1), the *area per nucleus* was estimated by the area of the corresponding Voronoi cell.

Figure 2.4 shows the result of the cell density estimation. In figure 2.4(a), one can see the Delaunay triangulation[5] of a set of segmented nuclei (from figure 2.3). The locally estimated cell diameter, $d_{cell}^{2D} \approx \sqrt{4/\pi(area\ per\ nucleus)}$, is plotted as function of distance to the spheroid border (figure 2.4(b)). One can see that in the outer parts cells are larger ($d_{cell}^{2D} = 16 - 17\mu m$) and decreases in size to a minimum ($d_{cell}^{2D} \approx 15\mu m$) the deeper you go inside the spheroid. This might be due to the larger fraction of proliferating cells in the periphery which as a consequence of cell growth on average have a larger size than quiescent cells. Even deeper (at $> 200\mu m$) the cell diameter increases again, which is rather an artifact of not considering the empty (non-cellular) area, and just reflects a lower cell density in the core region dominated by necrosis.

[4] A nucleus is represented as the center of mass of all pixels associated to the nucleus.
[5] The Delaunay triangulation is the dual representation of the Voronoi diagram.

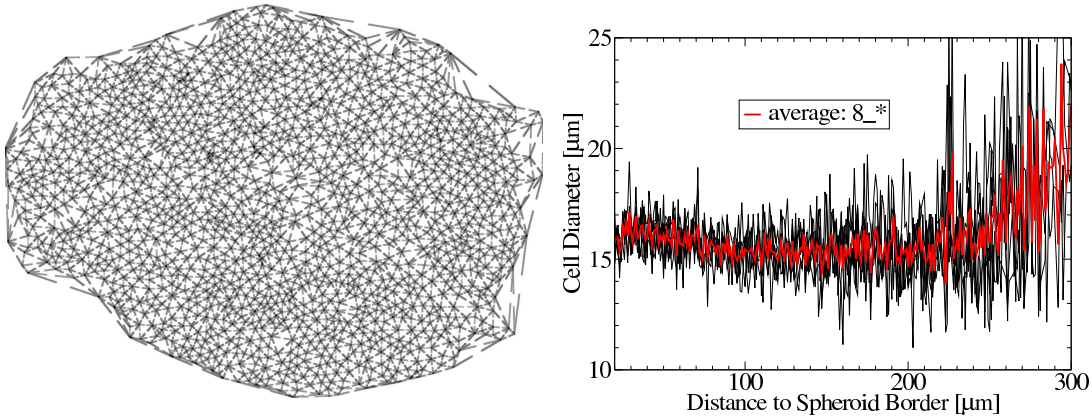

(a) Triangulation of cell nuclei (b) Radial Cell Size Profile

Figure 2.4: Cell density and cell size estimation. (a) The Delaunay triangulation of all segmented nuclei serves to estimate the cell sizes via its dual, the Voronoi diagram. (b) Average cell diameter as a function of distance to the spheroid border. The black curve is the average profile of six images (condition III, T3, see table 2.1) with bin size $1\mu m$ and the red curve is the gliding average with window size $10\mu m$.

Relating 2D Diameter (Cryosection) to 3D Diameter (Tissue)

The density of cells is defined by

$$\rho_{cells} = \frac{1cell}{1V_{cell}} = \frac{6}{\pi} d_{cell}^{-3}. \tag{2.10}$$

But how can one relate the nuclei density, ρ_{cells}^{2D}, within a two-dimensional tissue slice of thickness h_{slice} to the effective nuclei density in three dimensions, ρ_{cells}^{3D}? We assume the following

$$\frac{\rho_{cells}^{3D}}{\rho_{cells}^{2D}} = \frac{\text{number of cells intersecting with slice}}{\text{number of nuclei intersecting with slice}}. \tag{2.11}$$

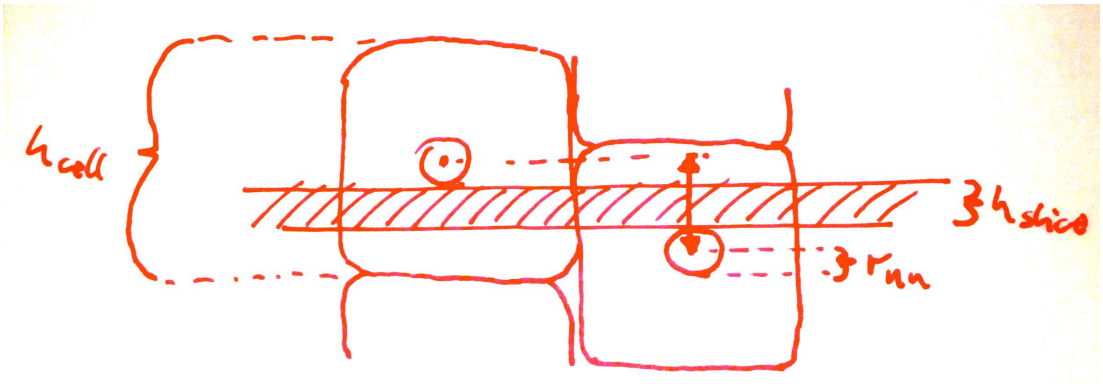

Figure 2.5: Schematic of cryo-section with height h_{slice} of a tissue of cells with height h_{cell} and nuclei radius r_{nu}.

Assuming all cells intersecting with the slice to be randomly transposed in lateral direction to the slicing plane and their nuclei to be in the center of the cell, then one can approximate the fraction of cells whose nuclei are intersected as well by

$$\frac{\text{number of nuclei intersecting with slice}}{\text{number of cells intersecting with slice}} \approx \frac{r_{nu} + h_{slice} + r_{nu}}{h_{cell}}, \tag{2.12}$$

where h_{cell} is the height of the cell, h_{slice} the thickness of the slice and $r_{nu} = d_{nu}/2$ the average nucleus radius.

Assuming cubic cell shapes ($h_{cell} = \sqrt[3]{\pi/6} d_{cell}$) and combining the equations 2.10, 2.11 and 2.12 lead to

$$d_{cell}^{3D} = \left[\sqrt[3]{6/\pi} \left(d_{cell}^{2D} \right)^3 (d_{nu} + h_{slice}) \right]^{1/4}. \tag{2.13}$$

Consequently, for given values of d_{nu} and h_{slice} (table 2.1(c)) the rescale radii for cells in the outer rim ($d_{cell}^{3D} = 16.9...18.2 \mu m$) and inside the spheroids ($d_{cell}^{3D} = 16.1...17.4 \mu m$). Both cell sizes are very close to each other. Assuming that almost no cells proliferate in the inner part of the spheroids and thus the measured radii represent the size cell have directly after division, this may suggests a low proliferating cell fraction even in the outer rim.

Alternative Method to Estimate the Cell Diameter

An alternative method to estimate the cell diameter from the images is to analyze the linear relationship between the number of cell nuclei and the distance to the spheroid border within a compact and spherical *in-silico* arrangement of cells. Then by applying

the same relation to the radial profile of the number of cells of the images can be used to approximate the average cell diameter.

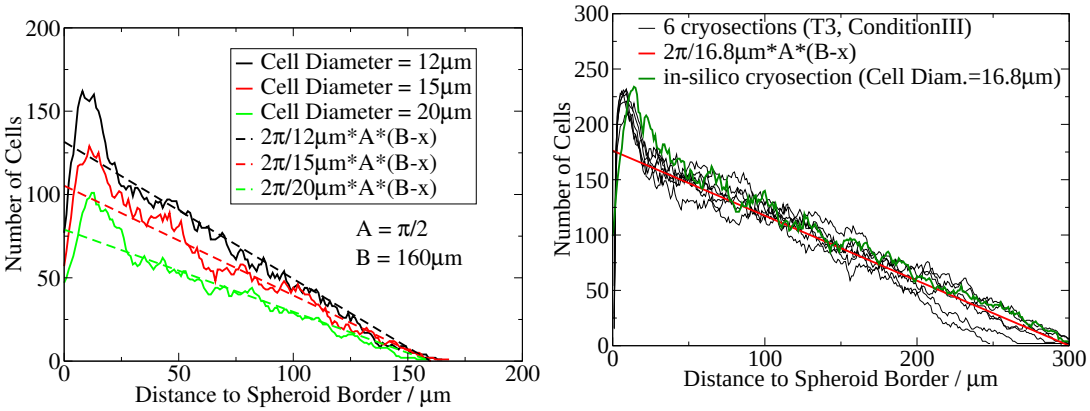

(a) *in-silico* arrangement (b) *in-silico* vs *in-vitro* arrangement

Figure 2.6: Cell diameter estimation. (a) The linear relation (*dashed line*) between the number of cells and distance to border can be adjusted *in-silico* (*solid lines*). (b) Fitting the same linear law to the curves extracted from images of *in-vitro* tumor spheroids gives a hint on the cell diameters.

As figure 2.6 illustrates, we find a cell diameter of $d_{cell} = 16.8\mu m$ which lies in the range of what was found above. Thus, in the following we will assume the cell diameter at the beginning of the cell cycle to be $d_{cell} = 16.8\mu m$.

Remark: The peek at the outer border is due to the rough surface of the spheroids. Consequently, a lot more cells are at the surface then predicted by the linear relation. The rougher the surface, the larger will be the peeks (in amplitude and width).

2.3.5 Estimation of Proliferating Cell Fraction

Ki67

The Ki-67 protein is a cell cycle specific protein and present during all cell cycle phases: in G_1, S and G_2 phase exclusively within the cell nucleus and during *mitosis* mostly relocated to the surface of the chromosomes. In cell in G_0 phase it is completely absent and thus an excellent marker for cell proliferation.

Automated Distinction

In order to quantify the cell proliferation, we have to distinguish between those nuclei which are *Ki67 positive* (*red*) and those which are not (*blue*). To distinguish between background noise (due to staining from different layer, image artifacts, etc.) and Ki67 positive nuclei we have to introduce hard measures which minimize the number of *"false positives"* and *"false negatives"*.

Via a *intensity threshold*, I^{Ki67}, we accept a pixel (x, y) to be Ki67 positive only if its red color intensity $I^{red}(x, y)$ is above a certain value

$$Ki67(x,y) = \begin{cases} 1 & , I^{red}(x,y) \geq I^{Ki67} \\ 0 & , I^{red}(x,y) < I^{Ki67} \end{cases} \tag{2.14}$$

Via a *fractional threshold*, φ^{Ki67}, we decide whether a nucleus X is Ki67 positive or not.

$$Ki67(X) = \begin{cases} 1 & , \frac{1}{|X|} \sum_{(x,y)\in X} Ki67(x,y) \geq \varphi^{Ki67} \\ 0 & , else \end{cases} \tag{2.15}$$

Depending on how one chooses the parameters I^{Ki67} and φ^{Ki67} one can control the acceptance of heterogeneously (small φ^{Ki67}) and weakly (small I^{Ki67}) stained nuclei.

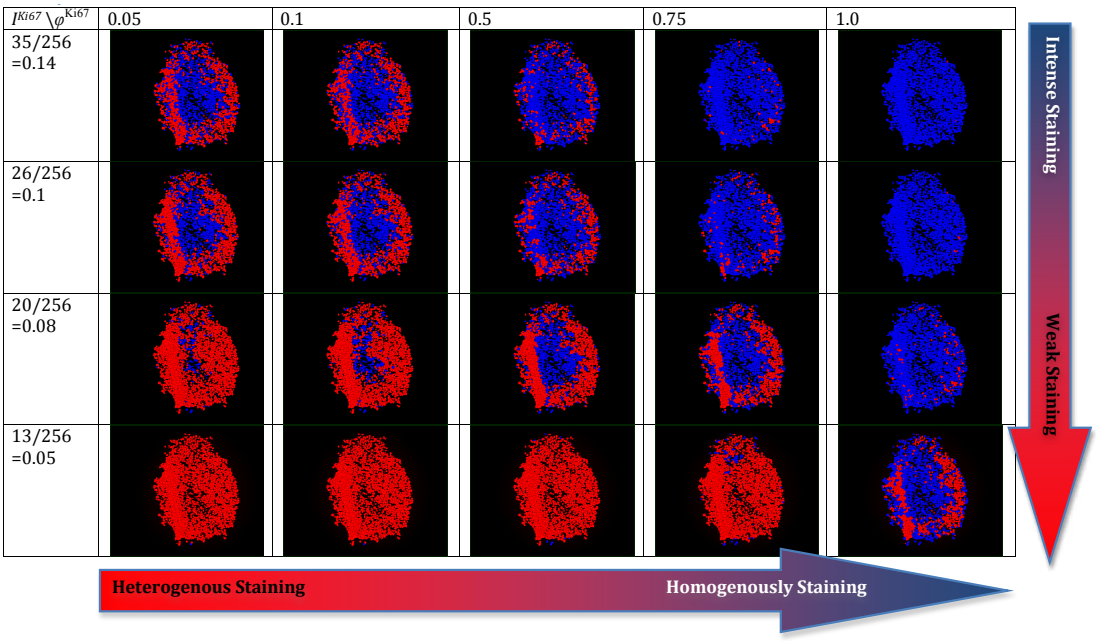

Figure 2.7: Sensitivity analysis for threshold parameters I^{Ki67} and φ^{Ki67}.

As figure 2.7 illustrates very different combinations of parameters lead to very similar patterns of proliferating cells in the outer parts and with a decreasing tendency toward the center. Although the global patterns look similar (e.g. $I^{Ki67} = 0.14, \varphi^{Ki67} = 0.1$ and $I^{Ki67} = 0.08, \varphi^{Ki67} = 0.75$) the detected cells might differ a lot and be a result of artifacts (as e.g. falsely detected cells covered by stained remainings of scattered cell from different layer/slice).

Evaluation of Method

In order to evaluate the predictive value of the method, one image section (see figure 2.10) was manually analyzed by distinguishing the visible nuclei into Ki67-positive and Ki67-negative by hand. Then for automated detection using different values for φ^{Ki67} and I^{Ki67}, we count the number of nuclei which are *true positive* (TP)[6], *true negative* (TN)[7], *false positive* (FP)[8] and *false negative* (FN)[9]. In the following one can calculate the *sensitivity* or *true positive rate* indicating the proportion of nuclei that tested positive of all the nuclei that actually are positive

$$TPR = \frac{TP}{TP + FN}, \tag{2.16}$$

the *specificity* or *true negative rate* indicating the proportion of nuclei that tested negative of all the nuclei that actually are negative

$$TNR = \frac{TN}{TN + FP}, \tag{2.17}$$

and the classification error indicating the proportion of falsely classified nuclei of all nuclei

$$\epsilon = \frac{FP + FN}{TP + FP + TN + FN}. \tag{2.18}$$

Figure 2.8 shows the values of the above-described indicators applying automated detection to the benchmark image in figure 2.9 (*left*) for wide parameter ranges of φ^{Ki67} and I^{Ki67}.

An good agreement (small classification error) between automated and manual Ki67 detection was reached for rather small fractions of the nuclei ($\varphi^{Ki67} \leq 0.2$) stained with a moderate intensity ($0.35 \leq I^{Ki67} \leq 0.5$). The parameter values which will be used in the following can be found in table 2.2 and the corresponding comparison of manually and automatically detected Ki67-positive nuclei is shown in figure 2.9.

[6] correctly detected to be positive
[7] correctly detected to be negative
[8] negative, but falsely detected to be positive
[9] positive, but falsly detected to be negative

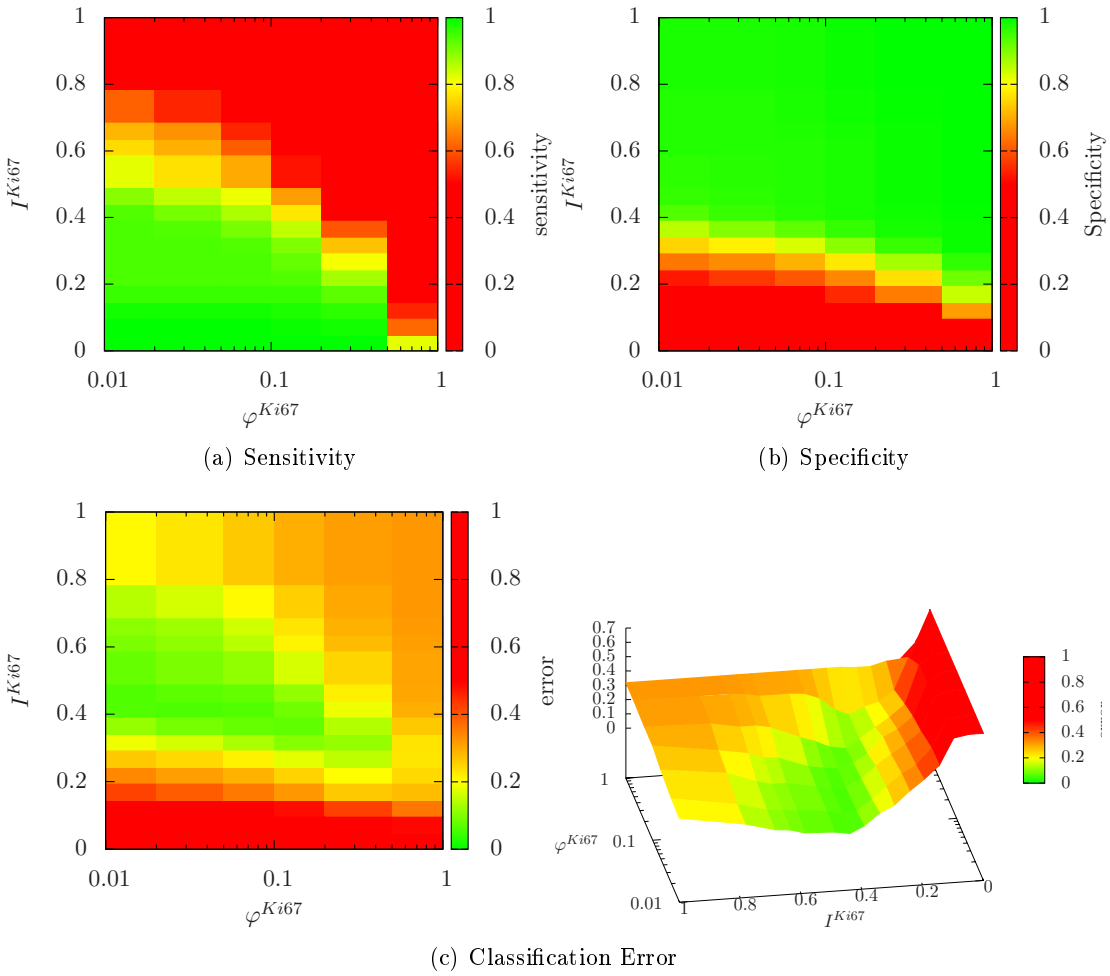

(a) Sensitivity

(b) Specificity

(c) Classification Error

Figure 2.8: Sensitivity analysis for threshold parameters I^{Ki67} and φ^{Ki67}.

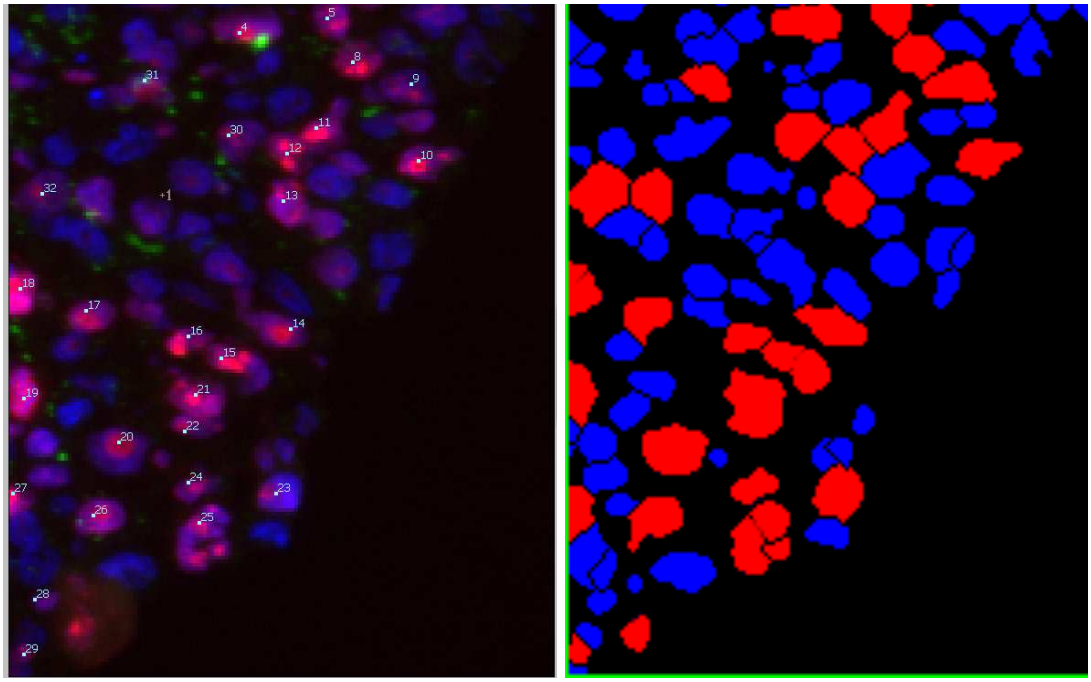

Figure 2.9: Manual versus automated image analysis. *left*: For one image the Ki67 positive nuclei were marked by hand. *right*: By successively varying the threshold parameters I^{Ki67} and φ^{Ki67} the automated detection showed comparable results.

Parameter	Value
$I^{HOECHST}$	0.15
I^{TUNEL}	0.45
φ^{TUNEL}	0.20
I^{Ki67}	0.35
φ^{Ki67}	0.05

Table 2.2: Image processing parameters.

Postprocessing: Proliferating Cell Fraction & Proliferating Cell Density

Once all Ki67 positive nuclei are detected, some statistical analysis can be done on the spheroids. By measuring the distance of each nucleus (represented by the center of mass of related pixels) (see section 2.3.1) to the closest spheroid border (see section 2.3.2) one can estimate the number of Ki67 positive and negative nuclei as a function of the distance to the outer border (see figure 2.10, *left*). Dividing the number of Ki67 positive nuclei by the total number of nuclei gives us a estimate of the proliferating cell fraction

(see figure 2.10, *right*). Multiplying the cell fraction with the cell density (see section 2.3.4) gives us the density of Ki67 positive nuclei.

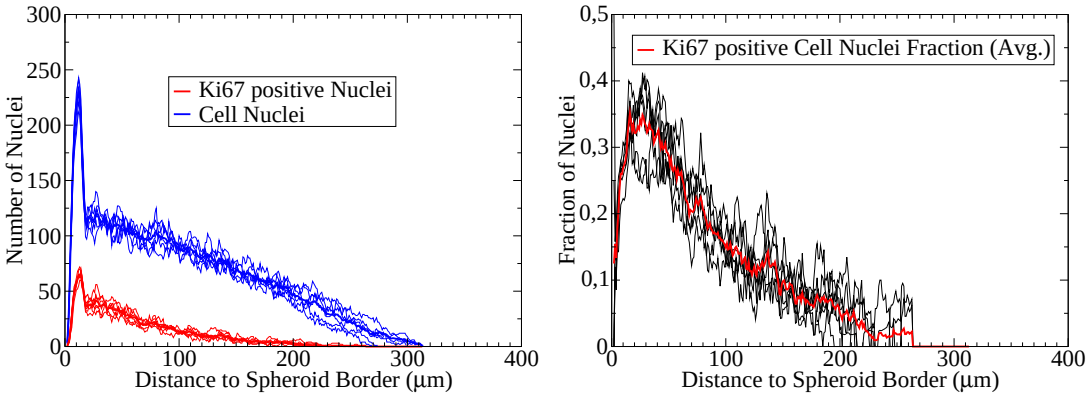

Figure 2.10: Proliferating cell fraction. *left* Radial profiles of the total number of nuclei (*blue*) and the nuclei detected to be Ki67 positive (*red*). *right* Dividing both profiles gives the radial profile of the fraction of proliferating cells. The proliferation profile (*thick line*) is a result of averaging over 6 independent curves (*thin line*) extracted from different images (T3, Condition III).

2.3.6 Estimation of Apoptotic/Necrotic Cell Fraction

A common method to identify apoptotic cells is the *terminal deoxynucleotidyl transferase dUTP nick end labeling* (TUNEL). It detects DNA fragmentation which typically occurs in the last phase of apoptosis, but might as well label the remainings of a necrotic cell.

In a similar procedure as for proliferating cells (see section 2.3.5), the necrotic cell nuclei can be detected using an *intensity threshold* I^{TUNEL} and a *fractional threshold* φ^{TUNEL} to detect TUNEL stained cells.

2.3.7 Estimation of Extra-Cellular Matrix Density

Beside Ki67 and TUNEL the images were stained for collagen type IV (ColIV) in green color (see figure 2.3(a)). ColIV is mainly found in the basal lamina, i.e. a layer of ECM secreted by the epithelial cells, which makes it a marker for ECM.

To quantify the ECM, we will use the local intensity of ColIV staining (green color channel), $[ECM] \sim I^{green}$. For each pixel (x, y) of the spheroid lumen (see section 2.3.2) we can determine the distance to the spheroid border (i.e. distance to closest border pixel), $\Delta_b(x, y)$, and average their ColIV intensities $I^{green}(x, y)$ as a function of

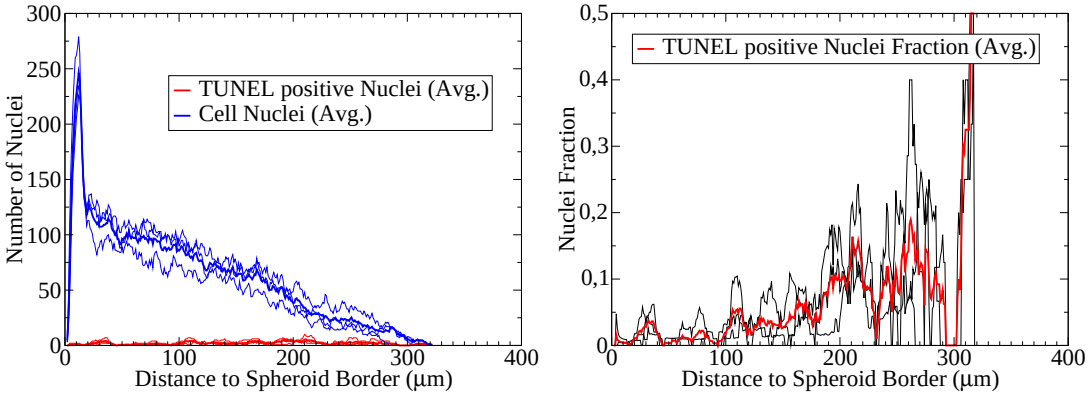

Figure 2.11: Apoptotic cell fraction. *left*: Radial profiles of the total number of nuclei (*blue*) and the nuclei detected to be TUNEL positive (*red*). *right*: Dividing both profiles gives the radial profile of the fraction of apoptotic cells. The apoptosis profile (*thick line*) is a result of averaging over 3 independent curves (*thin line*) extracted from different images (T3, Condition III).

the Δ_b

$$\overline{I}^{green}(\Delta_b) \quad = \quad \frac{\sum_{\Delta_b(x,y)=\Delta_b} I^{green}(x,y)}{\sum_{\Delta_b(x,y)=\Delta_b} 1} \tag{2.19}$$

Figure 2.12 shows the estimated ColIV intensity profiles for a image stack of spheroids grown under similar conditions.

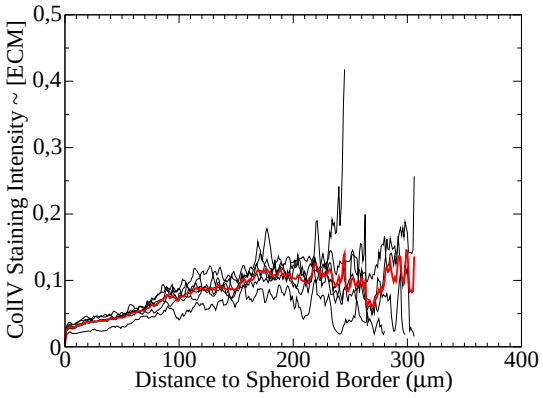

Figure 2.12: ColIV staining intensity profile. The extra-cellular matrix (ECM) profile (*thick line*) is a result of averaging over 6 independent ColIV staining intensity profiles (*thin line*) extracted from different images (T3, Condition III).

2.4 Conclusions & Discussion

With a number of image processing tools, we preprocessed stained cryosections of tumor spheroids which were grown under four different nutritional conditions [MM]. The cell nuclei have been segmented from the blue color channel (HOECHST staining) and the spheroid lumen was approximated by inflating the nuclei.

The cell size was estimated via a Voronoi tessellation of the segmented nuclei.

In the following we established an automated detection of proliferating and apoptotic nuclei. The red color channel intensities within the segmented nuclei were evaluated via two thresholds, a pixel-wise intensity threshold and a nuclei-wide fractional threshold, in order to decide if a nuclei is Ki67 (or TUNEL) positive and thus in proliferation (or apoptosis). Both threshold could be adjusted such that we get a good agreement between a few manually evaluated images and the automatic detection.

At last, the radial profiles of the proliferating and apoptotic nuclei fractions as well as the ECM density were determined as functions of distance to the spheroid border. The averaged profiles among all images of the same nutrimental condition and time point can be seen in figure 2.14 and 2.13. In addition to the proliferating/apoptotic nuclei fraction, figure 2.15 shows the density profiles of proliferating/apoptotic nuclei.

Cell Proliferation Commonly, it can be observed that the proliferating cell fraction (figure 2.14, left) reaches its highest value at a depth of 20-30μm. Toward the outer border and toward the spheroid center the proliferative activity continuously decreases. At a depth of 200-250μm the proliferating cell fraction approaches 0. Furthermore, with time advancing the profiles lower in amplitude. At T6 (= 46days) there is almost no proliferative activity anymore. So most of the cells became quiescent. An exception are the profiles of condition I - we remark that condition I has the lowest glucose per oxygen ratio of all conditions: $[G]/[O_2] = 3.6$ (for other conditions: II:17.9, III:89.3, IV:357). Here - in contrast to the other conditions - after an initial drop the proliferating cell fraction increases toward the spheroid center and with time advancing the profiles amplitude even increases. This might be due to the cells being deprived of glucose at the beginning. Later on, they digest the accumulating material of dying cells. Thus, the digestion of dead cells may allow them to regain proliferative activity. Small peeks in the profiles of other conditions (II and IV) in the spheroid center seem to confirm that.

Apoptosis The radial profiles of apoptosis (nuclei fraction and density, figures 2.14 and 2.15, left) have opposite shapes to the proliferation profiles. There is very little apoptosis found at the outer part, while toward the spheroid center it is increasing. In time, the profile amplitudes increase (from T3 to T5) and then drop to a very low level ($< 10\%$ at T6). It seems, that in the phase of growth saturation, the cells stopped

dividing and the spheroids remain at a size sufficiently small to nourish all cells and to avoid further cell death. Especially interesting is the comparison of condition II and III. For condition III there seems to be almost no apoptosis in the outer zone of a depth of around $150\mu m$ followed by a sudden increase. On the other hand, spheroids growing under nutrimental condition III initially show very few apoptosis (T3). The profiles have a smooth shape. Interestingly, at later stages (T4) those smooth profiles increase in amplitude among the whole spheroid. In the outer parts, one can observe now much more apoptotic cells than for condition II, though the amount of glucose in the medium is five times higher! This indicates that under condition III the reason for increased cell death in the outer regions can not be nutrimental deprivation. We suggest that it is due to accumulating lactate which cells produce as a waste product under over-saturation of glucose.

Extra-cellular Matrix (ECM) The ECM density (figure 2.13) shows very similar radial profiles for all conditions. At the outer border we find a base level of ECM density. With increasing depth the ECM density increases reaching a saturation at a value around 0.15. As cells in the outer parts are younger than cells deeper inside the spheroids the observed increase in ECM density might be a result of continuously produced ECM accumulating around the cells. The density of saturation might be the result of continuous production and the auto-degradation of ECM reaching an equilibrium. At a depth of around 150 μm the ECM density decreases toward the spheroid center. This coincides with the increased occurrence of apoptosis which seems to shift the equilibrium of production and degradation to lower values as the overall density of viable cells diminishes.

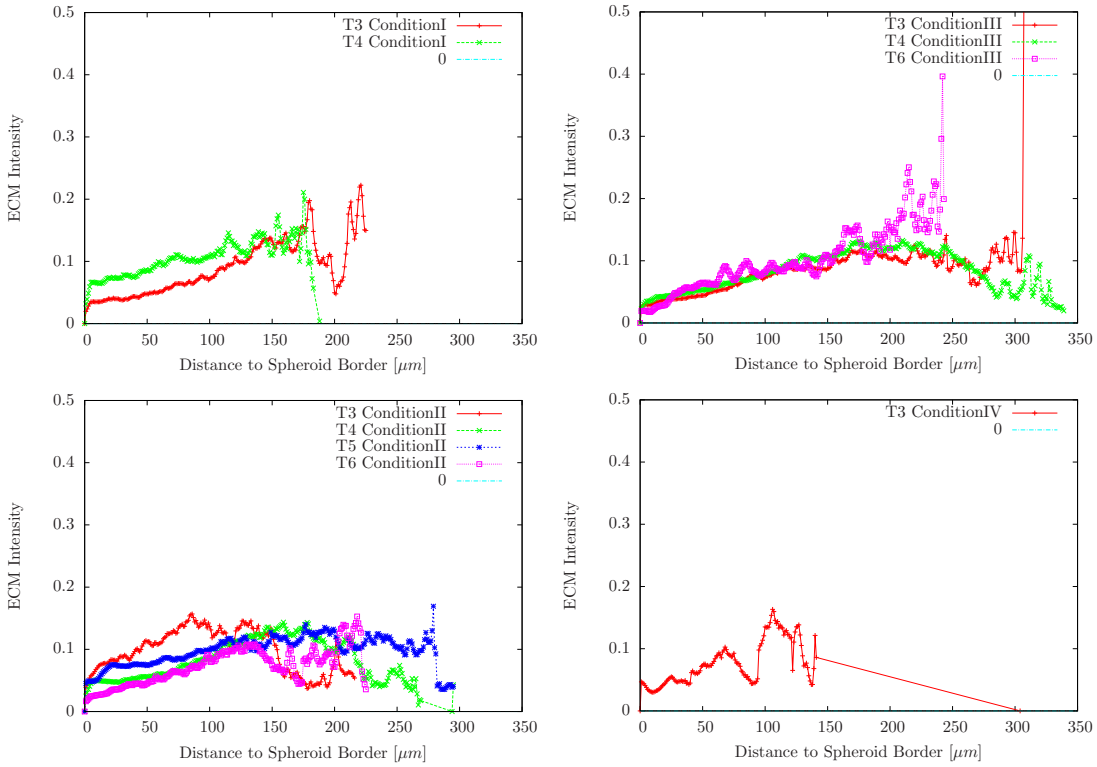

Figure 2.13: Extra-cellular matrix density. The curves show the radial profiles of the ColIV intensity. All curves are averages over the profiles extracted from single images taken at the same time Tx ($x \in \{3, 4, 5, 6\}$) and same culture condition $y \in \{I, II, III, IV\}$.

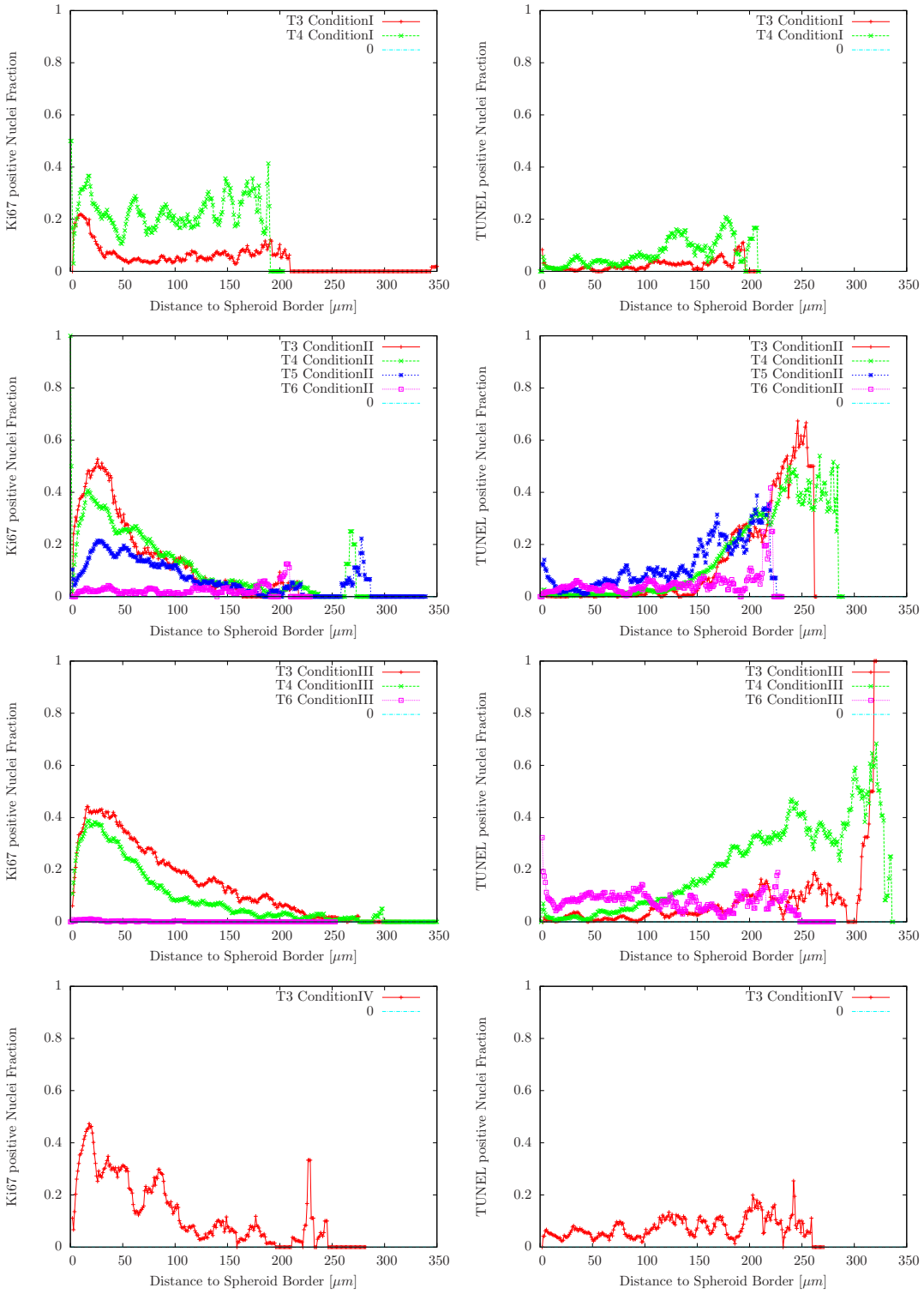

Figure 2.14: Proliferating and apoptotic nuclei fraction. The curves show the radial profiles of the Ki67 positive (*left*) and TUNEL positive (*right*) nuclei fractions. All curves are averages over the profiles extracted from single images taken at the same time Tx ($x \in \{3, 4, 5, 6\}$) and same culture condition $y \in \{I, II, III, IV\}$.

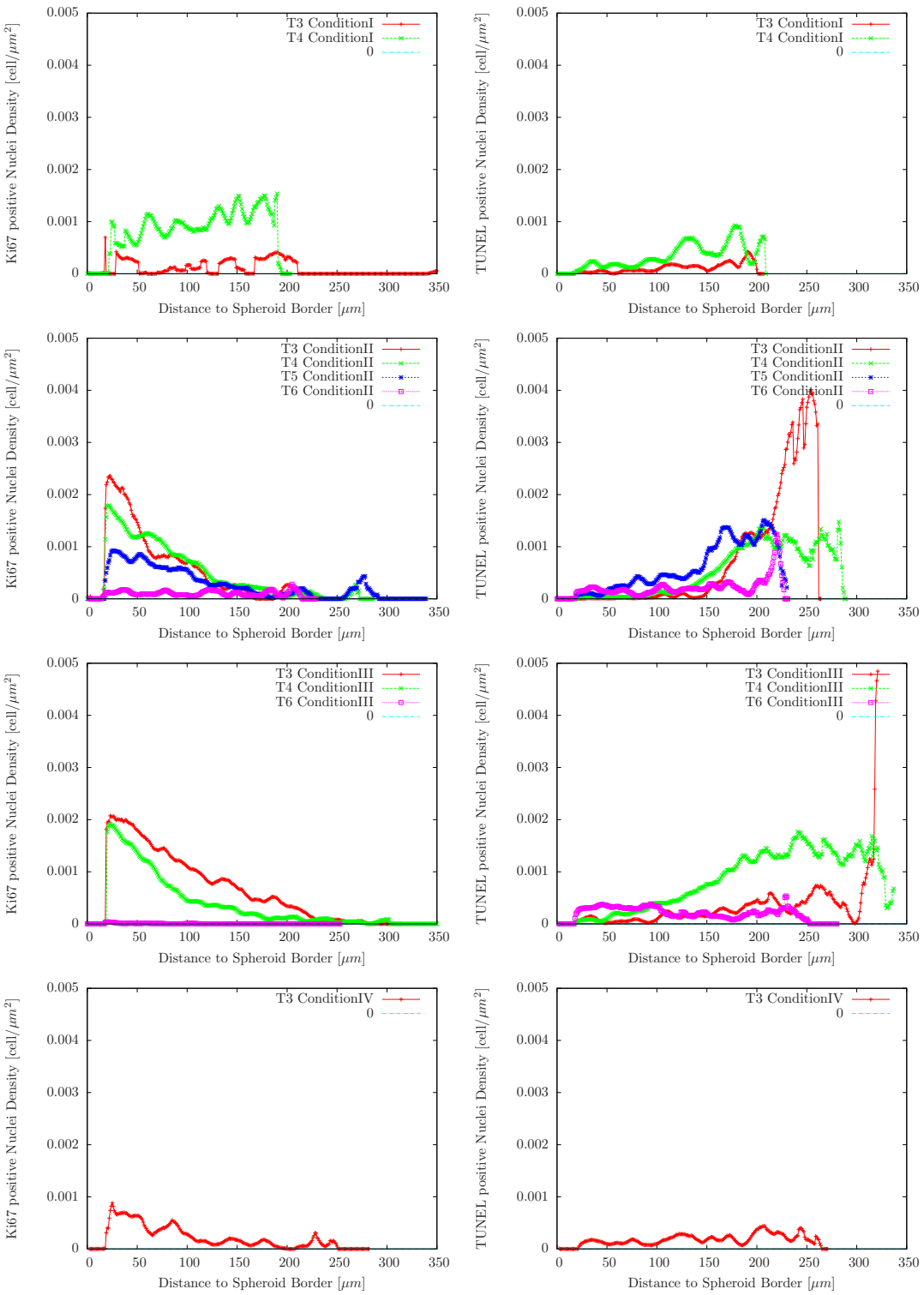

Figure 2.15: Proliferating and apoptotic nuclei density (2D). The curves show the radial profiles of the Ki67 positive (*left*) and TUNEL positive (*right*) nuclei densities. All curves are averages over the profiles extracted from single images taken at the same time Tx ($x \in \{3, 4, 5, 6\}$) and same culture condition $y \in \{I, II, III, IV\}$.

Chapter 3

Multi-scale Modeling Framework for Avascular Tumor Growth

The goal of this chapter is to successively set up a multi-scale model for *avascular tumor growth* based on common knowledge (literature) on tumor spheroids grown *in-vitro*. After a brief background on tumor spheroids, the different model components - for tumor cells and involved molecules - will be introduced. This model framework will be the subject of parameterization in the following chapter 4.

Contents

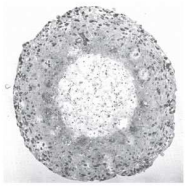

3.1 Multi-cellular Tumor Spheroids

3.1.1 Why spheroids?

MCTSs are a well established system for cultivation and study. MCTSs can be grown from many cell types (especially tumor cell lines) with little time and small efforts. Perfect system to study the population dynamics of a single cell type under very controlled conditions (impossible in in-vivo experiments).

3.1.2 Observation

Looking at MCTSs we are confronted with an interplay of very different mechanisms on the microscopic scale leading to a concentric organization on the macroscopic scale (see figure 1.3(b), ref. [HMD$^+$10]) and a sequential arrangement of distinguishable growth phases on the temporal scale (see figure 3.1, ref. [FS86, CZ83]):

1. *Geometric Progression* or *Exponential Growth Phase*: All cells are proliferating.
2. *Linear (radius) growth phase*: Cell proliferation is limited to a rim of a fixed thickness ΔL, while cells in the center are growth inhibited.
3. *Saturation*: The size of the tumor spheroid does not exceed a certain size. Probably due to
   (a) *homeostasis* of proliferating and dying cells as well as cell migration toward the center, or
   (b) *growth inhibition* induced by nutrient limitation and the accumulation of waste products.

Hereby, the occurrence of the single phases and their temporal extent depend very much on the cell type and the environmental conditions as the composition of the growth medium (nutrients, growth factors, substrates etc.).

Model-derived explanations for the occurrence of the different phases reach from growth and survival promotors and inhibitors (growth factors, nutrient limitation, lactate intoxication etc.)(e.g. [Cha96, WK97, JPGCF05, MMA$^+$09]) to mechanically induced growth inhibition (e.g. [AM02, BP03, DH03, DH05, SMH05, DHB07]).

3.1.3 Modeling Challenge

The difficulty is not to find *a* mechanism that qualitatively and/or quantitatively can describe the experimental observations, but to validate different possible mechanisms and identify *the* mechanism closest to "reality". This is the key of constructing a predictive tool.

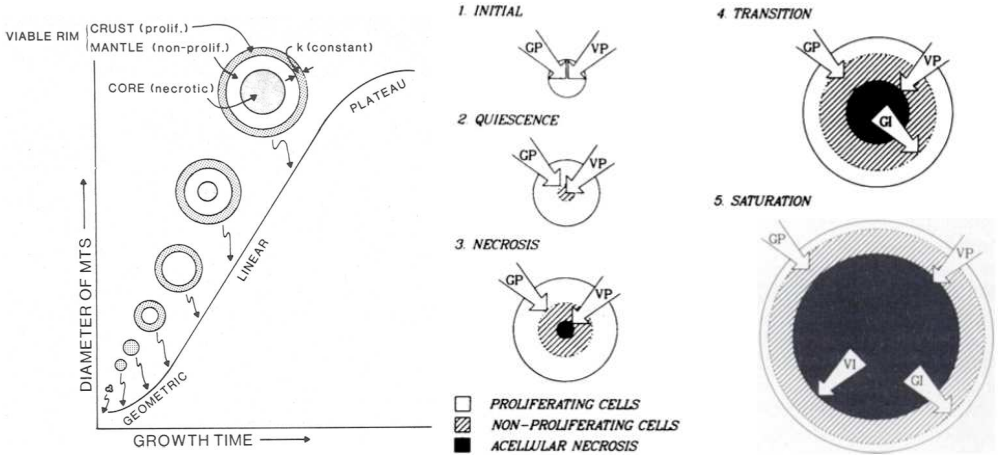

Figure 3.1: Temporal evolution of the concentric arrangement of MCTSs[CZ83]. A representation of the model for the interaction of growth promoters (GP), viability promoters (VP), growth inhibitors (GI) and viability inhibitors (VI) at different stages in the growth of a spheroid. Arrows indicate the direction and extent of penetration into or cut out of the spheroid; shading indicates the presence of proliferating cells, non-proliferating cells, and acellular necrosis. Details of the model are given in the text [FS86].

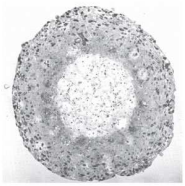

Thus, in this chapter we will construct a multiscale model framework for avascular tumor growth which comprises several mechanisms which on the macroscopic scale compete for the similar effects. E.g. mechanical vs. nutrient-limited growth inhibition, cell-cell-adhesion-driven vs morphogen-driven migration and starvation-induced vs. waste-product-induced cell death. In chapter 4, several opposing mechanisms will be evaluated in comparison to data.

3.2 A Stochastic Cellular Automaton Approach

The model used to represent the tumor cells and to mimic their spatio-temporal behavior is an extension of [RBH+09].

3.2.1 Infrastructure / Spatial Representation

Lattice-based and Agent-based:

In order to later on upscaling to large scales, we will be interested mainly in a lattice-based environment for biological cells. That means that our n-dimensional domain $\Omega \subset \mathbb{R}^n$ is subdivided into an spatial tessellation. Biological cells will be considered as individual discrete objects, also called *agents*, which populate the tiles of this tessellation and use it as a kind of infrastructure like cars a network of streets.

Cell Shapes and Choice of Tessellation:

Isolated cell can have very different cell shapes. Due to adhesion and the formation of cell-cell-bounds, cells in aggregation rather have a polygonal shape. As illustrated by figure 3.2 the Voronoi tessellation of a irregularly distributed set of construction points is a suitable representation of cell shapes and avoids sufficiently the occurrence of lattice artifacts [Dra05].

3.2.2 Spatio-Temporal Evolution & Model Processes

The spatial and temporal evolution of the system is considered to be stochastic following the characteristic distributions for the duration of the mimicked biological processes and the spatial directions. Therefore, the average system behavior is calculated by solving the corresponding master equation numerically with the Gillespie algorithm [Gil77] (see section B.2.2). Consequently, all temporal distribution will be limited to be exponential or Erlang distributed (see section B.2.3).

In the following the main biological processes taken into account and their modeled counterpart will be described in detail.

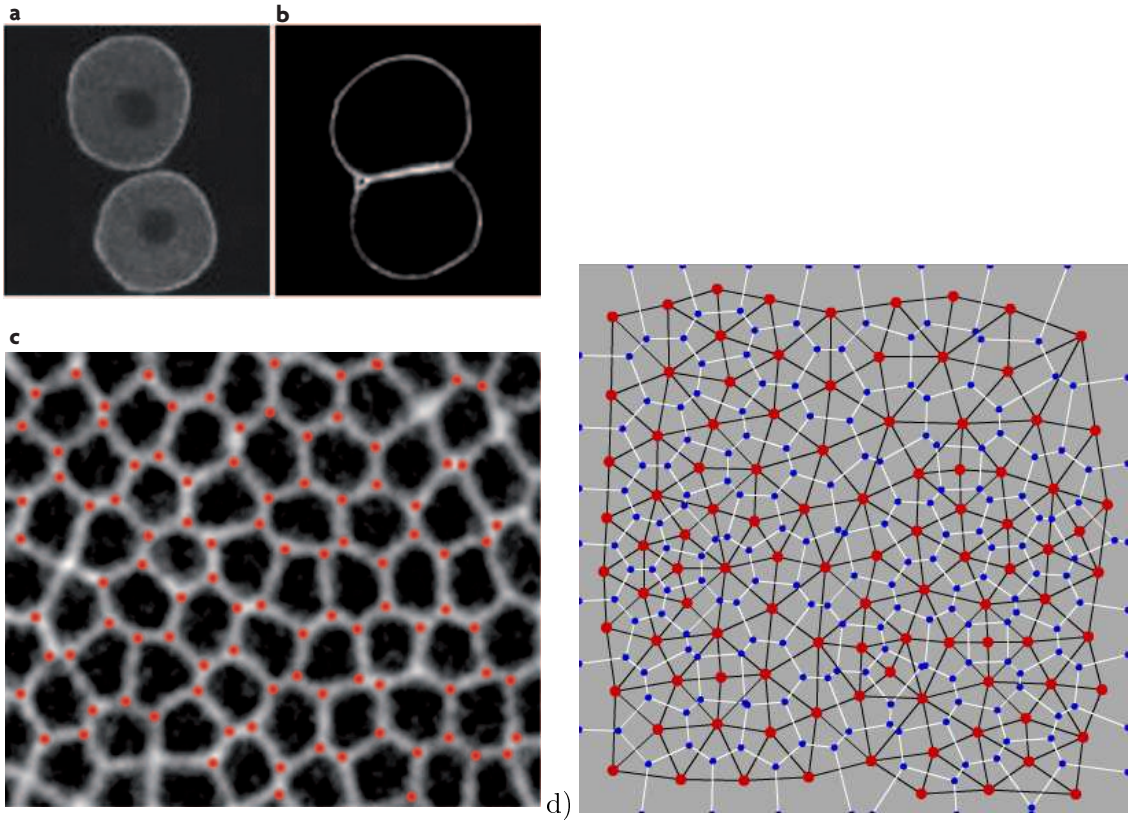

Figure 3.2: Cell shape in aggregation and Voronoi tessellation[LL07]. *a*) Isolated cell have a round shape, but depending on the cell type can have very different shapes. *b*) In contact with other cells they form cell-cell-bounds and rather flat interfaces. *c*) Cell aggregates have polyhedral pattern very similar to *d)* Voronoi tessellations composed of Voronoi cell (*white lines* and *blue vertices*). Its dual is the Delaunay triangulation (*black lines* and *red vertices*).

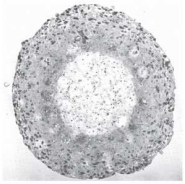

3.2.3 Cell Replication

Cell Cycle:

In order to perform a cell division a cell has to undergo a chain of steps and processes until it finally can physically divide into two separate cells. This chain of processes is called the cell cycle and can be mainly divided into the following phases: G1-phase, S-phase, G2-phase and M-phase (see figure 3.3(a)). Cells which are not dividing are generally arrested in the G0-phase. Then they are called quiescent. During the cell cycle cells have to double their genetic code (S-phase), volume (G1, S & G2-phase) and cell organelles.

The time each cell takes from the moment of entrance into the cell cycle until the physical division can vary among a population of cell and follows a specific distribution. The shape of this distribution might change between different cell types and environmental conditions.

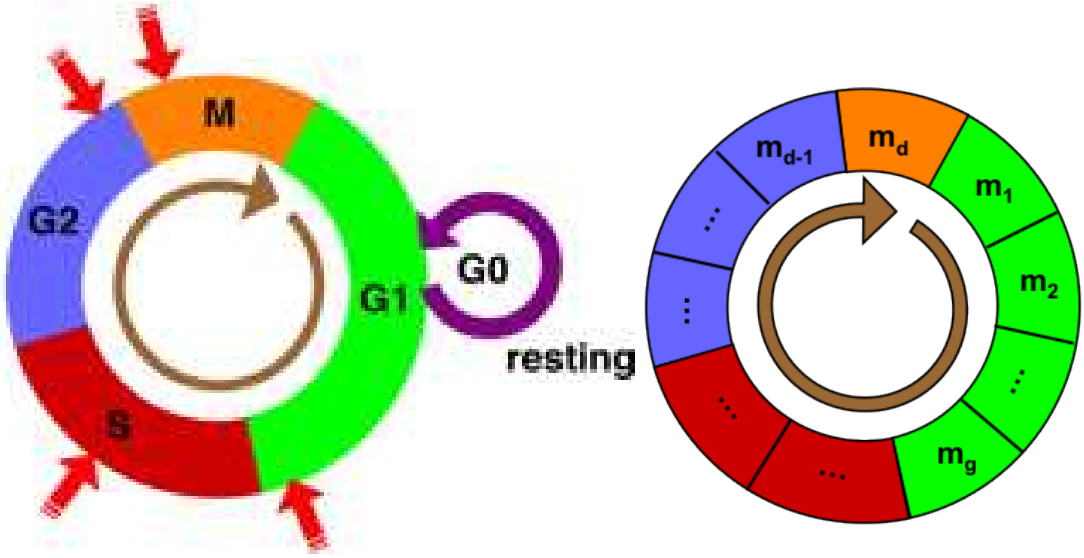

(a) cell cycle scheme (b) chain of Poisson processes

Figure 3.3: Cell cycle. (a) Schematic diagram of the cell cycle illustrates the cell cycle phases (*G1*, *S*, *G2* and *M*), the resting phase (*G0*) and the cell cycle checkpoints (*red arrows*). (b) Cell cycle is modeled by a chain of Poisson processes.

In the multi-cellular model the cell cycle is mimicked by a chain of Poisson processes which a cell has to pass until actually two cells emerge from it (see figure 3.3(b)). The waiting time of a process composed by Poisson processes becomes Erlang distributed with a distribution shape parameter $m \in \mathbb{N}$ which corresponds to the number

of sub-processes. This enables the model to capture a variety of different cell cycle time distribution shapes from exponentially distributed cell cycle times ($m = 1$) to very sharp Erlang-distributed cell cycle times ($m \to \infty$) (see figure 3.4 for examples). Measurements of cell-cycle time distributions have shown to be consistent with a gamma distribution ([Ken48, Pow55]) which is the continuous version of the Erlang distribution with $m \in \mathbb{R}$. On the other hand side, single subprocesses m_i $(m_1, m_2, ..., m_d)$ can be related to the different cell cycle phases (G1, S, G2 and M) or to specific events as checkpoints, volume growth (m_g) and cell division (m_d).

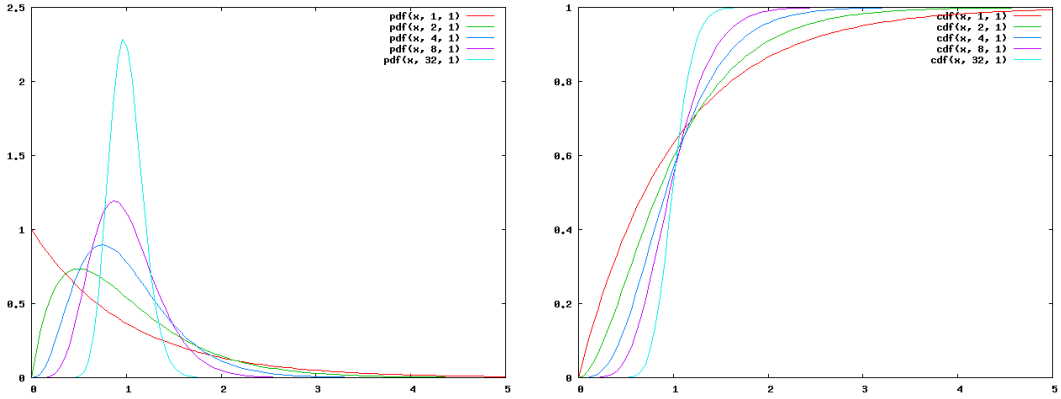

Figure 3.4: Sensitivity of Erlang distributed cycle times in respect to Erlang number m. *left:* Probability density function $p(x) = \frac{x^{m-1}e^{-x/(m\tau)}}{(m\tau)^m(m-1)!}$. *right:* Cumulative distribution function $cdf(x) = \sum_{n=0}^{m-1} \frac{1}{n!} e^{-x/(m\tau)} \frac{x}{m\tau}^n$.

Figure 3.5 compares the measured cell cycle time distribution of retinal progenitor cells [GZC+11] with the Erlang distribution. One can see that Erlang number $m = 10$ gives a reasonable fit and will be used in the following as the default value.

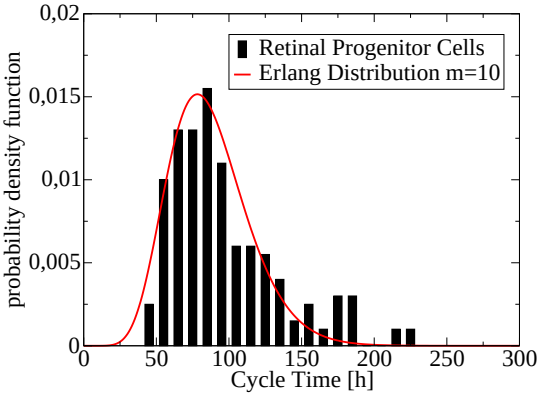

Figure 3.5: Cycle time distribution of retinal progenitor cells [GZC+11] (*black*) compared to a Erlang distributed cell cycle time for Erlang number $m = 10$ and division rate $\tau^{-1} = 87h^{-1}$ (*red*).

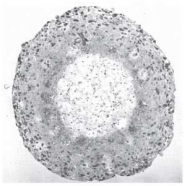

First Double Volume, Then Divide

Usually cells first double their volume during the G1-phase before they decide to replicate their DNA (S-phase) and divide into two daughter cells (M-phase). We define m_g the instant when the volume doubling takes place, $1 \leq m_g \leq m_d$. By default a cell in cell cycle step m_g will then occupy one randomly chosen free neighbor site.

Figure 3.6: Growing cell expandes to free neighbor site.

Spatial Growth Limitation

If there is no more free space available for a growing cell to expand to, the cell will become quiescent. Here the definition of "no space" varies a lot among different types of cells:

1. Contact-Inhibition: Many cells stop their growth and division in the case they are completely surrounded by other cells. This is know for example for epithelial cells which grow as a monolayer in petri dishes until convolution and then stop dividing.
2. Density-Inhibition: Tumor cells are known for their loss or perturbation of the mechanisms regulating cell proliferation. Thus even cells completely surrounded by other cells still continue to divide. Nevertheless, it was observed (ref. [FS86]) that only the outer rim of spheroids shows a proliferative activity. This implies a certain maximal distance ΔL which cells are able to rearrange their local neighborhood in order to double their cell volume and divide.

So generally speaking before a cell is expanding it evaluates its neighborhood within a radius of ΔL for free lattices sites.

Rearrangement / Shifting

In the case of a cell being completely surrounded by other cells a growing cell first pushes its neighboring cells along the shortest path toward the closest free lattice site before expanding to the liberated one (see figure 3.7).

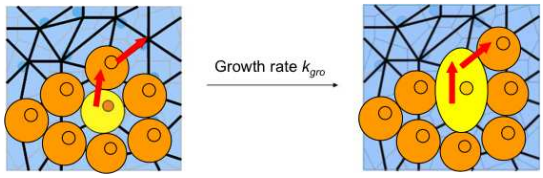

Figure 3.7: Growing cell shifts cells toward closest free lattice site before expanding to neighbor site.

Cell Division

At the end of the cell cycle, $m = m_d$, the mother cell will divide into two daughter cells by replacing the old agent by two new agents which each for its self will occupy one of the mother cells lattice sites.

Figure 3.8: At the end of the cell cycle the cell divides into two daughter cells.

3.2.4 Cell Motion

Cell motion in general can be mimicked by an "hopping" process moving one cell from one lattice site to a unoccupied neighboring site. The motion rate (corresponding to the cells velocity) and the probability distribution for $p_{i\to j}$ to move to from lattice site i to one of the neighboring site j determines the type of movement.

Diffusion (*in liquids*):

Cells which float in a liquid and do not actively move still perform a kind of random-walk-like movement. The solvent molecules of the media are self propelled by their thermal energy. Collisions between those molecules and the cell membrane will lead to a random drifting of cells, the so-called *Brownian motion*. The resulting spread of cells, and of other particles as well, due to random movement is called *diffusion*.

As the motion is performed unbiased and into arbitrary direction the probability $p_{i\to j}$ is homogeneously distributed, $\sum_j p_{i\to j} = 1$ and $\forall j, k : p_{i\to j} = p_{i\to k}$.

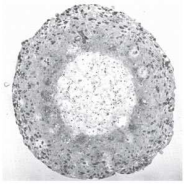

Figure 3.9: Diffusing cell moves randomly to neighbor sites.

The diffusion rate k_{diff} can be derived from the diffusion coefficient D_{cell}

$$k_{diff} = \frac{3D_{cell}}{dR^2} \tag{3.1}$$

where d is the number of spatial dimensions and R is the hopping distance (depends on the underlying lattice). The diffusion coefficient depends on the properties of the cell and the surrounding (liquid) media.

$$D_{cell} = \frac{k_B T}{6\pi\eta R_0} \tag{3.2}$$

where k_B is the Boltzmann constant, T is the temperature, η is the viscosity of the medium and R_0 the hydrodynamic radius of the cell which for the cells can be assumed to be approximately equivalent to the cells radius, $R_0 \approx R_{cell}$.

Parameter	Unit
k_{diff}	h^{-1}
R_{cell}	μm

Constant	Unit	Value	Reference
d	$-$	3	
k_B	JK^{-1}	1.38×10^{-23}	
T	K	310.15	at 37°C
η	$\mu N \cdot s \cdot m^{-2}$	700	for H_2O at 37°C

Migration & Cell-Cell-Adhesion:

Figure 3.10: Cell migrating into a niche in order to increase cell-cell-bounds.

Cells interact with other cells and substrate via adhesion and migration. There cell create bounds with other cells and/or underlying substrate and can release those bounds at other parts of their membrane. This way cells crawl into a certain direction.

This can be mimicked via a migration process with migration rate k_{mi} a biased direction motion taking into account the cohesive energies of cell-cell-bounds.

$$E_{i,j} := \begin{cases} 1 & \text{if } i \text{ and } j \text{ are cells} \\ 0 & \text{else} \end{cases} \tag{3.3}$$

If a cell is moving, it may lose and/or gain bounds. The energy balance is

$$\Delta E_{i \to j} := -\sum_{k \neq j} E_{i,k} + \sum_{k \neq i} E_{j,k} \tag{3.4}$$

The individual rates for a cell moving from lattice site i to a free neighbor site j is given by

$$k_{mi,i \to j} = k_{mi}\, e^{-\frac{\Delta E_{i \to j}}{E_{ref}}} \tag{3.5}$$

where E_{ref} is the reference energy controlling the degree of stochasticity and k_{mi} is a migration rate parameter controlling the migration speed. The total migration rate of a cell at lattice site i to move is given by

$$k_{mi,i} = k_{mi} \sum_{j} e^{-\frac{\Delta E_{i \to j}}{E_{ref}}}. \tag{3.6}$$

3.2.5 Cell Death

We can distinguish between two kinds of cell deaths: the so-called programmed cell death which in the following will be summarized under the expression *apoptosis*, and the premature traumatic cell death as a result of cellular injury, intoxication or hypo-nutrition which will be referred to as *necrosis*.

Apoptosis

Apoptosis can be caused by external signaling (as hormones and toxins) or internal events (as for example the detection of DNA damage, nutrient deprivation and hypoxia [SEK+96]).

As a reaction the cells activate the apoptotic pathways which in the following will lead to cell shrinkage, nuclear fragmentation, chromatin condensation, chromosomal DNA fragmentation and cell fragmentation into apoptotic bodies (see figure 3.11).

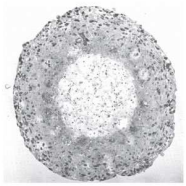

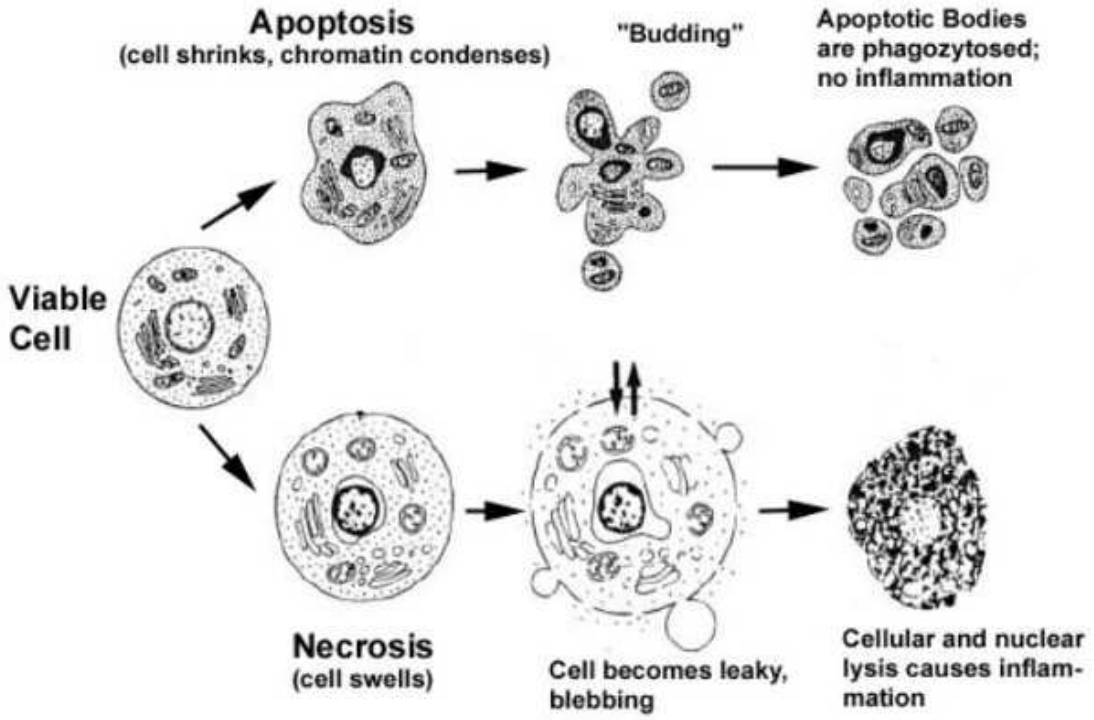

Figure 3.11: Hallmarks of the apoptotic and necrotic cell death process. Apoptosis includes cellular shrinking, chromatin condensation and margination at the nuclear periphery with the eventual formation of membrane-bound apoptotic bodies that contain organelles, cytosol and nuclear fragments and are phagocytosed without triggering inflammatory processes.The necrotic cell swells, becomes leaky and finally is disrupted and releases its contents into the surrounding tissue resulting in inflammation. Modified from [CdB02].

"These bodies are mostly engulfed by neighboring cells and in particular by macrophages. The macrophage recognizes the apoptotic cell fragments by their expression of phosphatidylserin on the outside of the plasma membrane. However, due to the absence of phagocytes in *in-vitro* culture apoptotic cells may undergo so-called *secondary* or *apoptotic necrosis*." [CdB02]

Necrosis (*defective apoptotic pathway*)

If dying cells are not able to initiate the apoptotic pathways because of cellular injury, intoxication or a dysfunctional apoptotic pathway as in the case of many cancer cell lines they will undergo *necrosis*.

"Necrosis is marked by cellular swelling, often accompanied by chromatin condensation and eventually leading to cellular and nuclear lysis with subsequent inflammation (3.11)." [CdB02]

Necrosis (*in-silico*)

As the model is mainly focusing on cancer cells cell death will be taken into account by necrosis (neglecting apoptosis) if certain survival conditions are locally not fulfilled anymore. Via a Poisson process (by default with Erlang number $m_{nec} = 1$) with rate k_{nec} a cell changes it state from "*dividing*" to "*necrotic*" (see fig. 3.12).

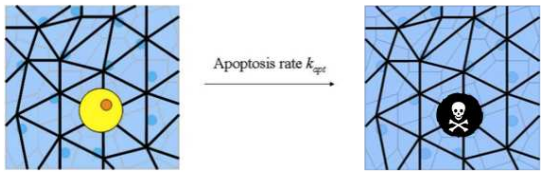

Figure 3.12: A dying cell changes its state to *necrotic*.

Phagocytosis (*in-vivo*)

Phagocytosis is the cellular process of engulfing solid particles by the cell membrane to form an internal phagosome by phagocytes and protists [Wikipedia]. Removing dead cell material is the main function of macrophages, a differentiated white blood cell. So phagocytosis can only take place in the presence of macrophages, but not in an *in-vitro* monoculture of cells.

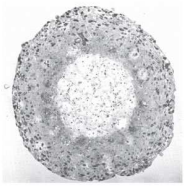

Lysis (*in-vitro*)

An alternative process is cell lysis. Lysis refers to the breaking down of a cell, often by viral, enzymatic, or osmotic mechanisms that compromise its integrity [Wikipedia]. As it is a passive process lysis takes much longer than phagocytosis. It depends very much on the embedding environment. Very often it is an incomplete process leaving some material un-lysed.

Lysis (*in-silico*)

Lysis will be mimicked by Poisson process (by default with Erlang number $m_{nec} = 1$) with rate k_{lys} which removes a cell in "*necrotic*" state from the lattice (see fig. 3.13).

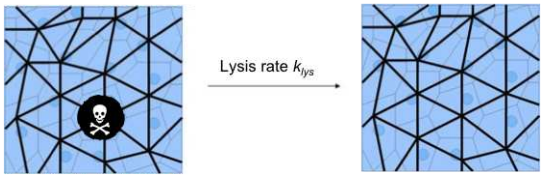

Figure 3.13: A necrotic cell is remove from the lattice via lysis.

3.3 Reaction-Diffusion Equations

3.3.1 Cell Metabolism

The central and most important pathways in the cell metabolism are the glucolysis and the citrate acid cycle (Krebbs cycle). During a stepwise process one molecule glucose is oxidized by O_2 to water and CO_2 to produce the cells energy current ATP. The simple chemical equation looks as following.

$$\text{glucose} + 6 \cdot O_2 + 36 \cdot \text{ADP} \rightarrow 6 \cdot H_2O + 6 \cdot CO_2 + 36 \cdot \text{ATP} \tag{3.7}$$

On a very low level of oxygen concentration cells can still remain viable by producing the essential ATP using the anaerobic way. Muscle cells, for example, are able to break down glucose molecules without using O_2 but excreting lactate.

$$\text{glucose} + 2 \cdot \text{ADP} \rightarrow 2 \cdot \text{lactate} + 2 \cdot \text{ATP} \tag{3.8}$$

This alternative way of metabolizing glucose is less efficient, because it yields only 2 ATP instead of 36, and creates an acid milieu which is harmful to cells. By experimental estimations of average oxygen and glucose uptake rates for another cell line a considerable deviation from the ideal ratio has been found with about 1:1 [KSDMKG00].

For EMT6/Ro cells, in [WNM+00] a ratio of about 1:3.9 is reported. Other works [FS85, JPGCF05] suppose that most of the glucose consumed (75%) flows through the anaerobic glycolysis and produces lactate as waste, while a minority (25%) flows through the Krebbs cycle and respiration; oxygen consumption is connected to glucose consumption through respiratory catabolism to generate CO_2, which rapidly diffuses away.

Continuum model: [G] & [O_2]

Glucose and oxygen are one of the main metabolites of most of the biological cells. In normal tissue they are provided sufficiently by vessels. On the other hand, in tumor spheroids and avascular tumors we can find regions lacking glucose (hypo-nutrition) and/or oxygen (hypoxia). This is mostly due to perturbed or missing regulatory mechanisms leading to uncontrolled cell growth and thus a higher energy demand.

The molecular dynamics is modeled by a classical system of reaction-diffusion equations

$$\partial_t u = D_u \nabla u + r(u) \tag{3.9}$$

where D_u is the diffusion coefficient of molecule $u \in \{[O_2], [G]\}$ and $r(u)$ the reaction. The diffusion should be chosen in dependance of the the environment (tissue, liquid etc.). The reaction term is reduced to the consumption by cells

$$r(u,x) = \begin{cases} -q(u,x) & \text{if } \sigma(x) = \text{tumor cell} \\ 0 & \text{else} \end{cases} \tag{3.10}$$

How to chose correctly your q depends on the cell type and the environmental conditions as well. Possible approaches are shown in figure 3.14.

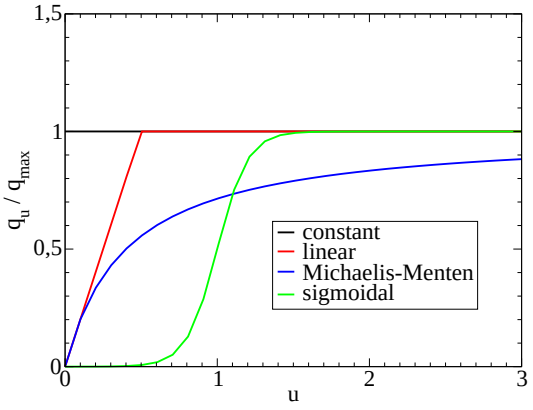

Figure 3.14: Different consumption rates:
a) constant consumption: $q(u) = k$,
b) piecewise linear: $q(u) = \min\{q_{max}, ku\}$,
c) Michaelis-Menten-like: $q(u) = q_{max} \cdot \frac{u}{u+k}$
d) Sigmoidal: $q(u) = q_{max} \cdot \frac{1}{1+e^{k(u_0-u)}}$

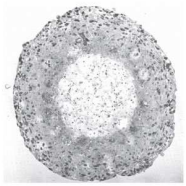

In experimental measurements of glucose and oxygen consumption for varying concentrations of glucose and oxygen it was observed that the concentrations of both molecules influence the consumption behavior [FS85](see figure 3.15). Casciari et al. [CSS92a] proposed a extended Michaelis-Menten-like consumption rate for glucose and oxygen

$$q_G = V_m^G \cdot \frac{[G]}{[G] + k_{mG}} \tag{3.11}$$

$$q_{O_2} = V_{mO_2} \cdot \frac{[O_2]}{[O_2] + k_{mO_2}} \tag{3.12}$$

where the maximum consumption rates V_{mG} and V_{mO_2} depend on the opposite nutrient

$$\begin{aligned} V_{mG} &= \left(A_G + \frac{B_G}{[O_2]} \right) \frac{1}{[H^+]^n} \\ V_{mO_2} &= \left(A_{O_2} + \frac{B_{O_2}}{[G][H^+]^m} \right). \end{aligned} \tag{3.13}$$

For small nutrient concentrations, both rates have an asymptotic behavior toward infinity and thus are unsuitable. In the following we will use a modified version for V_{mG} and V_{mO_2} which is cross-coupling both nutrients via a second Michaelis-Menten-like term and neglects the influence of protons (in acid milieu) on the consumption behavior (compared to equation 3.13)

$$\begin{aligned} V_{mG} &= q_G^{max} \left(1 - \left(1 - \frac{q_G^{min}}{q_G^{max}} \right) \frac{[G]}{[G] + k_G} \right) \\ V_{mO_2} &= q_{O_2}^{max} \left(1 - \left(1 - \frac{q_{O_2}^{min}}{q_{O_2}^{max}} \right) \frac{[O_2]}{[O_2] + k_{O_2}} \right) \end{aligned} \tag{3.14}$$

The parameters of equations were aquired by fitting equations 3.11, 3.12 and 3.13 to measurements of [FS85](see figure 3.15).

Coupling cellular & molecular Scale

In order to estimate the influence of the local glucose and oxygen concentration we need to understand the cells motivation for the measured uptake rates. Beside the usage as cell material glucose is mainly used to gain energy for cell maintenance and reproduction. This happens by oxydating glucose:

$$C_6H_{12}O_6 + 6O_2 \rightarrow 6CO_2 + 6H_2O \tag{3.15}$$

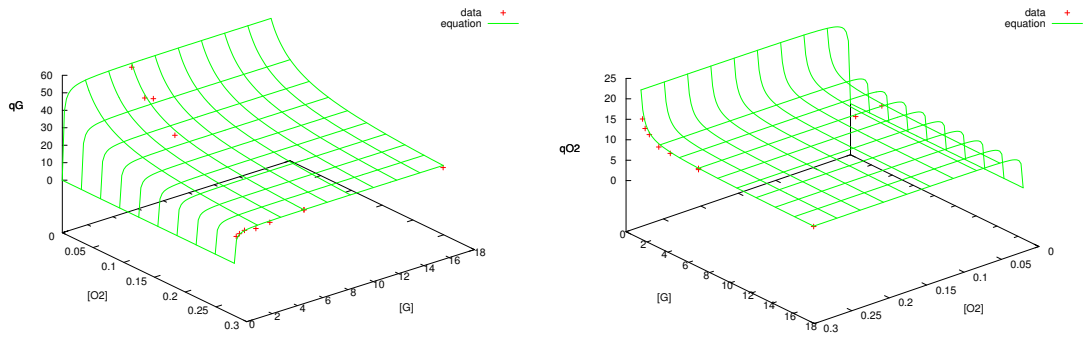

(a) Glucose consumption.

(b) Oxygen consumption.

Figure 3.15: Consumption rate of glucose (a) and oxygen (b) depend on both concentrations. The equations 3.11 and 3.12(*green*) are compared to measurements (*red dots*) in [FS85]. Units: mM for $[G]$ and $[O_2]$, $10^{-16} mM/h/cell$ for q_G and q_{O_2}.

The freed energy (ΔG = -2880 kJ per mole) is thereby stored in the cells energy current, ATP. Regarding the participation of oxygen we have to distinguish between a first anaerobic reaction step, the so-called glycolysis,

$$\text{Glucose} \xrightarrow{k_1} 2\text{Pyruvate} + 2\text{ATP} \tag{3.16}$$

and aerobic citric acid cycle.

$$\text{Pyruvate} + 3O_2 \xrightarrow{k_2} 17\text{ATP} \tag{3.17}$$

From measurements we know that

$$\frac{d[G]}{dt} = -k_1[G] = -q_G \tag{3.18}$$

$$\frac{d[O_2]}{dt} = -3k_2[\text{Pyruvate}][O_2]^3 = -q_{O_2} \tag{3.19}$$

The changes in ATP concentration can be written as following

$$\frac{d[ATP]}{dt} = 2k_1[G] + 17k_2[\text{Pyruvate}][O_2]^3 \tag{3.20}$$

Applying equations 3.18 and 3.19 we can reformulate equation 3.20 and obtain

$$\frac{d[ATP]}{dt} = 2q_G + \frac{17}{3}q_{O_2} \tag{3.21}$$

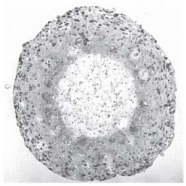

In reality a cell can not produce any ATP, if it doesn't consume any glucose anymore. So finally our equation should be extended to

$$\frac{d[ATP]}{dt} = 2q_G + 34 \underbrace{min\left\{q_G, \frac{1}{6}q_{O_2}\right\}}_{q_G^{aerobic}} \tag{3.22}$$

The percentage of aerobically and anaerobically metabolized glucose is then given by

$$\begin{aligned} q_G^{aerobic}/q_G &= min\left\{1, \frac{1}{6}\frac{q_{O_2}}{q_G}\right\} \\ q_G^{anaerobic}/q_G &= 1 - min\left\{1, \frac{1}{6}\frac{q_{O_2}}{q_G}\right\} \end{aligned} \tag{3.23}$$

Figure 3.16(a) illustrates nicely how cells regulate their consumption of glucose and oxygen under very different circumstances, hypo-nutrition (low glucose) and hypoxia (low oxygen), in such a way that a yield of ATP is maintained at a values between 80 and $100 \cdot 10^{-17} mM/h$ per cell. Based on this observation we can assume that EMT6/Ro cells which are continuously dividing need at least $80 \cdot 10^{-17} mM/h$.

On the other hand side, equation 3.22 implies that EMT6/Ro cells metabolize only 10% of the consumed glucose in the Krebbs-cycle - even under sufficient glucose and oxygen supply (see figure 3.16(b)). The other 90% only flow through the glycolysis (anaerobic) and are either fermented to lactate or used to build up other cell components (e.g. amino acids, nucleotides) nevertheless important for cell reproduction. Jiang et al. [JPGCF05] indicated a much lower fraction (75%) of anaerobically metabolized glucose.

Discretization

The processes on the molecular scale follow different time scales (*seconds - minutes*) than on the cellular scale (*hours*). We assume that the dynamics on the molecular scale perturbed by a change on the cellular scale (cell division, cell motion, cell death etc.) will a steady state within minutes. Thus the reaction diffusion equations (see equation 3.9) for glucose and oxygen can be solved for their steady states, $\partial_t u = 0$ for $u \in \{[G], [O_2]\}$,

$$0 = D_u \Delta u - c q_u \tag{3.24}$$

c being the local cell density. As both equations are coupled via their consumption rates q_G and q_{O_2} they will be solved iteratively in a single system by an implicit scheme for

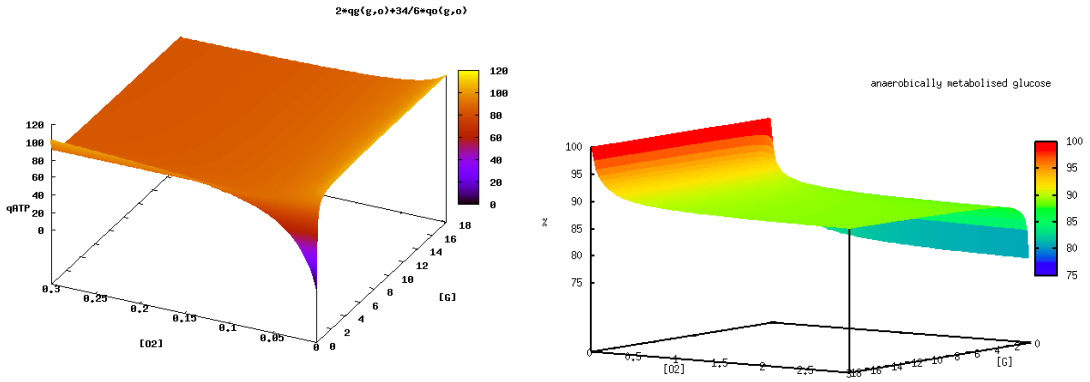

(a) ATP production. (b) Percentage of glucose metabolised anaerobically.

Figure 3.16: Cells requirement of ATP regulates the consumption of glucose and oxygen in such a way that the amount of produced ATP stayes constant (a) and switches smoothly between aerobic and anaerobic metabolism (b). Units: mM for $[G]$ and $[O_2]$, $10^{-17}mM/h$ for q_{ATP}.

diffusion and consumption.

$$\begin{aligned} u^{n+1}\big|_{\partial\Omega} &= u^b \\ \underbrace{D_u \Delta u^{n+1} - c\frac{q_u^n}{u^n}u^{n+1}}_{A^n \cdot u^{n+1}} &= \underbrace{0}_{b} \end{aligned} \tag{3.25}$$

The diffusion term (second derivative in space) is discretized by a first order *finite difference* scheme

$$\begin{aligned} D_u \Delta u &= D_u \left(\frac{\partial^2 u}{\partial x^2} + \frac{\partial^2 u}{\partial y^2} + \frac{\partial^2 u}{\partial z^2} \right) \\ \left(\frac{\partial^2 u}{\partial x^2} \right)_{i,j,k} &= \frac{u_{i-1,j,k} - 2u_{i,j,k} + u_{i+1,j,k}}{h^2} + \mathcal{O}(h^2) \\ \left(\frac{\partial^2 u}{\partial y^2} \right)_{i,j,k} &= \frac{u_{i,j-1,k} - 2u_{i,j,k} + u_{i,j+1,k}}{h^2} + \mathcal{O}(h^2) \\ \left(\frac{\partial^2 u}{\partial z^2} \right)_{i,j,k} &= \frac{u_{i,j,k-1} - 2u_{i,j,k} + u_{i,j,k+1}}{h^2} + \mathcal{O}(h^2) \end{aligned} \tag{3.26}$$

The system is updated by inverting matrix A^n

$$u^{n+1} = (A^n)^{-1} b \tag{3.27}$$

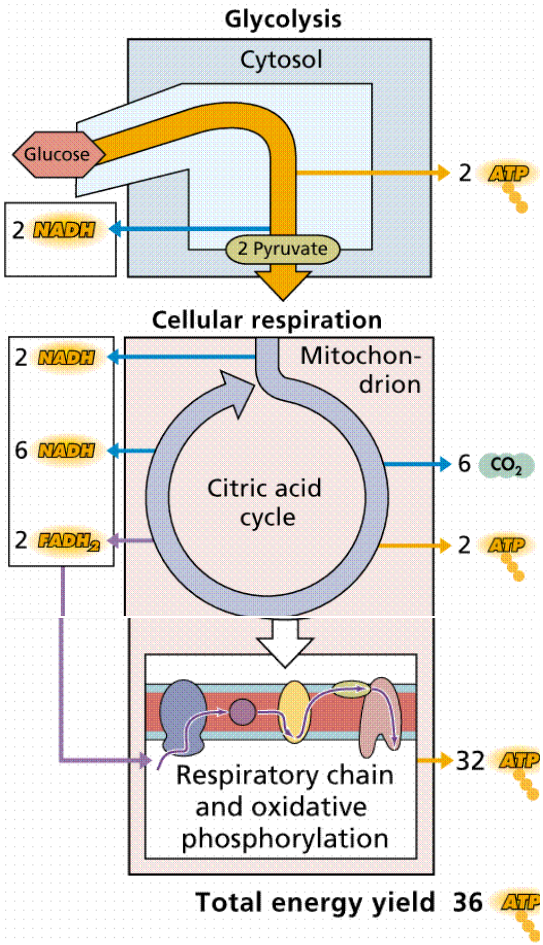

(a) Aerobic metabolic pathway: glycolysis and citric acid cycle.

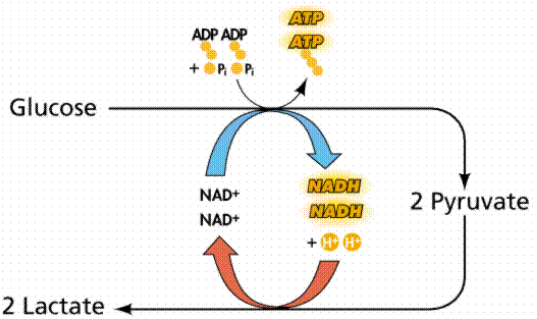

(b) Anaerobic metabolic pathway: glycolysis and lactate fermentation.

Figure 3.17: Metabolic pathways: glycolysis, citric acid cycle and lactate fermentation.

3.3.2 Lactate Fermentation

Under anaerobic conditions the cell accumulates pyruvate molecules from glycolysis (see equation 3.16 and figure 3.17(a)) as they can not be further processed in the *citric acid cycle* (or *Krebbs cycle*) without the presence of oxygen. On the other hand side, NADH can not be oxidized back to NAD^+ which is needed for the glycolysis to continue (see figure 3.17). To over come this shortcoming of NAD^+, the pyruvate will be reduced to lactate by incorporating a proton of NADH.

$$\text{Pyruvate} + \text{NADH} \xrightarrow{k_2} \text{Lactate} + \text{NAD}^+ \tag{3.28}$$

This process is called the *lactic acid fermentation* (see figure 3.17(b)).

Continuum Model: Lactate

In the model we assume lactate to be a direct side product of glucose metabolized in the anaerobic way. For each molecule of glucose entering the anaerobic lactate fermentation the cell will produce 2 molecules of Lactate. Assuming the lactate production rate to be $p_L \approx 2q_G^{anaerobic}$ and lactate to leak out of cells and diffuse among the tissue results in the following formulation of the lactate dynamics

$$\frac{d[L]}{dt} = \nabla \cdot (D_L \nabla [L]) + 2q_G + 2min\left\{q_G, \frac{1}{6}q_{O_2}\right\}, \tag{3.29}$$

where D_L is the diffusion coefficient (see table 3.1), q_G the glucose consumption rate (equation 3.11) and q_{O_2} the oxygen consumption rate (equation 3.12).

Discretization

To solve the lactate dynamics in time a *finite differences* scheme implicit in time for production and diffusion is used

$$\begin{aligned} [L]^{n+1}\big|_{\partial\Omega} &= [L]^b \\ \underbrace{[L]^{n+1} - dtD_L\Delta[L]^{n+1} - dtc\frac{p_L^n}{[L]^n}[L]^{n+1}}_{A^n \cdot u^{n+1}} &= \underbrace{[L]^n}_{b^n} \end{aligned} \tag{3.30}$$

The system is updated by inverting matrix A^n (see section C.3, algorithm 6)

$$u^{n+1} = (A^n)^{-1} b^n \tag{3.31}$$

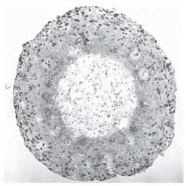

Table 3.1: Default Continuum Model Parameters

Parameter	Unit	Value	Reference
D_{O_2}	$\mu m^2/h$	6300000	[SMH05]
D_G	$\mu m^2/h$	378000	[SMH05]
D_L	$\mu m^2/h$	756000	[RLP+08]
k_G^G	mM	0.068049	fit for measurements in [FS85]
$k_G^{O_2}$	mM	0.030789	fit for measurements in [FS85]
q_G^{min}	mM/h	$14.727716 \cdot 10^{-17}$	fit for measurements in [FS85]
q_G^{max}	mM/h	$53.672035 \cdot 10^{-17}$	fit for measurements in [FS85]
$k_{O_2}^{O_2}$	mM	0.030752	fit for measurements in [FS85]
$k_{O_2}^G$	mM	0.100326	fit for measurements in [FS85]
$q_{O_2}^{min}$	mM/h	$10.171515 \cdot 10^{-17}$	fit for measurements in [FS85]
$q_{O_2}^{max}$	mM/h	$22.800151 \cdot 10^{-17}$	fit for measurements in [FS85]

Chapter 4

Parameterization of Avascular Tumor Model

In this chapter, we will systematically parametrize the avascular model introduced in chapter 3 to two different tumor cell lines: EMT6/Ro and SK-MES-1 cells. For the EMT6/Ro cell line, uniquely the growth curves under different nutrimental conditions will be used as a criteria. For the SK-MES-1 cell line, in addition to the growth curves, the concentric arrangement of cell phenotypes (proliferating, quiescent and apoptotic) and extra-cellular matrix density resulting from the simulations will be directly compared to the image processing results of chapter 2.

Contents

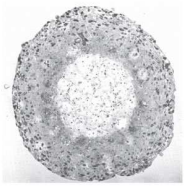

4.1 Results on EMT6/Ro Cell Line

A largely studied cell line in the past is the EMT6/Ro cell line [MKS82, MK84, FS85, FS86, CSS88, Fre88, WDMK90, FSJ$^+$91, CSS92b]. It is a mouse breast cancer cell line. The group around Freyer and Sutherland did a study of EMT6/Ro tumor spheroids [FS85, FS86]. One article of great interest was the growth data of spheroids growing under different nutrient conditions [FS86]:

(I): $[G] = 16.5mM$, $[O_2] = 0.28mM$
(II): $[G] = 16.5mM$, $[O_2] = 0.07mM$
(III): $[G] = 0.8mM$, $[O_2] = 0.28mM$
(IV): $[G] = 0.8mM$, $[O_2] = 0.07mM$

where $[G]$ and $[O_2]$ are the concentrations of glucose and oxygen in the growth medium.

Beside the total number of cells and the spheroid volumes as a function of time (see figure 4.1) they published the measurements of the glucose and oxygen consumption rates (see figure 3.15) of EMT6/Ro cells exposed to a large variety of nutrimental conditions.

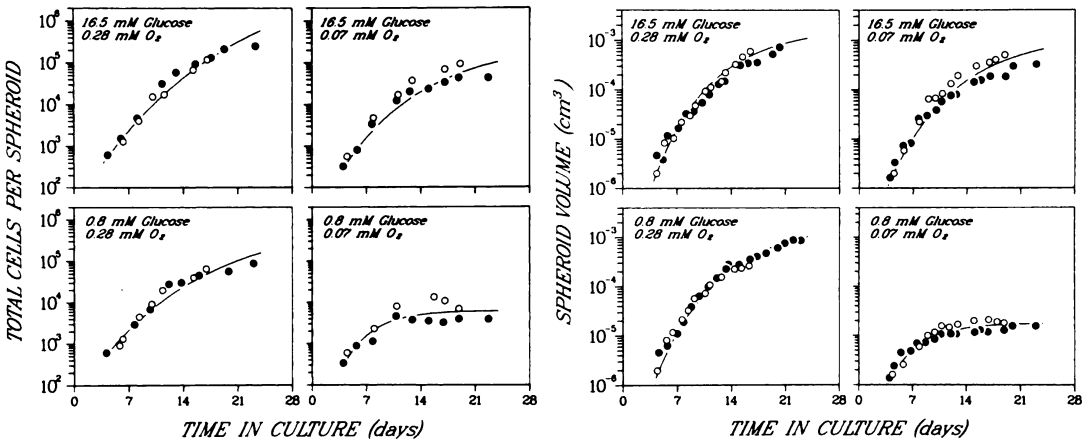

Figure 4.1: Growth rates of spheroids in terms of total spheroid cell content (left) and total spheroid volume (right) as a function of time in culture for growth in the indicated conditions. (○) and (●), individual values from two different experiments determined from diameter measurements; lines are nonlinear least- squares best fits to the Gompertz growth equation.From [FS86].

Due to the richness of literature about this cell line, the EMT6/Ro cells will be the target cell line for a first model parameterization following in the next sections.

4.1.1 Growth Dynamics Neglecting Nutrients

In this section we will parameterize the cellular model (described in section 3.2) neglecting nutrient limitation in order to adapt the purely cell-dependent parameters. As we are missing some information, at the beginning for this section a few assumptions have to be made.

Assumptions:

1. Cells proliferate with cycle time τ following an Erlang distribution with Erlang number $m_d = 10$ (observed for other cell types, see section 3.2.3).
2. For sufficiently supplied nutrients ($[G] = 25mM$ and $[O_2] = 0.28mM$), we can neglect the influence of nutrients on the growth curves (number of cells and spheroid volume versus time).
3. The proliferating rim has a constant size ΔL, within this rim all cells divide with probability 1.

Estimate the Growth Rate from Exponential Growth Phase:

We can estimate the growth rate (λ) from the apparent growth rate ($\lambda_{app}^{-1} = 43.5h$) measured during the exponential growth phase (see figure 4.2) and the relation between both rates for Erlang distributed cycle time with shape parameter $m = 10$ (see equation B.6 in section B.2.3).

$$\begin{aligned} \frac{dN}{dt} &= N \cdot \lambda_{app} \\ &= N/43.5h \\ \lambda^{-1} &= \lambda_{app}^{-1} \cdot m(2^{1/m} - 1) \\ &= 43.5h \cdot 0.72 \\ &\approx 31.22h \end{aligned} \tag{4.1}$$

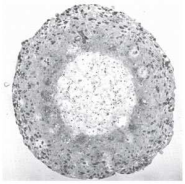

Estimate the Thickness of the Proliferating Rim:

After the initial exponential growth phase at about 10 days the expansion velocity of the radius converges against a constant value.

$$V = N \cdot \overline{V}_{cell} \tag{4.2}$$

$$R = \sqrt[3]{N \cdot \overline{V}_{cell}} \cdot \frac{3}{4\pi}$$

$$\frac{dR}{dt} = \Delta L \cdot \lambda_{app} \tag{4.3}$$

$$= k \cdot \sqrt[3]{\overline{V}_{cell}} \cdot \lambda_{app} \tag{4.4}$$

$$\frac{3}{4\pi}\frac{dN^{\frac{1}{3}}}{dt} = k \cdot \lambda_{app} = k/43.5h \tag{4.5}$$

$$k \approx 4$$

So k is the thickness of the outer proliferating rim of the spheroid in terms of number of cells.

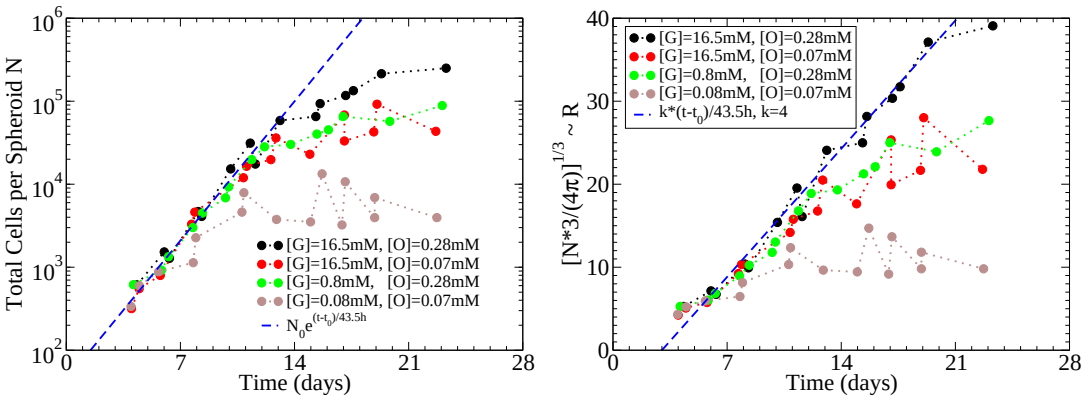

Figure 4.2: Estimation of growth rate (*left*) and thickness of proliferating rim (*right*). *Left*: An exponential growth law (*dashed line*) is compared to the experimental growth curves of the number of cells in time (*circles*). *Right*: A linear growth law (*dashed line*) is compared to the experimental growth curves of the third root of the number of viable cells in time (*circles*).

Fit Spheroid Volume: Cell Size

As we know that the outer growing cell layer must be approximately 4 cells thick we can relate this cell number to the actual cell size in the outer layer by fitting equation

4.4 to the radius expansion of the very same spheroids.

As figure 4.3 shows the expansion velocity is estimated to be $v = 1.32\mu m/h$. For given λ_{app} and k it can be decomposed into the thickness of the proliferating rim $\Delta L = 57.7\mu m$ (eq. 4.4) and the average cell volume within the proliferating rim $\overline{V}_{cell} = 3000\mu m^3$ (eq. 4.4 and 4.3). If we assume the proliferating cells are homogeneously distributed over all cell cycle phases and the cellular volume increases linearly in time then the cell volume can be assumed to vary between $V_{cell} = 2000...4000\mu m^3$.

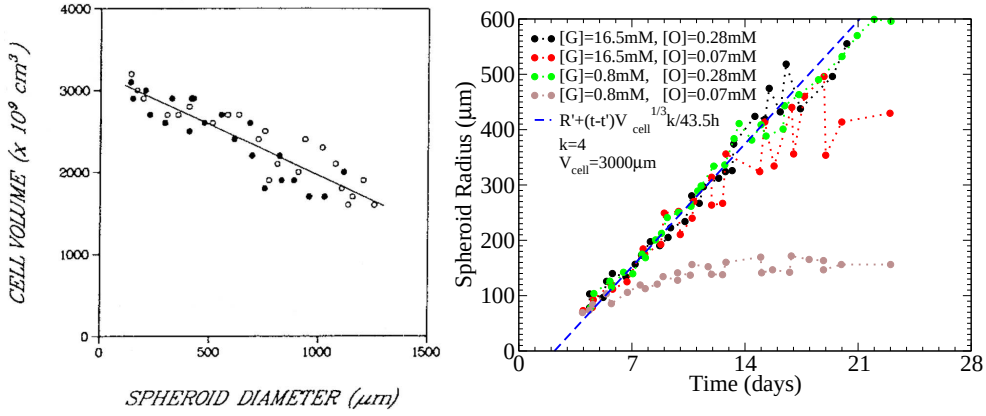

Figure 4.3: Estimation of average cell volume in proliferating rim. *Left*: Measurements of the average cell size in spheroids as function of the spheroid diameter [FS85]. *Right*: The power law spheroid radius (eq. 4.4) compared to experimental growth curves of the spheroid radius from [FS85].

Result:

Figure 4.4 and 4.5 show that a model parametrized with the values for the cell cycle time $\tau = 31.22h$, thickness of proliferating rim $k = 4$ (in cells) and the cell size $V_{cell} = 3000\mu m^3$ is able to explain the growth curves of the spheroid volume and the number of viable cells in time.

4.1.2 Growth Dynamics under Nutrient Limitation

In the following the cell model will be coupled with the continuum model for the glucose and oxygen kinetics discribed in section 3.3.1. Two different criteria for the cells decision for growth/quiescence and survival/death will be compared.

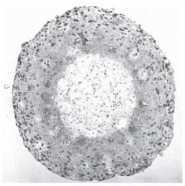

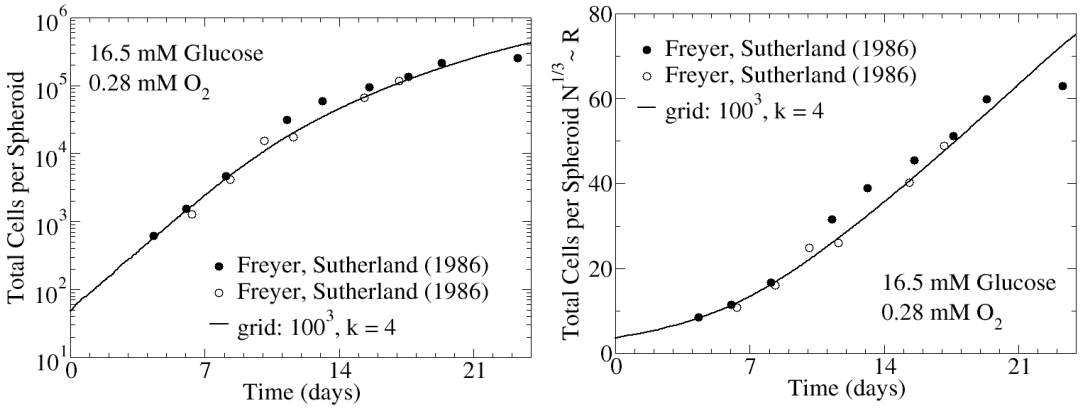

Figure 4.4: Temporal evolution of the total number of cells. Single cell based model (*line*) neglecting nutrient limitation compared to data of EMT6/Ro spheroid (*cirle*).

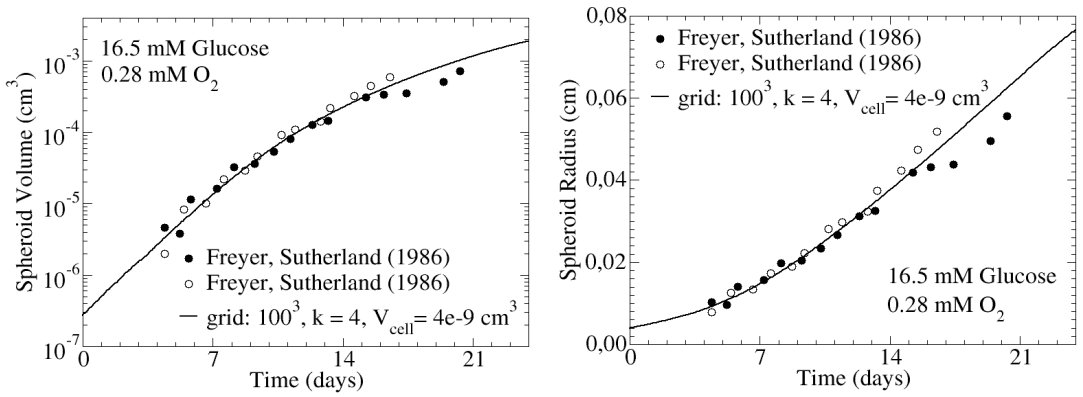

Figure 4.5: Temporal growth of spheroid radius (*right*) and volume (*left*). Single cell based model (*line*) neglecting nutrient limitation compared to data of EMT6/Ro spheroid (*cirlce*).

Critical Product of Glucose and Oxygen

For the cell kinetics, [SMH05] proposed a critical product of oxygen and glucose concentration to switch the cells behavior from proliferation to quiescence & necrosis. Cells only enter the cell cycle if the product of glucose and oxygen concentration exceeds a certain threshold [SMH05]. If not, cells become quiescent and enter necrosis. So we can summarize proliferation and necrosis conditions a following.

$$\vartheta_p := [G] \cdot [O_2] \geq P^{crit} \tag{4.6}$$
$$\vartheta_n := [G] \cdot [O_2] < P^{crit} \tag{4.7}$$

As we can see in figure 4.6, we only can fit the growth curves of changing the glucose concentration while keeping oxygen supply constant (or the way around). But the proposed kinetics is not able to explain a larger variety of different glucose and oxygen concentrations.

Critical ATP

Much better fits were obtained by relating the cell behavior to the amount of ATP a cell is able to produce under the given conditions (see equation 3.22)

$$\begin{aligned} \vartheta_p &:= p_{ATP} \geq p^p_{ATP} \\ \vartheta_n &:= p_{ATP} < p^n_{ATP} \\ p_{ATP} &= 2q_G + 34 \min\left\{q_G, \frac{1}{6}q_{O_2}\right\} \end{aligned} \tag{4.8}$$

Figure 4.7 shows the that amount of ATP a cell can gain from given nutrients (glucose and oxygen) seems to be a much more appropriate criterion for the cells decision about cell growth or quiescence and survival and cell death. The growth curves of the viable cells as well as the spheroid volumes match quiet nicely the experimental observations of conditions I, II and III (whether high glucose or oxygen concentration in growth medium) [FS85]. Nevertheless, without considering further mechanisms the model fails to explain saturation which is observed for condition IV (low glucose and oxygen concentration in growth medium). As the cells at the outer spheroid border are always sufficiently supplied with nutrients, they will continue to proliferate and cause the spheroid radius to continuously expand. The next section proposes one possible mechanism which can explain saturation via cell-cell-adhesion and biased migration.

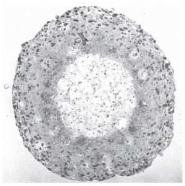

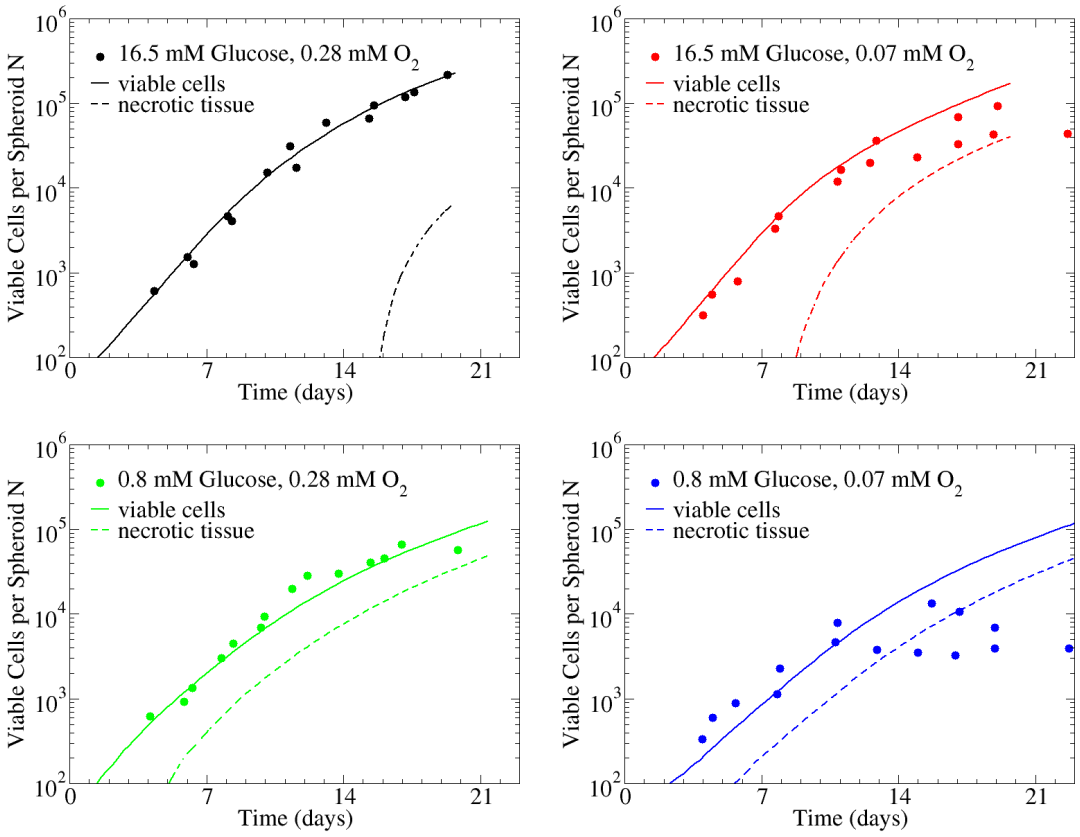

Figure 4.6: Fit of experimental data of growth EMT6/Ro tumor spheroids using a critical product of oxygen and glucose concentration as criteria for the cells decision on growth/quiescence and survival/death. The growth curves of the experimentally measured (*circles*) number of viable cells in time are compared to the simulation results (*solid line*) for four different nutrimental conditions. The *dashed lines* depict the number of necrotic cells.

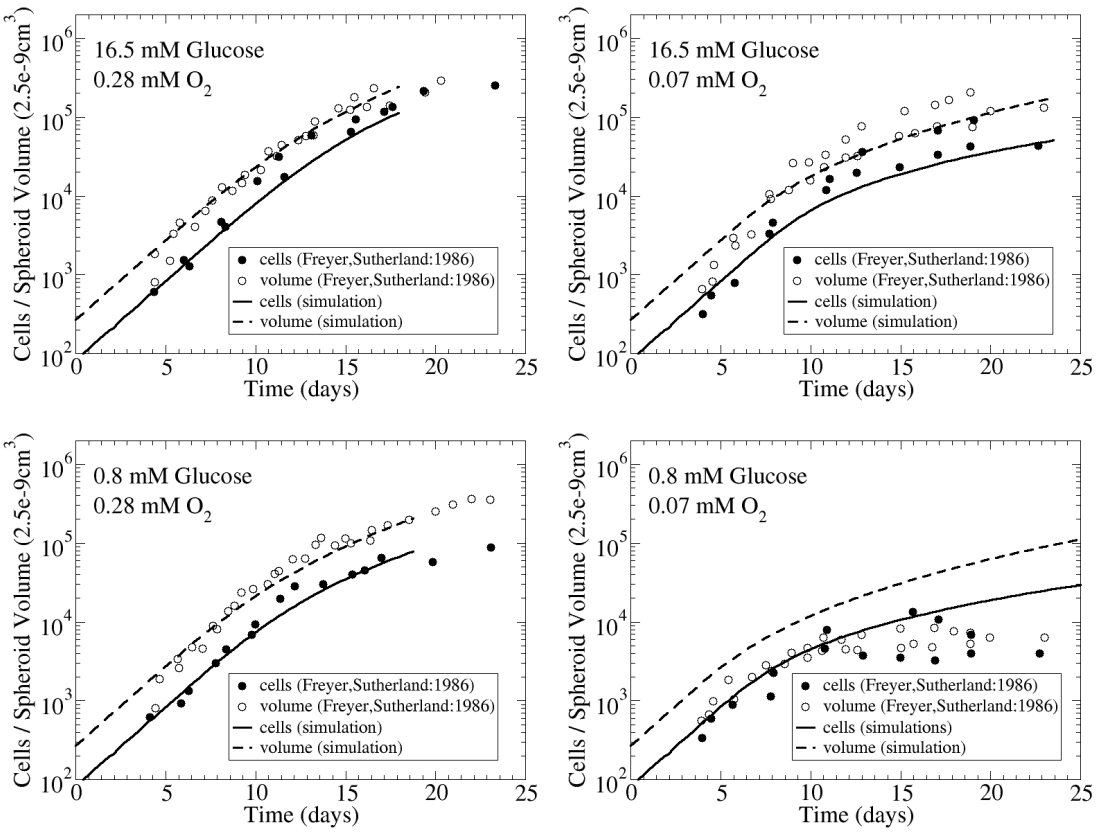

Figure 4.7: Fit of experimental data of growth EMT6/Ro tumor spheroids using a critical ATP production rate as criteria for the cells decision on growth/quiescence and survival/death. The growth curves of the experimentally measured number of viable cells (*black circles*) and the spheroid volumes (*white circles*) in time are compared to the simulation results (*solid line* for viable cells; *dashed lines* for spheroid volume) for four different nutrimental conditions.

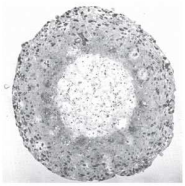

4.1.3 Saturation: Cell Adhesion

Biased migration

In the case of cell death (apoptosis, necrosis) inside of the spheroids, the "holes" left by the dead and lysed cells might be closed by the surrounding cells. Observations show that cells migrate in order to maximize the contact area with other cells.

Figure 4.8 shows the result of a simulation considering cell migration as described in section 3.2.4. The migration rate was assumed to be $k_{mi} = 2h^{-1}$ and the direction of migration was chosen to be biased by cell-cell-adhesion (see equation 3.4). That is, cells more probably migrate into a direction where they will increase the number of cell-cell-bonds. One can see that after an initial growth phase the spheroid volume saturates at around 2000 cells. Furthermore, one can see oscillations directly after saturation which in time become small. This is due to the fact that initially the tumor becomes larger than its saturation size. This leads to the dead of a large number of cells resulting in a population size smaller than the saturation size. So the oscillations are due to delays between phases of regrowth, death and "contraction" of the spheroid by migration. It can be compared to the behavior found in predator-prey-systems.

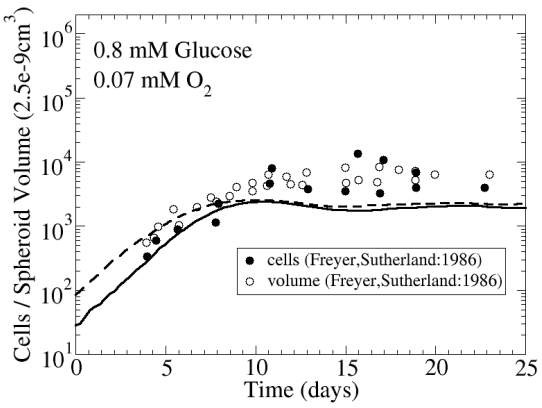

Figure 4.8: Fit of experimental data using a biased cell migration which takes the cell-cell-adhesion into account. The growth curves of the experimentally measured number of viable cells (*black circles*) and the spheroid volumes (*white circles*) in time are compared to the simulation results (*solid line* for viable cells; *dashed lines* for spheroid volume) for the condition of low nutriment concentrations: $[G] = 0.8mM$ and $[O_2] = 0.07mM$

4.2 Results on SK-MES-1 cell line

In the following subsections, a similar systematic parameterization procedure will be applied to the SK-MES-1 cell line. Figure 4.9 shows the growth curves of SK-MES-1 tumor spheroid growing under four nutrimental conditions [MM]:

(I): $[G] = 1mM$, $[O_2] = 0.28mM$
(II): $[G] = 5mM$, $[O_2] = 0.28mM$
(III): $[G] = 25mM$, $[O_2] = 0.28mM$

Table 4.1: Fit Parameters for EMT6/Ro Cell line

Parameter	Unit	Value / Range	Reference
d_{cell}	μm	15.1	fit from [FS85], see figure 4.3
k	-	4	fit from [FS85], see figure 4.2
m_d	-	10	fit from [GZC$^+$11], see figure 3.5
m_g	-	10	assumption
τ	h	31.2	fit from [FS85], see figure 4.2
k_{mi}	h^{-1}	2	estimation for [FS85]
k_{nec}	h^{-1}	0.007	assumption
k_{lys}	h^{-1}	0.35	assumption
P^{crit}	mM	0.025	[SMH05]
p^p_{ATP}	$mM/h/cell$	$40 \cdot 10^{-17}$	estimation for [FS86], see figure 3.16(a)
p^n_{ATP}	$mM/h/cell$	$40 \cdot 10^{-17}$	estimation for [FS86], see figure 3.16(a)

Table 4.2: Fit Parameters for SK-MES-1 Cell line

Parameter	Unit	Value / Range	Reference
d_{cell}	μm	16.8	estimated from [MM], see figure 2.4(b)
k	-	∞	no limited size of proliferating rim
ΔL	μm	130	fit from [MM], see figures 4.12(b) and 4.14
m_d	-	10	fit from [GZC$^+$11], see figure 3.5
m_g	-	10	assumption
τ	h	31.2	fit from [FS85], see figure 4.2
k_{mi}	h^{-1}	0	assumption
k_{nec}	h^{-1}	0.01	estimation, see figure 4.19
k_{lys}	h^{-1}	0.035	estimation, see figure 4.16
Φ^L	mM	10	estimation, see figure
p^p_{ATP}	$mM/h/cell$	$40 \cdot 10^{-17}$	estimation for [FS86], see figure 3.16(a)
p^n_{ATP}	$mM/h/cell$	$40 \cdot 10^{-17}$	estimation for [FS86], see figure 3.16(a)

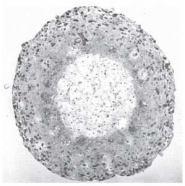

(IV): $[G] = 25mM$, $[O_2] = 0.07mM$

where $[G]$ and $[O_2]$ are the concentrations of glucose and oxygen in the growth medium. As a result of an image processing and analysis (chapter 2), the radial profiles of the proliferating and necrotic cell fractions as well as the extra-cellular matrix densities were given for different time points. Beside the growth curves, they will serve as an additional validation criterion by comparing them to the concentric arrangements emerging from model simulations. As for EMT6/Ro cells, the parameterization will be done successively by first neglecting any molecular dynamics and then step-wisely increasing the model complexity by the studying and identification of further dependencies.

4.2.1 Parameter Estimation Neglecting Nutrient Limitation

Analyzing the slopes of the spheroid volume (exponential growth phase) and the spheroid radius (linear growth phase) give us first preliminary information.

During the *exponential growth phase*, i.e. all cells are assumed to proliferate, the apparent growth rate λ_{app} can be estimated from the volume growth curves (see figure 4.9) using equation 4.9

$$V(t) = V_0 e^{(t-t_0)\lambda_{app}} \tag{4.9}$$

$$\frac{dV}{dt} = V\lambda_{app} \tag{4.10}$$

$$\approx v/5days \tag{4.11}$$

Assuming an Erlang distributed cell cycle time with Erlang number $m \approx 10$ (ref.) gives a growth rate of $\lambda = 1/3.5days$. So a cell division is taking place on average every $3.5days$ - which is extremely long! (typically its about $24h$) - or not all cells are dividing. In the following we will assume that only a forth of the initial bulk of cells enter the cell cycle while the rest stays in G_0.

During the *linear (radius) growth phase* the radius expansion rate can be measured

$$R(t) = R_0 + \Delta L(t - t_0)\lambda_{app} \tag{4.12}$$

$$\frac{dR}{dt} = \Delta L \cdot \lambda_{app} \tag{4.13}$$

$$\approx 14\mu m/day \tag{4.14}$$

Integrating the measured cell fraction in proliferation as a function of the distance to the spheroid border gives us the apparent growing radius fraction $\Delta L = 30.9...46.3\mu m$ (see figure 4.10).

$$\Delta L \approx \int_0^\infty \phi^{Ki67} \mathrm{d}l \tag{4.15}$$

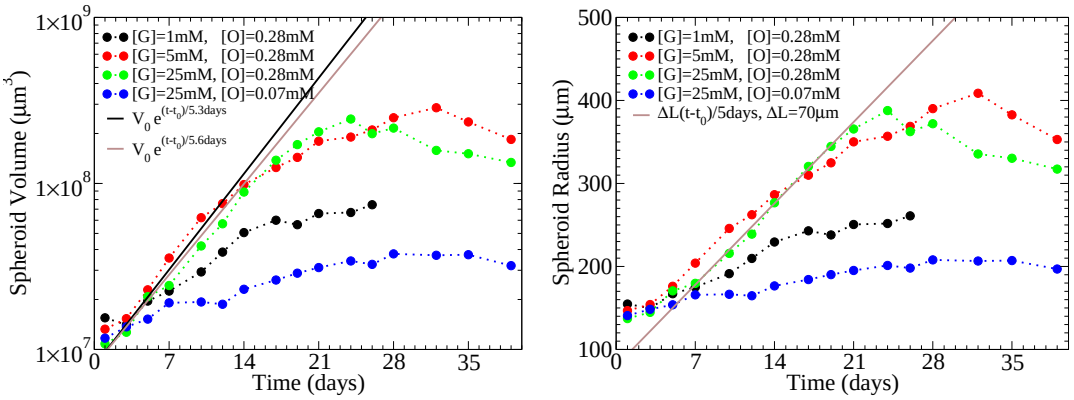

Figure 4.9: SK-MES-1 tumor spheroids growing under four different nutrimental conditions. The figures show the comparison of experimentally measured spheroid volumes (*left, circles*) and radii (*right, circles*) in time to an exponential (*left, line*) and linear (*right, line*) growth law. Data from [MM]

Following equation 4.13 cells divide with rate $\lambda = 1/38.1h$ ($\lambda_{app} = 1/53h$) for Erlang distributed cell cycle times ($m = 10$).

4.2.2 Cell Cycle Re-entrance: Deterministic or Probabilistic Cell Decision?

Many people assumed that the spheroids are organized radially and as a stack of well separable layers: growing outer layer, quiescent layer and necrotic core. So the probability that a cell (re-)enters the cell cycle, p^{re}, is changing with the distance d to the spheroid surface. In the following we will modify the division process ($m_d \rightarrow m_1$) such that the daughter cells reenter the cell cycle with probability p^{re} and become quiescent with probability $1 - p^{re}$. In the following, we will evaluate different assumptions of p^{re}.

Heavy Side Function (*deterministic cell decision*)

Following this assumption cells should be able to divide until a certain depth ΔL (distance to the spheroid surface) with a base probability p^{re}_{max}. All cells any deeper than ΔL will become quiescent.

$$p^{re} = p^{re}_{max} \cdot H_{d<d_{ref}} \tag{4.16}$$

Figure 4.11 shows a sensitivity analysis of the two parameters p^{re}_{max} and d_{ref}.

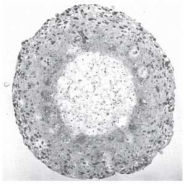

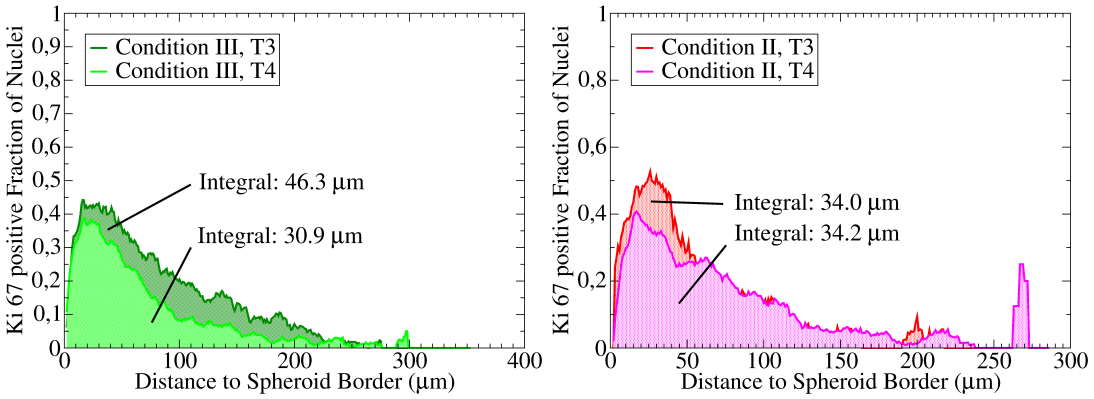

Figure 4.10: Proliferating radius fraction ΔL is estimated from the radial profiles of the proliferating cell fractions (see section 2.3.5) by integration over the distances to the spheroid border.

Hill Function (*probabilistic cell decision*)

The profiles can be smoothed out by using the *Hill function* instead of heavy side.

$$p^{re} = p^{re}_{max} \cdot \frac{d^n}{d^n + d^n_{ref}} \tag{4.17}$$

Exponentially Decaying (*probabilistic cell decision*)

Despite its good agreement with the experimentally determined proliferation profiles, the Hill function was introduced in biochemistry to describe the kinetics of cooperative enzyme-catalyzed chemical reactions and might thus be inappropriate.

On the cellular level a cell which wants to divide has reorganize its local environment in order to freely grow and divide. Surrounding cell have to be pushed away. Consequently, their cell-cell bonds have to be broken. The farther away a cell is from the spheroid surface the more cells it has to move and the more cell-cell bonds have to be broken. So the energy E a cell has to exert to reorganize its surrounding is proportional to its distance to the spheroid surface.

$$E \sim \frac{E_{ref}}{d_{ref}} \cdot d \tag{4.18}$$

E_{ref} is the energy needed to break the cell-cell bonds at a reference length d_{ref}.

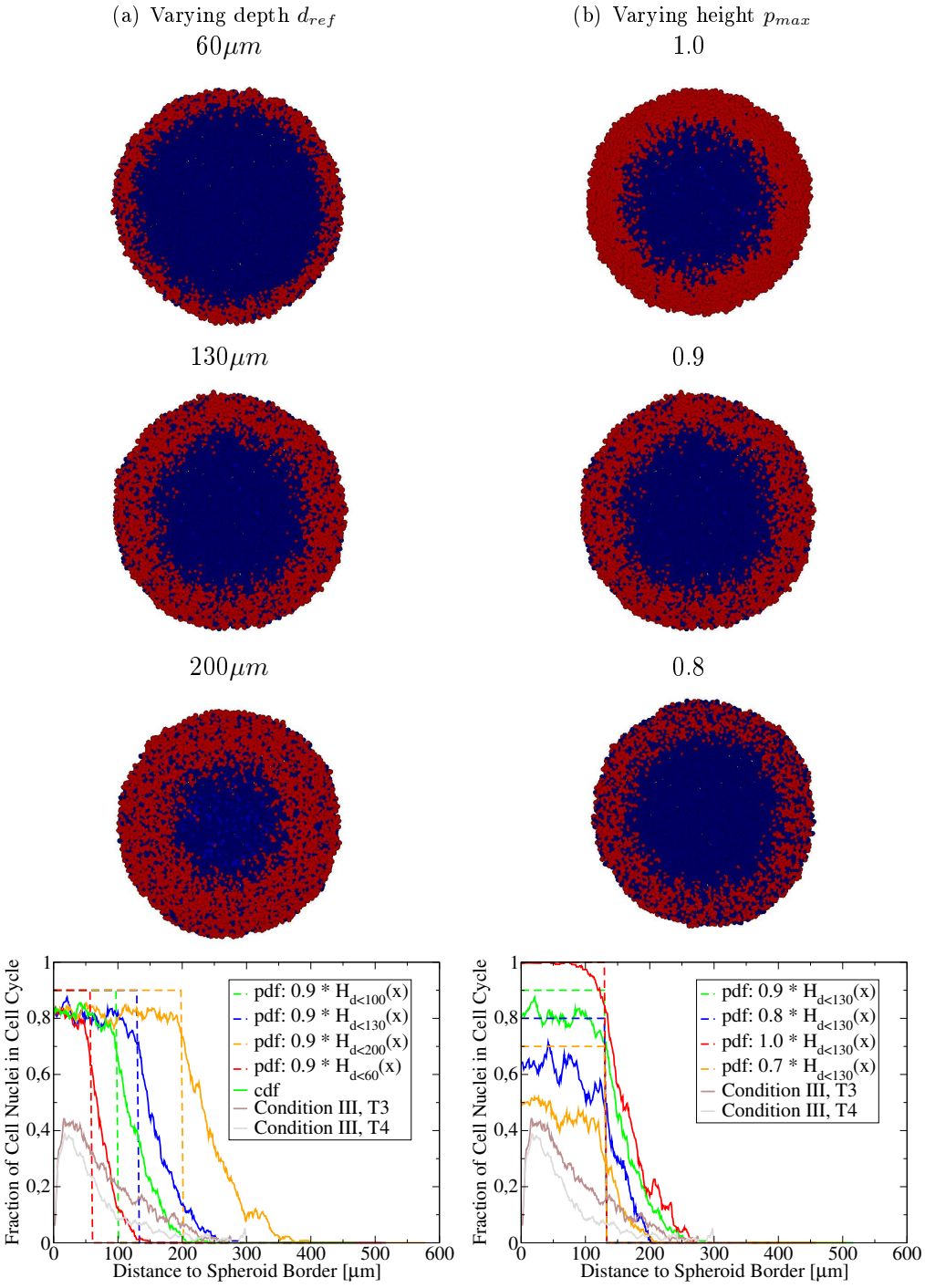

Figure 4.11: Deterministic cell decision: Heavy Side Function. *Bottom*: Comparison between the radial profiles of the proliferating cell fraction (*solid lines*) estimated from experimental data and simulation results. The different *in-silico* profiles result from the cell cycle reentrance probability function (*dashed lines*) being a Heavy side function rescaled in depth d_{ref} (a) and height p_{max} (b). *Top*: The corresponding cell arrangements of proliferating (*red*) and quiescent (*blue*) cells are shown.

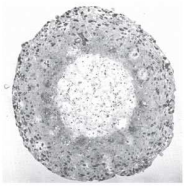

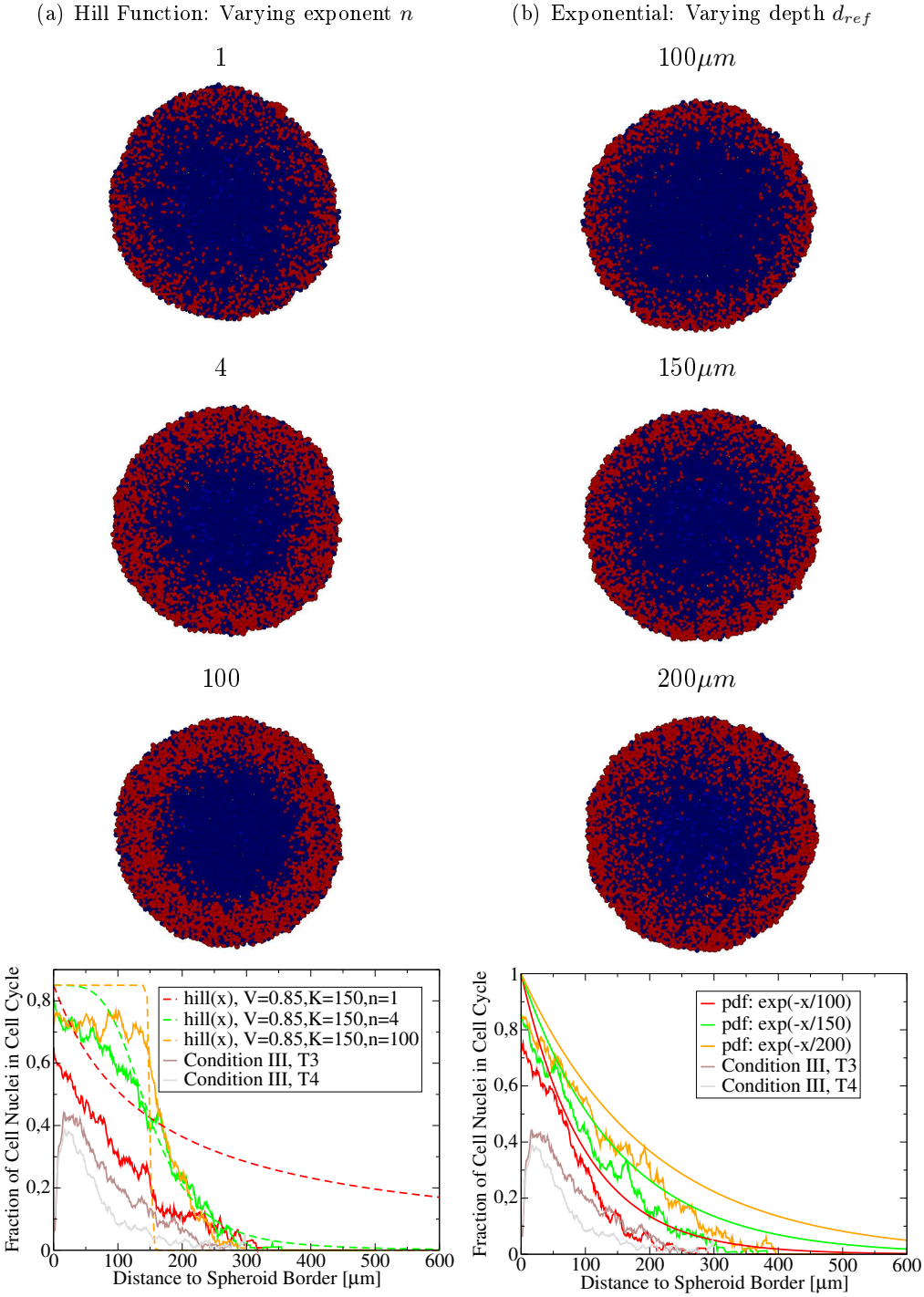

Figure 4.12: Probabilistic cell decision: Hill Function versus exponential decay. Comparison between the radial profiles of the proliferating cell fraction (*solid lines*) estimated from experimental data and simulation results. The different *in-silico* profiles result from the cell cycle re-entrance probability function (*dashed lines*) being assumed to be a Hill function (a) (with varying d_{ref}) or an exponentially decaying function (b) (with varying n). *Top*: The corresponding cell arrangements of proliferating (*red*) and quiescent (*blue*) cells are shown.

So the probability that a cell reenters the cell cycle, and thus reorganizes its surrounding, can be described by an approach from statistical mechanics

$$p^{re} = p^{re}_{max} \cdot e^{-\frac{\Delta E}{E_{ref}}} \tag{4.19}$$

and rewritten in terms of distance d by combining equation 4.18 and 4.19

$$p^{re} = p^{re}_{max} \cdot e^{-\frac{d}{d_{ref}}} \tag{4.20}$$

d_{ref} is the distance where the re-entrance probability is $p^{re} = \frac{1}{e}$. Figure 4.12(b) shows how the re-entrance probability p^{re} and the growing nuclei fraction ϕ_{gro} changes for varying d_{ref} and $p^{re}_{max} = 1$.

Conclusion

Neglecting nutrient limitation the integration of p^{re} over all possible distances $d \in [0, +\infty)$ to the closest unoccupied space (which in this case corresponds to the distance to the outer border) gives a good approximation of the apparent growing radius fraction ΔL .

$$\Delta L \approx \int_0^{+\infty} p^{re} \mathrm{d}d \tag{4.21}$$

For all previously described *deterministic* (eq. 4.16) and *probabilistic* (eq. 4.17 and 4.20) approaches this will result in the same $\Delta L'$

$$\Delta L \approx d_{ref} \cdot p^{re}_{max} \tag{4.22}$$

So by choosing d_{ref} and p^{re}_{max} in such a way that the resulting ΔL corresponds to the one estimated from the data ([MM], figure 4.10) will give us for all approaches the correct expansion speed of the spheroids in the case without nutrient limitation. In the case of nutrient limitation, which usually affects cells at a certain depth, the wrong choice of p^{re} will lead to wrong predictions. Example: If nutrients are limiting at a depth of ΔL then the expansion velocity will not change at all for deterministic density inhibition (eq. 4.16) while it would slow down for its probabilistic counterpart (eq. 4.20).

The comparison with experimentally estimated proliferation profiles indicate a rather probabilistic cell response to space limitation and thus will be our choice for the following simulations.

4.2.3 Extra-cellular Matrix

Studying in detail the proliferation profiles we observe a contra-intuitive drop in proliferative activity at the outer part of the spheroids. This is in direct contradiction to

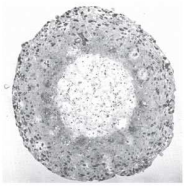

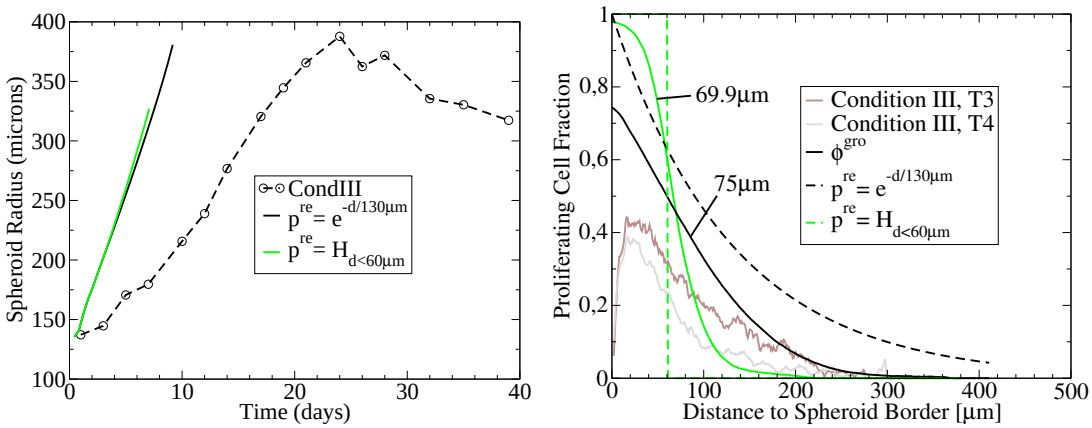

Figure 4.13: Radius expansion (*left*) and radial profile of proliferating cell fraction (*right*). Simulation results for two different re-entrance probability functions are compared with experimental data.

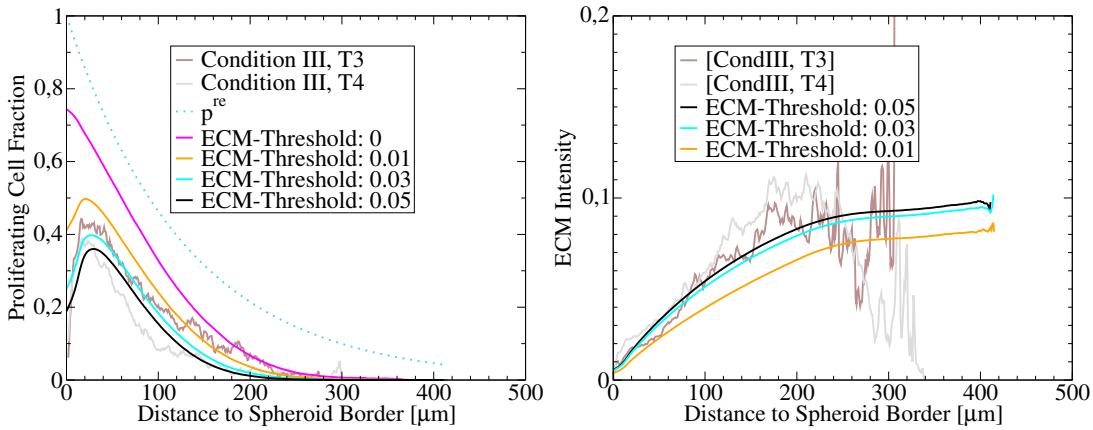

Figure 4.14: ECM dependency. Comparison of the radial profiles for the proliferating cell fraction (*left*) and ECM density between experimental data and simulation results. Simulations were done for different ECM growth thresholds.

strictly monotone profiles resulting from eq. 4.20. On the other hand, the drop correlates very well with the lack of extra-cellular matrix at the spheroid surface (see section 2.3.7).

As we can see in figure 2.13, SK-MES-1 cells produce ECM which slowly accumulates between cells, but does not exceed a certain value. This can be described by the following partial differential equation.

$$\frac{\partial[ECM]}{\partial t} = k_{ECM}^{prod} c - k_{ECM}^{deg}[ECM] \tag{4.23}$$

where k_{ECM}^{prod} is the production rate of ECM which depends on the local cell density c, and k_{ECM}^{deg} is the rate of auto-degradation. Cells only enter the cell cycle if sufficiently surrounded by ECM

$$p_{max}^{re} = \begin{cases} 1 & , ECM \geq \phi_{ECM}^{gro} \\ 0 & , else \end{cases} \tag{4.24}$$

Figure 4.14 illustrate that introducing this kind of ECM-dependency improves the fit the proliferation profiles now matching the initial drop and the ECM profiles using the parameters indicated in table 4.3.

Table 4.3: Model Parameters for ECM dependency.

Parameter	Unit	Value
k_{ECM}^{prod}	h^{-1}	0.0005
k_{ECM}^{deg}	h^{-1}	0.003
ϕ_{ECM}^{gro}	-	0.05

4.2.4 Nutrient-Driven Control of Cell Proliferation & Death (Single Condition)

Applying the same ATP-dependence on cell growth and survival as for EMT6/Ro cells (section 4.1.2, equation 4.8) will not lead to satisfying fits. As figure 4.15 shows the necrotic nuclei fraction profiles can not be fitted by large range of necrosis rates ($k_{nec} = 0...0.1h^{-1}$) and in-vivo lysis rate $k_{lys} = 0.35h^{-1}$.

For low necrosis rates we can observe some necrotic cells at a depth of $100\mu m$ leading to a synchronous increase of the proliferating cell fraction in the center. This is due to newly available free space cause by lysis of dead cells.

Increasing the necrosis rate will increase both fractions at the border of the necrotic core, but as a consequence will leave an almost empty hole in the center.

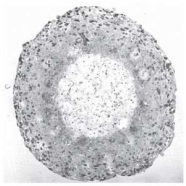

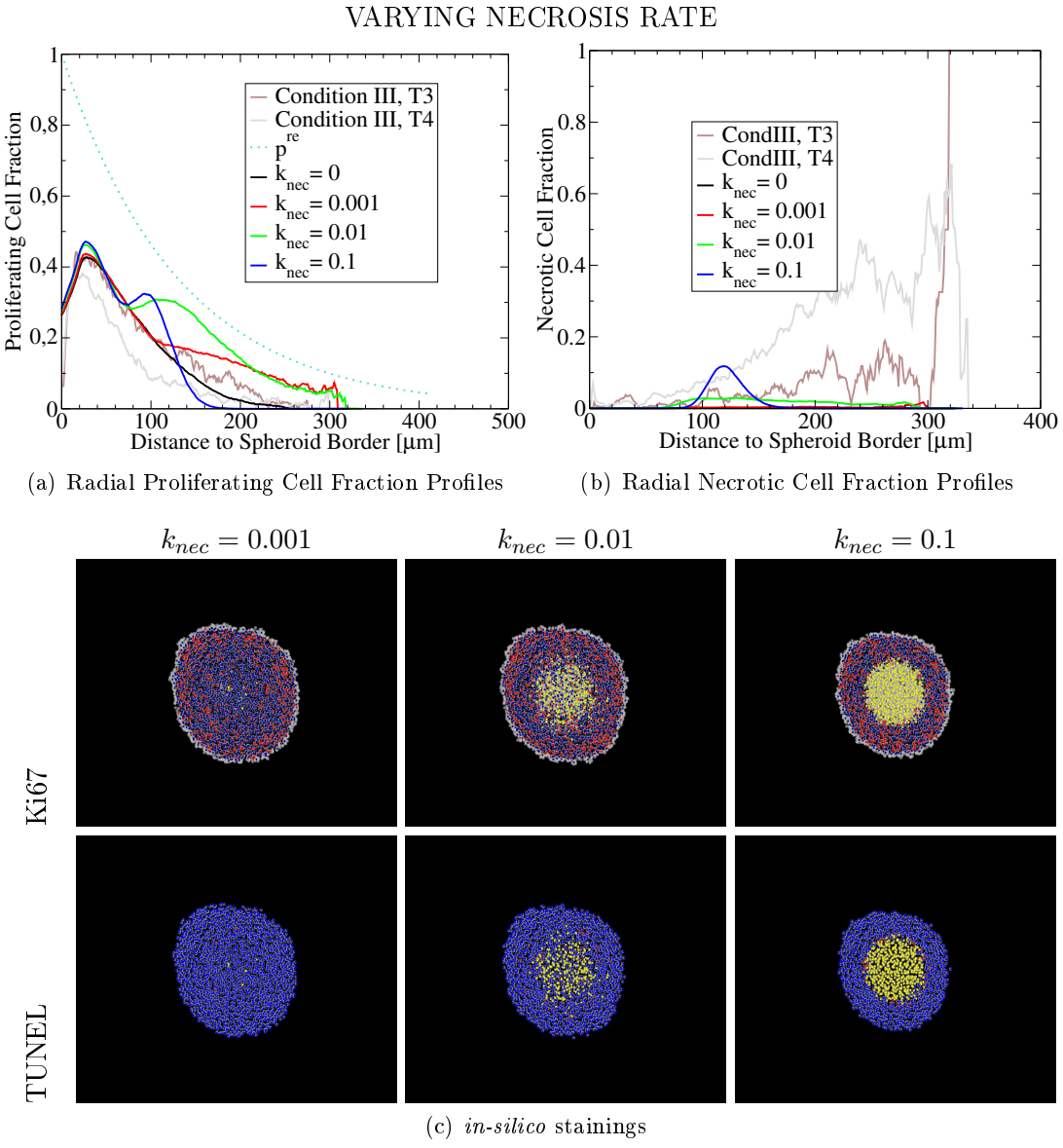

(a) Radial Proliferating Cell Fraction Profiles

(b) Radial Necrotic Cell Fraction Profiles

(c) *in-silico* stainings

Figure 4.15: Sensitivity analysis for necrosis rate. Comparison of radial proliferation (a) and necrosis (b) profiles between data and simulations using different necrosis rates k_{nec}. (c) The corresponding "*in-silico* stainings" show proliferating (Ki67, *red*), necrotic (TUNEL, *red*) and the lysated cells (*yellow*).

Problem:

If cells die at a depth of $100\mu m$ and are removed on average within 3h ($k_{lys} = 0.35h^{-1}$) then the very few remaining proliferating cells in this area are not capable to replace the dying cells and keep the dead cell fraction at the observed 10% (and more).

Hypothesis I : In-vitro Lysis Rate very low

In the absence of macrophages lysis of dead cells (apoptotic & necrotic) will be much slower in-vitro compared to in-vivo. Figure 4.16 shows how the fraction of necrotic cells increases when decreasing the lysis rate k_{lys}.

4.2.5 Nutrient-Driven Control of Cell Proliferation & Death (Two Conditions)

Hypothesis II : Schaller Kinetics & Morphogen-Driven Migration

In order to supply the necrotic core with living cell material, cells might migrate from the viable rim into the necrotic area. So, cell migration might be motivated by the material of a necrotic cell. Here we introduce a morphogen to the system of differential equations.

$$\begin{aligned} \frac{\partial [M]}{\partial t} &= \nabla \cdot (D_M \nabla [M]) + k_M^{prod} c_{nec} \\ [M]|_{\partial\Omega} &= 0 \end{aligned} \tag{4.25}$$

$[M]$ is the local concentration of morphogen. It is generated by necrotic cells of density c_{nec} with rate k_M^{prod} and diffuses with diffusion coefficient D_M. Cell migration on the other hand side is influenced by the morphogen concentration and the morphogen gradient $\nabla[M]$. The rate of a cell moving from lattice site i to a free lattice site j is given by

$$\begin{aligned} k_{mi,i\to j} &= k_{mi}\ e^{\frac{\nabla [M]_i \cdot (x_j - x_i)}{[M]_{ref}}} \\ &\approx k_{mi}\ e^{\frac{[M]_j - [M]_i}{[M]_{ref}}} \end{aligned} \tag{4.26}$$

where $[M]_i$ is the morphogen concentration in lattice site i, $[M]_{ref}$ is the reference concentration controlling the degree of stochasticity and k_{mi} is a migration rate parameter controlling the migration speed. The total migration rate of a cell at lattice site i to move is given by

$$k_{mi,i} = k_{mi} \sum_j e^{\frac{[M]_j - [M]_i}{[M]_{ref}}}. \tag{4.27}$$

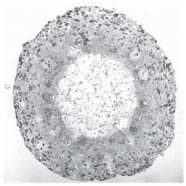

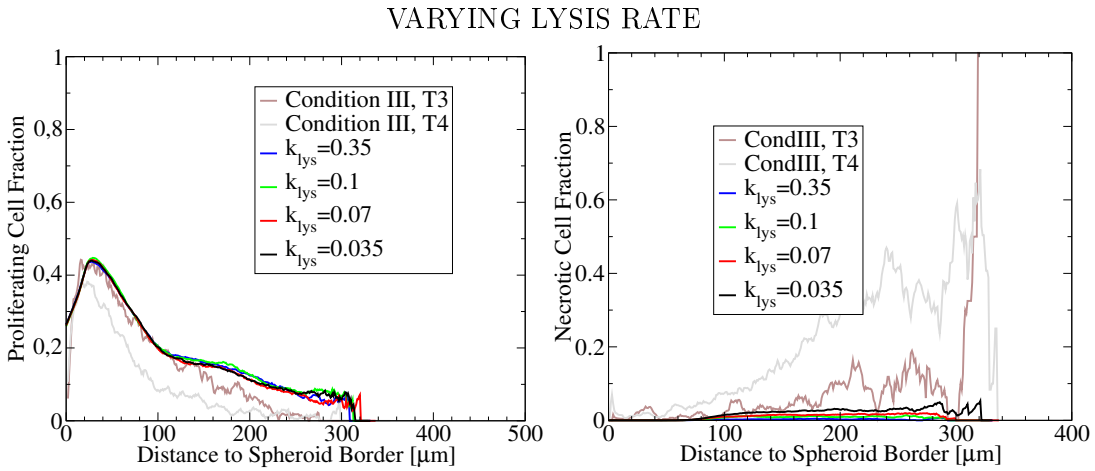

(a) Radial profiles of proliferation and necrosis, necrosis rate $k_{nec} = 0.001h^{-1}$

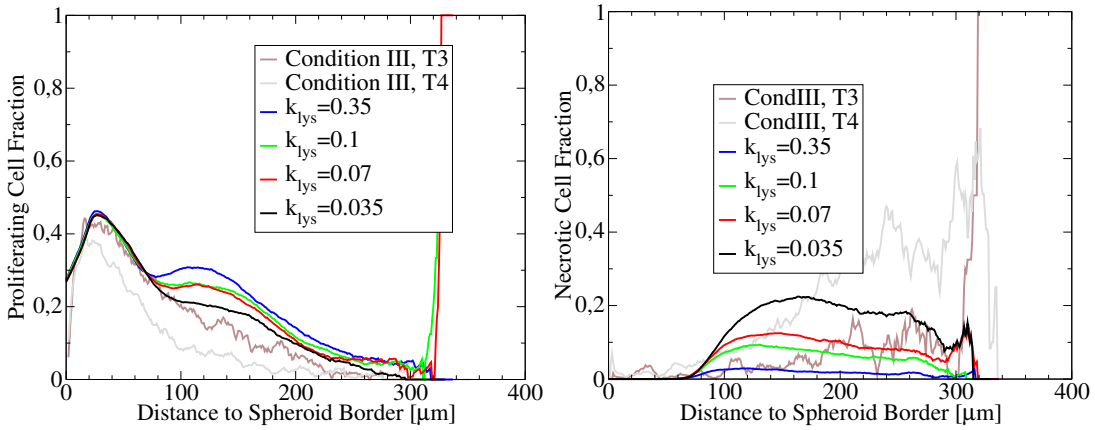

(b) Radial profiles of proliferation and necrosis, necrosis rate $k_{nec} = 0.01h^{-1}$

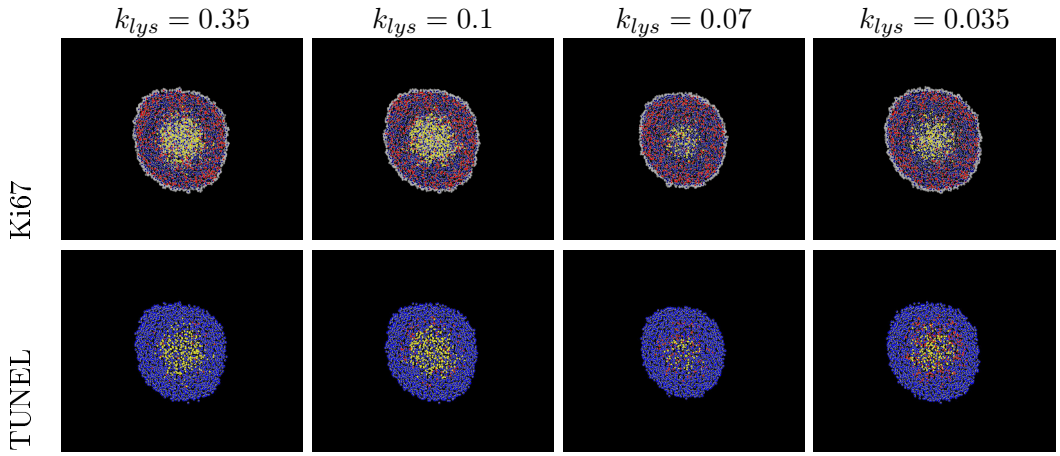

(c) *in-silico* stainings, necrosis rate $k_{nec} = 0.01h^{-1}$

Figure 4.16: Sensitivity analysis for lysis rate. Comparison of radial proliferation (*left*) and necrosis (*right*) profiles between data and simulations using different necrosis rates, $k_{nec} = 0.001h^{-1}$ (a) and $k_{nec} = 0.01h^{-1}$ (b). (c) The *in-silico* "stainings" for $k_{nec} = 0.001h^{-1}$ show proliferating (Ki67, *red*), necrotic (TUNEL, *red*) and the lysated cells (*yellow*).

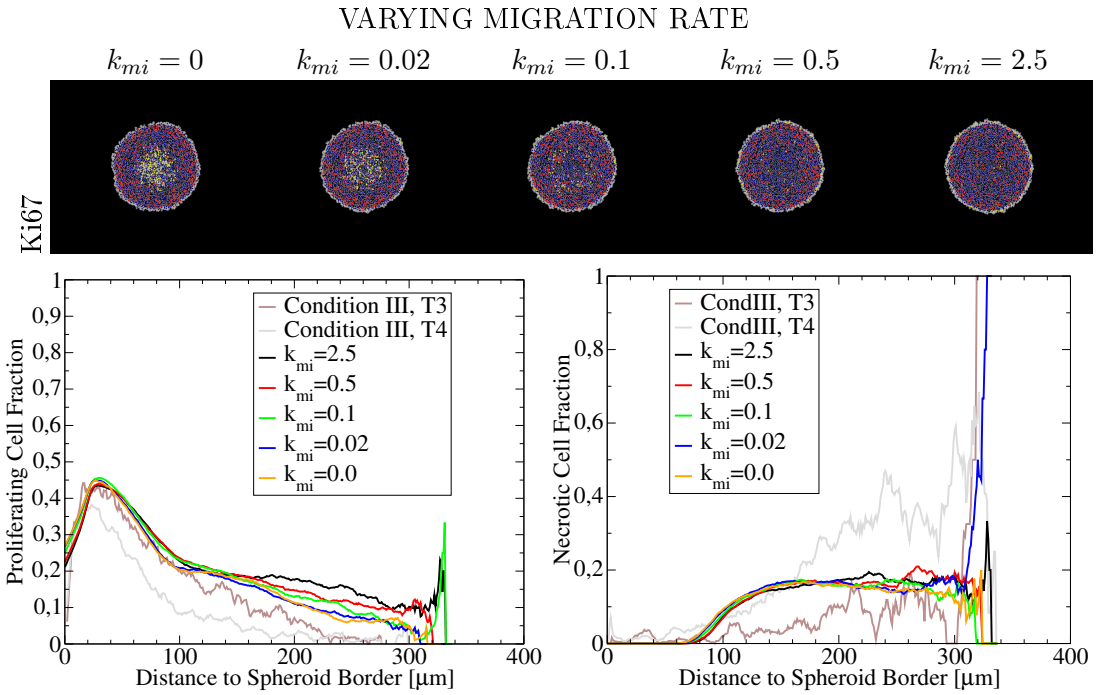

(a) Condition III: $[G] = 25mM, [O_2] = 0.28mM$

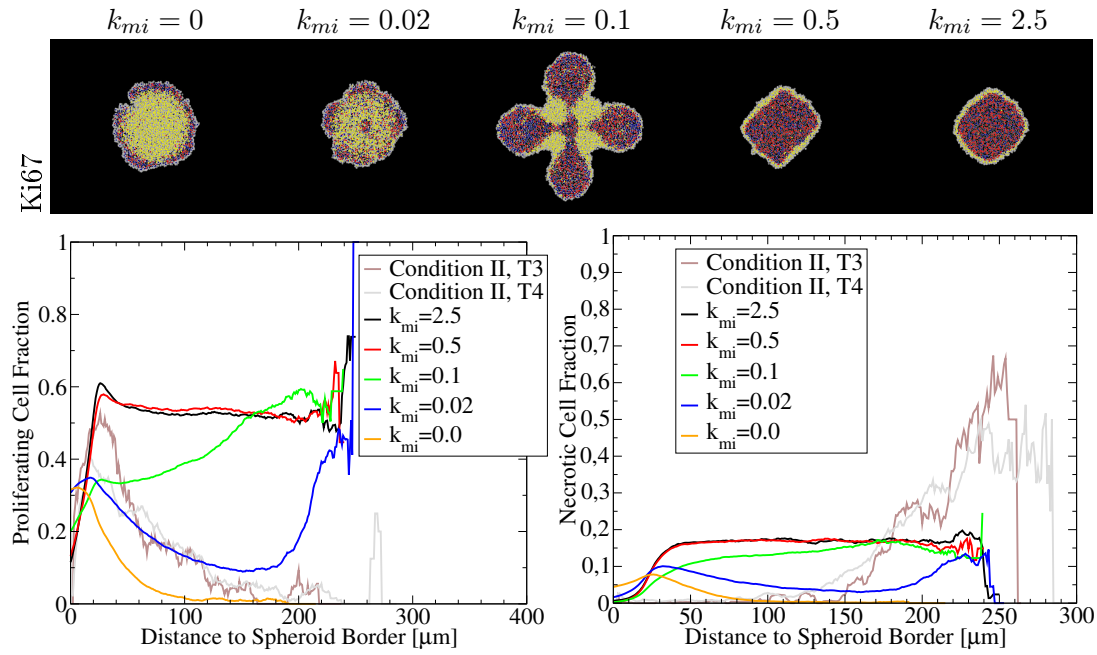

(b) Condition II: $[G] = 5mM, [O_2] = 0.28mM$

Figure 4.17: Sensitivity analysis for lysis rate. The collages for nutrimental condition III (a) and II (b) show the "stained" slices of *in-silico* spheroids when reached a radius of $300\mu m$ (*top*) and the radial profiles of the proliferating (*left*) and necrotic (*right*) cell fractions. The radial profiles emerging *in-silico* are compared to data. The simulations were done for different migration rates k_{mi}. The color code of the spheroid slices are: proliferating (*red*), quiescent (*blue*) and the lysated cells (*yellow*)

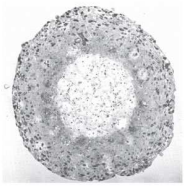

Hypothesis III : ATP Kinetics

Figure 4.18 shows simulation results of using the intra-cellular production of ATP molecules for given glucose and oxygen consumed under two different conditions. Varying the maximal glucose consumption rate via parameter q_G^{max}, one gets a good agreement of the radial proliferating and necrotic cell fraction profiles for condition III (see fig. 4.18(a)). Surprisingly, changing the consumption rate does almost not affect the profiles of condition II (see fig. 4.18(b)).

We can conclude that considering only the intra-cellular ATP for the cell decision can not explain both nutrimental conditions. A difference of a factor five in the growth medium glucose concentrations will always lead to a thinner viable rim in condition II, while the necrotic profiles suggest the contrary. One can even see, that the necrotic cell fraction in the outer parts is higher in condition III compared to condition II though the nutrient supply should be less limiting there. Consequently, we have to consider different criteria for both conditions which we explore in the next paragraph.

Hypothesis IV : ATP & Lactate Kinetics

While in condition II, one can see a dramatic increase in necrosis at a depth of around $150\mu m$, for condition III we see a smooth increase starting even at the outer border. Cell death in the outer regions can hardly be explained by starvation as in condition III the spheroids are sufficiently supplied with both, glucose and oxygen. On the other hand, we saw that well nourished cells gain 90% of their ATP from the anaerobic lactate fermentation (see section 3.3.2) even if enough oxygen is available. So in condition III cells accumulate much more of the rather harmful lactate than in condition II where cells are forced to optimize their metabolism at a certain point. In the following, we propose a second criteria for cell decisions on *growth or quiescence* and *survival or death*:

1. intra-cellular production of ATP molecules for given glucose and oxygen consumed
2. local lactate concentration

Then the proliferation and necrosis conditions can be summarized as follows

$$\begin{aligned} \vartheta_p &:= p_{ATP} \geq p_{ATP}^p \text{ and } [L] < [L]^p, \\ \vartheta_n &:= p_{ATP} < p_{ATP}^n \text{ and } [L] \geq [L]^n, \end{aligned} \tag{4.28}$$

where p_{ATP}^p is the required ATP production rate permitting proliferation and $[L]^p$ is the critical lactate concentration inhibiting proliferation. On the other hand, p_{ATP}^n is the required ATP production rate to insure survival and $[L]^n$ is the critical lactate concentration causing cell death.

Figure 4.19 shows simulation results of this combination of criteria for the cell decision. One can see that the lactate threshold does not affect the rather undernourished

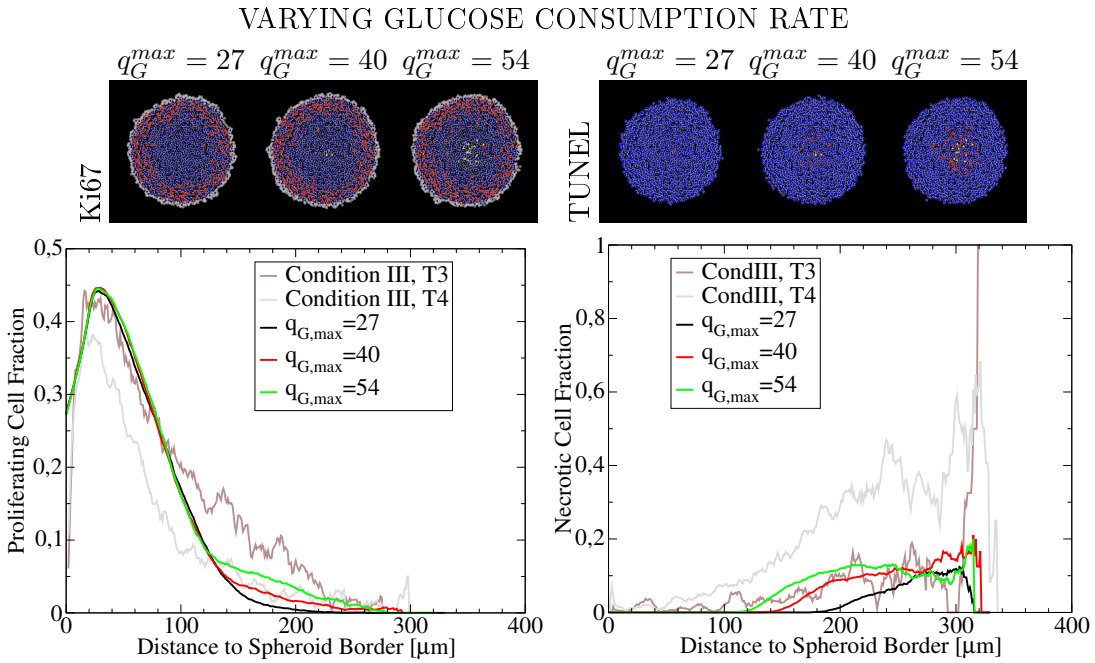

(a) Condition III: $[G] = 25mM, [O_2] = 0.28mM$

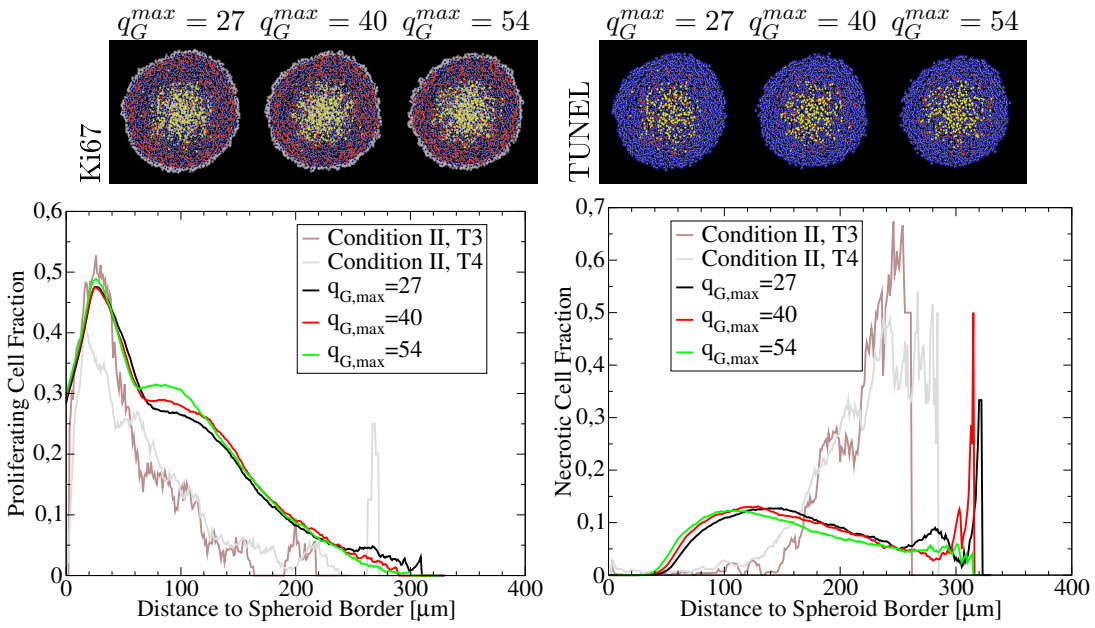

(b) Condition II: $[G] = 5mM, [O_2] = 0.28mM$

Figure 4.18: Sensitivity analysis for glucose consumption parameter $q_{G,max}$. The collages for nutrimental condition III (a) and II (b) show the "stained" slices of *in-silico* spheroids when reached a radius of $300\mu m$ (*top*) and the radial profiles of the proliferating (*left*) and necrotic (*right*) cell fractions. The radial profiles emerging *in-silico* are compared to data. The simulations were done for different values of glucose consumption parameter $q_{G,max}$. The color code of the spheroid slices are: proliferating (*red*, Ki67), quiescent (*blue*, Ki67), necrotic (*red*, TUNEL), viable (*blue*, TUNEL) and the lysated cells (*yellow*)

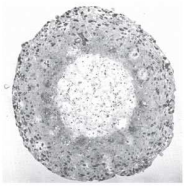

spheroids of condition II, but dramatically changes the size of the necrotic core in condition III.

Best Fit

Figures 4.20 and 4.21 show the best fitting parameter sets for all compared curves: growth curves and the radial profiles for the ECM intensity, proliferating cell fraction and necrotic cell fraction.

4.3 Conclusions & Discussion

We parametrized the multiscale model for avascular tumor introduced in chapter 3 to two different cancer cell lines: EMT6/Ro and SK-MES-1 cells. The constraints for EMT6/Ro were the growth curves of the number of viable cells and the spheroid volume in time measured for four different nutrimental settings. For SK-MES-1, in addition to the growth curves in time, the radial profiles of proliferating and necrotic cell fractions as well as the extra-cellular matrix densities were given for different time points. The profiles were a result of image processing and analysis of micrographs from the same experiments (chapter 2).

4.3.1 Parameter Estimation from Nutrient-Independent Data

For both cell lines, the purely cell-related (without involvement of molecules) parameters were estimated from the exponential and geometric growth phase from experiments were e.g. nutrient-limitation can still be excluded. Those parameters include the growth rate τ^{-1}, the apparent thickness of the proliferating rim ΔL (or respectively k in numbers of cells) and the cell size (for EMT6/Ro).

Mechanical Growth Inhibition One can assume that in order to grow, a cell has to rearrange its local environment. The energy needed for the rearrangement would be proportional to the cell-cell-bonds a cell has to break to push other cells toward unpopulated space. Thus, this energy E can be approximated by $E \sim \Delta_{free}$, where Δ_{free} is the distance to the closest unoccupied space. For EMT6/Ro cells we assumed all cells in the outer rim of thickness ΔL to proliferate with probability 1, while all other cells are quiescent. Thus, the cells decision to grow and divide depends on a threshold of E (or Δ_{free} respectively) and would be a deterministic decision. By comparison between the radial profiles of the proliferating cell fraction extracted from experimental images (SK-MES-1 spheroids) and the patterns emerging from simulations we could show that this assumption can not be true. A better agreement of the radial profiles

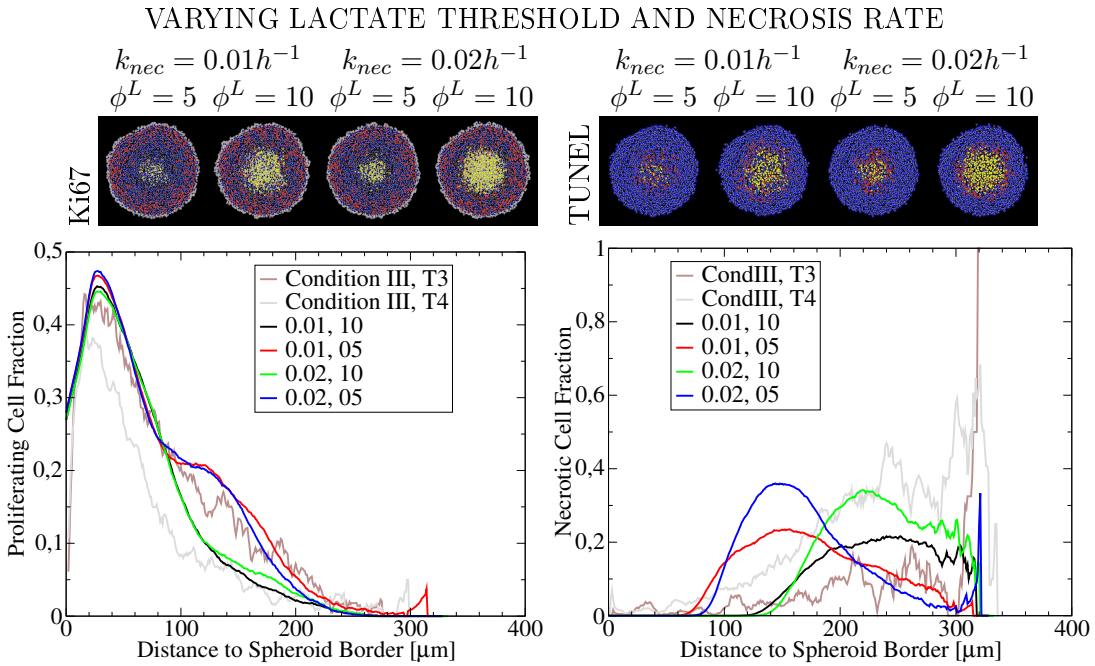

(a) Condition III: $[G] = 25mM, [O_2] = 0.28mM$

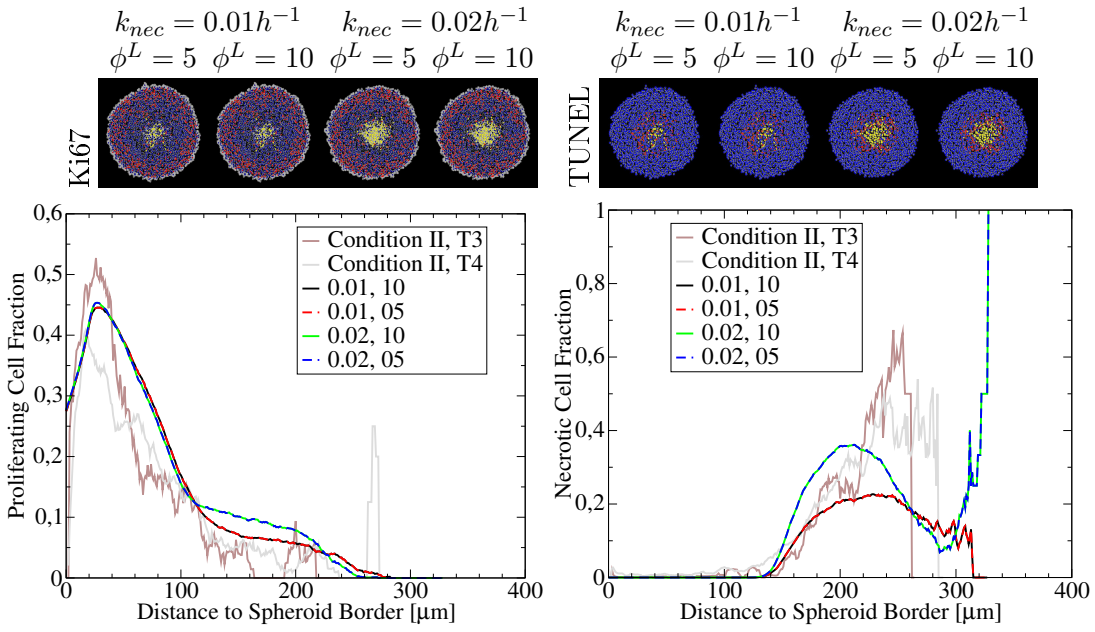

(b) Condition II: $[G] = 5mM, [O_2] = 0.28mM$

Figure 4.19: Sensitivity analysis for lactate threshold ϕ^L and necrosis rate k_{nec}. The collages for nutrimental condition III (a) and II (b) show the "stained" slices of *in-silico* spheroids when reached a radius of $300\mu m$ (*top*) and the radial profiles of the proliferating (*left*) and necrotic (*right*) cell fractions. The radial profiles emerging *in-silico* are compared to data. The simulations were done for different values of lactate threshold ϕ^L and necrosis rate k_{nec}. The color code of the spheroid slices are: proliferating (*red*, Ki67), quiescent (*blue*, Ki67), necrotic (*red*, TUNEL), viable (*blue*, TUNEL) and the lysated cells (*yellow*).

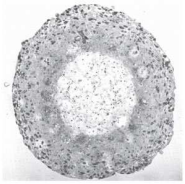

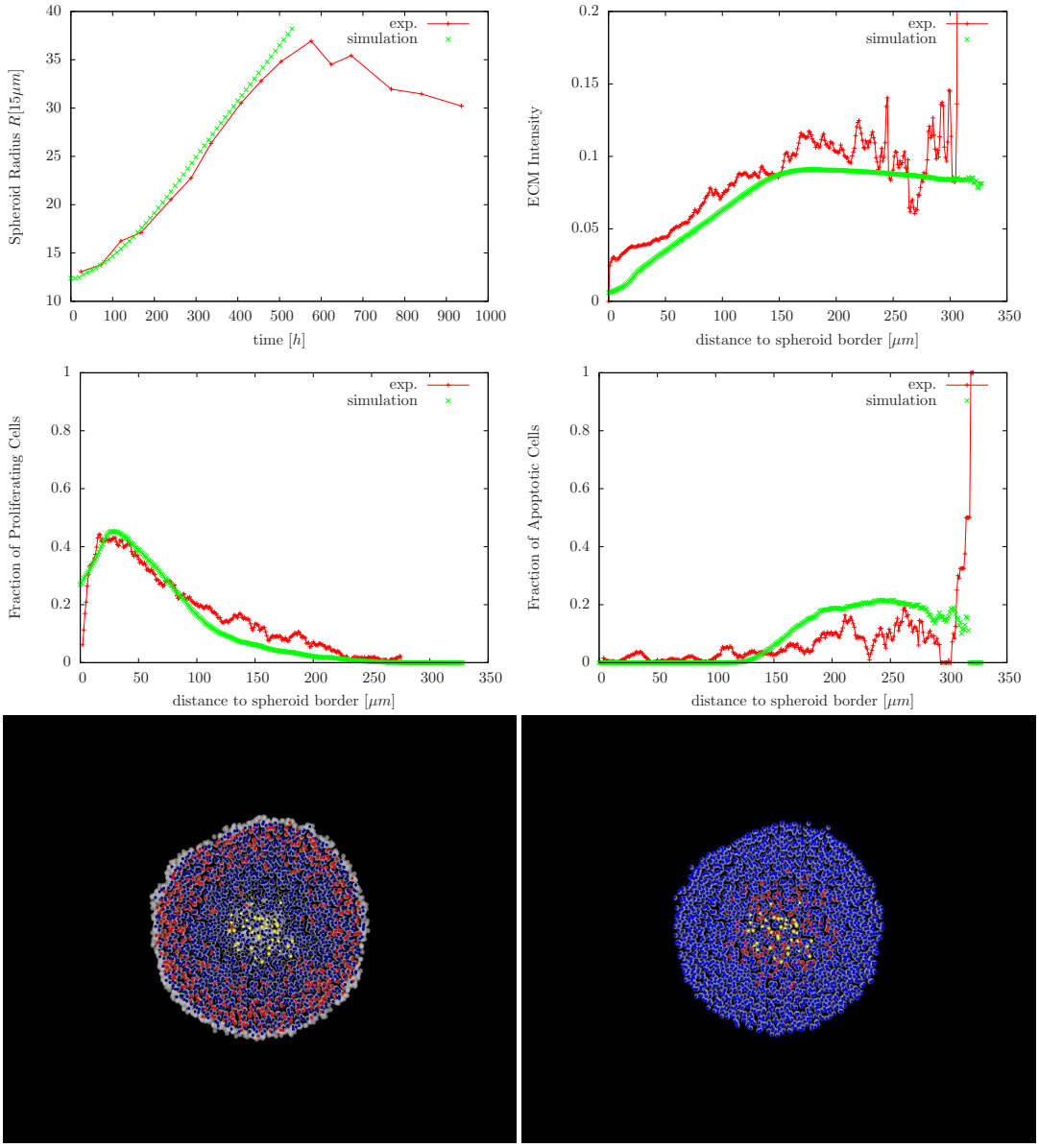

Figure 4.20: Best fit for condition III: $[G] = 25mM$ and $[O_2] = 0.28mM$. The collage shows the comparison between data and simulation results for the growth curves of the spheroid radius (*top, left*), the radial profiles of ECM density (*top, right*), proliferating cell fraction (*center, left*) and necrotic cell fraction (*center, right*). (*Bottom*): The slices of *in-silico* spheroids when reached a radius of $300\mu m$ indicate proliferating (*red, left*), quiescent (*blue, left*), necrotic (*red, right*), viable (*blue, right*) and the lysated cells (*yellow*)

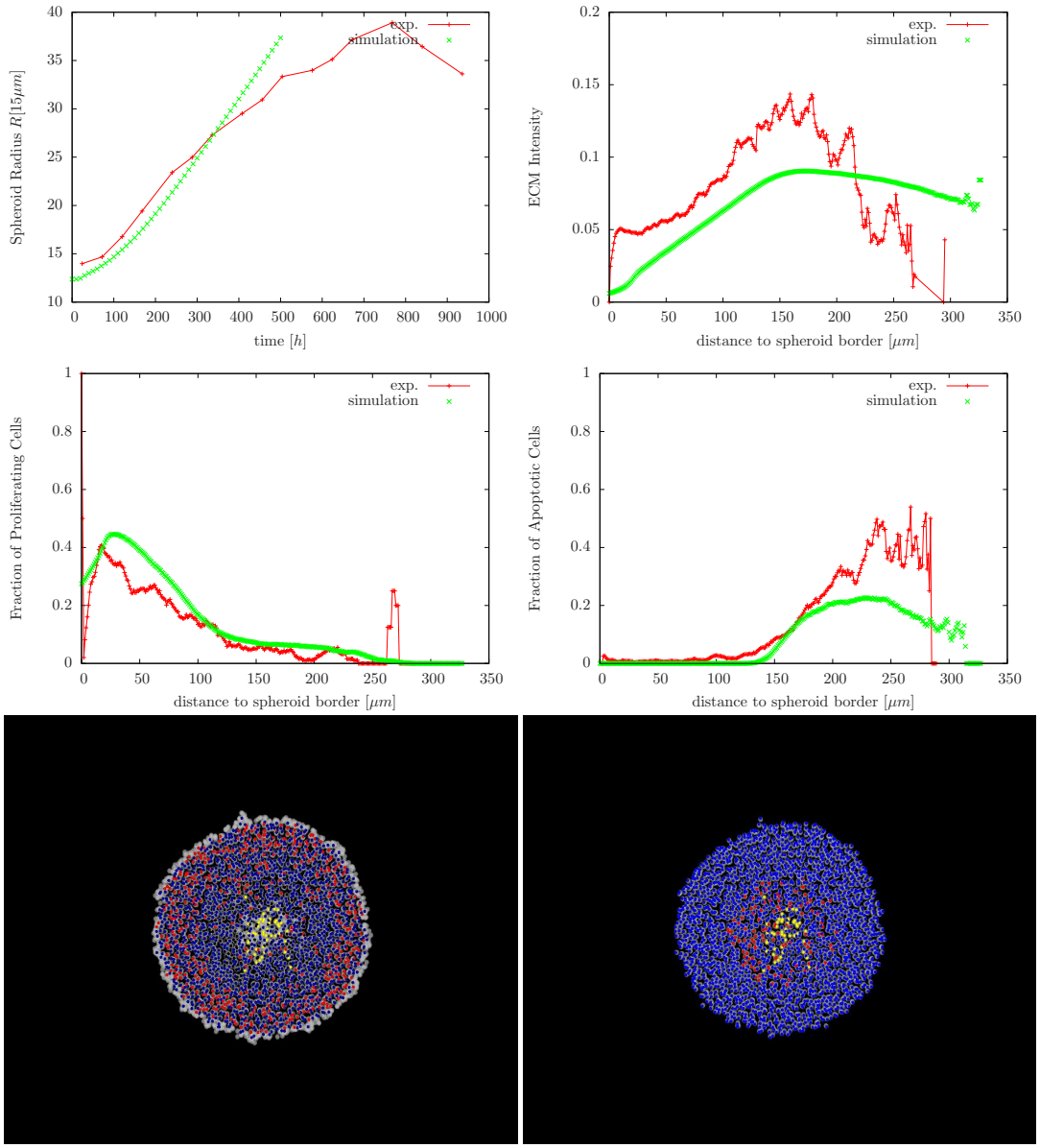

Figure 4.21: Best fit for condition II: $[G] = 5mM$ and $[O_2] = 0.28mM$. The collage shows the comparison between data and simulation results for the growth curves of the spheroid radius (*top, left*), the radial profiles of ECM density (*top, right*), proliferating cell fraction (*center, left*) and necrotic cell fraction (*center, right*). (*Bottom*): The slices of *in-silico* spheroids when reached a radius of $300\mu m$ indicate proliferating (*red, left*), quiescent (*blue, left*), necrotic (*red, right*), viable (*blue, right*) and the lysated cells (*yellow*).

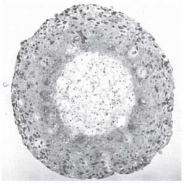

are obtained for probabilistic cell decisions were the probability to reenter into the cell cycle is smoothly decreasing function of Δ_{free}. We propose an exponential law.

Extra-Cellular Matrix (ECM) Requirement The low proliferating activity at the outer border of the SK-MES-1 spheroids could be explained by relating the cell-cycle reentrance to the local ECM density. Thus, a certain amount of ECM is required in order that cells reenter the cell cycle. The proposed reaction-diffusion equation shows a good agreement with radial profiles of ECM density.

4.3.2 Parameter Estimation from Nutrient-Dependent Data

Then, in a second step the influence of nutrient-limitation and metabolites on the cell growth and survival were studied.

ATP The ATP production rate assumed in this model considers the cells to maximize the outcome of ATP for all given glucose and oxygen concentrations. Depending on the ratio of glucose and oxygen concentration the metabolism will thus switch automatically between aerobic and anaerobic metabolism. Based on this assumption and the measured consumption rates, it could be shown that the ATP production rate stays constant for a wide range of glucose and oxygen concentrations. This suggests that cells regulate their glucose and oxygen consumptions in such a way that the ATP outcome is kept constant at a certain value.

For the EMT6/Ro cells two criteria for the cell decision on growth-quiescence and survival-death were evaluated for four nutrimental conditions: the critical product of the local glucose and oxygen concentration, and the production rate of ATP. Though, the ATP-threshold criterion shows a slightly better fit of condition I, II and III than the critical product, none of them is able to explain the growth saturation under condition IV.

While there is no significant difference between the critical oxygen-glucose-product and a critical ATP production for EMT6/Ro cells in respect to the overall agreement with the data, for the SK-MES-1 cell line using the critical ATP production leads too a much better fits than the critical oxygen-glucose-product. Nevertheless, ATP as the only criterion for cell death or survival does not suffice to explain the radial necrosis profiles of condition II and III.

Different Cell Types, Different Consumption Rates? By a sensitivity analysis it could be observed that a lower glucose consumption rate than originally estimated from measurements made for EMT6/Ro cells improves the fits of the SK-MES-1 cell line.

Lactate The automatic switch from aerobic to anaerobic metabolism introduced by the heuristic ATP production rate permits the estimation of lactate molecules produced per consumed glucose molecule. The different shapes of the radial necrosis profiles of condition II and III (SK-MES-1) and the rather high necrotic cell fraction for condition III (with 5 times larger glucose concentration compared to condition II) suggest that there might be different causes. Introducing lactate as an additional cause of death to the model can explain condition II and III.

The parameters of the best fit all four conditions of the EMT6/Ro cell line are shown in table 4.1.The best fitting parameters of SK-MES-1 cell line for condition II and III (without saturation) are summarized in table 4.2.

4.3.3 Growth Phases

The exponential and geometric growth phases could be reasonably explained for both cell lines (EMT6/Ro and SK-MES-1) for the examined conditions. For the SK-MES-1 cell line, the model should be validated for conditions I and IV. The phase of saturation could be explained by cell-cell-adhesion-driven migration in the case of very low glucose and oxygen medium concentrations. Here it has to be stated that in this case a necrotic core is not yet created. As soon as we a necrotic core establishes in the spheroid core, the cell-cell-adhesion-driven migration is not able anymore to stabilize the spheroids at a constant size (result not shown). It can be concluded at this point that short range interactions of cell-cell-adhesion are not sufficient to keep a large spheroid with a necrotic core together. The morphogen-driven migration as introduced might be an alternative due to the fact that it allows cells to communicate along the whole spheroid via a morphogen gradient (long range interaction). Nevertheless, the radial profiles extracted from micrographs taken during the phase of growth saturation show almost no proliferative activity. Thus, all cells seems to have become quiescent due to growth inhibitors from inside the tumor.

4.3.4 Validity of Hypothesis

Different model mechanisms have been proposed to explain the high necrotic cell fraction in the center of the spheroids (low in-vitro lysis rate, and morphogen-driven cell migration) and the high similarity of the proliferating and necrotic cell fractions of conditions II and III (different survival criteria: low lactate and high ATP concentration). Those mechanisms would have to be validated by further biological experiments.

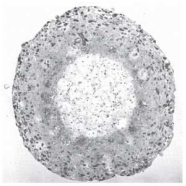

Part II

Tumor Vascularization Modelling & Parameter Acquisition

Chapter 5

Modeling Tumor Growth and Angiogenesis

In this chapter[1], we will propose an extension of the avascular model (chapter 3) by blood vessels and rules for tumor-induced vessel remodeling and angiogenesis mainly based on the vascular endothelial growth-factor (VEGF) and the dynamic properties of blood vessels (pressure, shear stress, etc.). Finally, the simulation results of three growth scenarios will be compared and discussed: (1) avascular tumor growth neglecting nutrient-limitation, (2) nutrient-limited tumor growth in a static blood vessel network and (3) tumor-induced angiogenesis.

Contents

[1] This chapter make reference to:
Drasdo, D., Jagiella, N., Ramis-Conde, I., Vignon-Clementel, I., Weens, W.
Modeling steps from a benign tumor to an invasive cancer: examples of intrinsically multi-scale problems. In: *From single scale-based models to multiscale modeling*, Eds. Chauviere, A. and Preziozi, L. and Verdier, C., 2009.

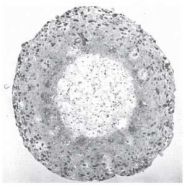

5.1 Angiogenesis and Impact on Tumor Progression

The transition from an in-situ tumor to invasive cancer is marked by a number of steps. This includes angiogenesis, the formation of new blood vessels to supply the growing tumor with oxygen and nutrientss. Angiogenesis is the process during which endothelial cells divide and generate new vessels sprouting towards the tumor as a response to angiogenesis factors secreted directly and indirectly by the tumor cells. Many angiogenesis factors have been identified so far [Wei07]. The most prominent one is probably VEGF which is related to platelet-derived growth factor (PDGF). A shortage of oxygen triggers an increase of the intracellular concentration of an active form of the protein hypoxia-inducible factor 1 (HIF-1) which then stimulates transcription of the VEGF gene. The protein VEGF is secreted into the extracellular space acting on the nearby endothelial cells as described above.

Different from monolayers and multicellular spheroids, which grow only up to about a millimeter in diameter, tumors growing in-vivo, e.g. Xenografts of human NIH3T3 cells in the mouse model [RBH$^+$09], can reach a size of several centimeters. As the multi-cellular spheroids the Xenografts have a largely spherical shape but in contrast to multi-cellular spheroids they are well vascularized and show only decent necrotic and apoptotic figures. Hence the induction of new vessels permits growth of tumor cell population up to about 3-4 magnitudes more than multi-cellular spheroids and, as in the case of NIH3T3 cells, is capable to avoid the formation of a central necrotic core.

5.2 Vascular Model

5.2.1 Growth factors

In this model, the endothelial growth factors are released by the (hypoxic) necrotic cells and diffuse into the tumor environment following the equation

$$\begin{aligned} \frac{\partial [VEGF]}{\partial t} &= D_{VEGF} \Delta [VEGF] \\ [VEGF] &= [VEGF]^{bv} \text{ at necrotic nodes} \\ [VEGF] &= 0 \text{ on the external boundary} \end{aligned}$$

where D_{VEGF} is the diffusion constant and $[VEGF]^{bv}$ the boundary source of growth factors released by the necrotic cells.

For a list of all the parameters used in the simulations, see Table 5.1.

5.2.2 Vascularization, angiogenesis and remodeling

The models for the vascularization and its adaptation to the micro-environment are largely inspired by the two-dimensional model of ref. [BR06] and the three-dimensional model in ref. [LR06]. We also refer to ref. [BR06] for biological references of every mechanism that these models describe.

Preexisting network: The preexisting network of vessels is generated on the random lattice, common with the tumor cells. The vessel orientation follows the three spatial directions, with an average distance between vessels of d^{bv}. Each node of the lattice is thus either free or occupied by a tumor cell (TC) or an endothelial cell (EC). Two neighboring EC nodes are linked by an edge e_{ij} of length $|e_{ij}|$ that represents a blood vessel of radius r_{ij}, initially at the homogeneous value of ${r_{ij}}^0$. Flow through a vessel Q_{ij} and pressure at the nodes P_i and P_j are computed in all the vessels based on the simplest resistance law (Poiseuille law) that linearly relates the pressure gradient in a segment with the flow through it. Poiseuille law reads as follow:

$$P_i - P_j = \frac{8\mu^{bv}|e_{ij}|}{\pi {r_{ij}}^4} Q_{ij}. \tag{5.1}$$

μ^{bv} is the dynamic viscosity of the blood, taken constant as a first approximation. Pressure is prescribed as a boundary condition at the entrances P_{in} and exits P_{out} of the network, and solved at nodes using Kirchoff's law. A measure of the shear stress f_{ij} in the vessel is calculated as a linear function of the pressure gradient and the radius: $f_{ij} = r_{ij}\,(P_i - P_j)$. We denote by ${f_{ij}}^0$ its value in the initial network.

Angiogenesis: A sprout can form from a blood vessel with a probability proportional to the time step divided by the endothelial proliferation time t_{EC}, if certain criteria are met. From a given EC node i, a new blood vessel that goes until the sprouting node j can emanate if the distance between the two existing EC nodes is smaller than a maximum length $l_{\max}$. In addition, along the possible new vessel path the nodes must be all free and the growth factor concentration higher than the threshold θ^{GF} that characterizes the angiogenic switch.

Remodeling: Within the living tumor zone (proliferating and quiescent zones), blood vessels cannot sprout but they can dilate due to proliferation induced by growth factors if the local growth factor concentration is above the threshold θ^{gf}. This occurs with a certain probability proportional to the time step divided by

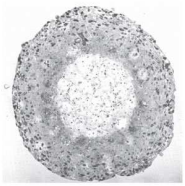

the endothelial proliferation time t_{EC}, up to a maximum diameter $d_{\max}$, with an increment of the radius r_{ij} of $1/2\pi(|e_{ij}|+1)$. In contrast, under-perfused vessels can also collapse due to the high pressure generated by the proliferation of tumor cells or disappear because they are not functional enough and thus experience themselves hypoxia, or are sensitive to the anti-angiogenic factors. This is modeled by the collapse of a vessel if its shear force is too low (${f_{ij}/f_{ij}}^0$ is below a critical value θ^{ss}) and the density of tumor cells is too large (percentage of TC nodes above p_c^{TC}), with a probability proportional to the time step divided by the collapsing time constant t_r. The vessel can also be removed with probability 0.5 if the flow is zero and the local concentration of oxygen is below a critical threshold $\theta_{bv}^{O_2}$.

The vascular network responds to the changes of the local micro environment by angiogenesis or remodeling. The local radius, pressure, flow and shear values are thus continuously updated. In turn, the changing vascular network influences the growth of the tumor as explained in the cellular model above.

Parameter	Value	Unit	Reference
D_{GF}	100	$\mu m^2/h$	[JPGCF05]
$[O_2]^{bv}$	0.07	mM	[FS85, FS86, JPGCF05],order of magnitude of [BR06]
$[G]^{bv}$	5.5	mM	[FS85, JPGCF05]
$[GF]^{bv}$	1	mM	[LR06]
d^{bv}	150	μm	order of magnitude of [LR06]
${r_{ij}}^0$	10	μm	[BR06]
μ^{bv}	0.1	Pas	order of magnitude from [Fun90]
P_{in}	100	Pa	defined up to a multiplicative constant
P_{out}	100	Pa	defined up to a multiplicative constant
l_max	100	μm	[LR06]
θ^{GF}	0.01	mM	[BR06]
θ^{O_2}	0.01	mM	[BR06]
t_{EC}	40	h	[BR06]
d_max	35	μm	[BR06]
θ^{ss}	0.5	$-$	[LR06]
p_c^{TC}	80	%	[LR06]
t_r	50	h	[LR06]
$\theta_{bv}^{O_2}$	0.01	mM	[LR06]

Table 5.1: Parameters of vascularization.

5.3 Results

We compared the growth of a tumor not constrained by nutrient and oxygen limitation with a tumor in a static blood vessel environment and a tumor that is able to modify the static blood vessel environment by triggering the formation of new blood vessels. In Figure 5.1, the radius of the tumor is plotted versus time for three cases: (1) with neither oxygen nor nutrient limitation, (2) with nutrient limitation but without the angiogenic switch, and (3) with nutrient limitation and angiogenesis.

In the "no limitation" scenario, oxygen and nutrients concentrations are set to be high enough to meet the tumor demands, both in space and time. All cells can divide and the tumor thus first expands exponentially (zone a of Figure 5.1). After some time, the cells in the center cannot divide anymore due to contact inhibition and they become quiescent. When the proliferating rim reaches a constant thickness, the radius becomes a linear function of time (zone c of Figure 5.1).

For the two other simulated scenarios there is *nutrient limitation*: oxygen and nutrients are supplied by sources (blood vessels) and diffuse out of them in the interstitial space but they are also locally consumed by the cells. As the tumor mass expands, there is a first period where demands are lower than supplies (as seen by the superposition of the three curves in zone a of Figure 5.1). Then, supplies cannot balance demands anymore, due to an increasing consumption: this is the *nutrient limitation* phase. This slows down the growth of the tumor, as can be seen by the decreasing slope in zone b of curves (2) & (3) of Figure 5.1.

After some time, the angiogenic switch occurs and enables the tumor to expand with a higher speed as indicated by the higher slope of the curve (3) compared to curve (2) in zone c of Figure 5.1: its demands of oxygen and nutrients are better fulfilled. Note that this slope is however lower than that of the *no limitation* scenario, since the latter constitutes an upper bound to the growth speed.

In addition to the tumor size, its structure varies significantly with the different environmental conditions. When there are neither oxygen nor nutrient limitations (Figure 5.2 1a&b&c, 2a, 3a), cells are either proliferating (yellow) or quiescent (green), but none of the cells are necrotic. In contrast, when oxygen or nutrients are lacking because their diffusions from blood vessels are not fast enough and their local concentrations are too low, necrotic cells (blue) appear in the center (Figure 5.2 2b&3b).

As a response to hypoxia and hyponutrition, cells produce growth factors that diffuse through the tissue, reach the existing blood vessels and finally trigger sprouting

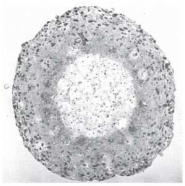

from them to create new blood vessels (Figure 5.2 3c). If no new blood vessels are created, the necrotic zone increases (blue region in Figure 5.2 2c larger than in Figure 5.2 3c, where only decent necrosis can be observed). Note the quiescent zones around the blood vessels inside the tumor (Figure 5.2 2c&3c): in these regions, there is enough oxygen and nutrients for the cells but they cannot divide due to contact inhibition of growth. As time goes, the case without limitation continues to growth with a spherical shape and without any necrosis (Figure 5.2 1c). In the limited case, the tumor continues to growth, although it tries to grow towards or along blood vessels (Figure 5.2 2c). In the angiogenic case, new vessels are forming towards and inside the tumor (Figure 5.2 3c) as it continues to grow with a speed closer to the no limitation case (Figure 5.1).

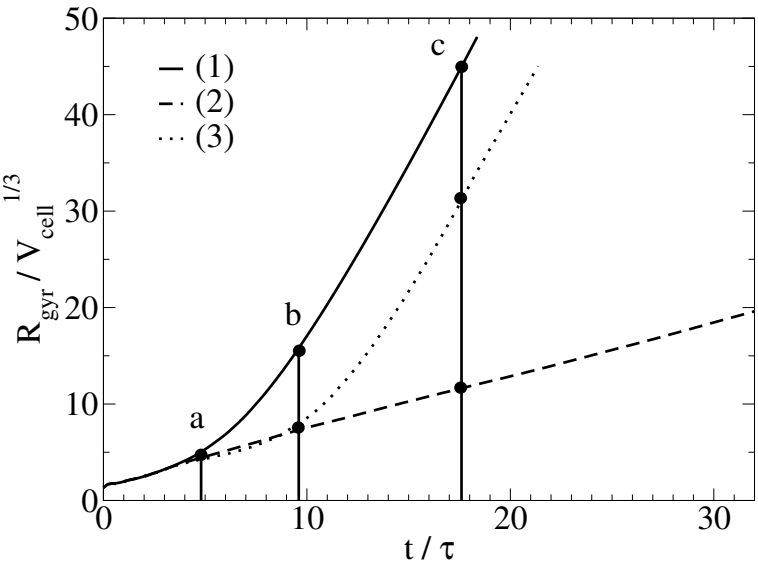

Figure 5.1: Time evolution of the radius of a tumor cell population for three different scenarios: (1) without any nutrient limitation (*solid line*), (2) nutrient limited growth in vascularized tissue (*dashed line*) and (3) nutrient limited growth inducing angiogenesis (*dotted line*).

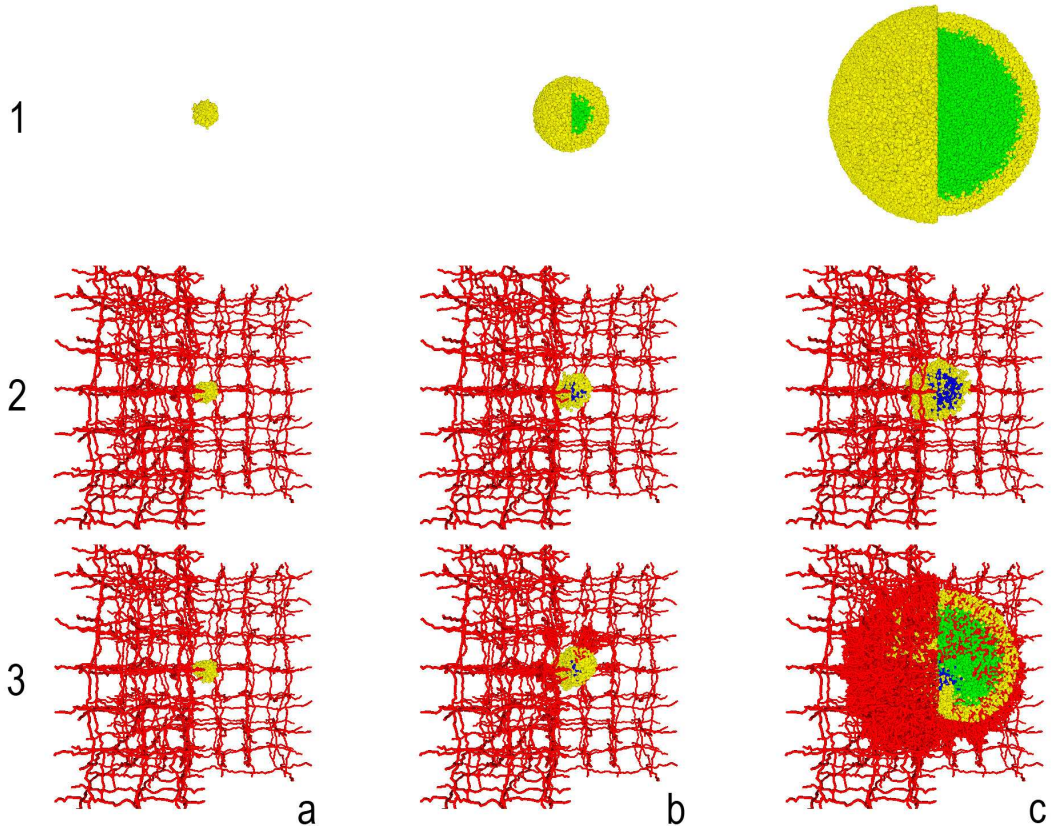

Figure 5.2: Screenshots from the simulations at times $t/\tau = 4.8$ (*left*), $t/\tau = 9.6$ (*center*) and $t/\tau = 17.6$ (*right*). Each figure is composed by an exterior view on the left-hand side and a central-cropped view of the simulated domain on the right-hand side. The colors indicate proliferating (*yellow*), quiescent (*green*) and necrotic cells (*blue*) as well as blood vessels (*red*). The upper sequence shows the reference simulation of growth without any nutrient limitation in contrast to the lower two sequences. The lower sequences show the scenarios of nutrient limited tumor growth in vascularized tissue without (*center*) and with angiogenesis (*bottom*).

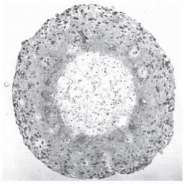

Chapter 6

Parameter Estimation from Perfusion Images

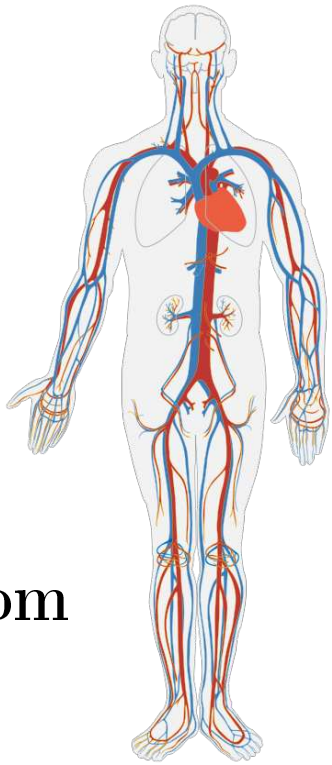

Figure 6.1: Simple diagram of the human circulatory system [wikipedia]

6.1 Introduction

Vascularization

The vascularization is composed of a complex three-dimensional tree-like structure. It can be subdivided into *arteries*, *veins* and *capillaries*. In the systemic circulation, arteries are the vessels which transport the oxygenated blood from the heart to the tissue. Veins carry back the oxygen-deficient blood to the heart. In the pulmonary circulation, it is the reverse. Capillaries are the micro-vessels connecting both, arteries and veins, and are mainly responsible for the molecular exchange between the blood and tissue (nutrition, oxygen, metabolites etc.).

The functionality of a vessel network is not only determined by its local properties as vessel diameter and permeability surface, but to a large extent results from the typological structure at the tissue scale. Optimal blood delivery to all parts of the tissue depends on the circulation which depends on the flow which depends on the interplay of topology and local properties.

So in order to parametrize an *in-silico* model of vascularized tissue and tumor-induced angiogenesis one needs to study carefully key aspects of vascularization. The reconstruction of vascularizations has been done e.g. from 3D X-ray micro-CT images of animal lungs filled with solid radio-opaque contrast agent by [YYR+10]. Tissue samples can also be analyzed with this method. It gives insight into the overall topological structure of the vascularization, except for the smallest vessels. Moreover it is a rather expensive and invasive technique. Other methods are the histological analysis of tissue slice to get quantitative information about the micro-vessel density, the vessel size distribution etc. Nevertheless, information of the three-dimensional organization

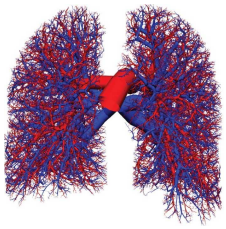

and functional properties of the micro-vascularization is not sufficiently accessible. In general, those techniques coincide with the sacrifice of the host (limited to animal experiments) and thus excludes the study of vascular change in time due to angiogenesis.

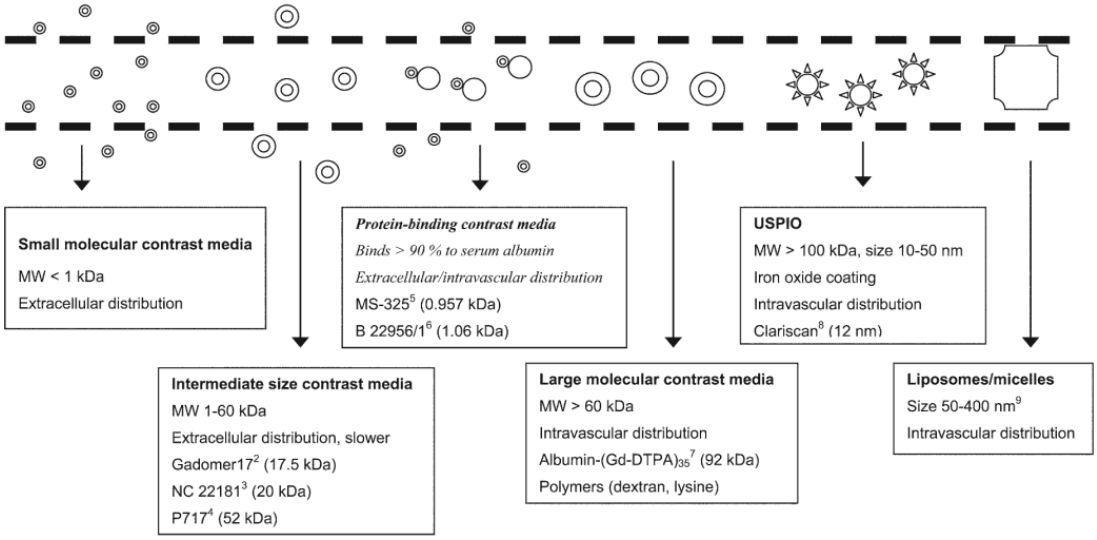

Figure 6.2: Different classes of contrast agents. Image from [FB03]

Non-invasive Imaging

A non-invasive technique widely used in clinical diagnosis is MRI. It permits to visualize polar molecules (especially the protons of hydrogen contained by water) in parts of the body. As different tissues contain different amounts of hydrogen they become distinguishable by the contrast in the resulting images. In Constrast Enhanced-Magnetic Resonance Imaging (CE-MRI) the visibility of blood vessels is increased even further by injecting CAs into the bloodstream which alters the visibility of protons in the tissue they are located. It can be distinguished between two relevant CAs (see figure 6.2): *Intra-vascular agents* stay in the blood vessels while *extravascular contrast agents* can leak through the vessel walls into the interstitial space (i.e. extra-vascular-extra-cellular space). As one can see in figure 6.3 showing a sequence of CE-MRI images of the lung one can clearly identify the large vessels. For small arteries and veins, one only sees their combined perfusion effect in an image voxel. The typical resolution of a voxel is $0.3mm \times 0.3mm \times 3mm$ ($3mm$ being the thickness of the slice), but it can vary a lot. In general one can state, that a higher spatial resolution (SR) results in a longer acquisition time. The acquisition time has an impact on the temporal resolution (TR)

in DCE-MRI. Some examples are: SR=$1.8 \times 2.1 \times 10mm^3$ and TR=$2.8ms$ [WRZ+12], SR=$1.9 \times 3.6 \times 4.0mm^3$ and TR=$1.5s$ [DRL+06], and SR=$0.23 \times 0.47 \times 2.0mm^3$ and TR=$14s$ [ESG+09].

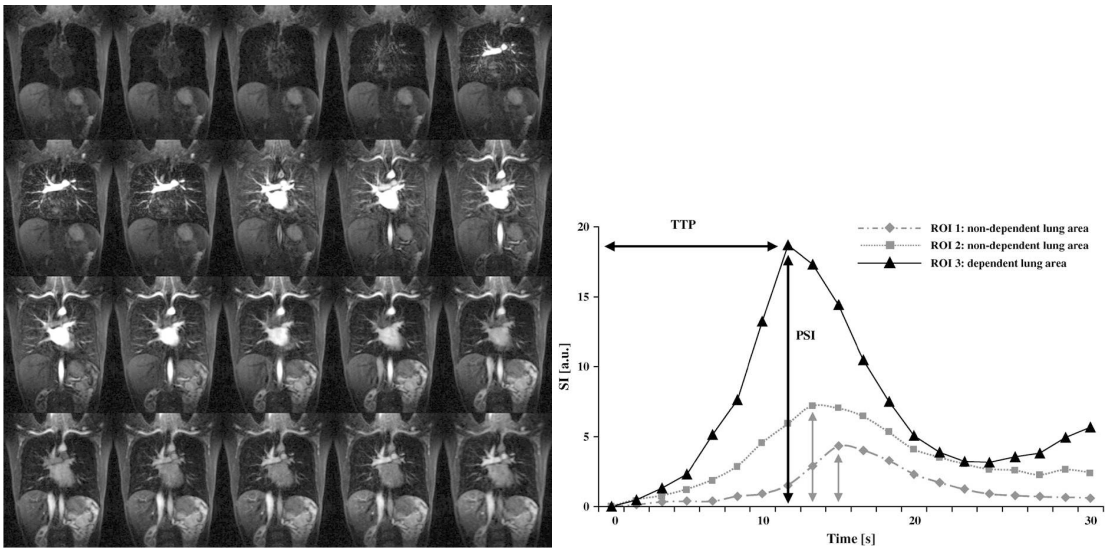

Figure 6.3: *left:*T1-weighted dynamic contrast-enhanced magnetic resonance imaging (MRI) of a volunteer. The images represent a single partition of a three-dimensional volume dataset covering the entire lung at different time points (interval, $1.5s$). After the injection of an MR contrast agent bolus, an enhancement of the pulmonary vessels as well as lung tissue can be observed. *right:* Time-signal intensity (SI) curves computed from contrast-enhanced perfusion MRI using regions of interest (ROI) localized in isogravitational nondependent lung (ROI 1 and 2) and dependent lung (ROI 3). Ref. [DRL+06]

Parameter Acquisition via Inverse Problem

In order to quantify the architectural (vascular volume fraction) and functional (flow and permeability) vessel properties the contrast kinetics are tracked in time via DCE-MRI. Here a temporal sequence of CE-MRI images of the same part of tissue is acquired and used to get some insight into the dynamic properties. The general idea is to fit a physiologically simple and non-spatial model describing the processes of CA perfusion to the observed CA intensity time curse in each voxel of the image sequence to recover the local parameters of vascular volume fraction, blood flow and vessel permeability (depending on the model).

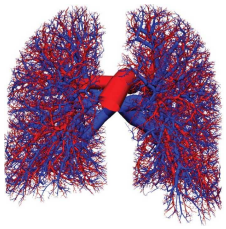

Similar techniques are DCE-CT and DCE-US. Though DCE-CT has a similar image quality as DCE-MRI it has the disadvantage of exposing the patients to ionizing radiation and is less suited to soft than solid tissues (e.g. bones, teeth etc.). On the other hand, DCE-US is based on Microbubble (MB)s used as purely intra-vascular agents. It is much cheaper than DCE-MRI and DCE-CT and has shown a similar predictability for non-progressive survival (of treated patients) as DCE-MRI [PHL$^+$08, LCC$^+$11]. Though it suffers from coarser spatial resolution.

For clinical diagnosis those techniques are important tools to detect the extent of tumoral tissue by the relative differences in the local vessel properties (e.g. vascular volume fraction) between healthy tissue and highly vascularized tumor tissue. But also to monitor the treatment with an anti-angiogenic drug [LCC$^+$11]. Nevertheless, little work was done on studying the errors introduced by using a physiologically simple pharmaco-kinetic model ([BSP$^+$91, BBH$^+$99, TK91, TBB$^+$99, BKL$^+$04, BZKG09] etc.) to model a physiologically complex process [LHBtHR10].

This Chapter:

This chapter proposes a process chain to create artificial contrast-enhanced perfusion data data (comparable to DCE-US, DCE-MRI and DCE-CT) for different *in-silico* vasculatures as a benchmark for the evaluation of inverse methods and to better understand the relationship between the recovered perfusion parameters and the underlying true vasculature (form & function).

Section 6.2 will focus on the construction of *in-silico* vasculatures representing typical test cases as a highly functional vascularization in healthy tissue and vasculatures locally modified by an embedded tumor. The vessel properties will be taken from literature. The construction laws are chosen such that the resulting properties agree with physiological observations from the literature.

In section 6.3 a numerical model will be proposed to simulate the perfusion of (purely *intra-vascular* as well as *extra-cellular*) agents through given *in-silico* vascularizations. As an outcome of the simulations *in-silico* MRI images will be discussed.

In section 6.4 an inverse method is applied to study its predictability by comparing recovered and original parameter maps for different topologies and settings.

6.2 Creating *in-Silico* Vasculature

6.2.1 Vessel and Voxel Arrangement

The vessels will be represented by a graph $G = (V, E)$ of vessel nodes V and vessel segments $E \subset V \times V$. For simplicity the vessels nodes will be placed on a *square lattice* (see figure 6.4, *dashed lines*). Two vessel nodes can be connected if they are in each

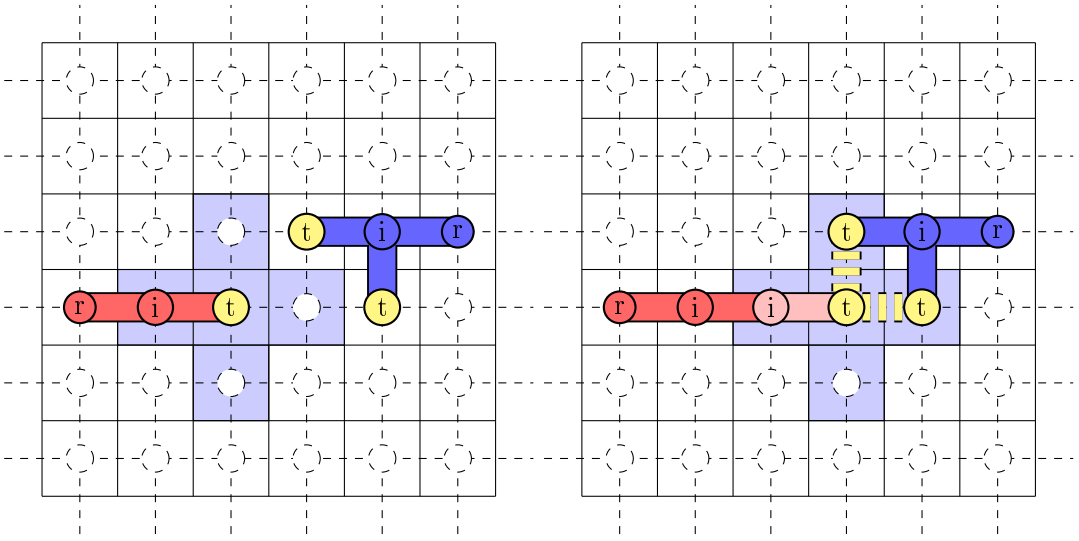

(a) Sprouting in *von Neumann Neighborhood* (b) Creating Inter-Tip-Connections

Figure 6.4: Arrangement of voxels (*solid lines*) and vessels (*dashed lines*) on a square lattice. Vessel nodes can sprout to free lattice sites within their *von Neumann neighborhood* (*light blue*). Here a *tip* (*yellow*, (a)) sprouts to the right becoming an *interior* vessel node (*pink*, (b)). Neighboring *tips* form inter-tip-connections.

other's *von Neumann neighborhood* (see figure 6.4, *blue squares*). So one vessel node could theoretically be connected with $2d$ neighboring nodes, d being the dimension of the lattice.

The dual of the vessel lattice is a square lattice as well. It describes the spatial partition into *voxels* (see figure 6.4, *solid lines*). Voxels are the three-dimensional counterpart of pixels. Here they will represent the spatial compartments of tissue.

6.2.2 Vessel Properties

Vessel nodes will be considered to be either a *root* (boundary to the unconsidered blood circuit of the body), *interior* or *tip* (tree leaves creating capillary connections with other tips) (see figure 6.4).

For a given vessel network we can calculate the following vessel geometrical and functional properties:

Vessel Radii: The radii of the vessel tip are assumed to be $r = 4\mu m$. Then the radii of the remaining vessel trees can be calculated recursively by

$$r^{\alpha}_{root} = r^{\alpha}_{left} + r^{\alpha}_{right}. \tag{6.1}$$

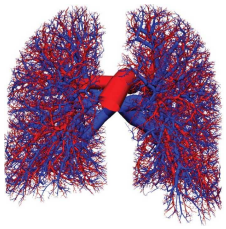

In literature the values of α vary between 2 and 3 depending on the vessel size and tissue. Kurz and Sandau [KS97] proposed $\alpha = 2.7$. We will use different values for arteries, $\alpha^{art} = 3$, and veins, α^{ven} as they were found to better fit the asymmetric network properties (see section 6.2.6).

Blood Viscosity: The apparent blood viscosity[1] was found to depend on the vessel radius and hematocrit. Hematocrit is the volume fraction of red blood cells in blood. It is normally about 0.45 for men and 0.40 for women [PSOH03]. The following equation published by Pries et al. [PSG+94] approximates the measured dynamic apparent blood viscosity for hematocrit of 0.45.

$$\eta(r) = 4 \cdot 10^{-6} \cdot \left(6e^{-0.17r} + 3.1 - 2.44e^{-0.06(2r)^{0.645}}\right) \tag{6.2}$$

r_{ij} being in μm and η in $kPa \cdot s$.

Pressure and Flow: In the microcirculation, the Reynolds and Womersley numbers are small, and thus flow is essentially steady unidirectional and developed. Hagen-Poiseuille flow is a good approximation [ref Fung book Circulation chapter] if detailed velocity and pressure around each red blood cell is not needed, as is the case in the present study. The relation between the flow, f_{ij}, through a vessel segment (i, j) and the pressure of its vessel nodes, $\Delta p_{ij} = p_i - p_j$, is described by the *law of Hagen-Poiseuille* as following.

$$f_{ij} = \frac{\pi}{8} \cdot \frac{r_{ij}^4}{\eta(r_{ij}) \cdot l_{ij}} \cdot \Delta p_{ij} = G_{ij} \cdot \Delta p_{ij} \tag{6.3}$$

G_{ij} is the inverse of the resistance to flow.

As both trees (venous and arterial) are separate from each other we assume all neighboring *tip* nodes to form inter-tip connections of capillary size ($r = 4\mu m$). The pressure in the vessel nodes can be calculated by applying the *Kirchoff-law* and solving a linear system of the relation between the pressure in node i and its neighbor nodes j.

$$\sum_j G_{ij} \cdot p_i - \sum_j G_{ij} \cdot p_j = 0 \tag{6.4}$$

The pressure in the root nodes is given in table 6.2. In the following the flow in the vessel segments are obtained by equation 6.3.

[1] Viscosity is a measure of the resistance of a fluid which is being deformed by either shear stress or tensile stress.

Shear Stress: The shear stress for Poiseuille flow is given by

$$\tau_{ij} = \frac{\Delta p_{ij}}{2 \cdot l_{ij}} \cdot r_{ij} \tag{6.5}$$

6.2.3 Initialization of Network

As a starting point the root nodes of the future arterial and venous vessel trees are placed. To insure blood flow at least one root of each vessel type (artery or vein) is needed. Optionally, an initial vessel is placed in the domain connecting an arterial and a venous root node.

6.2.4 Randomly Growing Blood Vessels from existing Network

In a naive approach vessels grow and branch randomly until all lattice points are occupied. Here we iterate over all vessel nodes. If at least one neighboring voxel (see section 6.2.1) is still not occupied by a vessel node then the vessel node sprouts with probability p^{spr} (table 6.1) to one of the free neighbor voxels. The vessel sprouting is done by adding another vessel node to the center of the targeted voxel and connecting it to the originating node of sprouting via a vessel segment. The new node becomes a *tip*. If the originating node was a tip as well it becomes a *interior*.

Algorithm:

1. For all vessel nodes $v_i \in V$ do
   (a) if v_i has free neighbor voxels sprout with probability $p^{spr} = 0.5$:
      i. add vessel node to randomly chosen free neighbor voxel: $V := V \cup \{v_j\}$
      ii. add vessel segment connecting both nodes: $E := E \cup \{(v_i, v_j)\}$
      iii. update v_j to *tip* and v_i to *interior*
2. Go back to (1.).

6.2.5 Capillary Shear Stress Homogenization

The aim of the algorithm described in the following is to create a blood vessel network consisting of arterial and venous vessel trees with a high functionality. That means that blood flow at the tree leaves is maximized and homogenized among the whole network.

For this purpose Goedde and Kurz [GK01] proposed a Monte-Carlo method which iteratively leads to non-functional vessels collapses (uniquely the tree leaves or tips) and functional vessels sprouts. A possible measure for functionality could be the (insufficient and sufficient) intra-vascular flow in the vessel tips. Goedde and Kurz [GK01] found that it is rather the capillary shear stress which regulates the vessel remodeling. An algorithm largely inspired by those assumptions can be summarized as the following.

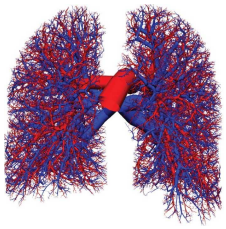

Algorithm:

1. Calculate the vessel radii (eq. 6.1), pressure (eq. 6.4), flow (eq. 6.3) and shear stress (eq. 6.5) in vessel network
2. Estimate minimum and maximum shear stress among all tip segments: τ_{min} and τ_{max}.
3. Perform a *vessel collapse/degeneration* for tips randomly chosen with probability $p_{ij}^{deg} = \frac{\tau_{max}-\tau_i}{\tau_{max}-\tau_{min}}$.
4. Perform 10 iterations of *vessel sprouting* of randomly chosen nodes (see section 6.2.4) with sprouting probability p^{spr} (table 6.1)
5. Go back to (1.).

Examples: Capillary Shear Stress Homogenization

Figure 6.5 shows how a completely randomly initialized vascularization (section 6.2.4) changes during shear stress homogenization (section 6.2.5). At the beginning the single arterial and venous trees fill up more or less well separated areas. Consequently, in many areas - especially inside those trees - there is very low and partially no flow at all as the pressure differences stay very small. Due to the collapse of non-functional vessels (inside the trees) and the survival of capillaries with high shear (usually at the interfaces of arterial and venous trees) the trees of different types (artery/vein) penetrate each other and increase their common interfaces. As a consequence the inter-tree-connections increase and with them the overall flow.

Figure 6.6 shows the same algorithm applied to a vascularization in a three-dimensional environment (of size $100 \times 100 \times 50$ voxels). Starting from a random vascularization with one arterial (centrally placed in the x-y-plane) and five venous root nodes (randomly spread among the domain border), most of the initial vascularization collapsed after the first iteration due to non-functionality (low shear stress). Already after 20 iterations the whole domain is filled with vessels and the overall flow maximized. I.e. the vascularization still changes by random collapse, but does not increase anymore in number of inter-tip-connections - especially in inter-tree-connections.

6.2.6 Comparison with Data

In several statistics over the properties of vessels of different size/diameter, it can be observed that there are differences between different types of tissues (e.g. pressure, see figure 6.9) and asymmetries between venous and arterial blood vessels (e.g. wall shear stress and blood velocity, see figures 6.10 and 6.11).

In order to take those asymmetries into account, in the following we will compare different functional properties (pressure, wall shear stress, blood flow and velocity) with

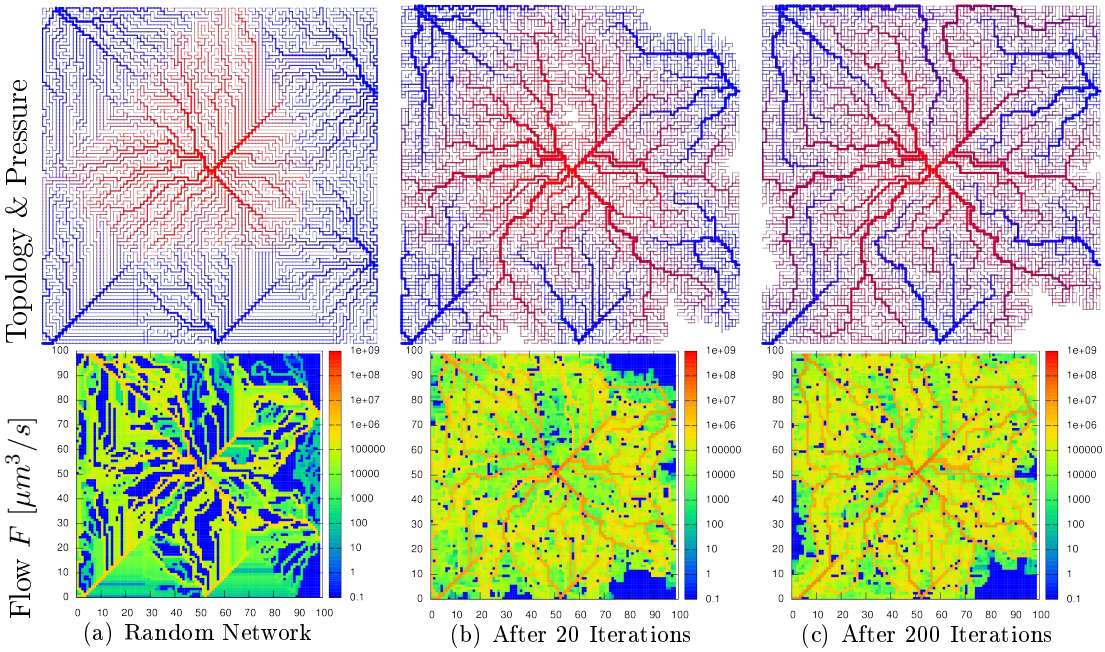

Figure 6.5: Capillary shear stress homogenization in 2D. (a): Vessel network after randomly extending the venous (*blue*) and arterial (*red*) root nodes until filling the whole domain (section 6.2.4). Blood vessel networks resulting from 20 (b) and 200 (c) iterations of collapsing blood vessels with low shear stress and random regrowth (section 6.2.5). The figures show the vessel arrangement (*top*) and the flow rates (*bottom*). The color in the topological maps visualize the intra-vascular pressure (*blue*= $2kPa$ and *red*= $12kPa$).

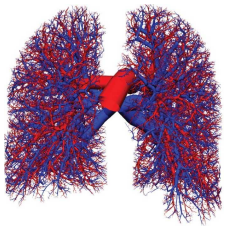

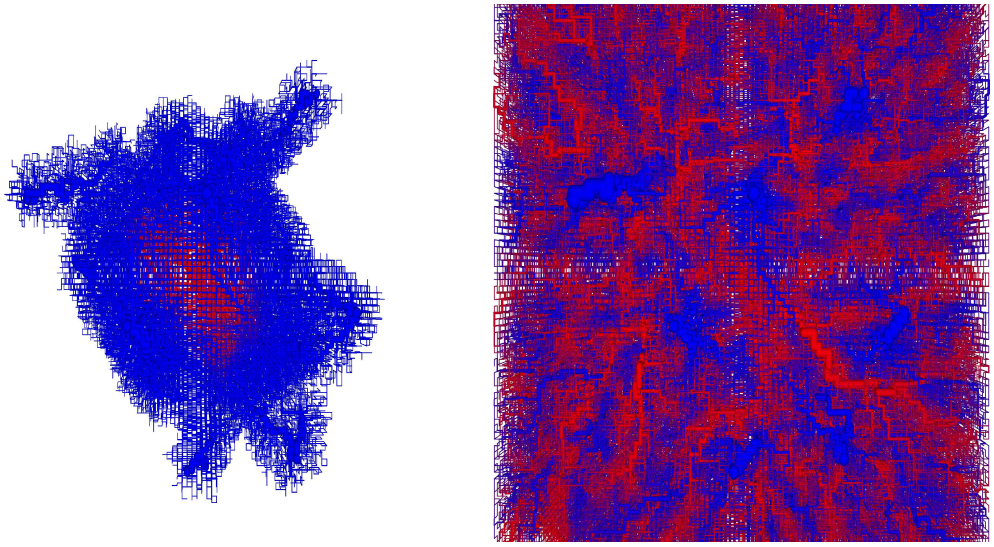

(a) After 1 Iteration (b) After 20 Iterations

Figure 6.6: Flow homogenization in 3D. (a) Vessel network after randomly extending the venous (*blue*) and arterial (*red*) root nodes until filling the whole domain. (b): Final blood vessel network after 20 iterations of collapsing blood vessels with low flow and random regrowth.

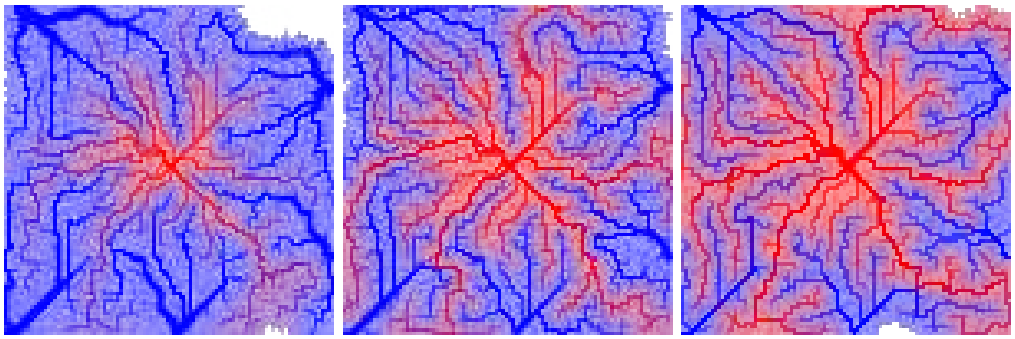

(a) A:3, V:2 (b) A:2.7, V:2.4 (c) A:2.7, V:2.7

Figure 6.7: Vascular networks (*in-silico*) created by the CSSH algorithm (200 iterations) and different combinations of power-law exponents.

measured data by varying the exponents α^{art} and α^{ven} of the power-law (eq. 6.1) which determine the radius distribution among the vascular trees.

Figure 6.7 shows three different vascularizations in a two-dimensional arrangement of voxels. The smaller the exponent α the larger the vessels grow in diameter toward the tree roots (and vice-versa). As we will see in the following the functional properties will strongly depend on the choice of α.

Figure 6.8 indicates that the flow rate is following a similar power law as the radius $f \approx r^{\alpha}$.

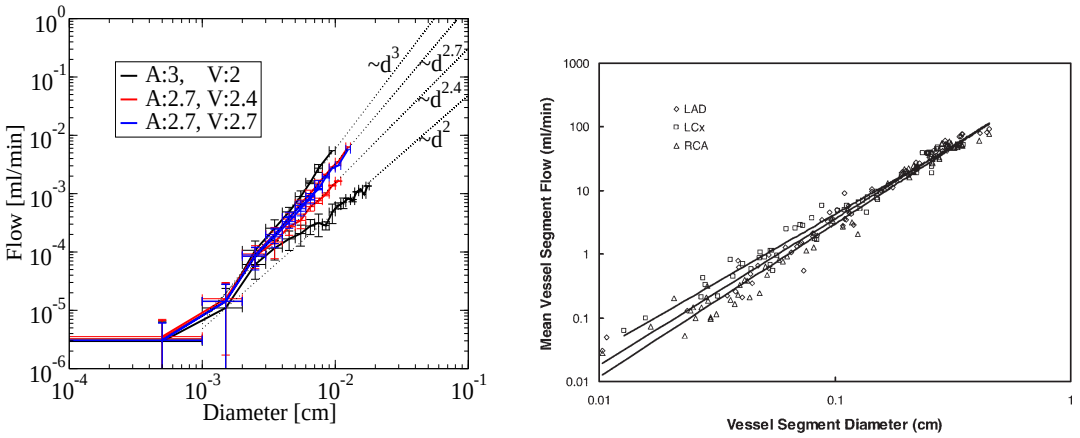

Figure 6.8: Blood flow. *left: in-silico* profiles of blood flow for different combinations of exponents for arterial and venous trees. The *right:* Time-averages flows measured in right coronary artery (RCA), left anterior descending coronary artery (LAD), and left circumflex artery (LCx) and respective exponents of 2.40, 2.30, and 2.13. Image from [HK07].

Figure 6.9 shows how pressure depends on α. The smaller α the less pressure changes inside the vessel tree. So low α exponents lead to pressure plateaus among the individual trees followed by a sudden pressure drop (or increase) at the capillary level. Large α's rather lead to a smooth transition of pressure between different trees.

The shear stress is the highest at the "bottle neck" of the vascular networks, the capillary interface between arterial and venus trees. Figure 6.10 shows that all *in-silico* vascularizations reach the same average capillary shear stress as found in literature. For larger venules the shear stress decreases to a flat plateau. In the arterial trees the shear stress increases again for larger arterioles after having reached a local minimum. The latter one was found *in silico* only for $\alpha = 3$.

As for the flow rate larger α's increase the blood velocity at the tree root nodes (see figure 6.11). For $\alpha = 3$ the blood velocity of $13mm/s$ at the root reaches the values

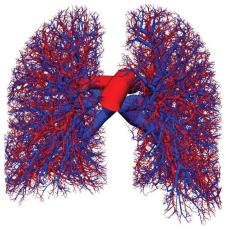

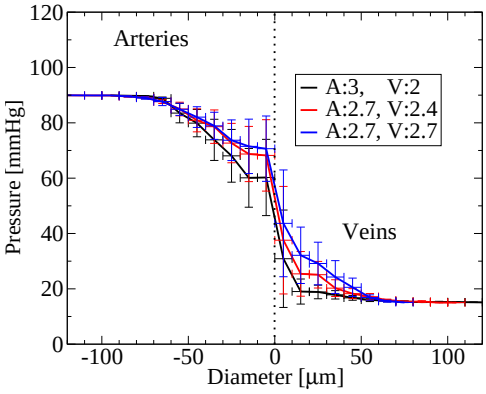

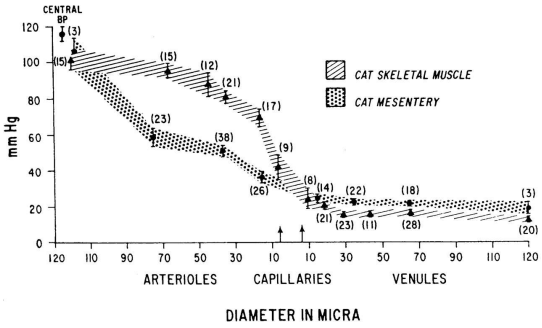

Figure 6.9: Intra-vascular pressure. *left: in-silico* profiles for different combinations of exponents for arterial and venous trees. *right:* Image from [FZ74]

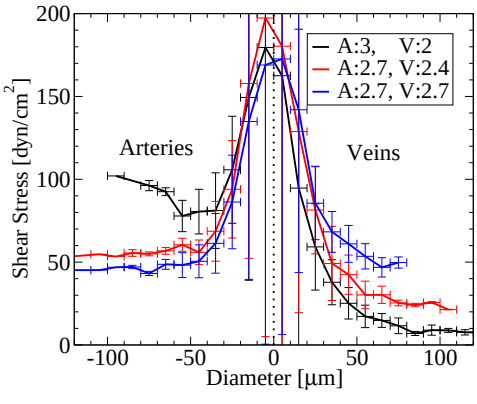

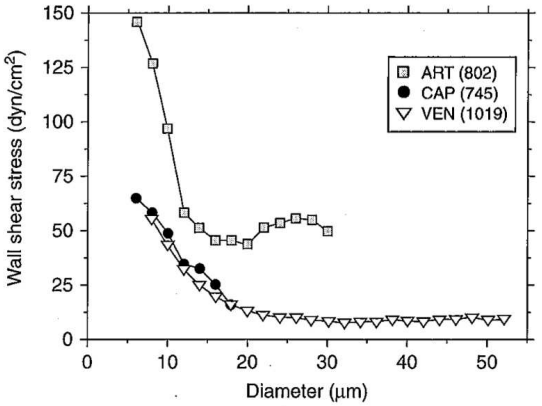

Figure 6.10: Intra-vascular wall shear stress. *left: in-silico* profiles for different combinations of exponents for arterial and venous trees. *right:* Image from [FB03]

found in literature for larger arterioles. An $\alpha = 2.7$ leads to much lower velocities of around $5 - 8mm/s$ rather corresponding to what was measured in veins.

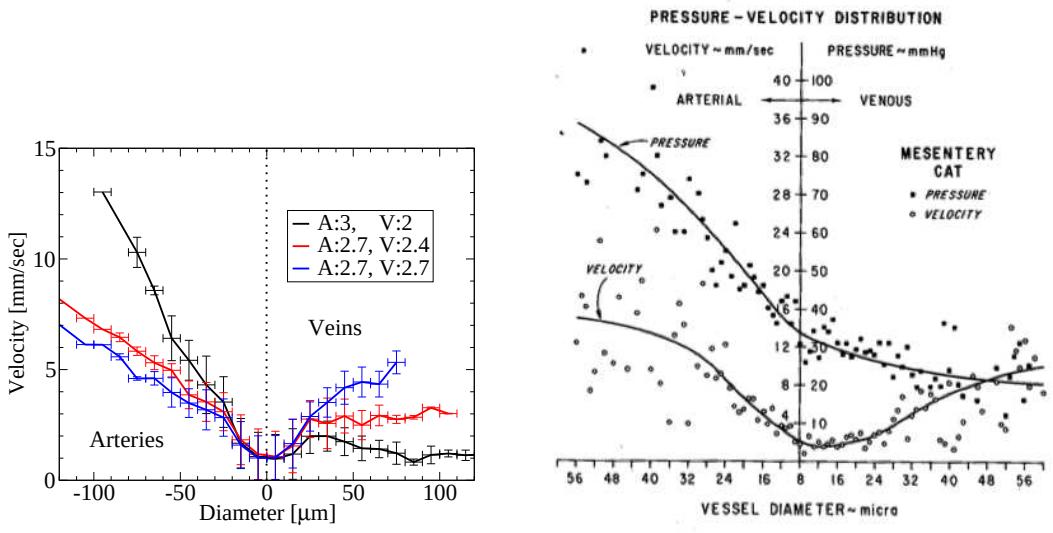

Figure 6.11: Blood velocity. *left: in-silico* profiles for different combinations of exponents for arterial and venous trees. *right:*Image from [PS08]

Conclusion: The high velocity and shear stress in large arterioles, as well as a rather smoothly decreasing pressure gradient indicate a large arterial power law exponent of $\alpha^{art} = 3$. For the venous counterpart the very low wall shear stress in larger venules and the constant pressure among all vessels preference a very low $\alpha^{ven} = 2...2.4$. On the other hand, the measured *in-vivo* velocities are only reached for at least $\alpha^{ven} = 2.7$. For all following simulations we will thus use $\alpha^{art} = 3$ and $\alpha^{ven} = 2.7$ (see table 6.2).

6.2.7 Vessel Remodelling in Tumorous Tissue and Angiogenesis

Inside growing tumors the conditions are different from "normal" or healthy tissue (see chapter 5). In order to create a "tumor-like" vascularization we will introduce two regions - a *tumor region* and a *necrotic core* - where the rules/parameters for the homogenization algorithm will be chosen differently.

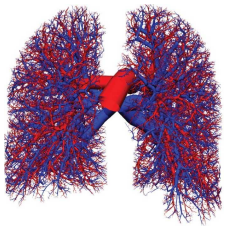

Increased Micro-vessel Density (MVD) in Tumorous Tissue

Due to a high proliferative activity the tumor cells consume much more nutrients than the quiescent cells in the surrounding healthy tissue. Consequently, an increased production of VEGF in hypo-nourished parts of tumor will stimulate vessel sprouting.

On one hand, the vessel sprouting probability p^{spr}_{tumor} is increased while the vessel collapse probability p^{deg}_{tumor} is decreased. Both values are assumptions (see table 6.1). On the other hand, the higher MVD is mimicked by connecting neighboring capillary ends with n parallel vessels. Consequently some algorithm-relevant vessel properties have to be adapted. The vessel radii power law changes to

$$r^{\alpha}_{root} = n_{left} r^{\alpha}_{left} + n_{right} r^{\alpha}_{right}. \tag{6.6}$$

The Hagen-Poiseuille-law modifies to

$$f_{ij} = \frac{\pi}{8} \cdot \frac{n_{ij} r^4_{ij}}{\eta(r_{ij}) \cdot l_{ij}} \cdot \Delta p_{ij} = G_{ij} \cdot \Delta p_{ij} \tag{6.7}$$

The plasma volume fraction in tumorous tissue was found increased by one order of magnitude (see table 6.4). In the following we assume $n = 10$ for inter-tip-connections inside tumoral regions (see table 6.1). Figure 6.12 shows three examples of different $n = 1$, 4 and 10. One can see how with larger n not only the inter-tip-connections increase, but the average vascular volume fraction as well due to equation 6.6.

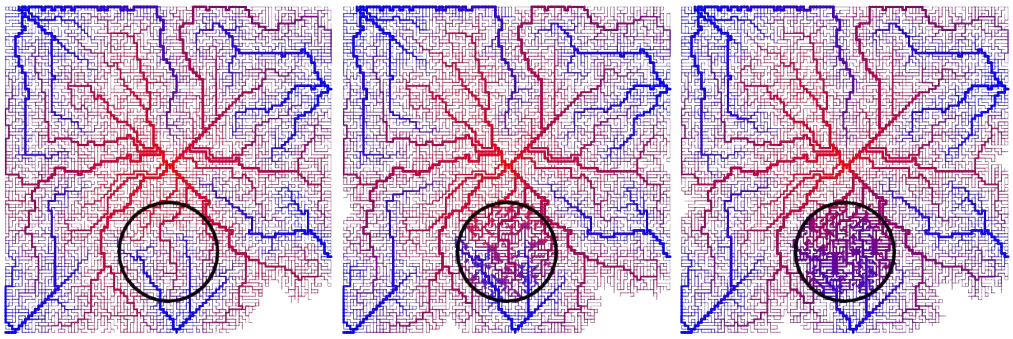

(a) $n = 1$ (b) $n = 4$ (c) $n = 10$

Figure 6.12: Vascular networks (*in-silico*) after 110 iterations of homogenization (100 without and 10 with tumor) and n parallel capillaries in the tumor region (black circle) of diameter $d_{tum} = 1.8mm$.

Increased Vessel Collapse in Necrotic Core

Beyond a certain size, the central parts of the tumor are not nourished sufficiently anymore. As a consequence, a necrotic core appears. It was observed that this necrotic

zone is not only lethal to tumor cells, but to endothelial cells and thus blood vessels as well.

The vessel sprouting probability $p^{spr}_{necrotic}$ is decreased and the vessel collapse probability $p^{deg}_{necrotic}$ increased in respect to healthy tissue. Here the choice of parameter was an heuristic assumption (see table 6.1).

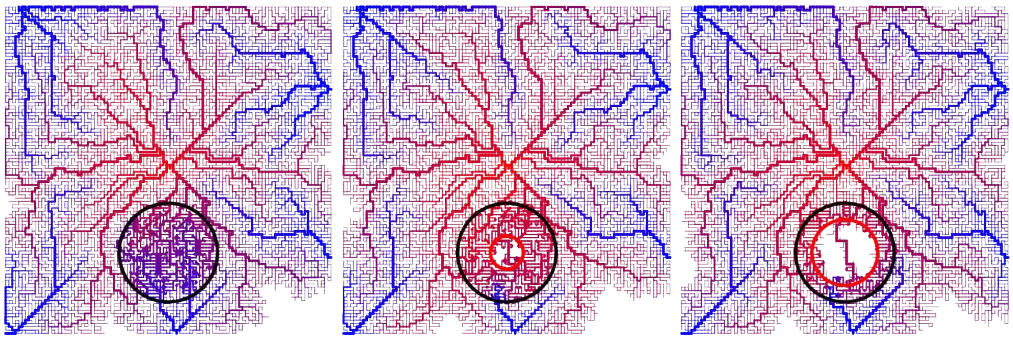

(a) $r_{nec} = 0\mu m$ (b) $r_{nec} = 300\mu m$ (c) $r_{nec} = 600\mu m$

Figure 6.13: Vascular networks (*in-silico*) after 110 iterations of homogenization (100 without and 10 with tumor and necrotic core), $n = 10$ parallel capillaries in the tumor region (black circle) and a necrotic core of different size r_{nec}.

	Normal Tissue	Tumor	Necrotic Core
Sprouting Probability	$p^{spr}_{normal} = 0.5$	$p^{spr}_{tumor} = 1$	$p^{spr}_{necrotic} = 0.1$
Degeneration Probability	$p^{deg}_{normal} = \frac{\tau - \tau_{min}}{\tau_{max} - \tau_{min}}$	$p^{deg}_{tumor} = p^{deg}_{normal}/10$	$p^{deg}_{necrotic} = p^{deg}_{normal} \cdot 10$
Micro-Vessel Density	$n_{normal} = 1$	$n_{tumor} = 10$	$n_{necrotic} = 10$

Table 6.1: Construction parameters varying in "healthy", tumorous and necrotic tissue zones.

6.3 Perfusion Model

6.3.1 Microscopic Contrast Agent Concentration

The contrast-agent CA is here considered as a diluted specie that does not affect the velocity of the fluid that contains it. At each point in the blood or the interstitial space,

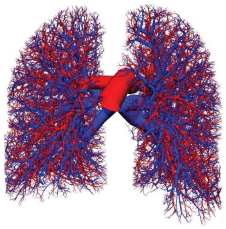

Parameter	Unit	Value	Description
r^{tip}	μm	4	radius of vessel segment at tips
α^{art}	$-$	3	power law exponent for arterial vessel segments
α^{ven}	$-$	2.7	power law exponent for venous vessel segments
l	μm	60	length of vessel segment (lattice constant)
p^{art}	kPa	12	pressure at arterial roots
p^{ven}	kPa	2	pressure at venous roots

Table 6.2: Vessel properties for arterial and venous trees.

Variable	Unit	Description
p_i	kPa	pressure at vessel node i
r_{ij}	μm	radius of vessel segment ij
f_{ij}	$\mu m^3 \cdot s^{-1}$	flow through vessel segment ij
Δp_{ij}	kPa	pressure difference among vessel segment ij
η_{ij}	$kPa \cdot s$	blood viscosity in vessel segment ij
τ_{ij}	kPa	shear stress in vessel segment ij
$k_{PS} = PS$	$\mu m^3 \cdot s^{-1}$	exchange rate between vessel and interstitial space
S_{ij}	μm^2	blood vessel surface
C_A	mM	marker concentration in arterial roots
C_P	mM	marker concentration in vessel
C_I	mM	marker concentration in interstitial space
C	mM	total marker concentration
V_P	μm^3	volume of vessels
V_I	μm^3	volume of interstitial space
$V = V_P + V_I$	μm^3	total volume

Table 6.3: Variables.

mass conservation of the CA leads to the following mass CA concentration equation [PG08]

$$\frac{\partial C}{\partial t} + \nabla \cdot (C\vec{v}) + \nabla \cdot \vec{J} = 0 \; x \in \Omega_m \tag{6.8}$$

assuming that no reaction occures. C is the concentration of CA. $\vec{v}$ is the velocity of the fluid containing CA, and $\vec{J}$ is the flow of CA relative to the velocity of the fluid.

Blood Vessels

In a given blood vessel, $\vec{v}$ is given by Poiseuille flow (see equation 6.3). It is a unidirectional axisymmetric velocity, in the direction of the blood vessel axis, with a parabolic profile that is the same at each cross-section of the vessel axis, going from 0 at the vessel border to a maximum velocity at the center, such that

$$\vec{v_{max}} = 2fA, \tag{6.9}$$

where f is the volumetric flow rate inside the vessel, and A its cross-sectional area. Diffusion is neglected.

Interstitial Space

In the interstitial space, no advection is considered. However, there exists CA diffusion which is described by Fick's 2nd law of diffusion (see section 6.3.3)

$$\vec{J} = -D\Delta C, \tag{6.10}$$

where D is the diffusion coefficient of CA.

Membrane Flux

At the interface between the blood vessels and the interstitial space, the blood vessel walls are modeled as a permeable membrane. The diffusion flux across a membrane is described by Fick's 1st law of diffusion (see section 6.3.2).

6.3.2 Diffusion Flux across Membrane (Fick's 1st Law)

The flux J of a molecule diffusing in a given medium can be described by the first Fick's law [Fic55b, Fic55a, Fun90]

$$J = \frac{1}{S}\frac{\mathrm{d}Q}{\mathrm{d}t} = -D\frac{\partial C}{\partial x}, \tag{6.11}$$

where J represents the flux and dQ the amount of a substance diffusing in time dt across a plane of area S under an instantaneous gradient $\frac{\partial C}{\partial x}$. C is the concentration of the substance and D its diffusion coefficient at a definite temperature in the medium.

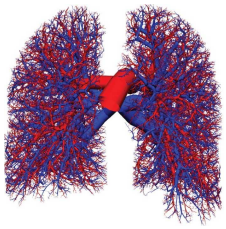

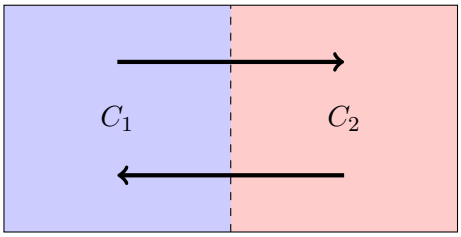

Assuming the simplest model of diffusion or kinetic formulation across a membrane [PG08], equation 6.11 simplifies to

$$\frac{dQ}{dt} = -\frac{DS}{H}(C_1 - C_2), \tag{6.12}$$

H being the thickness of the permeable membrane. The change in concentration on each side of the membrane, C_1 and C_2, can be described by

$$\begin{aligned} V_1\frac{dC_1}{dt} &= -\frac{DS}{H}(C_1 - C_2) \\ V_2\frac{dC_2}{dt} &= \frac{DS}{H}(C_1 - C_2) \end{aligned} \tag{6.13}$$

where V_1 and V_2 are the corresponding compartment volumes.

6.3.3 Diffusion & Advection in Space (Fick's 2nd Law)

Fick's second law [Fic55b, Fic55a, Fun90] predicts how diffusion causes the concentration field to change with time. It can be derived from Fick's first law and mass balance

$$\frac{\partial C}{\partial t} = -\frac{\partial}{\partial x}\vec{J} = \frac{\partial}{\partial x}\left(D\frac{\partial}{\partial x}C\right) \tag{6.14}$$

In higher dimensions the first derivative ($\frac{\partial}{\partial x}$) generalizes to the gradient (∇)

$$\frac{\partial C}{\partial t} = \nabla \cdot (D\nabla C) \tag{6.15}$$

If the diffusion coefficient is constant we can further simplify to

$$\frac{\partial C}{\partial t} = D\nabla^2 C = D\Delta C \tag{6.16}$$

6.3.4 Macroscopic (Multi-Phase) Perfusion Model

On larger scales, each piece of tissue is modeled by a multiphase continuum that include the following components: blood plasma P and interstitial space I (see figures 6.14 and 6.15). The cellular compartment will be neglected as all CA considered do not enter into the cells.

Blood Plasma

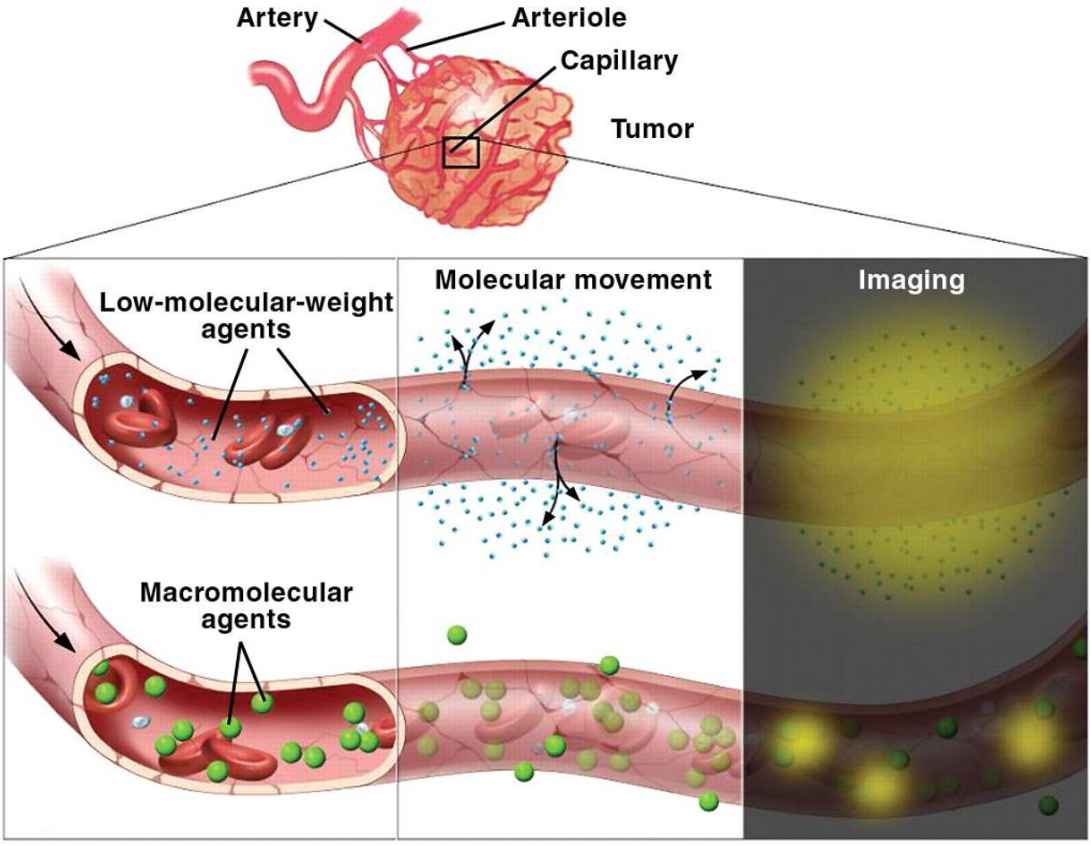

Figure 6.14: Perfusion of two different types of CA. The CA is transported by the blood through the blood vessels. Depending on its molecular weight CA passes (or does not pass) the vessel walls into the interstitial space, and diffuses in the interstitial space. Image modified from [TKO+09]

Multiphase equations can be obtained at the macroscopic level by integration of the microscopic equations inside the two phases (plasma and interstitial spaces). Assuming no diffusion or dispersion of the CA inside the blood, and that blood vessel walls are permeable membranes following kinetics of equation 6.13, the mass concentration of CA

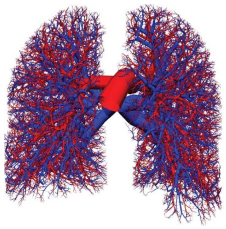

inside the plasma of volume V_P in a small volume of tissue V follows

$$\begin{aligned} \frac{\partial}{\partial t}\left(\frac{V_P}{V}C_P\right) + \nabla\cdot\left(\frac{V_P}{V}C_P\vec{v_M}\right) &= -\frac{D_M S_M}{H_M V}(C_P - C_I) \text{ in } \Omega, \\ C_P|_{\partial\Omega} &= C_A \text{ (entering flow)}, \end{aligned} \tag{6.17}$$

where C_A is the blood plasma concentration in the feeding arteries. C_P is the averaged microscopic plasma CA concentration in V and C_I is the averaged interstitial CA concentration in V. $\vec{v_M}$ is the macroscopic blood velocity, and $D_M S_M / H_M$ the macroscopic membrane exchange rate, both will be defined later.

Interstitial Space

Assuming no transport in the interstitial space, the mass concentration of interstitial space CA follows

$$\begin{aligned} \frac{\partial}{\partial t}\left(\frac{V_I}{V}C_I\right) &= \nabla\cdot\left(D_I^{eff}\nabla C_I\right) + \frac{D_M S_M}{H_M V}(C_P - C_I) \text{ in } \Omega, \\ \frac{V_I}{V}\frac{\partial C_I}{\partial t}\bigg|_{\partial\Omega} &= 0 \text{ (homogeneous Neumann B.C.)} \end{aligned} \tag{6.18}$$

where D_I^{eff} is the effective diffusion coefficient due to the fact that the molecules are not diffusing freely among the whole volume, but are limited by the cell and vessel borders. So the diffusion becomes

$$D_I^{eff} = \frac{D_I \phi_I \delta}{\tau} \tag{6.19}$$

where $\phi_I = \frac{V_I}{V}$ is the porosity[2], $\delta < 1$ is the constrictivity[3] (ratio of the diameter of the diffusing particle to the pore diameter), and $\tau > 1$ is the tortuosity[4]. If we assume that constrictivity and tortuosity balance each other we get

$$\frac{\partial}{\partial t}\left(\frac{V_I}{V}C_I\right) = \nabla\cdot\left(D_I^{eff}\frac{V_I}{V}\nabla C_I\right) + \frac{D_M S_M}{H_M V}(C_P - C_I) \tag{6.20}$$

with symmetric boundary conditions (Neumann conditions) considering the situation to be comparable in the neighboring environment.

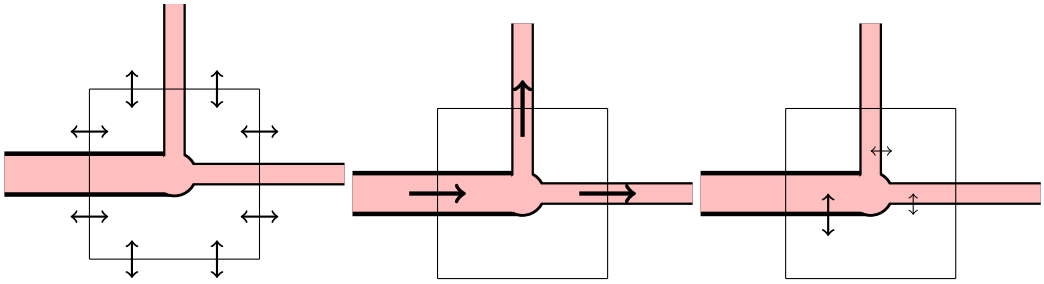

(a) diffusion (b) transport (c) exchange

Figure 6.15: Scheme of inter-compartmental fluxes

6.3.5 Discretization

The above described equations 6.17 and 6.20 are solved on the voxel lattice defined in section 6.2.1. Via the *finite volumes method* we calculate the fluxes between the compartments of neighboring voxels (see figure 6.15(b) and 6.15(a)) and within the same voxel (see figure 6.15(c)). In the following, we take into account the knowledge of the underlying microvasculature.

Intravascular Macroscale Properties

The intravascular compartment of a voxel is defined by the volume $V_{P,i}$ occupied by all vessel segments j connected to the central node i.

$$V_{P,i} = \sum_j \frac{1}{2} \pi r_{ij}^2 l_{ij} \tag{6.21}$$

r_{ij} is the radius and l_{ij} the length of vessel segment (i, j). The voxel exchange rate is defined as

$$K_{PS,i} = \left(\frac{D_M S_M}{H_M} \right)_i . \tag{6.22}$$

[2]Porosity is a measure of the void spaces in a material, and is a fraction of the volume of voids over the total volume, between 0 and 1, or as a percentage between 0-100%.

[3]Constrictivity is a dimensionless parameter used to describe transport processes (often molecular diffusion) in porous media. Constrictivity is viewed to depend on the ratio of the diameter of the diffusing particle to the pore diameter.

[4]Tortuosity is a property of curve being tortuous (twisted; having many turns).

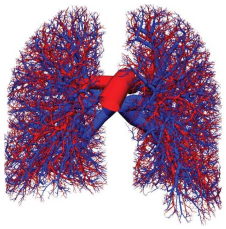

Given the fact that the microscopic blood vessel network is known, it is natural to calculate the voxel exchange rate by

$$K_{PS,i} = \sum_j \frac{1}{2} P_{ij} S_{ij} \tag{6.23}$$

where P_{ij} is the permeability and $S_{ij} = 2\pi r_{ij} l_{ij}$ the surface of vessel segment (i, j).

Upwind Scheme for Intra-vascular Transport

To discretize equation 6.17 in space, the first-order upwind scheme was chosen for the transport term:

$$\frac{dC_{P,i}}{dt} = \sum_j \frac{f_{ij}^{in}}{V_{P,i}} C_{P,j} - \sum_j \frac{f_{ij}^{out}}{V_{P,i}} C_{P,i} - \frac{K_{PS,i}}{V_{P,i}} (C_{P,i} - C_{I,i}) \tag{6.24}$$

where f_{ij}^{in} are only the flows entering the voxel i and f_{ij}^{out} the flows leaving it.

Explicit in Time (Forward Euler) Intravascular Discretization

Solving these Ordinary Differential Equations (ODEs) explicitly in time leads to the following update during time dt between time step n and $n+1$

$$C_{P,i}^{n+1} = C_{P,i}^{n} + \frac{dt}{V_{P,i}} \left(\sum_j f_{ij}^{in} C_{P,j}^{n} - \sum_j f_{ij}^{out} C_{P,i}^{n} - K_{PS,i} (C_{P,i}^{n} - C_{I,i}^{n}) \right) \tag{6.25}$$

Implicit in Time (Backward Euler) Intravascular Discretization

These equations can alternatively be solved implicitly in time

$$C_{P,i}^{n+1} \left[1 + \frac{dt}{V_{P,i}} K_{PS,i} + \sum_j \frac{dt}{V_{P,i}} f_{ij}^{out} \right] - \sum_j C_{P,j}^{n+1} \left[\frac{dt}{V_{P,i}} f_{ij}^{in} \right] - C_{I,i}^{n+1} \left[\frac{dt}{V_{P,i}} K_{PS,i} \right] = C_{P,i}^{n} \tag{6.26}$$

Extra-vascular Macroscale Properties

Neglecting the cellular compartment, the interstitial compartment is defined by the extra-vascular volume $V_{I,i}$

$$V_{I,i} = V_i - V_{P,i} \tag{6.27}$$

where V_i is the volume of the voxel i.

Centered Scheme for Extra-vascular Diffusion

Equation 6.20 can be discretized in space by the

$$\frac{dC_{I,i}}{dt} = \frac{D}{2dx^2}\sum_j \left(1 + \frac{V_{I,j}}{V_{I,i}}\right)(C_{I,j} - C_{I,i}) + \frac{K_{PS,i}}{V_{I,i}}(C_{P,i} - C_{I,i}), \tag{6.28}$$

where dx is the lattice constant of the underlying voxel lattice.

Explicit in Time (Forward Euler) Extra-vascular Discretization

Solving equation 6.20 explicitly in time leads to the following update during time dt between time step n and $n+1$

$$C_{I,i}^{n+1} = C_{I,i}^{n} + \frac{dt}{V_{I,i}}\left(\frac{D}{dx^2}\sum_j \frac{V_{I,i} + V_{I,j}}{2}\left(C_{I,j}^{n} - C_{I,i}^{n}\right) + K_{PS,i}(C_{P,i}^{n} - C_{I,i}^{n})\right). \tag{6.29}$$

Implicit in Time (Backward Euler) Extra-vascular Discretization

Solving equation 6.20 implicitly in time leads to the following update during time dt between time step n and $n+1$

$$\begin{aligned} &C_{I,i}^{n+1}\left[1 + \frac{dtD}{2dx^2}\sum_j\left(1 + \frac{V_{I,j}}{V_{I,i}}\right) + \frac{dt}{V_{I,i}}K_{PS,i}\right] - \sum_j C_{I,j}^{n+1}\left[\frac{dtD}{2dx^2}\left(1 + \frac{V_{I,j}}{V_{I,i}}\right)\right] \\ &-C_{P,i}^{n+1}\left[\frac{dt}{V_{I,i}}K_{PS,i}\right] = C_{I,i}^{n} \end{aligned} \tag{6.30}$$

Choice of Numerical Method

Stability: To solve the hyperbolic partial differential equation 6.25 a necessary condition for convergence is the Courant-Friedrichs-Lewy (CFL) condition [CFL28]

$$v\frac{dt}{dx} \leq Cr \tag{6.31}$$

where v is the velocity and Cr a dimensionless constant. With respect to the above described scheme the velocity corresponds to $v = f/S$ with S being the cross-sectional area of a blood vessel segment. dx is the length of the segment. The chosen time step dt needs to fulfill the following condition for the whole network

$$dt \leq Cr \min_i\left\{\frac{V_{P,i}}{f_i}\right\} \tag{6.32}$$

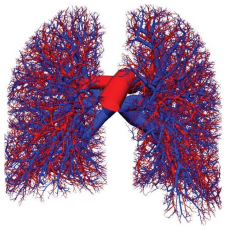

Equation 6.26 is implicit and thus unconditionally stable if solved alone.

The implicit scheme costs more computation time per iteration as a matrix has to be inverted, while the explicit scheme allows direct update. But the time step for the implicit scheme can be chosen to be much larger than for the explicit one from the stability point of view.

Accuracy: On the other hand, the implicit scheme will always introduce numerical diffusion. For the inverse problem the CA perfusion simulations avoid numerical diffusion in order to exclude misinterpretation of inaccurate data caused by numerical errors.

Thus, for simulations which do not demand a very high accuracy the implicit scheme will be used. This is the case for all perfusion images in section 6.3) of intra- and extra-vascular agents whose main purpose is to study the impact of different vascular topologies and properties on the spatial and temporal appearance of color intensity in the image sequences. For accurate simulations needed for the inverse problem in section 6.4 the explicit scheme will be used. In order to reduce numerical diffusion several approaches can be pursued: increasing the spatial and temporal order of the numerical scheme or refining the space (and time). For the one-dimensional case this was studied in section C.2.2. Second order transport schemes reduce dramatically the diffusivity, but cannot be applied directly to a network topology. Thus, spatial and temporal refinement was chosen. Here blood vessel segments (transport equation) will be refined by sub-nodes to decrease the numerical diffusion. As figure C.1 shows, $Cr = 0.1$ and 30 vessel sub-nodes resulting in sub-segments of length $l/30 = 2\mu m$ (see table 6.2) lead to sufficient accuracy.

6.3.6 Parameters & Border Conditions

Arterial Input Function

Parker et al. [PRM+06] propose a functional form of the arterial input function (Arterial Input Function (AIF)) derived and averaged over a population of 113 AIF's measured in the *descending aorta* or *iliac arteries* of patients (see figure 6.16).

$$C_A(t) = \sum_{n=1}^{2} \frac{A_n}{\sigma_n \sqrt{2\pi}} \cdot e^{-(t-T_n)^2/(2\sigma_n)^2} + \alpha e^{-\beta t}/(1 + e^{-s(t-\tau)}) \tag{6.33}$$

Permeability

The exchange rate K_{PS} $(\mu m^3/min)$ indicates the volume of fluid that passes a membrane in a certain amount of time. It can be written as the product of the surface of

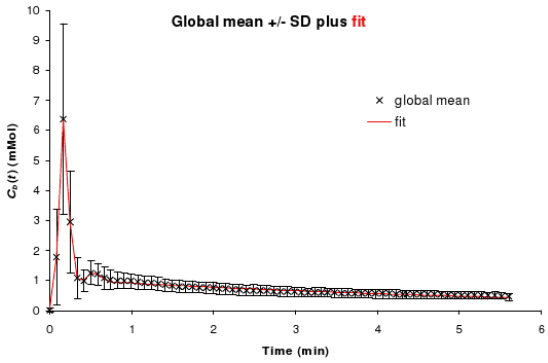

Parameter	Value	Unit
A_1	0.809	$mM \cdot min$
A_2	0.330	$mM \cdot min$
T_1	0.171	min
T_2	0.365	min
σ_1	0.056	min
σ_2	0.132	min
α	1.050	mM
β	0.169	min^{-1}
s	38.078	min^{-1}
τ	0.483	min

Figure 6.16: Global mean (crosses) and model fit to data (red). Error bars depict +/- 1 SD across the population of 113 AIFs.

the membrane, S (μm^2), and the permeability coefficient, P ($\mu m/min$)

$$K_{PS} = P \cdot S = \frac{DS}{H} \tag{6.34}$$

or as the product of the diffusion coefficient, D, and the membrane surface, S, divided by the membrane thickness, H.

As approximation the average vessel surface per tissue volume, $E(S/V)$, or per plasma volume, $E(S/V_P)$, can be estimated from a typical *in-silico* vascularization (figure 6.5(c)) created by CSSH (section 6.2.5). In the literature, the average values of $E(K_{PS}/V)$ and $E(K_{PS}/V_P)$ can be found. For both, literature and *in-silico* estimations, see table 6.4. Then the order of magnitude of P (considered homogeneous over the domain for now, but could be modified to take into account increased leakiness of some tumor vessels, etc) can be approximated by

$$P \approx \frac{E(K_{PS}/V)}{E(S/V)} \approx \frac{E(K_{PS}/V_P)}{E(S/V_P)}. \tag{6.35}$$

By given values for $E(K_{PS}/V)$ and $E(K_{PS}/V_P)$ (see table 6.4) one can estimate a range of $P =$ The average vessel surface per tissue volume in one representative *in-silico* vascularization was found to be $E(S/V) = 0.0135 \mu m^{-1}$. Thus the permeability is assumed to be $P = 0.12 - 25 \mu m/s$ for vessels in healthy tissue and $P = 0.086 \mu m/s$ in carcinoma. In the following we will assume a constant permeability for all vessels $P = 0.1 \mu m/s$ (see table 6.5).

Locally, K_{PS} varies according to 6.34 and the local S.

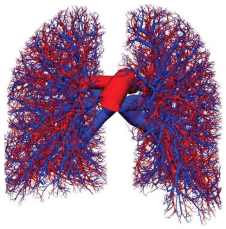

Diffusion coefficient

The diffusion coefficient is CA-specific. Values found in literature [LLK+09] were of the same order of magnitude as water molecules (see table 6.4). In the following we will assume the diffusion coefficient to be $1000\mu m^2/s$ (see table 6.5).

Variable	Unit	Value	Ref
K_{PS}/V	min^{-1}	0.2 (0.01-1)	[BZKG09]
K_{PS}/V_P	min^{-1}	1.2 (+/-0.5)	pectoral muscle, [BKL+04]
	min^{-1}	0.86 (+/-0.62)	carcinomas, [BKL+04]
F/V	min^{-1}	0.5 (0.1-1)	[BZKG09]
F/V_P	min^{-1}	2.4 (+/-1.3)	pectoral muscle, [BKL+04]
	min^{-1}	2.4 (+/-0.7)	carcinomas, [BKL+04]
ϕ_P	–	0.04 (0.01-0.1)	[BZKG09]
	–	0.04 (+/-0.01)	pectoral muscle, [BKL+04]
	–	0.2 (+/-0.07)	carcinomas, [BKL+04]
ϕ_I	–	0.1 (0.02-0.35)	[BZKG09]
	–	0.09 (+/-0.01)	pectoral muscle, [BKL+04]
	–	0.34 (+/-0.06)	carcinomas, [BKL+04]
S/V	μm^{-1}	0.0135	*in-silico* estimation after CSSH
S/V_P	μm^{-1}	0.166	*in-silico* estimation after CSSH
D	$\mu m^2/s$	$1.13(0.94 - 1.28) \times 10^3$	Healthy pancreas [LLK+09]
	$\mu m^2/s$	$1.15(0.74 - 1.60) \times 10^3$	Pancreatic cancer [LLK+09]
P	$\mu m/s$	0.12 (0.12- 0.25)	healthy tissue, estimate from [BKL+04, BZKG09]
	$\mu m/s$	0.086	carcinoma, estimate from [BKL+04]

Table 6.4: Values from the literature or own estimation.

.

Parameter	Unit	Value (Range)	Ref
D	$\mu m^2/s$	1×10^3	assumption
P	$\mu m/s$	0.1	assumption

Table 6.5: Perfusion model parameters.

.

6.3.7 Perfusion of Intra-Vascular Agents (DCE-US)

A novel ultrasound method employing microbubbles (MB) contrast offers portable, non-invasive dynamic assessment of tumor blood flow. A MB contrast agent (Definity, Lan-

theus, Boston) is infused to produce vascular enhancement on nonlinear ultrasound imaging. The MBs, the size of red blood cells, remain intravascular. MBs are disrupted with an ultrasound pulse and the wash-in of new bubbles is imaged. This method, DCE-US, measures blood flow, velocity and vascular volume in multiple planes.

The following examples will explore possible cases of tissues perfused by a purely intra-vascular CA. Later on, in section 6.3.8 perfusion extra-cellular agents used for DCE-MRI is explored.

Comparing Differently Homogenized Vascularizations (without Tumor)

Figure 6.17 shows the result of performing the simulation of CA perfusion on the three example vascularizations (figure 6.5) of different degree of shear stress homogenization (see section 6.2.5). The images depict screenshots of the macroscopic CA concentrations, $C = \phi_P C_P + \phi_I C_I$, at different times of the perfusion simulation (2, 10, 30 and 180sec).

The *random vessel network* (figure 6.17, top row) is very poorly perfused. The overall amount of CA is very small (few CA arrives at the peripheral venes) and many parts of the tissue stay completely undelivered (large dark patches between large vessels).

Already *20 iterations of shear stress homogenization* (figure 6.17, center row) increase the total amount of perfused CA dramatically and leave just a few areas without circulation.

After *200 iterations of shear stress homogenization* (figure 6.17, bottom row) the total amount of perfused CA doesn't increase very much, but furthermore decreases the number and size of unperfused areas. The existence of still unperfused areas is more due to fact that the simulations were restricted to two dimensions. As overlapping vessels are not allowed some arterial capillaries are blocked by large arteries and thus stay inaccessible to venous capillaries (and vice-versa).

Comparing Different Scales

In DCE-MRI the images are acquired from a thin cross-section of tissue where the color intensity of each pixel is a projection of the CA intensity in a tissue voxel. The voxel resolution can vary a lot. In general one can state, that a higher spatial resolution (SR) results in a longer acquisition time. The acquisition time has an impact on the temporal resolution (TR) in DCE-MRI. Some examples are: SR=$1.8 \times 2.1 \times 10 mm^3$ and TR=$2.8ms$ [WRZ+12], SR=$1.9 \times 3.6 \times 4.0 mm^3$ and TR=$1.5s$ [DRL+06], and SR=$0.23 \times 0.47 \times 2.0 mm^3$ and TR=$14s$ [ESG+09]. DCE-MRI has to make a compromise between spatial and temporal resolution as one needs to capture the temporal features as the CA intensity oscillations after a bolus injection (see fig. 6.16) and spatial features of the tissue as blood vessels. At typical resolutions, fine structures as capillaries ($\varnothing = 8\mu m$) and small vessels ($8 < \varnothing < 100\mu m$) can not be captured anymore as single objects but

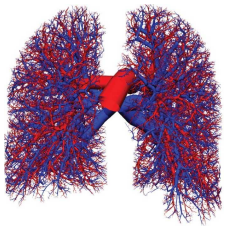

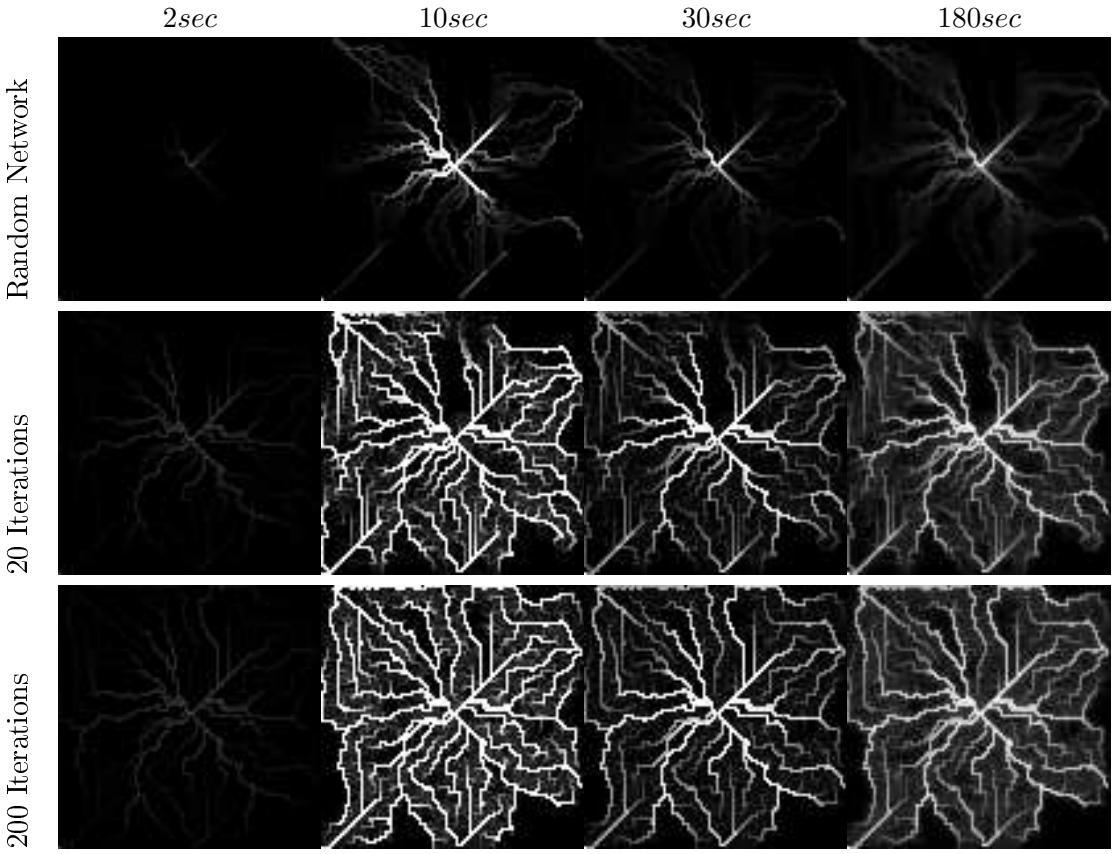

Figure 6.17: Impact of shear stress maximization on the blood perfusion. Images show the contrast agent (CA) intensities per voxel at different moments in time after CA injection into the blood stream. The three rows correspond to different levels of capillary shear stress homogenization.

will contribute to the average CA intensity in each image pixel. So it is important to understand if the vessels contribution can still be recognized in the resulting perfusion images and to which extend the image resolution averages out important information.

To mimic coarser image resolutions the original voxels of size $60 \times 60 \times 60 \mu m^3$ will be grouped in larger voxels of size $300 \times 300 \times 60 \mu m^3$ for two-dimensional arrangements and of size $300 \times 300 \times 3000 \mu m^3$ for three-dimensional arrangements.The CA intensities on the coarse scale are then an average among all the fine scale CA intensities within one coarse voxel.

On larger scales the image resolution exceeds the size of fine structures. Blood vessels become less visible as each voxels CA intensity represents the average of a whole region. While in the first stage of perfusion - especially the first peak if the AIF ($10sec$) - large vessels are still recognizable (compare bottom row of fig. 6.17 and fig. 6.18) at later time ($180sec$) the difference between regions of large vessels and small vessels dissolve on coarse scale (fig. 6.18) while on the fine scale (fig. 6.17) they are still visible.

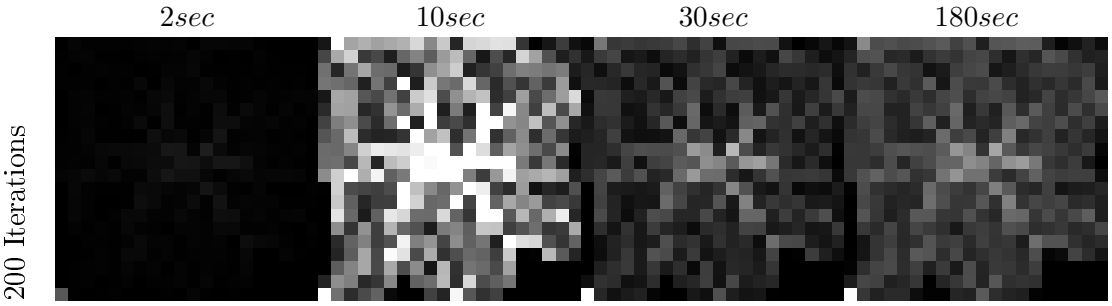

Figure 6.18: Coarse image resolution. Images show the contrast agent (CA) intensities averaged over several voxels (image pixel = $300 \times 300 \times 60 \mu m^3$) at different moments in time after CA injection into the blood stream. The perfusion simulation was done in a network after 200 iterations of capillary shear stress homogenization.

Embedded Tumor: High Micro-vessel Density

Assuming the permeability to be equal for all vessels ($P^{normal} = P^{tumor} = 0 \mu m/s$), but the capillary density within the tumor region to be increased by factor 10 ($n_{tumor} = 10$, $n_{normal} = 1$) leads to the results shown in figure 6.19.

The tumor becomes already visible during the two peaks of the AIF ($10sec$ and $30sec$) due to its increased MVD. On the long term the visibility decreases at the same extend as in the surrounding tissue as it suffers from the same "wash-out"/elimination. If the permeability is the same the tumor can not benefit from larger amounts of accumulated CA in the interstitial space.

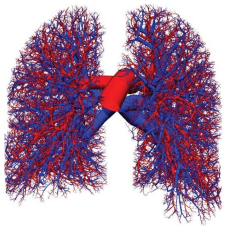

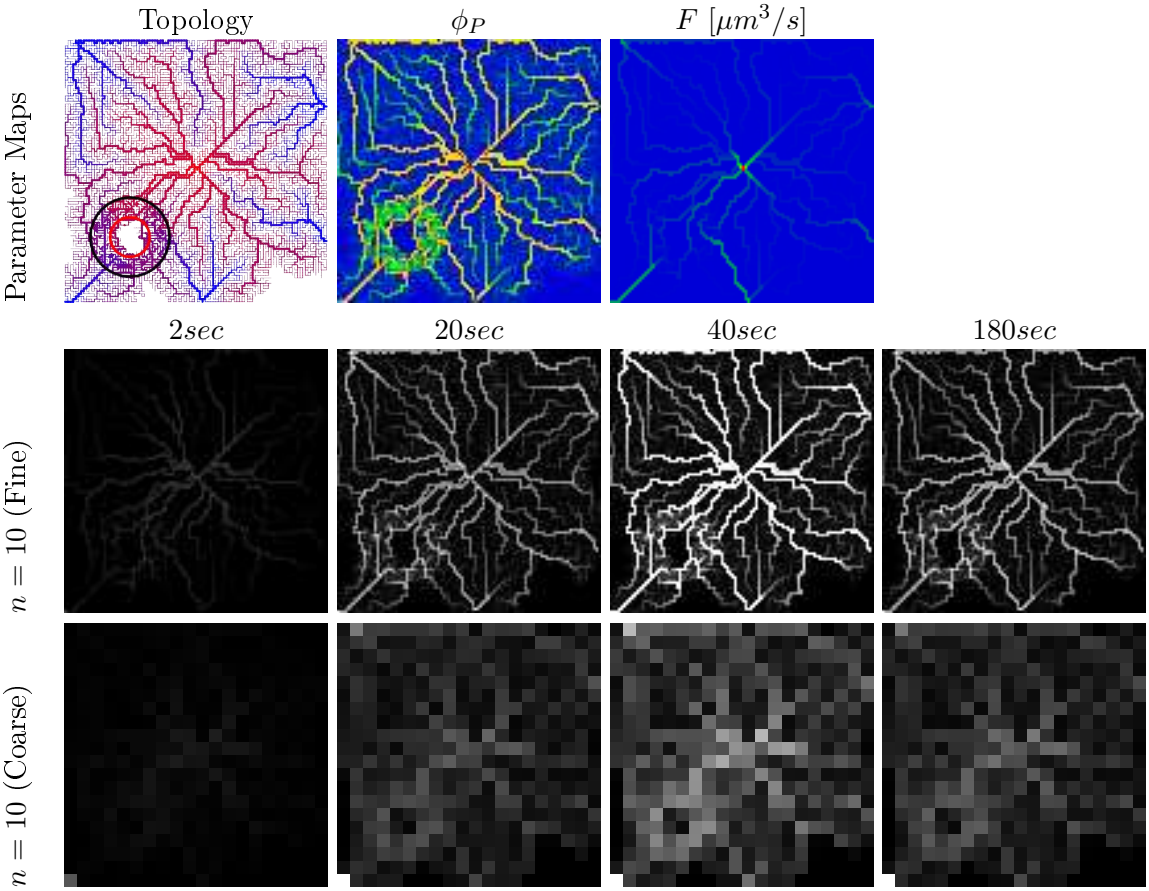

Figure 6.19: Increased micro-vessel density in the tumor region. *Top row:* Parameter maps show the vessel network, vascular volume fraction and the flow rate. *Bottom rows:* Images show the contrast agent (CA) intensities in the voxels (image pixel = $60 \times 60 \times 60 \mu m^3$) and averaged over several voxels (image pixel = $300 \times 300 \times 60 \mu m^3$) at different moments in time after CA injection into the blood stream. The micro-vessel density in the tumor region is 10 times higher than in the surrounding.

Sensitivity MVD

Figure 6.20 shows how different degrees of MVD in the tumor region affect the visibility of the tumor in the CA intensities. As expected, a more vascularized tumor shows more contrast agent in that region.

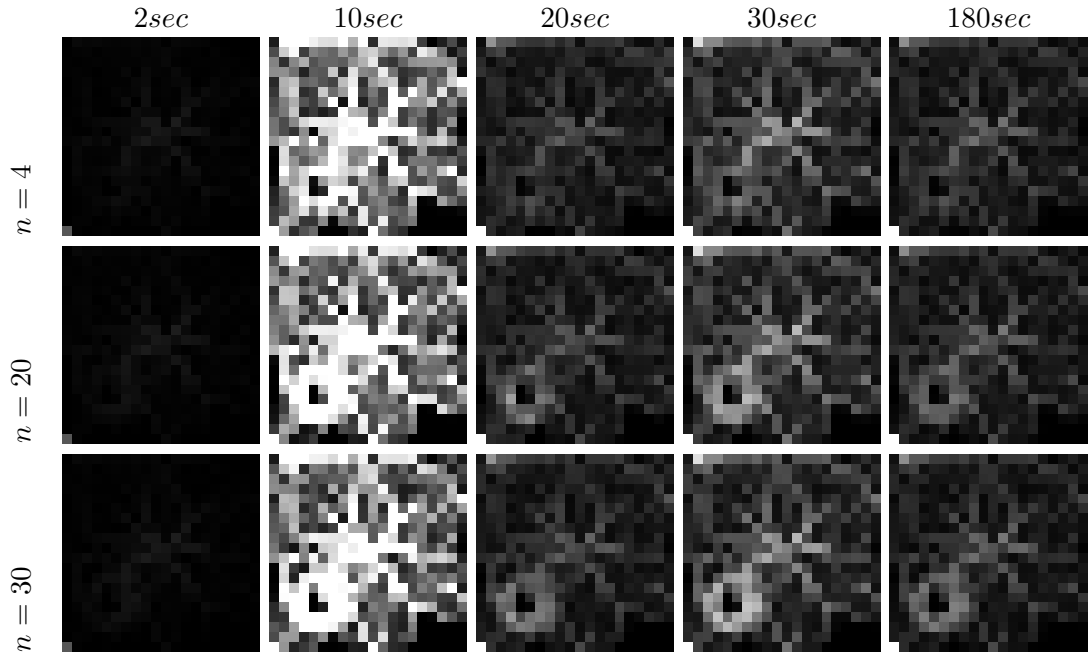

Figure 6.20: Varying capillary density in tumor region. Images show the CA intensities averaged over several voxels (image pixel = $60 \times 60 \times 60 \mu m^3$) at different moments in time after CA injection into the blood stream. The micro-vessel density in the tumor region is n times higher than in the surrounding.

2D versus 3D

Initial Remarks: In the third dimension the opposing arterial and venous vessel trees can much better penetrate each other than in two dimensions leading to a much more homogeneously perfused tissue. On the other hand, the vessel trees have to fill up the tree dimensional space instead of a surface. Consequently, the trees are much larger as are the diameters of the tree roots and the flow passing through.

Tumor embedded in well-perfused Vascularization: Figure 6.21 shows the result of the three-dimensional example of a non-permeable ($P = 0$) vascularization embedding

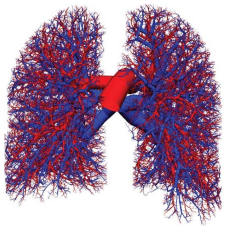

a tumor. At $10sec$ one can see the CA streaming from the centrally placed artery into the vascularization. After $20sec$ the CA spread already among the whole network. Over time the intra-vascular CA concentration diminishes and thus results in a lower CA intensity per voxel.

On an arbitrary slice on the high resolution (voxel size $60\mu m \times 60\mu m \times 60\mu m$, *top*) one sees a part of the central artery and some of the large vessels. As the tumor was not intersected it is not visible in the image.

On the coarse solution (voxel size $300\mu m \times 300\mu m \times 3000\mu m$, *bottom*) typically used in DCE-MRI one can nicely see the tumor (bright area) and its necrotic core (black spot) in the lower part of the tissue at around $20sec$ after the CA injection into the blood. Large vessels are not identifiable as they are average out by the depth of the voxels.

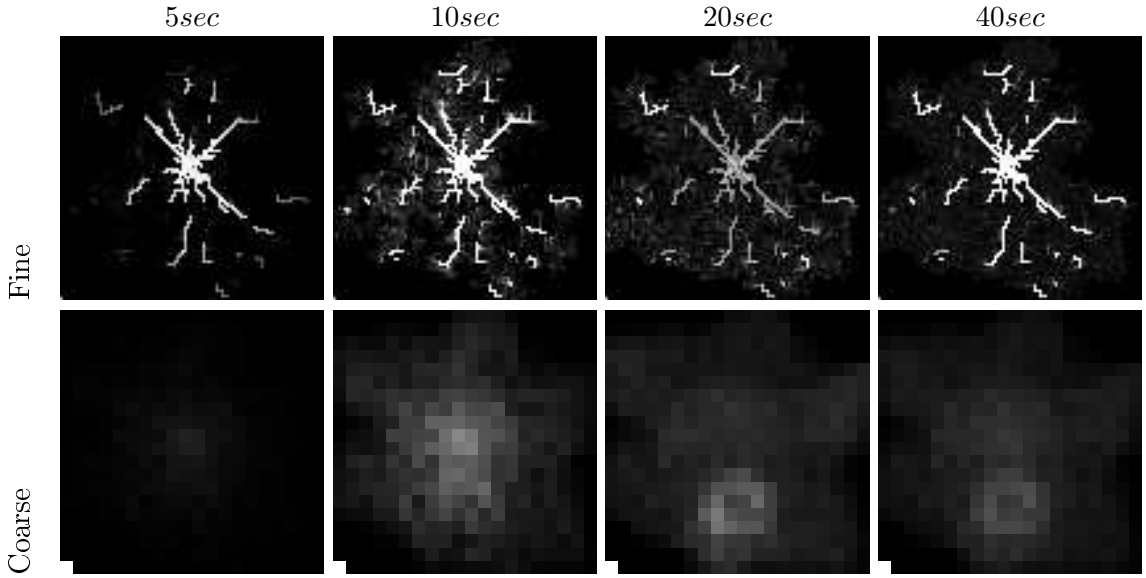

Figure 6.21: Increased capillary density in tumor region. Images show the contrast agent (CA) intensities in the voxels within a slice of a three-dimensional vessel arrangement not intersecting the tumor (*top*, image pixel $= 60 \times 60 \times 60\mu m^3$) and averaged among many voxels (*bottom*, image pixel $= 300 \times 300 \times 3000\mu m^3$) at different moments in time after CA injection into the blood stream. The micro-vessel density in the tumor region is 10 times higher than in the surrounding.

Tumor far away from Single Feeding Vessel: Figure 6.22 shows the snapshots of CA perfusion through a vascularization with a single feeding vessel. One can see how the contrast agent streams into the vascularization from the left where the arterial

root node is located. After around $20s$ it reaches the center of the tissue. A part of the tumor becomes visible. After $40s$ the CA spread among the whole vascularization. Now the tumor as a whole can be identified as the bright area in the lower part of the tissue with its necrotic core visible as a black spot.

In contrast to the example above where the blood needs to pass the capillaries to reach the veins, here the blood can flow with very little resistance from the arterial root node (left) through the large vessel directly toward the venous root (right). Consequently, the surrounding vascularization even after CSSH stays less perfused. Comparing figure 6.21 and 6.22, one can notice that it takes twice the time to homogeneously deliver the CA to the whole network. In the first case this is reached immediately after the bolus (section 6.3.6) passed the artery the first time ($20s$) while in the latter it needs two passes.

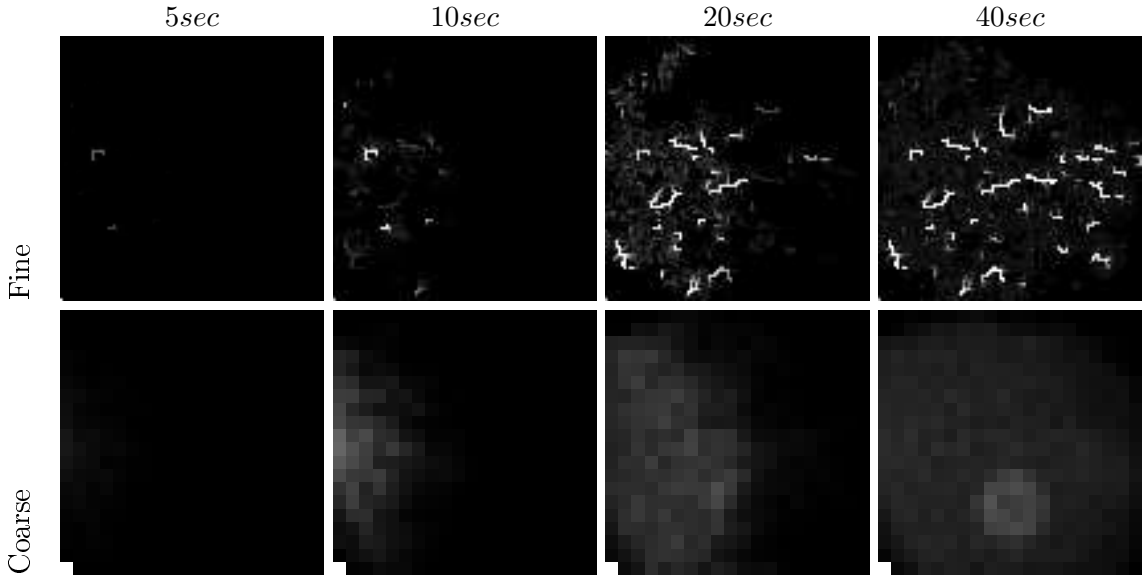

Figure 6.22: Increased capillary density in tumor region. Images show the contrast agent (CA) intensities in the voxels within a slice of a three-dimensional vessel arrangement not intersecting the tumor (*top*, image pixel = $60 \times 60 \times 60 \mu m^3$) and averaged among many voxels (*bottom*, image pixel = $300 \times 300 \times 3000 \mu m^3$) at different moments in time after CA injection into the blood stream. The micro-vessel density in the tumor region is 10 times higher than in the surrounding.

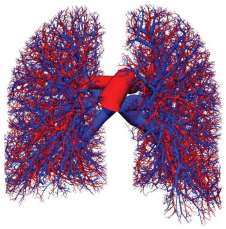

6.3.8 Perfusion of Extra-Cellular Contrast Agents (DCE-MRI)

Embedded Tumor: Normal Permeability & Increased MVD

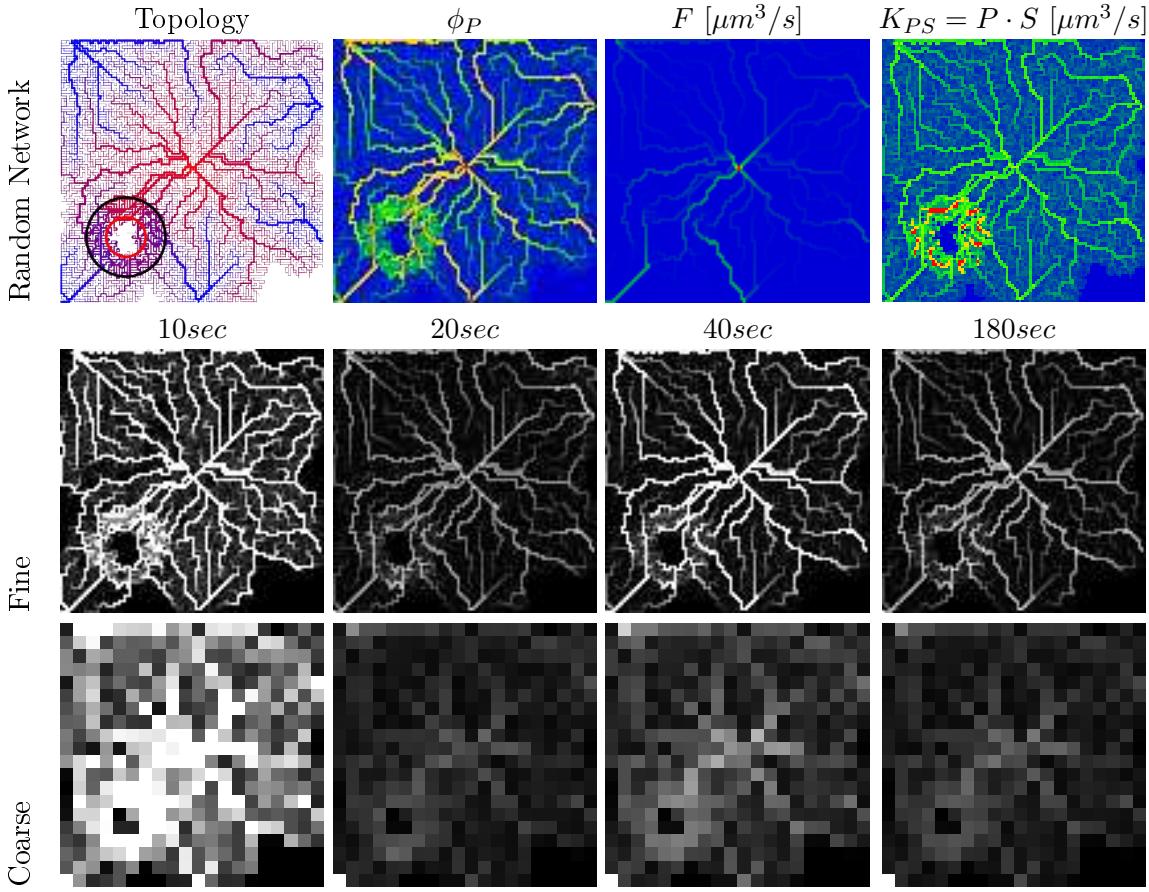

Figure 6.23: 2D vascularization was created from a random vascularization, followed by 100 iterations of capillary shear stress homogenization, followed by further 10 iterations with embedded tumor (*black circle*) and necrotic core (*red circle*). *Top*: Topology and parameter maps. *Center*: Macroscopic CA concentration in voxels of size $(60\mu m)^3$ and *bottom*: $(300\mu m)^2 \times 60\mu m$.

Embedded Tumor: High Permeability ("Leaky" Vessels) & Normal MVD

Typically tumors are more visible in DCE-MRI images. There can be several reasons for an increase accumulation of CA in the tumoral regions. Assuming the capillary density

within the tumor region to be similar to the normal tissue ($n_{tumor} = n_{normal} = 1$), but the permeability to be 100 times higher ($P^{normal} = 0.1\mu m/s$, $P^{tumor} = 100\mu m/s$) leads to the results shown in figure 6.24.

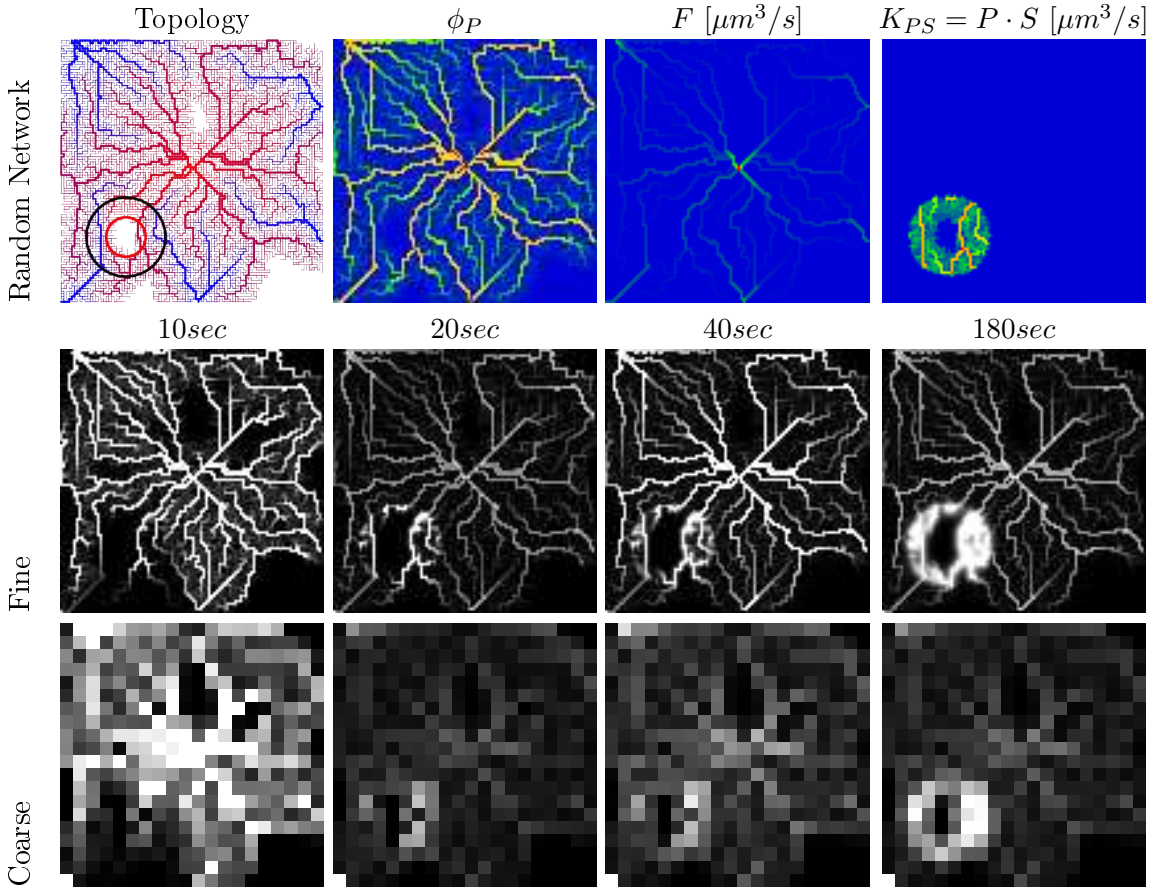

Figure 6.24: 2D vascularization was created from a random vascularization, followed by 100 iterations of capillary shear stress homogenization, followed by further 10 iterations with embedded tumor (*black circle*) and necrotic core (*red circle*). *Top*: Topology and parameter maps. *Center*: Macroscopic CA concentration in voxels of size $(60\mu m)^3$ and *bottom*: $(300\mu m)^2 \times 60\mu m$.

After the first two peaks of the AIF passed the tissue ($10sec$ and $30sec$) the large vessels become flooded by CA and are nicely visible in the *in-silico DCE-MRI images*. As the tumor vasculature is not more functional or denser than in the surrounding tissue the tumor itself can not be recognized from the images.

After the first peaks ($> 30sec$) we see the elimination of CA from the blood which

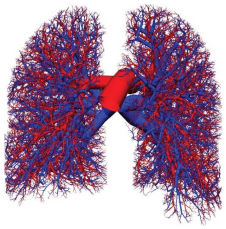

leads to a steady decrease of intra-vascular CA and thus a decreasing brightness. At the same time more and more contrast passes the vascular membrane and diffuses into the interstitial space. So while the CA concentration in large vessels decreases it accumulates in the interstitial space around the highly permissive vessels in the tumor periphery. The un-vascularized necrotic core stays dark.

Conclusion: Highly permeable vascularization is visible rather on the long term of DCE-MRI while a locally increased MVD is visible during the peaks of the AIF. The latter is dominated by the fast transport/flow through the vascular network, while the first depends on the rather slow intra-extra-vascular diffusion. Consequently, one needs to study different phases of the DCE-MRI sequences to gain information about different properties of the vascularization.

6.4 Parameter Estimation from DCE-MRI Data

Looking at DCE-MRI you just get macroscopic information of how the total concentration of CA changes in the single parts (voxels) of a tissue. The exact structure of the vascularization in each voxel and the interconnection between voxels is completely unknown. Thus, very simplified and non-spatial models mimicking the microcirculation of CA in each voxel separately are used as fit functions for an inverse procedure to recover this information.

As the coarseness of the data and the lack of spatial consideration during the inverse procedure might lead to wrong conclusion the aim of this section is to study the outcome of such an inverse procedure in comparison with the parameters used for the direct model to produce the data.

6.4.1 2-Compartment-Model (Brix II Model)

For data acquisition from MRI data there are a number of two-compartment models (ref. [BSP+91, BBH+99, TK91, TBB+99]) used to characterize the tissue microcirculation and quantify regional blood flow, capillary permeability, and relative compartmental volumes. In the following we will focus only on the model proposed by Brix et al. [BBH+99].

As figure 6.25 shows the space will be assumed to be subdivided into two compartments: the *plasma compartment* and the *interstitial space* compartment. The plasma compartment is fed from the artery, with blood flow rate F going in and out of the compartment. The membrane diffusion is mimicked by the intra-vascular-extra-vascular exchange rate K_{PS}.

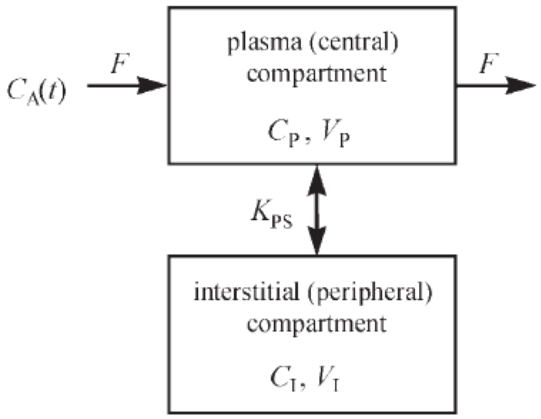

Figure 6.25: Two compartment model describing the tissues microcirculation of a contrast agent.

Model Equations

The corresponding equations derived from *conservation of mass* are

$$\frac{\partial C_P}{\partial t} = -\frac{F}{V_P}(C_P - C_A) - \frac{K_{PS}}{V_P}(C_P - C_I) \tag{6.36}$$

for the concentration of contrast agent in the *plasma compartment*, C_P, and

$$\frac{\partial C_I}{\partial t} = \frac{K_{PS}}{V_I}(C_P - C_I) \tag{6.37}$$

for the concentration of contrast agent in the *interstitial space*, C_I. V_P and V_I are the volumes of the two compartments.

Numerical Scheme (Intra-vascular Marker)

Numerically we can solve the system of equations for each time step dt using an implicit scheme in time

$$\begin{aligned} \frac{C_P^{n+1} - C_P^n}{dt} &= \frac{F}{V_P}(C_A^n - C_V^{n+1}) - \frac{K_{PS}}{V_P}(C_P^{n+1} - C_I^{n+1}) \\ \frac{C_I^{n+1} - C_I^n}{dt} &= \frac{K_{PS}}{V_I}(C_P^{n+1} - C_I^{n+1}) \end{aligned} \tag{6.38}$$

Both equation reduce to the following linear system

$$\underbrace{\begin{pmatrix} \left[1 + \frac{dt}{V_P}F + \frac{dt}{V_P}K_{PS}\right] & \left[-\frac{dt}{V_P}K_{PS}\right] \\ \left[1 - \frac{dt}{V_I}K_{PS}\right] & \left[\frac{dt}{V_I}K_{PS}\right] \end{pmatrix}}_{A} \cdot \underbrace{\begin{pmatrix} C_P^{n+1} \\ C_I^{n+1} \end{pmatrix}}_{u^{n+1}} = \underbrace{\begin{pmatrix} C_P^n + \frac{dt}{V_P}FC_A^n \\ C_I^n \end{pmatrix}}_{b^n} \tag{6.39}$$

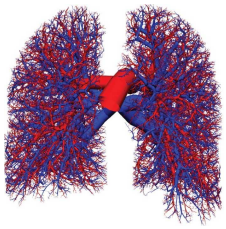

and can be solved by simply inverting matrix A

$$\begin{pmatrix} C_P^{n+1} \\ C_I^{n+1} \end{pmatrix} = A^{-1}b^n \tag{6.40}$$

The total concentration of contrast agent in the tissue is

$$C = \frac{V_P C_P + V_I C_I}{V} \tag{6.41}$$

6.4.2 Inverse Procedure

The temporally sampled evolution of the mean CA concentration $C[i]$ is compared to the sampled 2-compartment solution $C(i \cdot dt)$ for each voxel using mean squares as a distance measure.

$$S(\beta) = \sum_i (C[i] - C(i \cdot dt, \beta))^2 \tag{6.42}$$

To get the best fitting set of parameters β, S is minimized using the Levenberg-Marquardt algorithm (see section D.4) with $\lambda = 0.1$ for 100 iterations.

6.4.3 Examples & Results

1D without Vascular Permeability

As a very first example a one-dimensional arrangement of 100 voxels was chosen. The size of each voxel is $60\mu m \times 60\mu m \times 60\mu m$. In the center of each voxel there is one vessel node. The vessel nodes of neighboring voxels are connected by vessel segments (see figure 6.26(a)). The pressure difference between the extremities of the vessel is $10kPa$.

As figure 6.26(b) shows the Brix2 compartment model with three fit parameters $\beta = \{\phi_P, K_{PS}, F\}$ (assuming $\phi_P = 1 - \phi_I$) gives a good fit in voxels which are very close to the artery mimicked by the arterial input function. The farther away the worst the fit. The best fitting parameters for each voxel are shown in figure 6.27 (*green line*). While the vascular volume fraction ϕ_P and the intra-/extra-vascular exchange rate K_{PS} are very close to the originally used values, the flow rate F is completely underestimated. This is due to the later "arrival" of the AIF which is fitted by lower flow rate.

To overcome this drawback of Brix2 we can just add a temporal delay for the arterial input function as a forth parameter $\beta = \{\phi_P, K_{PS}, F, t_0\}$ taking into account the delayed arrival of the AIF for voxels far away from arteries. Figure 6.26(c) shows how such a improved Brix2+Delay model improves the fit in all voxels.

Looking at the fit parameters (figure 6.27, *red line*) confirms the much better agreement with the original parameters for volume fraction and flow rate as well.

(a) Topology

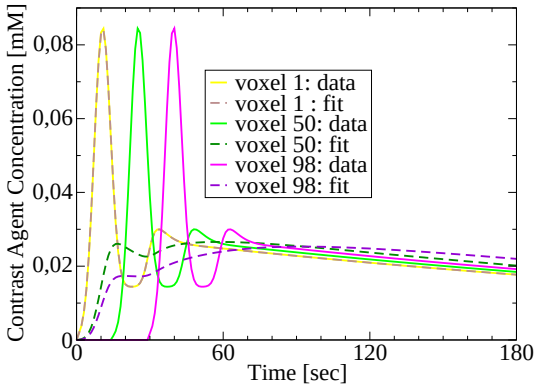

(b) Brix2 Fit Curves with 3 Voxels

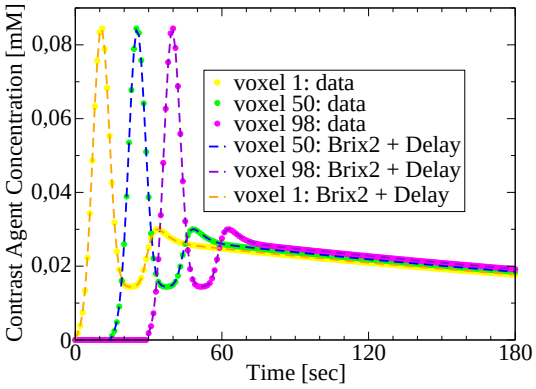

(c) Brix2+Delay Fit Curves for 3 selected Voxels

Figure 6.26: Contrast agent transport along a non-permeable vessel within one-dimensional voxel arrangement. (a) The one-dimensional topology of the non-permeable blood vessel. The color indicate the pressure gradient (red=12kPa, blue=2kPa). (b) Comparison between direct method and Brix2 fit curve. (c) Comparison between direct method and Brix2+Delay fit curve. The curves show the contrast agent time course in the arterial root voxel (*yellow*), central voxel (*green*) and venous root voxel (*magenta*)

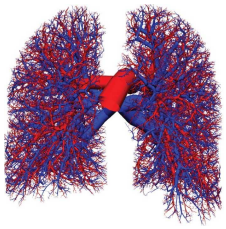

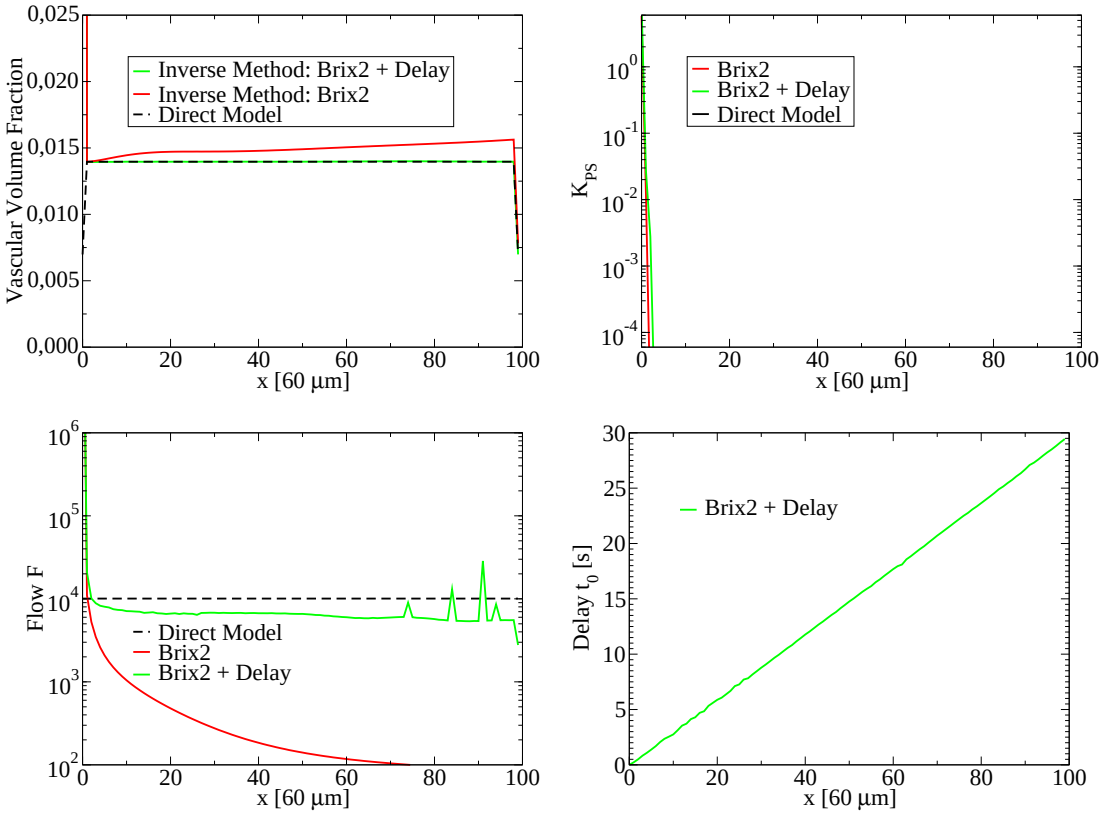

Figure 6.27: Parameter comparison between values used for direct method (*dashed line*) and the values recovered by Brix2 (*red*) and Brix2+Delay (*green*). x denotes the voxel in the one-dimensional arrangement. Units: F and K_{PS} in $\mu m^3/s$.

1D with Vascular Permeability

Using exactly the same arrangement as in the example before one can now add some permeability ($P = 0.1$) to the vessels.

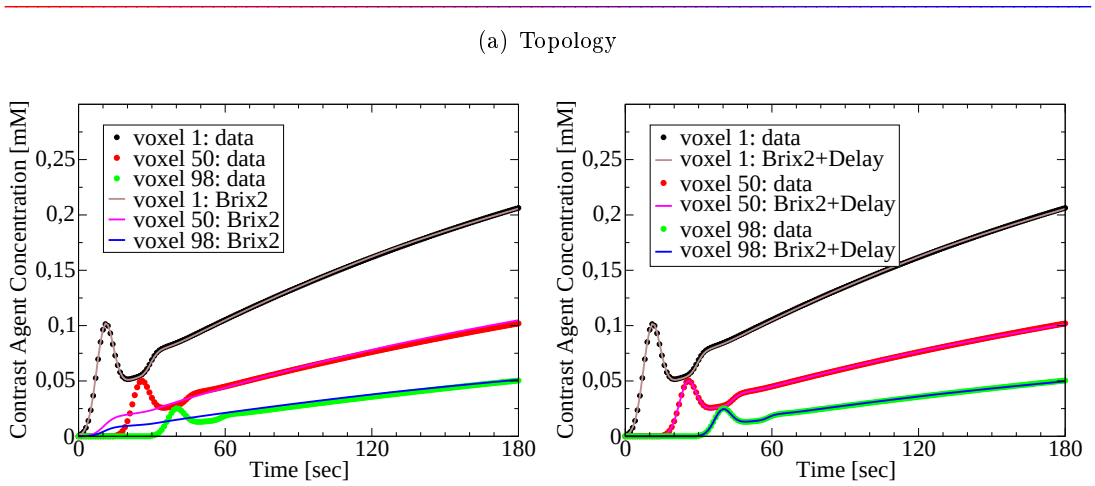

(a) Topology

(b) Brix2 Fit Curves for 3 selected Voxels

(c) Brix2+Delay Fit Curves for 3 selected Voxels

Figure 6.28: Contrast agent transport along a permeable vessel within one-dimensional voxel arrangement. (a) The one-dimensional topology of the permeable blood vessel. The color indicate the pressure gradient (red=12kPa, blue=2kPa). (b) Comparison between direct method and Brix2 fit curve. (c) Comparison between direct method and Brix2+Delay fit curve. The curves show the contrast agent time course in the arterial root voxel (*black/brown*), central voxel (*red/magenta*) and venous root voxel (*green/blue*)

Figure 6.28 shows that the voxel-wise fits are better for Brix2 with time delay than the original Brix2 as in the example without permeability.

The fit parameters (see figure 6.29) for the vascular volume fraction ϕ_P and the intra-/extra-vascular exchange rate K_{PS} are only close to the original values for voxels close to the artery. The farther away from the artery the more they diverge. Both values seem to be underestimated due to the misinterpreted loss of intra-vascular CA caused by the vascular permeability. On the other hand, the flow rate F, though it is underestimated, stays stable along the whole domain.

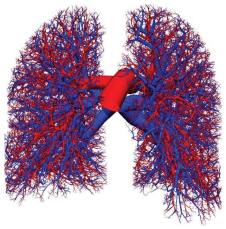

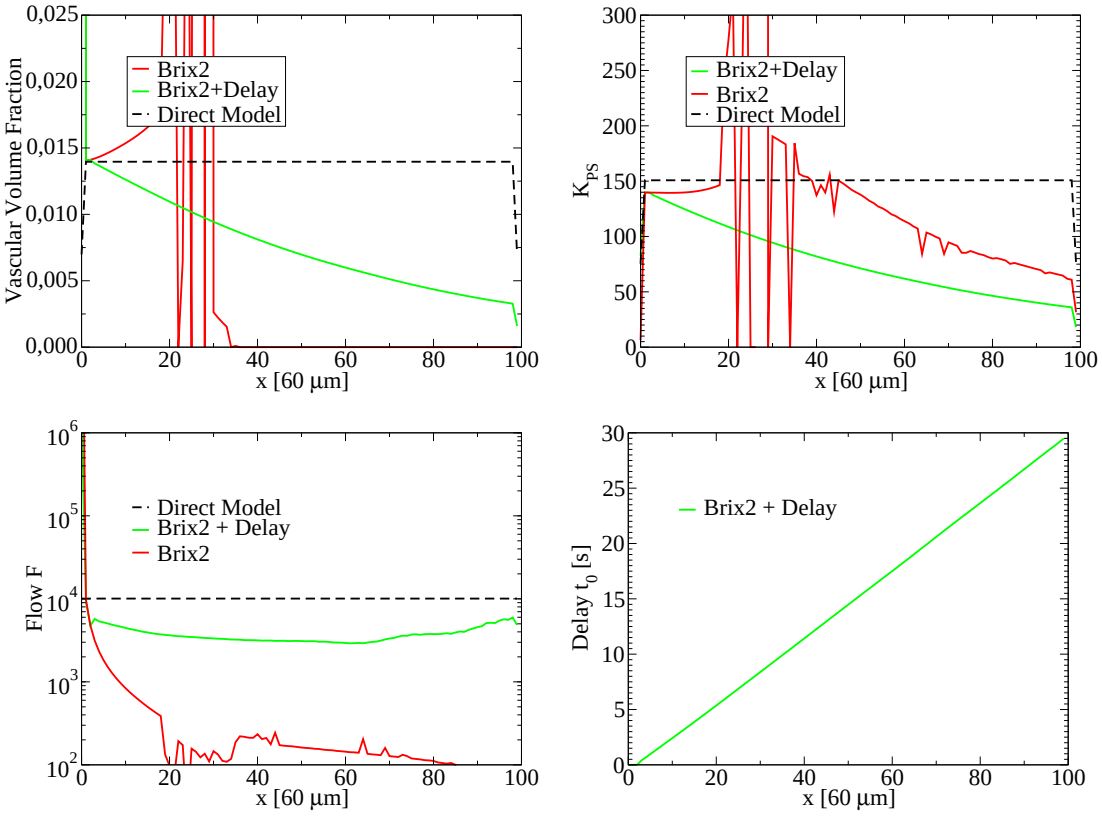

Figure 6.29: Parameter comparison between values used for direct method (*dashed line*) and the values recovered by Brix2 (*red*) and Brix2+Delay (*green*). x denotes the voxel in the one-dimensional arrangement. Units: F and K_{PS} in $\mu m^3/s$. .

2D in Symmetric Arrangement (without Permeability)

In the two dimensional example illustrated in figure 6.30(a) the vessel trees are completely symmetrically organized. Thus at each arterial branch the flow and the vascular volume split up equally among the two sub-trees. At branches at in the venous tree two equal flows merge into one large vessel. Figure 6.30(b) shows the time CA concentration curves of three voxels (marked in fig. 6.30(a)): the arterial root, a capillary and the venous root. The curves in both root nodes have identical shapes with a small time delay at the venous root. The amplitude in the capillary is smaller due to the smaller vascular volume fraction.

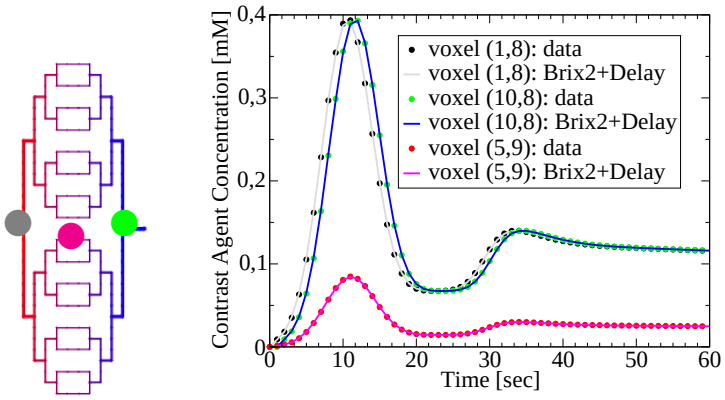

(a) Topology (b) Brix2+Delay Fit Curves for 3 selected Voxels

Figure 6.30: Contrast agent transport along a non-permeable symmetric vessel network within two-dimensional voxel arrangement. (a) The symmetric topology of the non-permeable blood vessel. The color indicate the pressure gradient (red=12kPa, blue=2kPa). (b) Comparison between direct method and Brix2+Delay fit curve. The curves show the contrast agent time course in the arterial root voxel (*grey*), capillary voxel (*magenta*) and venous root voxel (*green*)

Although delayed Brix2 perfectly fits the time CA concentration curves of all voxels the parameter estimation partially underestimates the flow rate while recovering the exact vascular volume fractions. This confirms the observations done in the one-dimensional case.

2D in Tumor Embedding Vascularization

Figure 6.32(a) shows the topology of an asymmetric vascularization created by 200 iterations of CSSH from initially 4 venous and one arterial root node followed by further

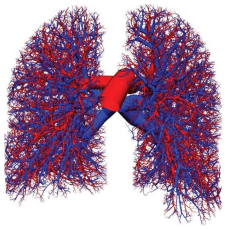

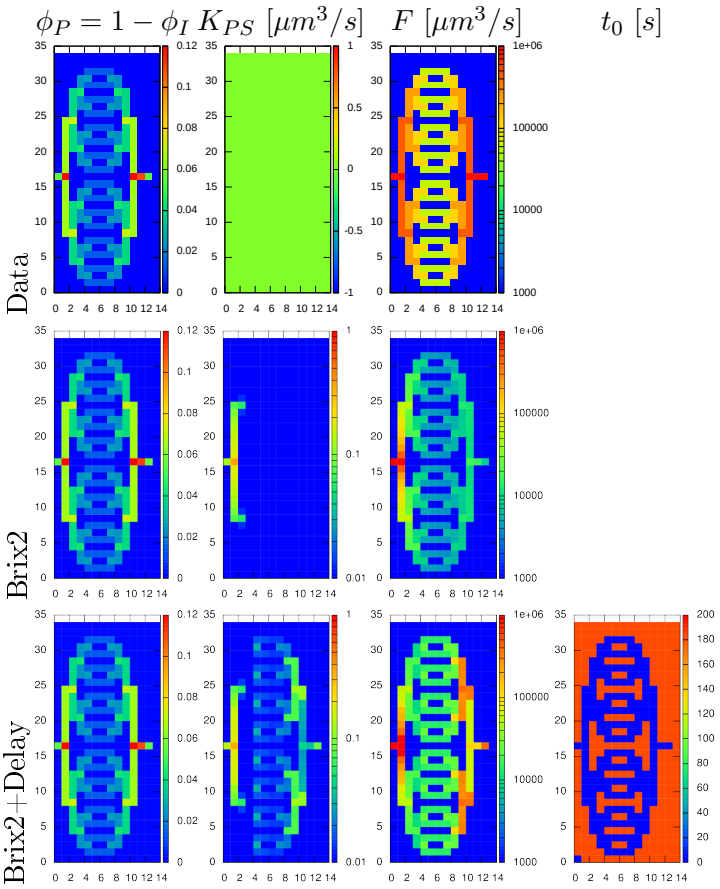

Figure 6.31: Parameter comparison. Parameter maps show the values of vascular volume fraction Φ_P, exchange rate K_{PS}, flow rate F and time delay t_0 (only for Brix2+Delay) used for the direct method and recovered by Brix2 and Brix2+Delay.

10 iterations after embedding a tumor.

Figure 6.32(b) shows the time CA concentration curves of the direct model for four different voxels: the arterial root node, the venous root node and two nodes within the tumor region (close to large vessel, away from large vessel). Delayed Brix2 fits well.

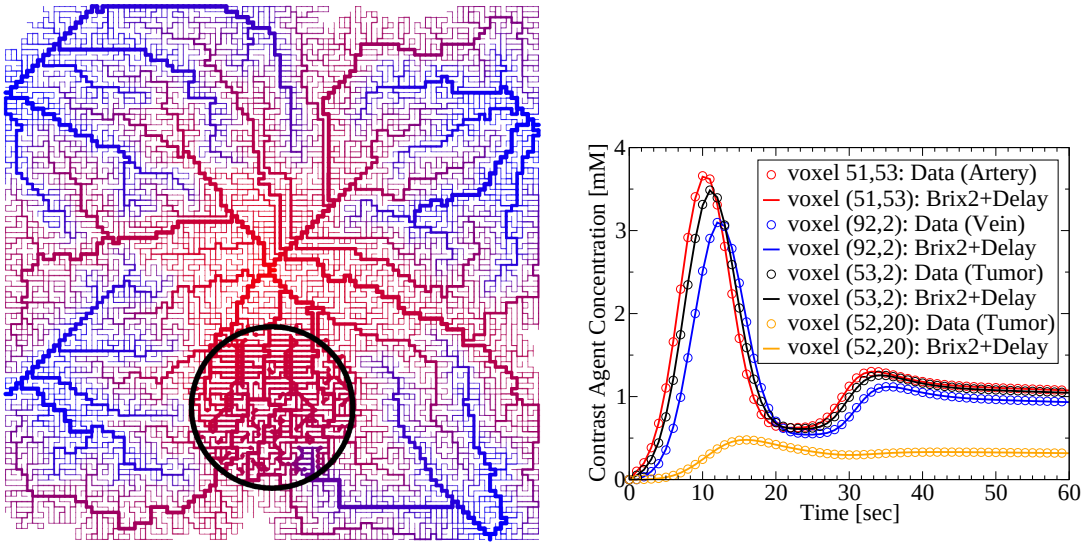

(a) Topology (b) Brix2+Delay Fit Curves for 2 selected Voxels

Figure 6.32: Contrast agent transport along a non-permeable asymmetric vessel network embedding a tumor within a two-dimensional voxel arrangement. (a) The symmetric topology of the non-permeable blood vessel. The colors indicate the pressure gradient (red=12kPa, blue=2kPa). (b) Comparison between direct method and Brix2+Delay fit curve. The curves show the contrast agent time course in the arterial root voxel (*red*), capillary voxel (*yellow*), intermediate voxel with large vessel (*black*) and venous root voxel (*blue*)

As can be seen in figure 6.33 in the asymmetric case as well the vascular volume fraction is nicely recovered. Nevertheless, comparing the parameter maps for the flow rate F indicates an underestimation of almost three orders of magnitude for the venous root nodes. Thus the error for vessels far away from the feeding artery increases tremendously.

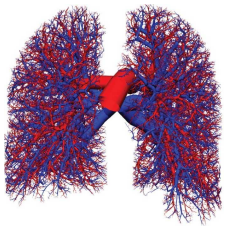

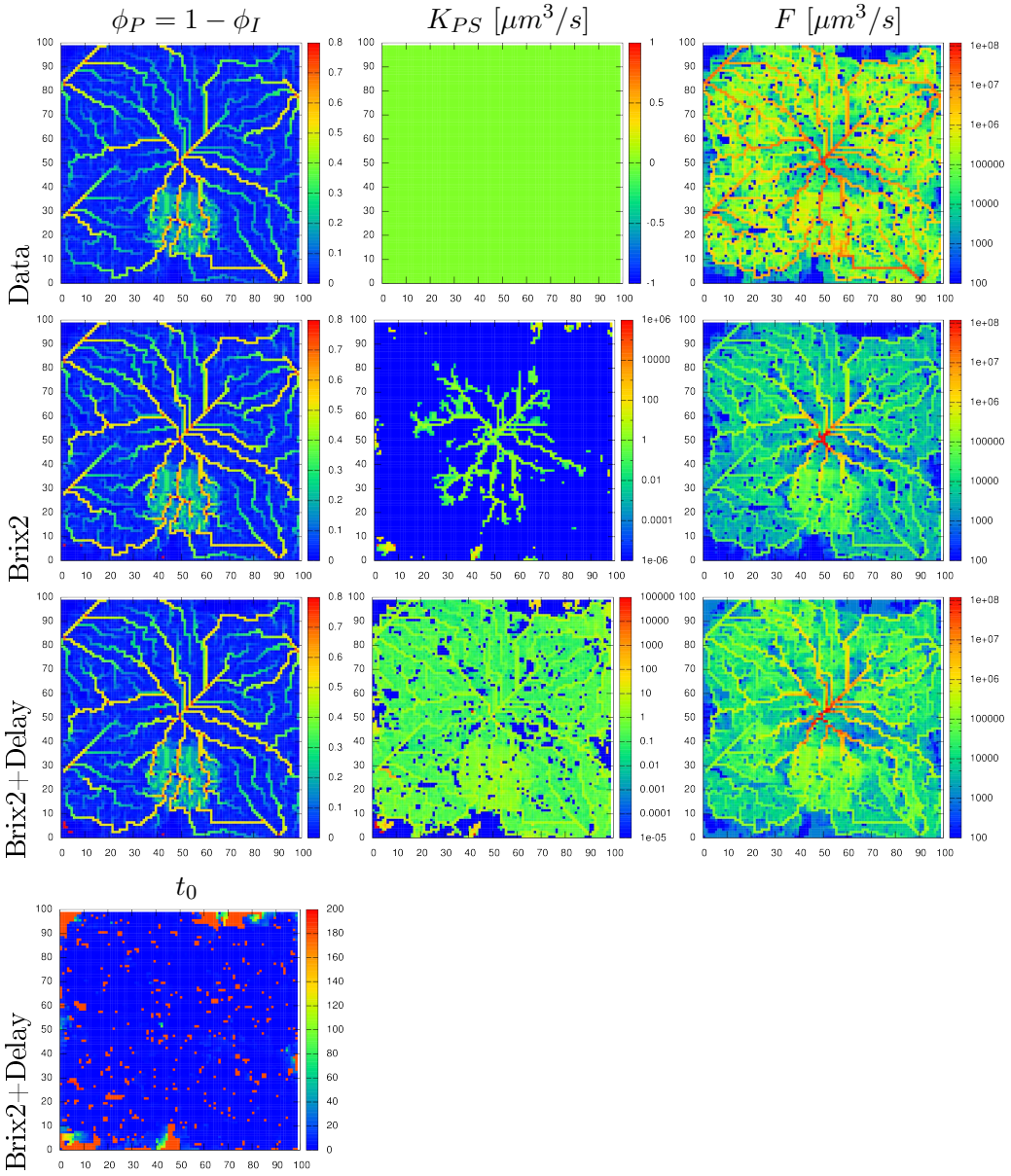

Figure 6.33: Parameter comparison. Parameter maps show the values of vascular volume fraction Φ_P, exchange rate K_{PS}, flow rate F and time delay t_0 (only for Brix2+Delay) used for the direct method and recovered by Brix2 and Brix2+Delay.

6.5 Upscaling: Does the Transition to Larger Scales still permit Accurate Parameter Estimation?

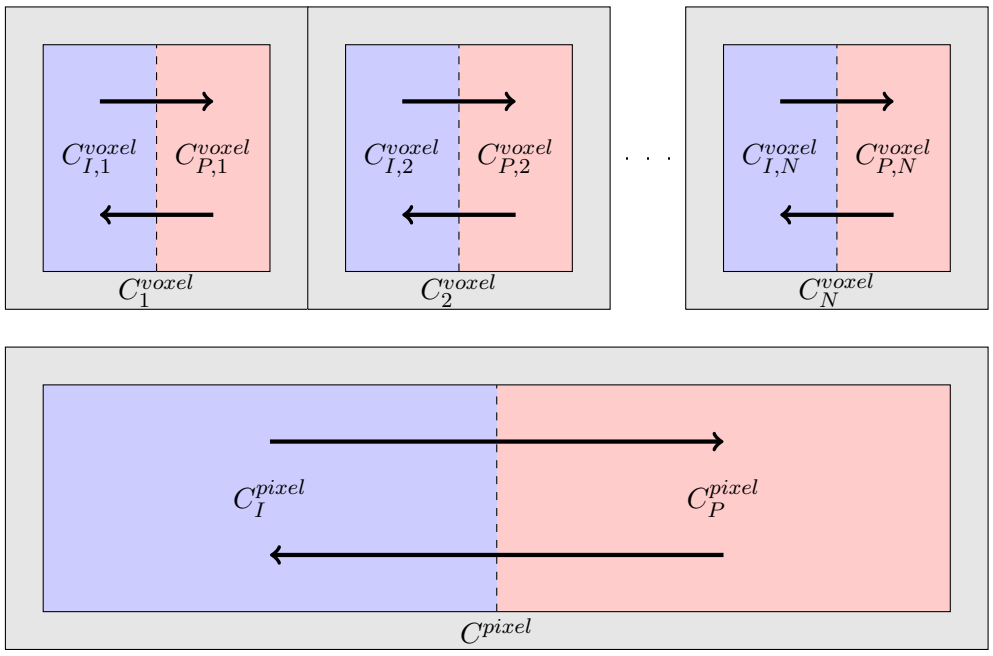

$$\begin{aligned} V_P \frac{dC_P}{dt} &= K_{PS}(C_I - C_P) \\ V_I \frac{dC_I}{dt} &= -K_{PS}(C_I - C_P) \\ C(t) &= \phi_I C_I + \phi_P C_P \end{aligned} \tag{6.43}$$

Assuming we have a 2-compartment model describing the dynamics in the subunits of a domain (neglecting for now all inter-subunit relations) which in the following will be referred to as *voxels*. Now by coarse-graining, the voxels will be grouped as blocks of N voxels which we will refer to as the *pixels*.

Question: If we try to infer parameters on the coarse scale (*pixel*) from data which is a result from dynamics on the fine scale how much can one trust those parameters (error estimation) and what is there meaning for the fine scale?

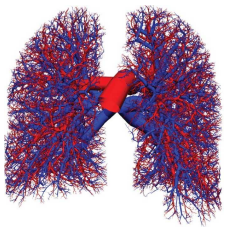

6.5.1 Local Concentrations (Voxels)

Phasic concentrations are defined as C_I within the interstitial space and C_P in the plasma compartment.

$$\begin{aligned} C_P &= Q_P/V_P \\ C_I &= Q_I/V_I \end{aligned} \tag{6.44}$$

where Q_P and Q_I are the amounts of substance in the respective compartments of size V_P and V_I.

Macroscopic concentrations are defined as C. It is the averaged concentration among a voxel or pixel and can be derived from the phasic concentrations by

$$Q = Q_P + Q_I \tag{6.45}$$
$$VC = V_P C_P + V_I C_I \tag{6.46}$$
$$C = \phi_P C_P + \phi_I C_I \tag{6.47}$$

where V is the total volume of both compartments and ϕ_P and ϕ_I the compartmental volume fractions corresponding to V.

6.5.2 Upscaling Concentrations (From Voxels to Pixel)

Upscaling Volume Fractions

The compartmental volumes just sum up

$$V_P^{pixel} = \sum_{i=1}^{N} V_{P,i}^{voxel} \tag{6.48}$$

If all voxels have the same size ($V^{voxel} = V^{pixel}/N$) then the volume fractions can be upscaled to the pixel by

$$\phi^{pixel} = \frac{1}{N} \sum_{i=1}^{N} \phi_i^{voxel} \tag{6.49}$$

Upscaling Phasic Concentration

The phasic compartmental concentrations C_P and C_I can be upscaled from the *voxel* to *pixel*-scale as follows (for C_P)

$$Q_P^{pixel} = \sum_i^N Q_{P,i}^{voxel} \tag{6.50}$$

$$V_P^{pixel} C_P^{pixel} = \sum_i^N V_{P,i}^{voxel} C_{P,i}^{voxel} \tag{6.51}$$

$$C_P^{pixel} = \frac{\sum_i^N V_{P,i}^{voxel} C_{P,i}^{voxel}}{V_{P,i}^{pixel}} \tag{6.52}$$

$$= \frac{\sum_i^N V_{P,i}^{voxel} C_{P,i}^{voxel}}{\sum_i^N V_{P,i}^{voxel}} \tag{6.53}$$

Upscaling Macroscopic Concentration

The macroscopic concentrations C can be upscaled from the *voxel* to *pixel*-scale as follows

$$Q^{pixel} = \sum_i^N Q_i^{voxel} \tag{6.54}$$

$$C^{pixel} = \frac{\sum_i^N Q_i^{voxel}}{V^{pixel}} \tag{6.55}$$

$$= \frac{\sum_i^N V_i^{voxel} C_i^{voxel}}{V^{pixel}} \tag{6.56}$$

$$= \frac{1}{N} \sum_i^N C_i^{voxel} \tag{6.57}$$

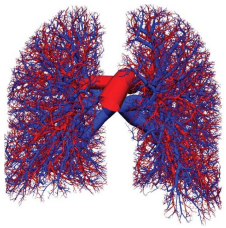

6.5.3 Upscaling (Effective) Permeability

The effective permeability surface product of a pixel is the sum of all permeability surface products for all vessel membranes in this voxel.

$$K_{PS}^{pixel} = \frac{D_M}{H_M} S_M^{pixel} \tag{6.58}$$

$$= \frac{D_M}{H_M} \sum_i^N S_{M,i}^{voxel} \tag{6.59}$$

$$= \sum_i^N K_{PS,i}^{voxel} \tag{6.60}$$

6.5.4 Estimating the Apparent Permeability

Applying an inverse method to the observation on the coarse scale, $C^{pixel}(t) = \sum_i C_i^{voxel}(t)/N$, we want to use the same model as was used on the fine scale to produce $C_1^{pixel}(t), ..., C_N^{pixel}(t)$ as fit function (e.g. equation 6.43). In this case the coarse observations of changes in time would be interpreted purely on the coarse scale. This can be described by the *conservation of mass*:

$$dQ^{pixel} = \sum_i^N dQ_i^{voxel} \tag{6.61}$$

In the case of model 6.43 this gives

$$dQ^{pixel} = K_{PS}^{pixel}(C_P^{pixel} - C_I^{pixel}) \tag{6.62}$$

$$= \sum_i^N K_{PS,i}^{voxel}(C_{P,i}^{voxel} - C_{I,i}^{voxel}) \tag{6.63}$$

We can see that the apparent K_{PS}^{pixel} emerging at the coarse scale depends on the compartmental volume fractions (on both scales), the local exchange rates $K_{PS,i}^{voxel}$ as well as

the local phasic concentrations $C_{P,i}^{voxel}$ and $C_{I,i}^{voxel}$

$$K_{PS}^{pixel} = \frac{\sum_i^N K_{PS,i}^{voxel}(C_{P,i}^{voxel} - C_{I,i}^{voxel})}{(C_P^{pixel} - C_I^{pixel})} \tag{6.64}$$

$$= \frac{\sum_i^N K_{PS,i}^{voxel}(C_{P,i}^{voxel} - C_{I,i}^{voxel})}{\frac{\sum_i^N V_{P,i}^{voxel} C_{P,i}^{voxel}}{\sum_i^N V_{P,i}^{voxel}} - \frac{\sum_i^N V_{I,i}^{voxel} C_{I,i}^{voxel}}{\sum_i^N V_{I,i}^{voxel}}} \tag{6.65}$$

$$= \frac{\sum_i^N K_{PS,i}^{voxel}(C_{P,i}^{voxel} - C_{I,i}^{voxel})}{\frac{\sum_i^N \phi_{P,i}^{voxel} C_{P,i}^{voxel}}{\sum_i^N \phi_{P,i}^{voxel}} - \frac{\sum_i^N \phi_{I,i}^{voxel} C_{I,i}^{voxel}}{\sum_i^N \phi_{I,i}^{voxel}}} \tag{6.66}$$

$$= N \cdot \frac{\sum_i^N K_{PS,i}^{voxel}(C_{P,i}^{voxel} - C_{I,i}^{voxel})}{\sum_i^N \frac{\phi_{P,i}^{voxel}}{\phi_P^{pixel}} C_{P,i}^{voxel} - \frac{\phi_{I,i}^{voxel}}{\phi_I^{pixel}} C_{I,i}^{voxel}} \tag{6.67}$$

Necessary assumptions for time-invariant K_{PS}^{pixel}:

- const. volume fractions among pixel: $\phi_{P,i}^{voxel} = \phi_P^{pixel}$, $\phi_{I,i}^{voxel} = \phi_I^{pixel}$

$$K_{PS}^{pixel} = N \cdot \frac{\sum_i^N K_{PS,i}^{voxel}(C_{P,i}^{voxel} - C_{I,i}^{voxel})}{\sum_i^N C_{P,i}^{voxel} - C_{I,i}^{voxel}} \tag{6.68}$$

- const. exchange rate among pixel: $K_{PS,i}^{voxel} = K_{PS}^{voxel}$

$$K_{PS}^{pixel} = N \cdot K_{PS}^{voxel} \tag{6.69}$$

Figure 6.34 shows three test examples where the equations 6.43 were solved independently within N voxels with:

- constant volume fractions, but varying $K_{PS,i}$ among the voxels
- varying volume fractions, but constant $K_{PS,i}$ among the voxels
- constant volume fractions and $K_{PS,i}$ among the voxels

One can see that only for constant volume fractions and $K_{PS,i}$ among all voxels the apparent K_{PS} is identical to the effective K_{PS} (see equation 6.60).

Figure 6.35 shows a sensitivity analysis of the apparent K_{PS} to different degrees of heterogeneity of local volume fractions and $K_{PS,i}$.

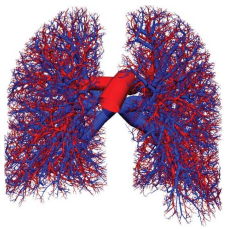

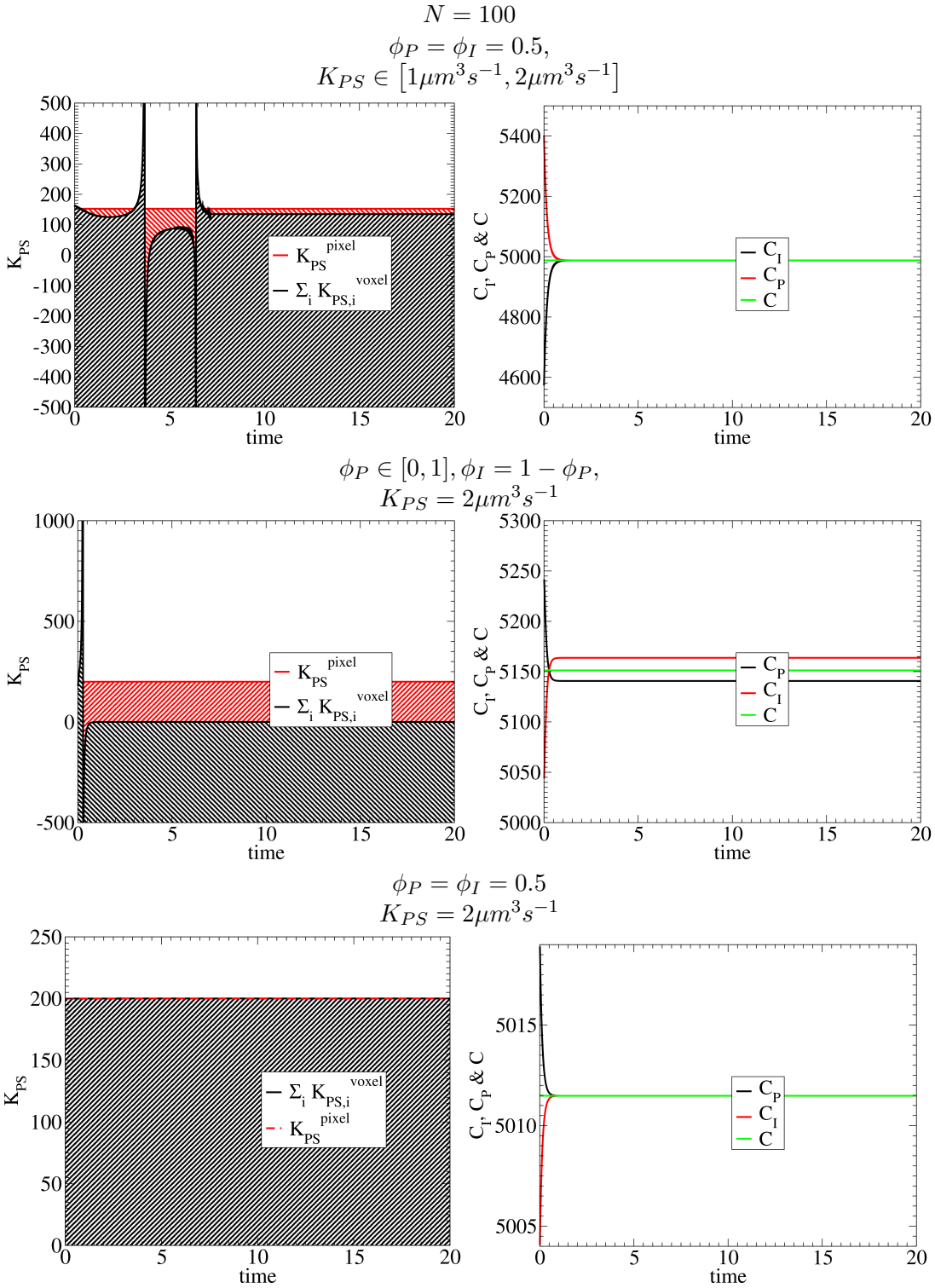

Figure 6.34: Two compartment model describing the tissues microcirculation of a contrast agent.

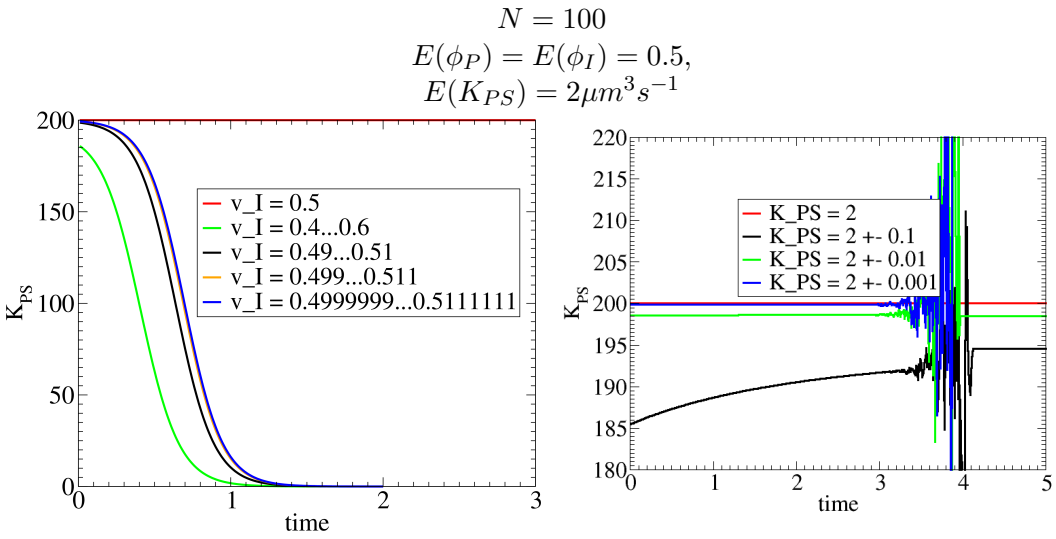

Figure 6.35: Two compartment model describing the tissues microcirculation of a contrast agent.

6.5.5 Error Estimation between Effective and Apparent Permeability

absolut error:

$$\epsilon_a = \left|\left| K_{PS}^{pixel} - \sum_i^N K_{PS,i}^{voxel} \right|\right| \tag{6.70}$$

$$= \frac{\sum_i^N K_{PS,i}^{voxel}(C_{P,i}^{voxel} - C_{I,i}^{voxel})}{\frac{1}{N} \cdot \sum_i^N \frac{\phi_{P,i}^{voxel}}{\phi_P^{pixel}} C_{P,i}^{voxel} - \frac{\phi_{I,i}^{voxel}}{\phi_I^{pixel}} C_{I,i}^{voxel}} - \sum_i^N K_{PS,i}^{voxel} \tag{6.71}$$

$$= \sum_i^N K_{PS,i}^{voxel} \cdot \frac{\alpha_i}{\beta} - \sum_i^N K_{PS,i}^{voxel} \tag{6.72}$$

$$= \sum_i^N K_{PS,i}^{voxel} \cdot \frac{\alpha_i}{\beta} - K_{PS,i}^{voxel} \tag{6.73}$$

$$= \sum_i^N K_{PS,i}^{voxel} \cdot \frac{\alpha_i - \beta}{\beta} \tag{6.74}$$

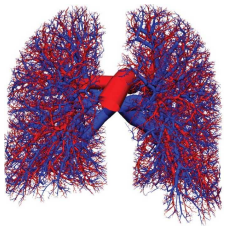

relative error:

$$\epsilon_r = \left|\left| \frac{K_{PS}^{pixel} - \sum_i^N K_{PS,i}^{voxel}}{K_{PS}^{pixel}} \right|\right| \tag{6.75}$$

$$= \frac{\sum_i^N K_{PS,i}^{voxel} \cdot \frac{\alpha_i}{\beta} - \sum_i^N K_{PS,i}^{voxel}}{\sum_i^N K_{PS,i}^{voxel} \cdot \frac{\alpha_i}{\beta}} \tag{6.76}$$

$$= \frac{\sum_i^N K_{PS,i}^{voxel} \cdot \alpha_i - K_{PS,i}^{voxel} \beta}{\sum_i^N K_{PS,i}^{voxel} \cdot \alpha_i} \tag{6.77}$$

$$= 1 - \frac{\sum_i^N K_{PS,i}^{voxel} \beta}{\sum_i^N K_{PS,i}^{voxel} \cdot \alpha_i} \tag{6.78}$$

6.5.6 Upscaling Flow

The total flow through a voxel (or pixel) is the sum of all flows entering the voxel (or pixel) at its outer borders.

$$F^{pixel} = \sum_{i \in pixel, j \notin pixel} F_{i \to j}^{voxel} \tag{6.79}$$

6.6 Conclusion & Discussion

6.6.1 Vascularization

We established a framework to create generic vascularizations as benchmark environment to simulate contrast agent perfusion and produce *in-silico* dynamic contrast enhanced perfusion images which later on were used to study the accuracy of an inverse method. Though, chosen a very simple square lattice topology, the vessel properties had a good agreement with experimental measurements.

In future work - especially for the integration of such a vascular model into an predictive multi-scale model - it could be interesting to generalize the framework toward a more realistic and lattice-free approach. This would allow to approach more realistic branching angles and different vessel densities.

6.6.2 Perfusion & Numerical Methods

The explicit upwind scheme in combination with a refinement of blood vessel segments was able to produce reliable data for the inverse problem. The needs for space and time refinement to avoid numerical diffusion could be replaced by a higher order scheme: Lax-Wendroff or Flux-Limiter (SuperBee, Minmod etc.). The problem is that higher

order schemes are not well defined for numerical problems on graphs as they are whether 1D, 2D nor 3D.

6.6.3 Inverse Problem

It is possible to use non-spatial inverse methods as Brix2 or delayed Brix2 to get an idea of the local vessel properties (volume fraction, permeability, flow rate), but not (in all cases) an exact estimate. In the case of a *purely intra-vascular* agent, one gets a good recovery of the volume fractions (plasma and interstitial space) used in the direct model. The flow rate on the other hand was in all cases found to be underestimated the farther the region of interest was away from the feeding artery. The underlying reason is currently not clear. This might be the effect of both: a remaining numerical diffusion in the direct problem of the extra-vascular agent case and an overlap of different transport velocities in the asymmetric networks.

Numerical Diffusion

As it can be seen in figure 6.26 and 6.30 the numerical diffusion was reduced dramatically by refining the vessel segments and the time step. A remarkable drop in the estimated flow rate can be observed (see figures 6.27 and 6.31) the farther away a voxel is located from the feeding artery. If this drop should be due to the small remaining numerical diffusion in the direct problem then this would suggest a high sensitivity of the inverse problem to small modifications in the shape of the curves. Parameter estimations in *in-vivo* measurements would thus already by the level of noise lead to very doubtful results. Here a more extensive and systematic sensitivity analysis should be done on the influence of small perturbations (noise and numerical errors) to the outcome of the inverse problem.

Network Asymmetries

On the other hand, network asymmetries as they are the reality in *in-vivo* lead to profiles composed of a specter of input signals transported at different velocities among the network. Thus neglecting the contributions of different flow rates and delays to the input signal of each voxel will in an optimistic case just give an relative estimate of the real properties. Here the inverse method could be already improved by replacing the AIF by a population of AIFs with individual flow rates and delays. This would multiply the number of fit parameters, but correct the correspondence to the true local properties while keeping the inverse problem a non-spatial problem.

Permeability

The perfusion of agents leaking into the extra-vascular space adds further difficulties. The drain of contrast agent along the path of transport leads to lower amplitudes of the input signals in voxels far away from feeding arteries. A non-spatial model not considering the loss in between the feeding artery and the voxel/region of interest will compensate this lack of information by other fit parameters. As can be seen in figure 6.29 it mainly reflects in an underestimation of the plasma volume fraction ϕ_P and the intra-extra-vascular exchange rate K_{PS}. An improvement could be reached by estimating the loss as a function of distance from the feeding artery whether directly by automated artery detection or by time delay parameter t_0 (figure 6.29). The estimate would stay very rough as the loss is approximated in a heuristic way, but would have the advantage of keeping the inverse problem non-spatial. For an exact quantification one would have to take the inter-voxel fluxes into account. Then the complexity of the inverse problem would be equal to the direct problem.

Conclusion

Non-spatial inverse methods give a good estimate of the relative differences of vessel properties in neighboring voxels, but are only capable to a very limited extent to make exact parameter estimations in order to parametrize models. With minor extensions the non-spatial model used for the inverse problem could improve dramatically in accuracy for data of purely intra-vascular CA perfusion (DCE-US). For extra-cellular agents leaking into the interstitial space the inter-voxel relations have to be taken into account.

Conclusion and Perspectives

Chapter 7

Conclusion & Perspectives

7.1 Avascular Tumor Growth Model & Parameterization

A multi-scale model was constructed and parametrized to explain data of EMT6/Ro cells grown under four different nutrient conditions. This includes exponential growth, mechanically-limited growth, nutrient-limited growth and saturation. Then in a second step, it was adapted to the SK-MES-1 cell line under additional consideration of the concentric arrangements of cell phenotypes (proliferating, quiescent and necrotic cells) and the extra-cellular matrix densities. Those were extracted from micrographs of cryosected and stained spheroids at different instances of the growth process by a quantitative image analysis chain.

We could show, that it is important to guide experiments in order to capture the right mechanisms explaining certain observed phenomena. For quantitative predictions this is even essential. By comparison of the extracted radial profiles with the *in-silico* arrangements emerging from model simulation, many possible mechanisms leading to the same macroscopic phenomena can be reduced to the most plausible one(s).

For example, it could be shown that the proliferating rim of spheroids does not correspond to the outermost layer uniquely containing proliferating cells which is followed by a layer of uniquely quiescent cells. The radial profiles extracted from spheroid micrographs rather suggest a smoothly decaying fraction of proliferating cell toward the spheroid center. Nevertheless, based on the first assumption - of a compact proliferating rim - the growth curves of EMT6/Ro spheroids could be explained, while at the same time the smoothly decaying radial proliferation profiles led to good fits of the growth curves of SK-MES-1 spheroids (for two different nutrient medium conditions). Especially, for studying nutrient-limited growth scenarios the predictions would be incorrect if the wrong mechanism is selected: a smoothly decaying, but deeper proliferating zone would be more affected by nutrient-limitation than a compact and thinner one.

Furthermore, ATP and lactate were identified to mainly control cell growth and survival during the exponential and geometric growth phase of tumor spheroids. A necessary requirement for cells to reenter into the cell cycle seems to be sufficient supply of extra-cellular matrix. Growth saturation comes along with an overall decrease in proliferative activity as well as necrosis instead of an homeostasis of both.

Growth saturation could however not be explained satisfyingly by the mechanisms currently captured by the model and should be the subject of further investigation. As the outermost cells become quiescent as well while still sufficiently supplied with nutrients, a growth inhibition by waste products or metabolites as lactate accumulating in the spheroid center might be a reason.

7.2 Modeling Tumor Growth & Angiogenesis

The avascular model was extended to the *in-vivo* situation by incorporating endothelial cells which populate the same lattice as the tumor cells and form a vessel network on the tissue scale. Via vessel remodeling and angiogenesis rules, it could be shown that the initially slowly expanding tumor overcomes its nutrient-limitation by recruiting new vessels sprouting from already existing nearby vasculature.

Nevertheless, the underlying angiogenesis rules require a verification with experimental data. A promising source of information are dynamic enhanced perfusion images. As they are acquired in a non-invasive way (e.g. by magnetic resonance imaging, computer tomography or ultrasound) they are ideal to long-time monitor the changes in vascularization during tumor progression (angiogenesis and necrosis) or therapy.

Parameter Inference from Dynamic Enhanced Perfusion Images

In order to understand what kind of data can be acquired and under which precision, we studied one common parameter inference procedure with an *in-silico* phantom vascularization.

We created a framework to create generic vascularizations as benchmark environment to simulate contrast agent perfusion and produce *in-silico* dynamic contrast enhanced perfusion images which later on were used to study the accuracy of an inverse method. Non-spatial inverse methods give a good estimate of the relative differences of vessel properties in neighboring voxels, but are only capable to a very limited extent to make exact parameter estimations in order to parametrize models. With minor extensions the non-spatial model used for the inverse problem could improve dramatically in accuracy for data of purely intra-vascular contrast agent (CA) perfusion (dynamic contrast enhanced ultrasound). For extra-cellular agents leaking into the interstitial space the results indicate that the inter-voxel relations have to be taken into account. In such a case, inverse methods for spatio-temporal models (as the direct model) would

be warranted but would require a different magnitude of computational time to infer parameters.

7.3 Upscaling

The single cell-based model reaches its upper computational limit at a tissue size of a few millimeters. To study certain cancer related phenomena as for example angiogenesis the model has to reach the centimeter scale.

Two possibilities to upscale the model to the centimeter scale are:

1. Coarse Graining: occupying one lattice site with maximally N cells, $0 \leq n \leq N$. Figures 7.1, 7.2 and 7.3 show that the model parameters can be rescaled in such a way that the dynamics is still the same.
2. Hybrid-Coarse-and-Single-Cell-Based Model: in order maximize the resolution where necessary and coarse grain where no accuracy is needed, a hybrid model could be used which automatically switches the resolution depending on its need (see figure 7.4)

While these methods have been successfully sought for the core cell model, its extension to the nutrient-limited and vascularized models would be an interesting challenge to pursue.

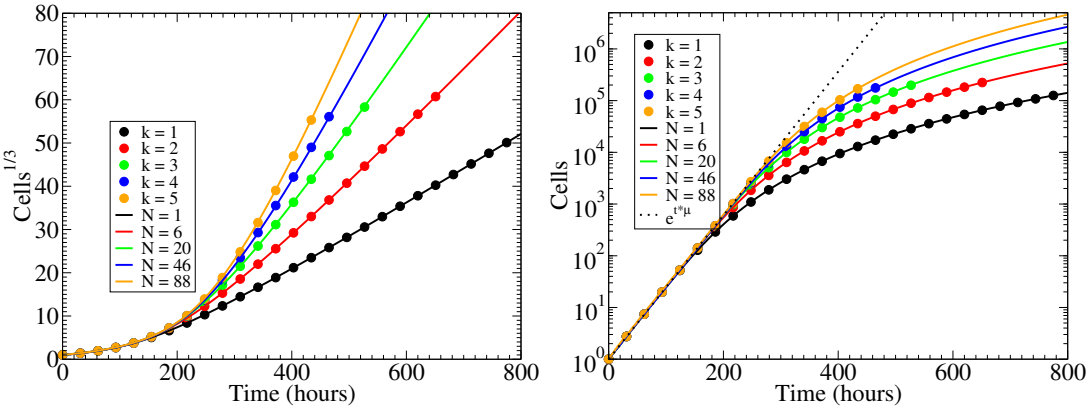

Figure 7.1: Single-cell-based (*dots*) vs. coarse-grained model (*lines*): Cells divide within an exponentially distributed cell-cycle time ($m = 1$).

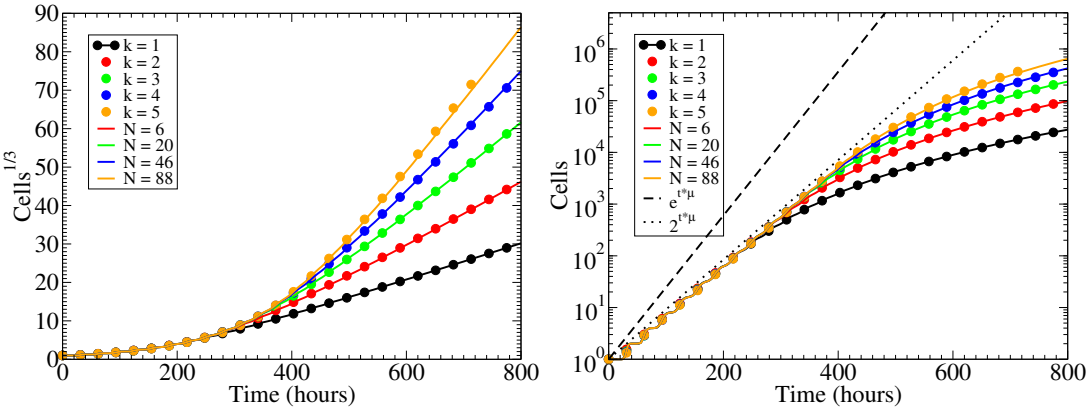

Figure 7.2: Single-cell-based (*dots*) vs. coarse-grained model (*lines*): Cells divide within an Erlang distributed cell-cycle time ($m = 100$).

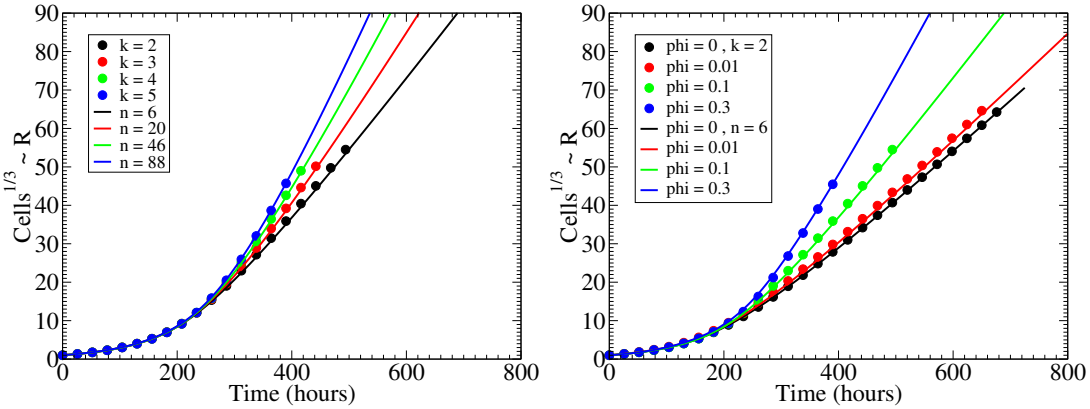

Figure 7.3: Single-cell-based (*dots*) vs. coarse-grained model (*lines*): Cells divide within an exponentially distributed cell-clycle time ($m = 1$) and migrate.

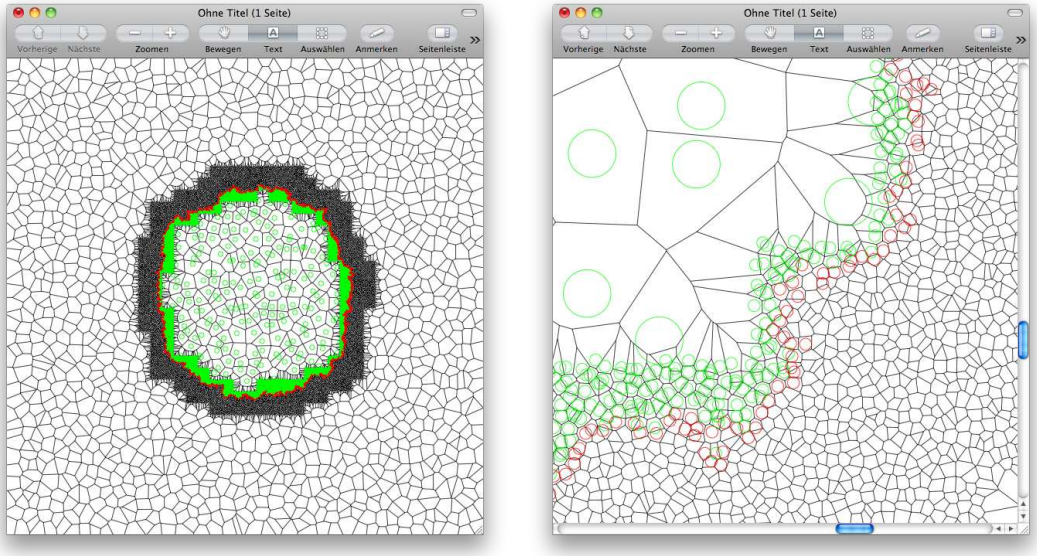

Figure 7.4: Hybrid-Model. Regions of interest are high-resoluted while others are coarse. With the growing tumor front the high-resoluted quiescent cells (*green*) will be coarse-grained while free space invaded by the proliferating tumor cells (*red*) are refined.

Appendix A

Spatial Discretization

Spatial models are applied only to a part of the world while everything else is neglected.

Definition A.1 (*Domain*)

A domain is a set $\Omega \subset \mathbb{R}^n$ in the n-dimensional space.

The interactions with the outside is defined by boundary condition.

As digital computers are only able to handle a finite number of elements instead of continuum representation the spatial (and temporal) dimensions have to be represented by their discrete counterparts. For the spatial dimension this is done by the *tesselation* of the domain Ω.

Definition A.2 (*Cells & Tessellation*)

Tessellation is the sub-division or partition of a domain Ω into a set of cells $\hat{\Omega} := \{\phi \subset \Omega\}$ *with no overlaps, $\forall \phi_i, \phi_j : \phi_i \cap \phi_j = \emptyset$, and no gaps, $\bigcup \phi_i = \Omega$.*

In general the *cells* of a tessellation can have any shape, but in most cases they will be described by *polytope*.

Definition A.3 (*n-Polytope*)

A n-polytope is a geometric object with flat sides in d dimensions. Example: The 2-polytope is known as polygon and the 3-polytope as polyhedron.

The elements n-dimensional polytopes are composed of are summarized in table A.1.

The following sections will focus on different ways how to discretize a finite space by regular and irregular tessellations and how to define neighborhoods on such tesselations.

Dimension	Element Name
0	Vertex
1	Edge
2	Face
3	Cell
⋮	⋮
j	j-face - element of rank $j = -1, 0, 1, 2, 3, ..., n$
⋮	⋮
$n-1$	Facet - $(n-1)$-face
n	Body - n-face

Table A.1: Elements of a n-polytope.

A.0.1 Duality: Lattices and Tesselations

We can distiguish between two types of graphes: Tesselations subdivide the space into tiles, while lattices discribe the neighborship relations between those tiles.

A.1 Regular Lattice

Definition A.4 (*Regular Cells & Tessellations*)

A n-polytope is called regular if all its elements or j-faces (for all $0 \leq j \leq d$, where n is the dimension of the polytope) - cells, faces and so on - are also transitive. A regular tessellation is a highly symmetric tessellation made up of congruent regular polytopes.

In two dimensions there exist only three regular tessellations: those made up of equilateral triangles, squares, or hexagons. In three and higher dimensions it is just one: the cubic or d-hypercubic honeycomb. The three-dimensional counterparts of the triangular and hexagonal tessellation, the tetrahedral and rhombic dodecahedral honeycomb, do not fulfill the regularity condition anymore, but are less strict *uniform tessellations*.

Definition A.5 (*Uniform Cells & Tessellations*)

A uniform tessellation is composed by uniform polytopes. A polytope is uniform if its facets are regular polytopes and it is vertex-transitive (i.e. there is an isometry mapping any vertex onto any other).

A.2 Triangulation

A triangulation is a special kind of tessellation as it cells are . In advanced geometry, in the most general meaning, triangulation is a subdivision of a geometric object into simplices.

Definition A.6 (*Simplex*)

A simplex is a generalization of the notion of a triangle or tetrahedron to arbitrary dimension. Specifically, an n-simplex is an n-dimensional polytope which is the convex hull of its n + 1 vertices.

In particular, in the plane it is a subdivision into triangles, hence the name. Different branches of geometry use slightly differing definitions of the term.

Definition A.7 (*Triangulation*)

A triangulation $\mathcal{T}$ of $\Omega \subset \mathbb{R}^n$ is a subdivision of Ω into n-dimensional simplices such that any two simplices in $\mathcal{T}$ intersect in a common j-face, $j < n$, or not at all.

Let $S \subset \Omega$ be a set of points then Ω can be triangulated by subdividing Ω into simplices whose vertices are a subset of S. Then S is called a set of construction points of the resulting triangulation $\mathcal{T}_S$. The number of possible triangulation for a given set of construction S can be very large.

Definition A.8 (*Delaunay Triangulation*)

A Delaunay triangulation for a set P of points in $\mathbb{R}^n$ is a triangulation $\mathcal{DT}(P)$ such that no point in P is inside the circumsphere of any simplex in $\mathcal{DT}(P)$. Delaunay triangulations maximize the minimum angle of all the angles of the simplex in the triangulation; they tend to avoid skinny simplices.

A point set triangulation, i.e., a triangulation of a discrete set of points $P \subset \mathbb{R}^n$ is a subdivision of the convex hull of the points into simplices such that any two simplices intersect in a common face or not at all and the set of points that are vertices of the subdividing simplices coincides with P. The Delaunay triangulation is a famous triangulation of a set of points where the circum-hypersphere of each simplex contains none of the points.

The Delaunay triangulation of a discrete point set P in general position corresponds to the dual graph of the Voronoi tessellation for P.

A Voronoi diagram is a special kind of decomposition of a metric space determined by distances to a specified discrete set of objects in the space, e.g., by a discrete set of

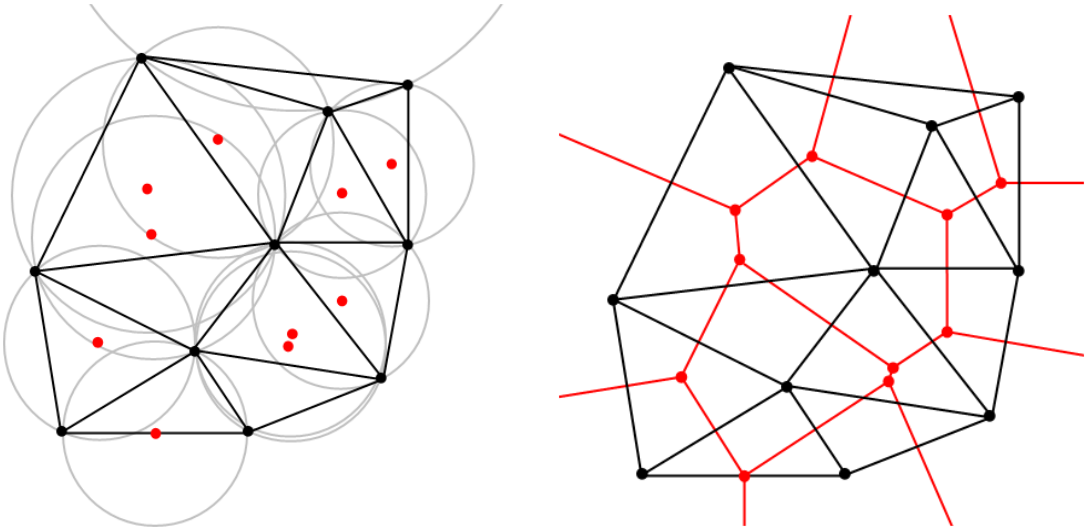

Figure A.1: Dualism: *left*: The Delaunay triangulation with all the circumcircles and their centers (in red). *right*: Connecting the centers of the circumcircles produces the Voronoi diagram (in red).

points. In the simplest case, we are given a set of points P in the plane, which are the Voronoi sites. Each site p has a Voronoi cell, also called a Dirichlet cell, $V(p)$ consisting of all points closer to p than to any other site. The segments of the Voronoi diagram are all the points in the plane that are equidistant to the two nearest sites. The Voronoi nodes are the points equidistant to three (or more) sites. [wikipedia]

A.3 Construction Algorithms

There are several algorithms to create a Delaunay triangulation from a point cloud S. Most of them have a running time of $\mathcal{O}(n \log n)$.

A.3.1 Flip

One of the first algorithms to construct a Delaunay triangulation was proposed by Lawson [Law77]. It is based on the circumstance that a triangulation $\mathcal{T}$ can be transformed into an other triangulation $\mathcal{T}'$ via flipping the edge of two adjacent triangles if and only if they form a *convex quadrilateral*[Law72].

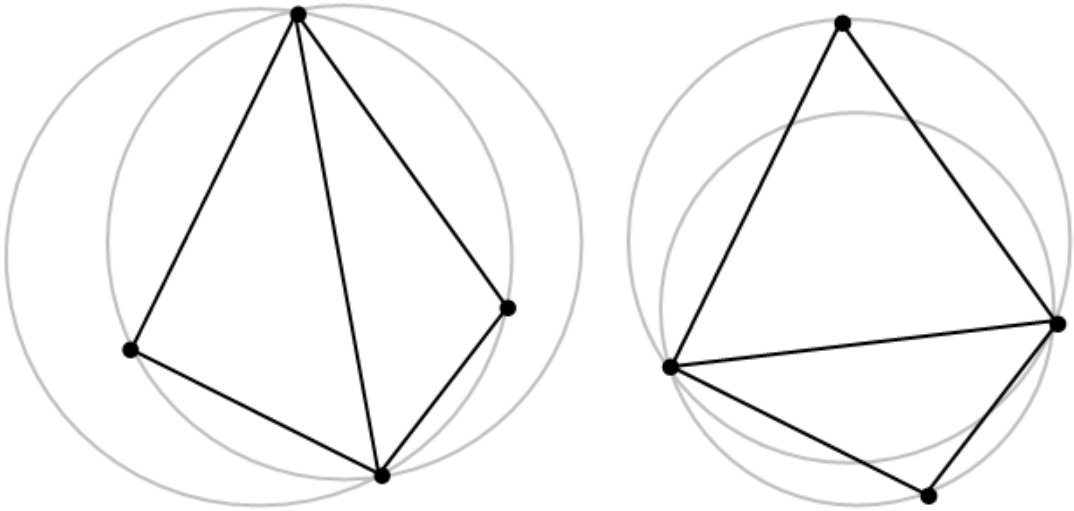

Figure A.2: Flip Algorithm: *left*: Triangles not fulfilling the Delaunay criterion. *right*: The triangles after the middle edge has been flipped.

The algorithm starts with an initial triangulation of all points which must not fulfill the Delaunay condition. The only requirement is that the edges are not overlapping.

Then for every triangle it has to be checked if an other point lays inside its circumcircle. If this is the case the common edge with the adjacent triangle containing this point will be switched as illustrated in figure A.2. This way the triangulation becomes locally Delaunay, but might reintroduce a violation of the Delaunay condition to the neighboring triangles. In the worst case all triangles have to be revisited which leads to a running time of $\mathcal{O}(n^2)$.

A.3.2 Incremental Algorithm

The idea of the incremental algorithms is to add points iteratively to an existing *Delaunay triangulation* (for example a super triangle containing all points to insert) by re-triangulating only the affected region (see section A.4).

A.3.3 Alternative Construction Algorithms

Alternatives to the flip (section A.3.1) and incremental algorithm (section A.3.2) are *Divide and Conquer*, *Sweepline* and *Sweehull*.

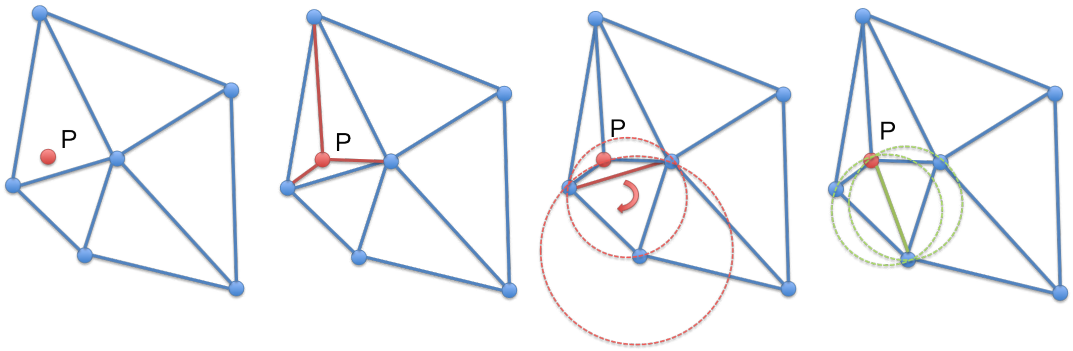

(a) local re-triangulation (b) edge flipping

Figure A.3: Incremental Algorithm (I): (a) Triangle containing new point p is replaced by 3 new triangles. (b) The neighboring triangles which don't fulfill the Delaunay criterion flip edges until all triangles are Delaunay.

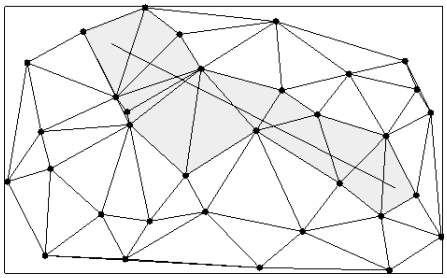

Figure A.4: Search Algorithm: Walk through the triangulation following the shortest path toward the triangle containg point p.

A.4 Point Insertion

a) Insertion & local Edge Flip

One possibility to do this is to look for the triangle t which contains the new point p and replace it by 3 new triangles by connecting each edge of t with p (see figure A.3(a)). Then for all neighboring triangles which don't fulfill the Delaunay condition anymore the edges have to be flipped until the Delaunay condition is fulfilled again (see figure A.3(a) and section A.3.1).

In the worst case we have to test all triangles to find the one containing p. This would result in a complexity of order $\mathcal{O}(n)$ for the search algorithm. Depending on the data structure this can be reduced to $\mathcal{O}(\sqrt{n})$ by a direct walk from a randomly chosen triangle among neighboring triangles toward the triangle containing p (see figure A.4). After the local retriangulation we might have to flip all triangles to reestablish the

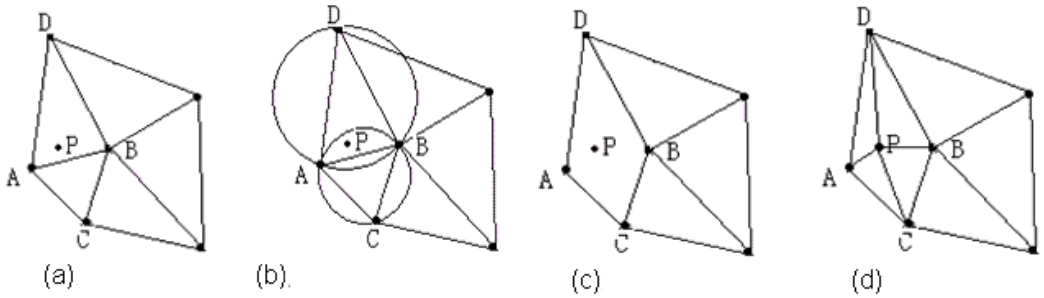

Figure A.5: Incremental Algorithm: *left*: Triangles not fulfilling the Delaunay criterion. *right*: The triangles after the middle edge has been flipped.[Geo]

Delaunay condition which leads to a complexity of $\mathcal{O}(n)$. So for n points the algorithm is of order $\mathcal{O}(n^2)$.

b) Local Delaunay Triangulation

The second possibility was proposed by Bowyer and Watson [Bow81, Wat81]. Here the above described local re-triangulation of one triangle followed by the edge flipping of neighboring was replaced by a single re-triangulation step.

First all triangles whose circumcircle contain the new point p (see figure A.5(b)) will be removed from the triangulation leaving cavity (see figure A.5(c)). Then the remaining edges in the cavity can be connected with p and added to the triangulation as new triangles (see figure A.5(d)). The insertion algorithm has complexity $\mathcal{O}(1)$. So the overall algorithm depends mainly on the search algorithm and takes $\mathcal{O}(n \log n)$ time.

Algorithm 1 Bowyer-Watson Algorithm

form super triangle, enclosing all points $p \in V$
for all $p \in V$ **do**
1. insert vertex $p \in V$ into triangulation
2. find circumcircles containing p with corresponding triangles
3. remove triangles to get insertion polygon
4. retriangulate insertion polygon by simply adding edges to p

end for
remove super triangle

A.5 Point Deletion

The point deletion is the inverse procedure of inserting a point into the triangulation. At first all triangles containing the point p are removed from the triangulation leaving a cavity. Then the vertices of the cavity have to be re-triangulated without violating the Delaunay condition of the neighboring triangles.

In principle we have a stack containing all edges of the cavity. Then for each edge we count the number of triangles that can be created with other points in the cavity and fulfill the Delaunay condition. If the number of possible triangles is exactly one then this new triangle is added to the triangulation. The old edge which is now not a part of the cavity anymore is removed from the stack. If the new edges were already edges of the cavity then they are removed as well. If not they are added to the stack as new part of the cavity.

The algorithm stops when the stack is empty and all edges are retriangulated.

Algorithm 2 Point Deletion Algorithm

```
remove triangles containing point p
initialize list with all edges of the remaining cavity
initialize queue with all vertices of the remaining cavity
repeat
  take vertex v from queue
  if only one edge e in list creates a valide triangle with v then
    add triangle to triangulation
    remove e from stack
  end if
  add vertex v to queue
until stack is empty
```

Appendix B

Stochastic Spatio-Temporal Cellular Automata

B.1 Environment

B.1.1 Discretization

The environment is subdivided by the *Voronoi tesselation* of a set of irregularily distributed points, so-called *construction points*. The distribution of those points is guided by two principles:

1. *Global regularity*: The points are homogenously distributed among an underlying square lattice with lattice constant l, id est each square of the square lattice containes exactly one construction point.

2. *Local irregularity*: Within each square the point is placed randomly.

While global regularity ensures a homogenous distribution of points among the domain and limits the volume variation of the resulting Voronoi cells, local irregularity avoids lattice-artifacts due to symmetry-effects. An other advantage of this choice of construction is the inherent one-on-one relation between the Voronoi cells and squares on both lattices which later can be easily used for solving partial differential equations with the finite differences method.

The *lattice contant* is choosen such that $l = \left(\frac{\pi}{6}\right)^{\frac{1}{3}} d_{cell}$, where d_{cell} is the diameter of a cell at the beginning of the cell cycle. In that case the average volume of the Voronoi cells ($\approx l^3$) is equal to the volume of a cell ($V_{cell} = \frac{\pi}{6} d_{cell}^3$).

B.1.2 Neighborhood

B.2 Cellular automaton model

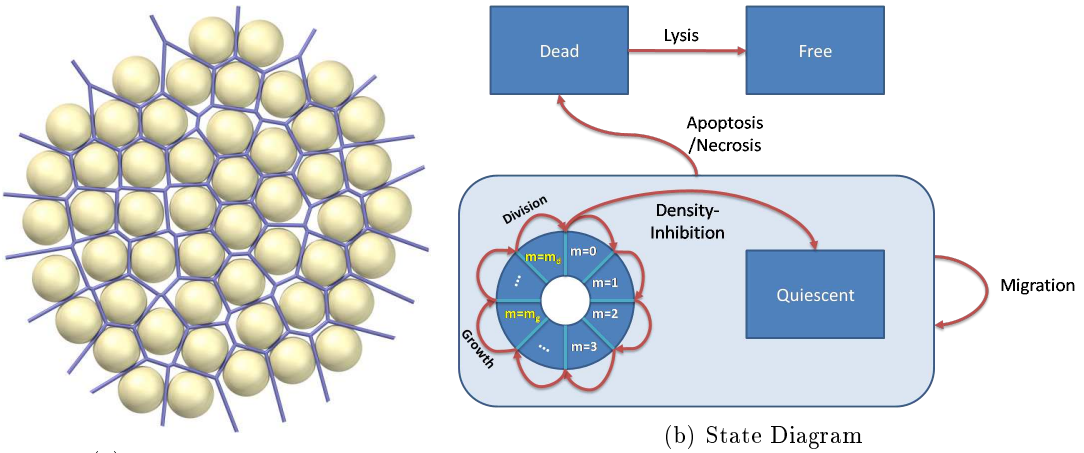

(a) Voronoi Tesselation

(b) State Diagram

Figure B.1: A cell is defined by its position, its internal state and a set of transition rules.

B.2.1 Cells & Population

Biological cells are represented individually in the model. The state of each cell $c_i = (X_i, q_i)$ consists of its position $X_i \subset X$, i.e. each cell can occupy one or two lattice sites (Voronoi cells), and its internal state $q_i \in Q = \{m = 0, ..., m = m_d, quiescent, apoptotic\}$ (see fig. B.1(b)). The population can then be defined as the assembly of all cells $C = (c_i)$.

B.2.2 State Transitions & Temporal Evolution

Cells change their states (position, internal state) and in many cases as well of their environment via transition rules. The general form of transitions can be defined chemical reaction-like

$$A \xrightarrow{\mu} B \tag{B.1}$$

ster Equation where A is the original state, B the resulting state and μ the transition rate.

The systems spatio-temporal evolution can be described by the master equation

$$\frac{\partial P(C,t)}{\partial t} = \sum_{C'} \mu_{C' \to C} P(C',t) - \mu_{C \to C'} P(C,t) \tag{B.2}$$

where C is the current state of a cell population and C' any other state. In a system where the state space $\mathcal{C}$ can become very large it is almost impossible to solve the master equation analytically. Assuming all processes to be Poisson processes, i.e. their waiting time τ are exponentially distributed, Gillespie[Gil77] proposed an exact stochastic simulation algorithm (SSA) to numerically solve the master equation. The idea is to perform random walks through the state space $\mathcal{C}$. At each point in time the next transition was chosen randomly by from all possible transitions. The probabilities of each transition was derived from the second term of the master equation (see eq. B.2).

Gillespie Algorithm

$$P(C \to C') = \frac{1}{\mu_\Sigma} \cdot \mu_{C \to C'} \tag{B.3}$$

$$\mu_\Sigma = \sum_{C'} \mu_{C \to C'} \tag{B.4}$$

The passed time Δt is an exponentially distributed random number and can be calculated by

$$\Delta t = \frac{1}{\mu_\Sigma} \log\left(\frac{1}{\xi}\right) \tag{B.5}$$

where ξ is a unit-interval uniform random number, i.e. $\xi \in [0, 1)$, and μ_Σ is total rate of transition out of state C.

It was shown that for a sufficient number of realizations the mean behavior converges against the exact solution of the master equation. Figure B.2(c) illustrates how the SSA converges against the analytical solution for a non-spatial birth process (see example B.2.2).

Example : Birth process Let the problem be a simple non-spatial birth process where the system state represents the actual population size $C \in \mathbb{N}$ and the state space contains all possible population sizes $\mathcal{C} := \mathbb{N}$. The division rate of each cell in the system is μ. Consequently, the total transition rate is $\mu_\Sigma = C \cdot \mu$.

B.2.3 Cell Cycle Time Distribution & Synchronisation

The above described SSA algorithm is based on Poisson processes (see sec. B.2.2) which imply exponentially distributed waiting times τ. From processes like the cell cycle we know that they follow a rather tighter gaussian-like distribution than an exponential distribution. If we subdivide a process into m Poisson subprocesses in such a way that $\mu_i^{sub} = \mu \cdot m$, $1 \leq i \leq m$, then the waiting time τ becomes Erlang-distributed with shape parameter m.

Erlang Distribution

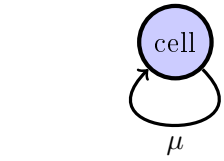

(a) State diagram of single cell.

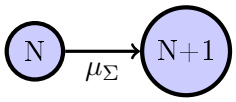

(b) State diagram of population.

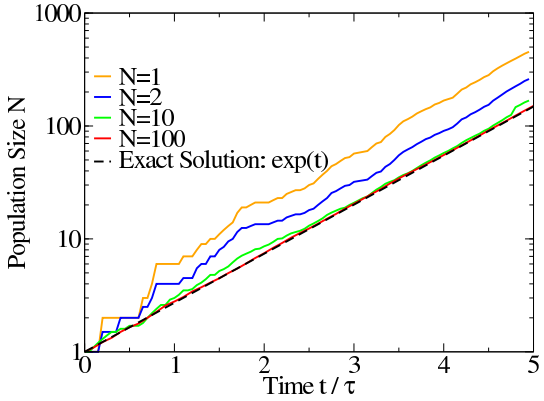

(c) Exponentially distributed cycle times

Figure B.2: Non-spatial birth process simulated with the SSA. (c) Examples B.2.2: the growth curves are averages over a different number of realizations N. **??** Example B.2.3: the growth curves are averages over 1000 realizations using different simulated with the averaged over a different number of realizations using a different Erlang number M.

Example : Example: Erlang distributed birth process Let the problem be a non-spatial birth process. The cell cycle of each cell is subdivided into $m \geq 1$ processes with rate $\mu^{sub} = m \cdot \tau^{-1}$. So the cells internal state is its current cell cycle phase $q_i \in \{1, ..., m\}$. After passing all m processes a cell divides into two daughter cells with $q_i = 1$ and $q_j = 1$. The system state is defined as the set of the current cell cycle phase $C := \{q_i : i \text{ is a cell}\}$ of all cells in the system. The problem can be reduced to

- N_i being the number of cells in cell cycle phase i
- $C := \{N_i\}_{i=1,...,m}$ is the population state
- $\{N_i, N_{i+1}\} \xrightarrow{N_i \mu_i} \{N_i - 1, N_{i+1} + 1\}$ for $1 \leq i < m$
- $\{N_m, N_1\} \xrightarrow{N_m \mu_m} \{N_m - 1, N_1 + 2\}$

Figure B.3 shows that the growth speed of the whole population slows down by increasing the number of subprocesses m. A good approximation for the change of the growth velocity was indicated [Dra05] to be

$$\mu_{eff} = m(2^{1/m} - 1)\mu \tag{B.6}$$

On the other hand side cells divide simultaneously and their cell cycles stay synchronized.

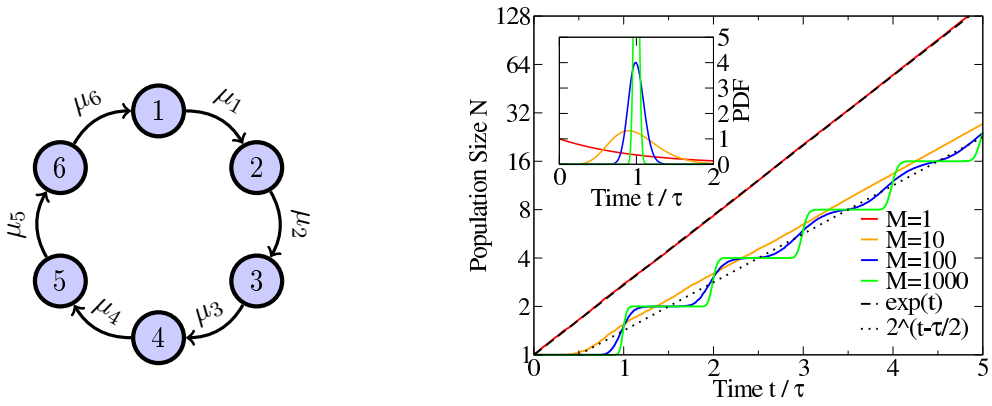

(a) State diagram of single cell

(b) Erlang distributed cycle times

Figure B.3: Non-spatial birth process with Erlang distributed cycle times (see example B.2.3). (a) The state diagram shows the transitions between subsequent cell cycle phases i of a single cell and the related transition rates μ_i. (b) : the growth curves are averages over 1000 realizations using different simulated with the averaged over a different number of realizations using a different Erlang number M.

B.2.4 Space & Space Limitation

Cell Position

The cell divsion is not only influenced by internal mechanisms, but the spatial arrangement as well. In order to do this the cell state will be extended to

$$c_i = \{X_i, q_i\} \tag{B.7}$$

where $X_i \subset X$ is the space occupied by the cell and $q_i \in Q$ the internal state of the cell. If $X \subseteq \mathbb{R}^3$ then the cells can take any possible shape in the three-dimensional space. For computational reasons the space will rather be a discrete tessellation of $\mathbb{R}^3$, in our case a Voronoi tessellation as described in section B.1.

Cell Size & Growth

In order to gain volume, for example for a following cell division (see section B.2.4), cells can extend to reachable (in general neighboring) parts of the domain $X_{ext} \subset \hat{\Omega}$.

$$\{q, X\} \xrightarrow{\mu^{(g)}} \{q, X_{new}\} \tag{B.8}$$

$$X_{new}/X \subseteq X_{ext} \tag{B.9}$$

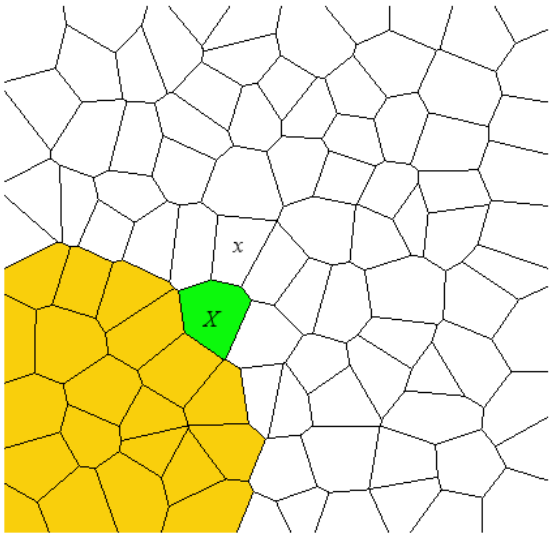

where $X \subset \Omega$ is the cells old position and X_{new} the cells position after expansion. In general we can assume that the cells will extend to the close neighbor hood. The generalized transitionNow we can define multiple spatial constraints to the cell growth by the choice of growth rate, $\mu_x^{(g)} = \mu_{X \to X \cup \{x\}}^{(g)}$, and the reachable area of expansion, X_{ext}.

Example : Example: Contact Inhibition In monolayers we can observe that cells stop growing and dividing as soon as they are surrounded by other cells. The mechanism which is regulating this behavior is called *contact inhibition*. The cells growth rate can be defined as the following

$$\mu_{X \to X \cup \{x\}}^{(g)} = \begin{cases} P(X \to X \cup \{x\}) \cdot \mu^{(g)} & ,\text{if } x \text{ is free} \\ 0 & ,else \end{cases} \tag{B.10}$$

The probability $P(X \to X \cup \{x\})$ that a cell expands to $x \in X_{ext}$ out of all possible expansion sites in X_{ext} can be choosen to be uniformly distributed beween all available (free) sites

$$P(X \to X \cup \{x\}) = \frac{1}{|free(X_{ext})|} \tag{B.11}$$

$$\sum_{x \in free(X_{ext})} P(X \to X \cup \{x\}) = 1 \tag{B.12}$$

$$\sum_{x \in free(X_{ext})} \mu_{X \to X \cup \{x\}}^{(g)} = \mu^{(g)} \tag{B.13}$$

$$free(X) := \{x \in X | x \text{ is not occupied by a cell}\} \tag{B.14}$$

Structured vs. Unstructured Lattice:

There are structured lattice topologies like the most commonly used square lattice or the hexagonal and triangular lattices. The equivalents in three dimensions are cubic, rhombic dodecaedrical honey comb (see figure B.4).

In structured lattices we have the set connectivity of the grid which makes it easy to find the neighboring nodes of a given node, this can be done by addition. Unstructured lattices call for a list of neighbors to be stored for each node, this is due to the arbitrary connectivity between the nodes. This makes structured lattices less memory heavy.

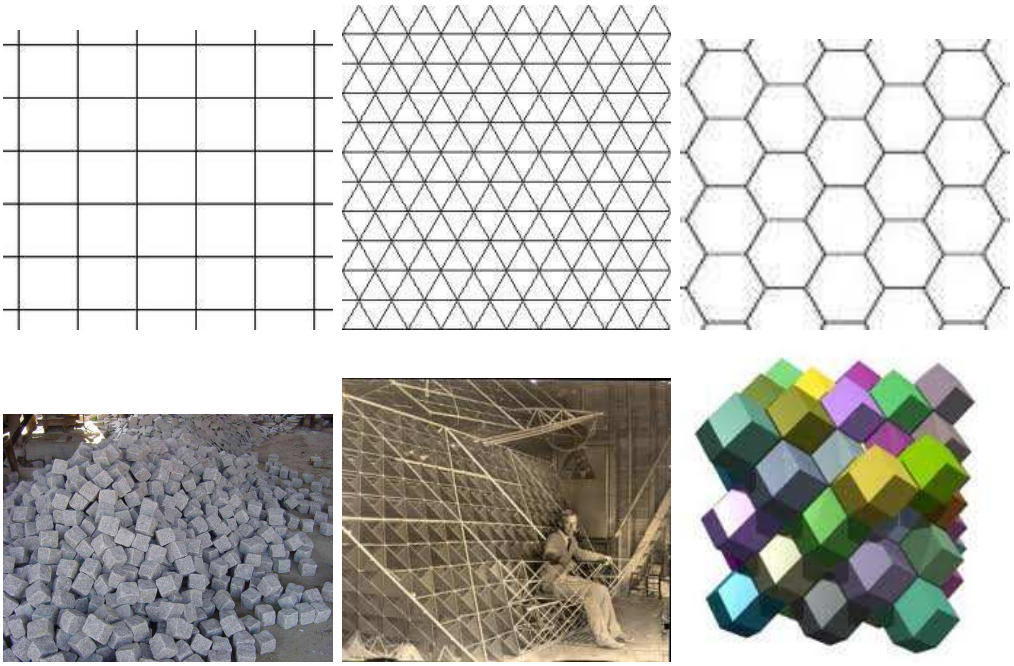

Figure B.4: Regular tesselations of the the plane (top: square, triangular and hexagonal lattice) and the space (bottom).

On the other hand side, the symmetric nature of structured lattices can lead to artifacts due to privileged directions for all kind of propagating processes performed on the lattice. Figure B.5 illustrates how different lattice topologies lead to different population shapes to due lattice symmetries. The simulations were done by a simple cellular automaton with fix time step permitting cells to divide to a randomly chosen unoccupied neighboring lattice site (see algorithm 3).

So in the following we will only focus on unstructured lattices.

Algorithm 3 Cellular Automaton for Cell Proliferation

```
occupied(p, n) = "vertex p is occupied by a cell at time n"
neighbors(p, q) = "vertices p and q are neighboring lattice sites"
while abortion criteria not reached do
  for all p ∈ P do
    if occupied(p, n) then
      occupied(p, n + 1) := true
      if ∃q : neighbors(p, q)∧!occupied(q, n) then
        randomly chose unoccupied neighbor site q
        occupied(q, n + 1) := true
      end if
    end if
  end for
  n := n + 1
  t := t + Δt
end while
```

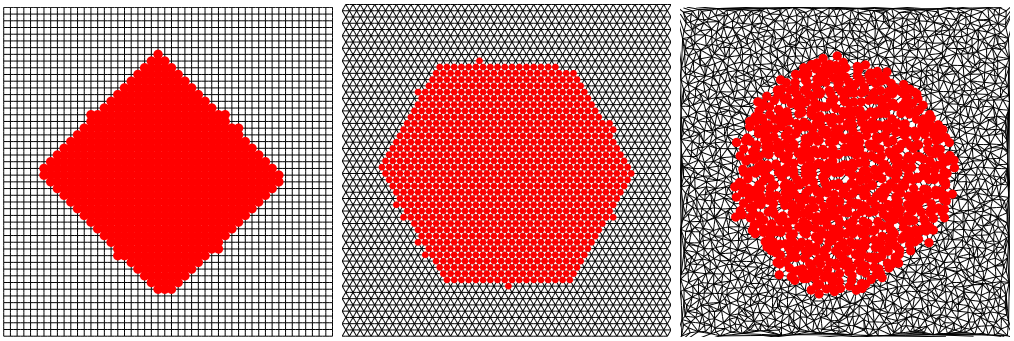

Figure B.5: Regular tesselations of the the plane (top: square, triangular and hexagonal lattice) and the space (bottom).

Global Rearrangements: Shifting

In many cases cells are even growing even if they are completely surrounded by other cells. In this case cell growth coincides with the movement of the surrounding cells away from the growing cell. "In the case were there is no free neighboring site cells are pushed away along the shortest track to the nearest free site so that a free adjacent place for the offspring occurs."[RBH+09]

Example : Example: Density Inhibition & Shifting Cells will grow if the cells around are not too dense, i.e. if within a radius of l there is at least one free lattice sites.

$$\mu^{(g)} = \begin{cases} \tau^{-1} & ,\text{if } \exists x \in free(neigh^l(X)) \\ 0 & ,else \end{cases} \tag{B.15}$$

If the cell can freely expand without shifting other cells away, $\exists x \in free(neigh^1(X))$, then the choice of its expansion side is random following uniform distribution between all possible choices.

$$\mu^{(g)}_{X \to X \cup \{x\}} = P(X \to X \cup \{x\}) \cdot \mu^{(g)} \tag{B.16}$$

$$P(X \to X \cup \{x\}) = \frac{1}{|free(X_{ext})|} \tag{B.17}$$

If there is no free lattice site within the immediate neighborhood, $free(neigh^1(X)) = \emptyset$, cells will be pushed along the shortest track to the nearest free lattice site.

$$\forall x \in free(neigh^l(X)) : x \neq x^{nearest} \to \min_{y \in X} |x^{nearest} - y| < \min_{y \in X} |x - y| \tag{B.18}$$

Cell Motion

Agents/cells can move among the domain by "hopping" from one lattice site to a neighboring one. The hopping rate is defined for the overall velocity of movement. The choice of the probability distribution among the destination sites depends on the kind of movement.

Cell Division & Cell Cycle Reentrance

Is a cell c_0 dividing into two daughter cells, c_1 and c_2, then the formerly occupied space X_0 will be divided and associated to the new cells

$$\{q, X\} \xrightarrow{\mu^{(d)}} \{q_1, X_1\}, \{q_2, X_2\} \tag{B.19}$$

$$X_1 \cup X_2 = X \tag{B.20}$$

$$X_1 \cap X_2 = \emptyset \tag{B.21}$$

Subsequently the two daughter cells can reenter the cell cycle, $q_1 = q_2 = 1$, or become quiescent, $q = \{quiescent\}$ depending on external circumstances.

APPENDIX B. STOCHASTIC SPATIO-TEMPORAL CELLULAR AUTOMATA

Appendix C

Partial Differential Equations

C.1 Parabolic Equation: Diffusion

C.1.1 Finite Difference Method

Principle: derivatives in the partial differential equation are approximated by linear combinations of function values at the grid points.

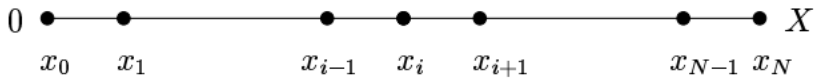

In 1D a domain $\Omega = (0, X)$ is discretized in the following manner:

$$\begin{aligned} u_i &\approx u(x_i), \\ i &= 0, 1, ..., N \end{aligned} \tag{C.1}$$

where $x_i = i\Delta x$ are the discrete lattice/mesh points and $\Delta x = \frac{X}{N}$ the mesh size.

A 2D domain $\Omega = (0, X) \times (0, Y)$ is discretized as follows

$$\begin{aligned} u_{i,j} &\approx u(x_i, y_j), \\ i &= 0, 1, ..., N \\ j &= 0, 1, ..., M \end{aligned} \tag{C.2}$$

where $\Delta x = \frac{X}{N}$ and $\Delta y = \frac{Y}{N}$ are the mesh sizes in both directions. In many cases the mesh size is chosen to be similar for all directions, $\Delta x = \Delta y = h$.

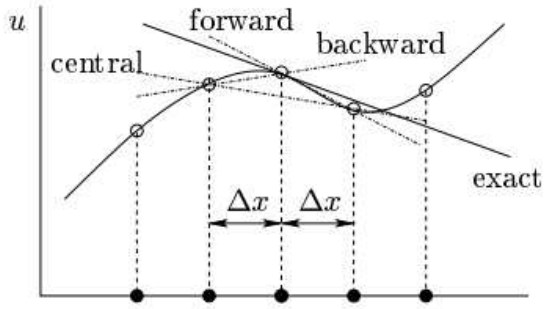

Approximation of first-order derivatives: by doing a Taylor series expansion $u(x) = \sum_{n=0}^{\infty} \frac{(x-x_i)^n}{n!}(\frac{\partial^n u}{\partial x^n})_i$ of u in point x we get

T_1: for $x = x_{i+1}$:
$u_{i+1} = u_i + \frac{(\Delta x)}{1}(\frac{\partial u}{\partial x})_i + \frac{(\Delta x^2)}{2}(\frac{\partial^2 u}{\partial x^2})_i + \frac{(\Delta x^3)}{6}(\frac{\partial^3 u}{\partial x^3})_i + ...$
T_2: for $x = x_{i-1}$:
$u_{i-1} = u_i - \frac{(\Delta x)}{1}(\frac{\partial u}{\partial x})_i + \frac{(\Delta x^2)}{2}(\frac{\partial^2 u}{\partial x^2})_i - \frac{(\Delta x^3)}{6}(\frac{\partial^3 u}{\partial x^3})_i + ...$

Accuracy of finite difference approximations

$$
\begin{aligned}
T_1 : \left(\frac{\partial u}{\partial x}\right)_i &= \underbrace{\frac{u_{i+1}-u_i}{\Delta x}}_{\text{forward differences}} \underbrace{-\frac{(\Delta x)}{2}\left(\frac{\partial^2 u}{\partial x^2}\right)_i - \frac{(\Delta x)^2}{6}\left(\frac{\partial^3 u}{\partial x^3}\right)_i - ...}_{\text{truncation error } \mathcal{O}(\Delta x)} \\
T_2 : \left(\frac{\partial u}{\partial x}\right)_i &= \underbrace{\frac{u_i-u_{i-1}}{\Delta x}}_{\text{backward differences}} \underbrace{+\frac{(\Delta x)}{2}\left(\frac{\partial^2 u}{\partial x^2}\right)_i - \frac{(\Delta x)^2}{6}\left(\frac{\partial^3 u}{\partial x^3}\right)_i + ...}_{\text{truncation error } \mathcal{O}(\Delta x)} \qquad \text{(C.3)} \\
T_1 - T_2 : \left(\frac{\partial u}{\partial x}\right)_i &= \underbrace{\frac{u_{i+1}-u_{i-1}}{2\Delta x}}_{\text{central differences}} \underbrace{-\frac{(\Delta x)^2}{6}\left(\frac{\partial^3 u}{\partial x^3}\right)_i - ...}_{\text{truncation error } \mathcal{O}(\Delta x)^2}
\end{aligned}
$$

Approximation of second-order derivatives:

$$
T_1 + T_2 : \left(\frac{\partial^2 u}{\partial x^2}\right)_i = \underbrace{\frac{u_{i+1}-2u_i+u_{i-1}}{(\Delta x)^2}}_{\text{central differences}} \underbrace{+\frac{(\Delta x^2)}{12}(\frac{\partial^4 u}{\partial x^4})_i + ...}_{\text{truncation error } \mathcal{O}(\Delta x)^2} \qquad \text{(C.4)}
$$

In three dimensions for similar mesh sizes for all dimensions, $\Delta x = \Delta y = \Delta z = h$:

$$\begin{aligned}
\nabla \cdot (\nabla u) &= \frac{\partial^2 u}{\partial x^2} + \frac{\partial^2 u}{\partial y^2} + \frac{\partial^2 u}{\partial z^2} \\
\left(\frac{\partial^2 u}{\partial x^2}\right)_{i,j,k} &= D_u \frac{u_{i-1,j,k} - 2u_{i,j,k} + u_{i+1,j,k}}{h^2} + \mathcal{O}(h^2) \\
\left(\frac{\partial^2 u}{\partial y^2}\right)_{i,j,k} &= D_u \frac{u_{i,j-1,k} - 2u_{i,j,k} + u_{i,j+1,k}}{h^2} + \mathcal{O}(h^2) \\
\left(\frac{\partial^2 u}{\partial z^2}\right)_{i,j,k} &= D_u \frac{u_{i,j,k-1} - 2u_{i,j,k} + u_{i,j,k+1}}{h^2} + \mathcal{O}(h^2)
\end{aligned} \tag{C.5}$$

C.2 Hyperbolic Equation: Transport

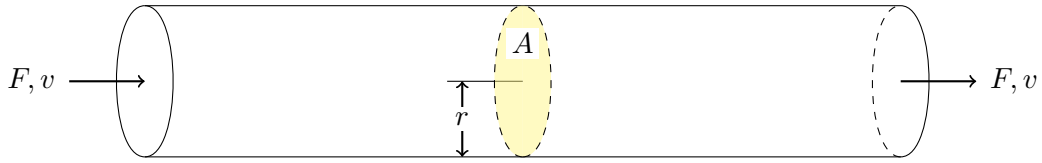

Let u be an unknown variable The transport of particles along a blood vessel depends on the velocity v and the size (radius) r.

$$\frac{\partial u}{\partial t} + \nabla \cdot (vu) = 0 \tag{C.6}$$

Let us consider a unidirectional flow along the axis of the vessel. transport is thus only along this direction.

C.2.1 Finite Volume Method

The finite volume method discretizes the volume into finite volume elements. In this 1D example, the lateral fluxes are considered to be zero. The unknown u_i associated

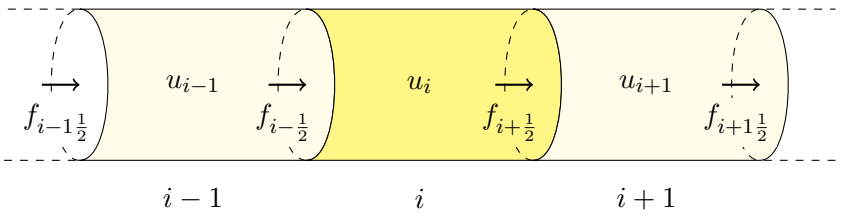

with the volume V_i is its average volume concentration u_i^n at each time step $n\Delta t$. The

transport equation (eq. C.2.2) is integrated over each volume element and solved by calculating the fluxes among the surface of the given elements.

$$u_i^{n+1} = u_i^n + \frac{\Delta t}{\Delta V_i}\left(flux_{i-\frac{1}{2}} - flux_{i+\frac{1}{2}}\right) \tag{C.7}$$

The fluxes depend on the flow rate f across the surfaces and the particle concentration u at the surface.

C.2.2 Piece-wise Linear Flux Approximation

As the concentration is here the average value among the whole element (i) the values at the interfaces ($i-\frac{1}{2}$ and $i+\frac{1}{2}$) can be approximated by piece-wise linear interpolation

$$\begin{aligned} flux_{i-\frac{1}{2}} &= f_{i-\frac{1}{2}}\left(u_{i-1} + \frac{1}{2}\delta u_{i-1}\right) \\ flux_{i+\frac{1}{2}} &= f_{i+\frac{1}{2}}\left(u_i + \frac{1}{2}\delta u_i\right) \end{aligned} \tag{C.8}$$

where u_i (or u_{i-1}) is the *upstream sampling value* and δu_i (or δu_{i-1}) the estimated *gradient* at the surface. Several explicit schemes are proposed to approximate those gradients:

$$\text{Upwind: } \delta u_i^{UW} = 0 \tag{C.9}$$

$$\text{Centered Euler: } \delta u_i^{CE} = (u_{i+1} - u_i) \tag{C.10}$$

$$\text{Lax-Wendroff: } \delta u_i^{LW} = (u_{i+1} - u_i)\cdot(1 - f_{i+\frac{1}{2}}\frac{\Delta t}{\Delta V_i}) \tag{C.11}$$

$$\text{Beam-Warming: } \delta u_i^{BW} = u_i - u_{i-1} \tag{C.12}$$

$$\text{Fromm: } \delta u_i^{FR} = \frac{1}{2}(u_{i+1} - u_{i-1}) \tag{C.13}$$

$$\begin{aligned} \text{Min Mod: } \delta u_i^{mm} =& \min\{\max\{u_i - u_{i-1}, 0\}, \max\{u_{i+1} - u_i, 0\}\} \\ &+ \max\{\min\{u_i - u_{i-1}, 0\}, \min\{u_{i+1} - u_i, 0\}\} \end{aligned} \tag{C.14}$$

$$\begin{aligned} \text{Superbee: } \delta u_i^{sb} =& (sign(u_i - u_{i-1}) + sign(u_{i+1} - u_i)) \\ &\cdot \min\{|u_i - u_{i-1}|, |u_{i+1} - u_i|, \frac{1}{2}\max\{|u_i - u_{i-1}|, |u_{i+1} - u_i|\}\} \end{aligned} \tag{C.15}$$

Solving equation with the upwind scheme, a necessary condition for convergence is the CFL condition [CFL28]

$$v\frac{dt}{dx} \leq Cr \tag{C.16}$$

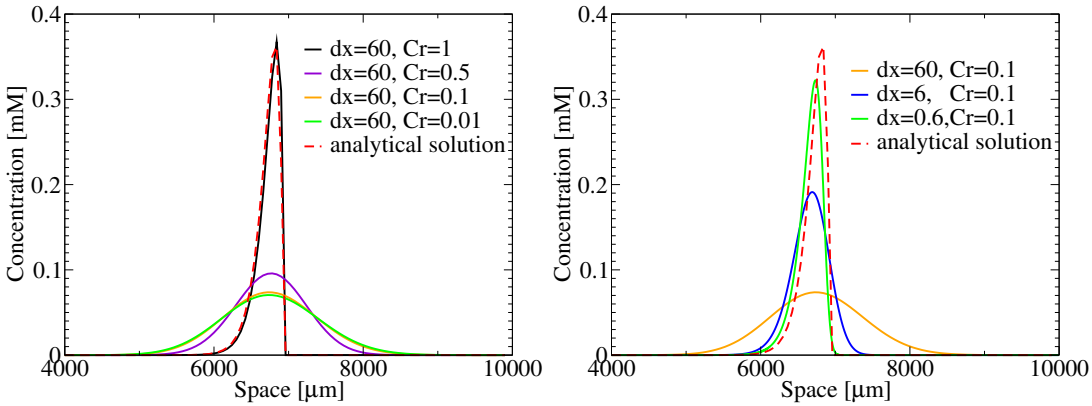

Figure C.1: Upwind scheme. $\mathcal{O}(\Delta x, \Delta t)$

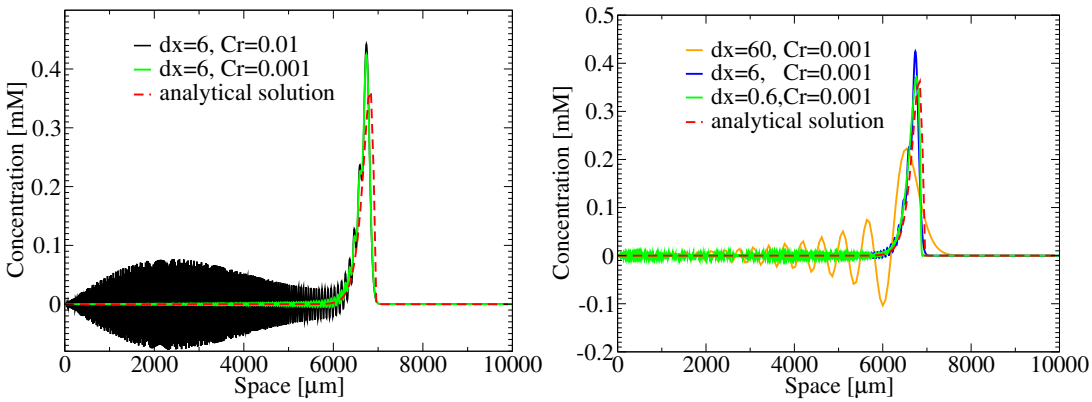

Figure C.2: Lax-Wendroff scheme. $\mathcal{O}(\Delta x^2, \Delta t^2)$

where v is the velocity and Cr a dimensionless constant.

Figure C.1 shows that for $Cr = 1$ the upwind scheme gives the exact solution while for smaller values of Cr the solution becomes diffusive and converges against a certain shape. Refining in space decreases the numerical error. Figures C.2, C.3 and C.4 show the same sensitivity analysis for Cr and dx for Lax-Wendroff, Fromm and Beam warming. Those profiles are less diffusive, but more dispersive. I.e. they cause oscillations.

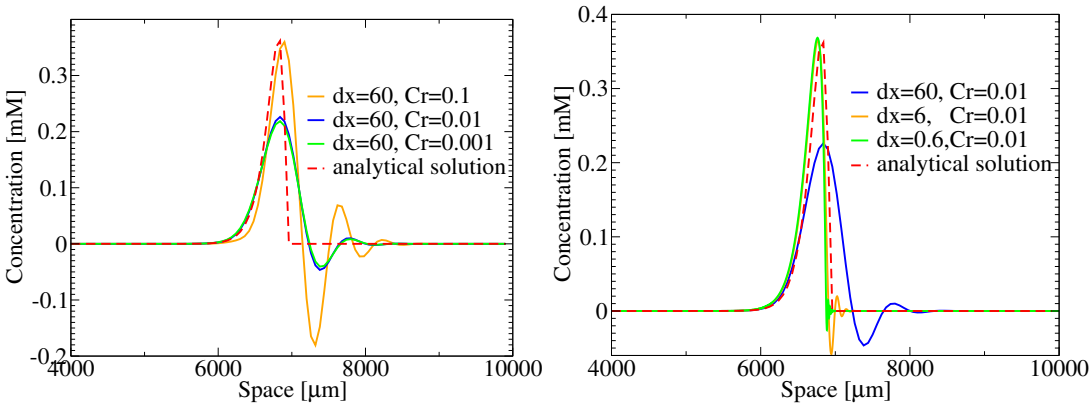

Figure C.3: Fromm scheme. $\mathcal{O}(\Delta x^2, \Delta t^2)$

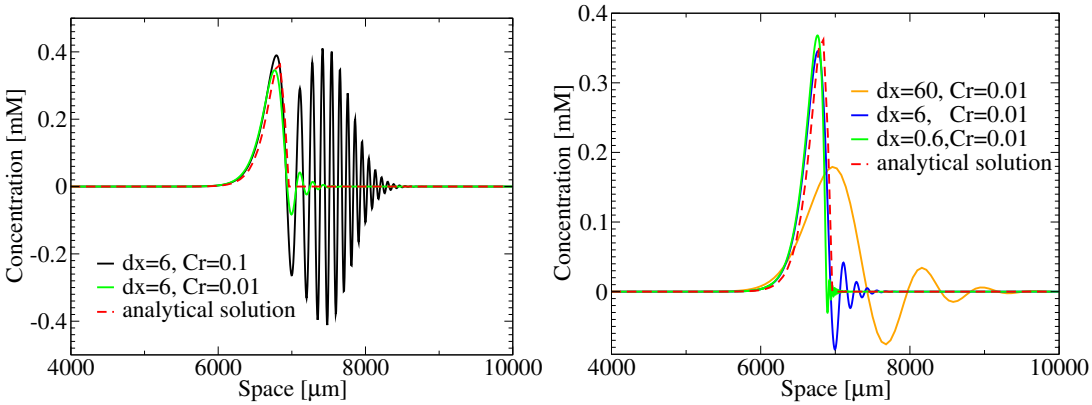

Figure C.4: Beam warming scheme. $\mathcal{O}(\Delta x^2, \Delta t^2)$

C.3 Solver

C.3.1 Conjugate Gradient

The conjugate gradient method is an algorithm for the numerical solution of particular systems of linear equations, namely those whose matrix is symmetric and positive-definite. It was developed by Hestenes and Stiefel [HS52].

Algorithm 4 Conjugate Gradient Algorithm

$r_0 = b - Ax_0$
$p_0 = r_0$ (or $p_0 = M^{-1}r_0$ with preconditioner)
for $i = 1, 2, 3...$ **do**
  $\alpha_i = \frac{r_i^T r_i}{p_i^T A p_i}$ (or $\alpha_i = \frac{r_i^T M^{-1} r_i}{p_i^T A p_i}$ with preconditioner)
  $x_{i+1} = x_i + \alpha_i p_i$
  If x_{i+1} is accurate enough then quit
  $r_{i+1} = r_i - \alpha_i A p_i$
  $\beta_i = \frac{r_{i+1}^T r_{i+1}}{r_i^T r_i}$ (or $\beta_i = \frac{r_{i+1}^T M^{-1} r_{i+1}}{r_i^T r_i}$ with preconditioner)
  $p_{i+1} = r_{i+1} + \beta_i p_i$ (or $p_{i+1} = M^{-1} r_{i+1} + \beta_i p_i$ with preconditioner)
end for

C.3.2 Bi-Conjugate Gradient

The bi-conjugate gradient method provides a generalization to non-symmetric matrices, but it is numerically unstable.

C.3.3 Bi-Conjugate Gradient Stabilized

The bi-conjugate gradient stabilized method (BiCGSTAB) is an iterative method developed by H. A. van der Vorst [vdV92, Saa03] for the numerical solution of non-symmetric linear systems. It is a variant of the bi-conjugate gradient method (BiCG) and has faster and smoother convergence than the original BiCG as well as other variants such as the conjugate gradient squared method (CGS). It is a Krylov subspace method.

To solve a linear system $Ax = b$, *BiCG-STAB* starts with an initial guess x_0 and proceeds as follows:

Algorithm 5 Bi-Conjugate Gradient Algorithm

$r_0 = b - Ax_0$
$\hat{r}_0 = b - A^T\hat{x}_0$
$p_0 = r_0$ (or $p_0 = M^{-1}r_0$ with preconditioner)
$\hat{p}_0 = \hat{r}_0$ (or $\hat{p}_0 = \hat{r}_0 M^{-1}$ with preconditioner)
for $i = 1, 2, 3...$ **do**
  $\alpha_i = \frac{\hat{r}_i^T r_i}{\hat{p}_i^T A p_i}$ (or $\alpha_i = \frac{\hat{r}_i^T M^{-1} r_i}{\hat{p}_i^T A p_i}$ with preconditioner)
  $x_{i+1} = x_i + \alpha_i p_i$
  If x_{i+1} is accurate enough then quit
  $\hat{x}_{i+1} = \hat{x}_i + \alpha_i \hat{p}_i$
  $r_{i+1} = r_i - \alpha_i A p_i$
  $\hat{r}_{i+1} = \hat{r}_i - \alpha_i A^T \hat{p}_i$
  $\beta_i = \frac{\hat{r}_{i+1}^T r_{i+1}}{\hat{r}_i^T r_i}$ (or $\beta_i = \frac{\hat{r}_{i+1}^T M^{-1} r_{i+1}}{\hat{r}_i^T r_i}$ with preconditioner)
  $p_{i+1} = r_{i+1} + \beta_i p_i$ (or $p_{i+1} = M^{-1} r_{i+1} + \beta_i p_i$ with preconditioner)
  $\hat{p}_{i+1} = \hat{r}_{i+1} + \beta_i \hat{p}_i$ (or $\hat{p}_{i+1} = \hat{r}_{i+1} M^{-1} + \beta_i \hat{p}_i$ with preconditioner)
end for

Algorithm 6 BiCG-STAB Algorithm

$r_0 = b - Ax_0$
Choose an arbitrary vector $\hat{r}_0$ such that $(\hat{r}_0, r_0) \neq 0$, e.g., $\hat{r}_0 = r_0$
$\rho_0 = \alpha = \omega_0 = 1$
$v_0 = p_0 = 0$
for $i = 1, 2, 3...$ **do**
  $\rho_i = (\hat{r}_0, r_{i-1})$
  $\beta = (\rho_i / \rho_{i-1})(\alpha / \omega_{i-1})$
  $p_i = r_{i-1} + \beta(p_{i-1} - \omega_{i-1} v_{i-1})$
  $v_i = A p_i$
  $\alpha = \rho_i / (\hat{r}_0, v_i)$
  $s = r_{i-1} - \alpha v_i$
  $t = As$
  $\omega_i = (t, s)/(t, t)$
  $x_i = x_{i-1} + \alpha p_i + \omega_i s$
  If x_i is accurate enough then quit
  $r_i = s - \omega_i t$
end for

Appendix D

Curve Fitting

Curve fitting is the process of constructing a curve, or mathematical function, that has the best fit to a series of data points, possibly subject to constraints. Curve fitting can involve either interpolation, where an exact fit to the data is required, or smoothing, in which a "smooth" function is constructed that approximately fits the data. A related topic is regression analysis, which focuses more on questions of statistical inference such as how much uncertainty is present in a curve that is fit to data observed with random errors. Fitted curves can be used as an aid for data visualization, to infer values of a function where no data are available, and to summarize the relationships among two or more variables. Extrapolation refers to the use of a fitted curve beyond the range of the observed data, and is subject to a greater degree of uncertainty since it may reflect the method used to construct the curve as much as it reflects the observed data. [wikipedia]

D.1 Least Squares Problem

The objective consists of adjusting the parameters of a model function to best fit a data set. A simple data set consists of n points (data pairs) (x_i, y_i), $i = 1, ..., n$, where x_i is an independent variable and y_i is a dependent variable whose value is found by observation. The model function has the form $f(x, \beta)$, where the m adjustable parameters are held in the vector β. The goal is to find the parameter values for the model which "best" fits the data. The least squares method finds its optimum when the sum, S, of squared residuals

$$S = \sum_{i=1}^{n} r_i^2 \tag{D.1}$$

is a minimum. A residual is defined as the difference between the value predicted by the model and the actual value of the dependent variable

$$r_i = y_i - f(x_i, \beta). \tag{D.2}$$

An example of a model is that of the straight line. Denoting the intercept as β_0 and the slope as β_1, the model function is given by $f(x, \beta) = \beta_0 + \beta_1 x$. See linear least squares for a fully worked out example of this model. A data point may consist of more than one independent variable. For an example, when fitting a plane to a set of height measurements, the plane is a function of two independent variables, x and z, say. In the most general case there may be one or more independent variables and one or more dependent variables at each data point. [wikipedia]

D.2 Gradient Decent

Gradient descent is based on the observation that if the real-valued function $f(\beta)$ is defined and differentiable in a neighborhood of a point β, then $f(\beta)$ decreases fastest if one goes from β in the direction of the negative gradient of f at β, $-\nabla f(\beta)$. It follows that, if

$$\alpha = \beta - \gamma_n \nabla f(\beta) \tag{D.3}$$

for $\gamma > 0$ a small enough number, then $f(\alpha) \leq f(\beta)$. With this observation in mind, one starts with a guess for a local minimum of f, and considers the sequence such that

$$\beta_{n+1} = \beta_n - \gamma \nabla f(\beta_n), n \geq 0 \tag{D.4}$$

We have

$$f(\beta_0) \geq f(\beta_1) \geq f(\beta_2) \geq ..., \tag{D.5}$$

so hopefully the sequence β_n converges to the desired local minimum. Note that the value of the step size γ is allowed to change at every iteration. [wikipedia]

D.3 Newton-Gauss method

The distinctive property of least-squares problems is that given the Jacobian matrix J, we can essentially get the Hessian ($\nabla^2 f(x)$) for free if it is possible to approximate the r_j s by linear functions ($\nabla^2 r_j(x)$ are small) or the residuals ($r_j(x)$) themselves are small. The Hessian in this case simply becomes

$$\nabla^2 S(\beta_n) \approx J(\beta_n)^T J(\beta_n) \tag{D.6}$$

Then we obtain the Gauss-Newton method by iteratively calculating

$$J(\beta_n)^T J(\beta_n)\Delta\beta_n \quad = \quad -J(x)^T r(x) \tag{D.7}$$

and updating

$$\beta_{n+1} = \beta_n + \Delta\beta_n. \tag{D.8}$$

D.4 Levenberg-Marquardt algorithm

The Levenberg-Marquardt algorithm (LMA) interpolates between the Gauss-Newton algorithm (GNA) and the method of gradient descent.

$$\left(\underbrace{J(\beta_n)^T J(\beta_n)}_{\text{Gauss-Newton}} + \underbrace{\lambda I}_{\text{gradient descent}} \right) \Delta\beta_n \quad = \quad -J(x)^T r(x) \tag{D.9}$$

Replacing the identity matrix, I, with the diagonal of $J^T J$, avoids slow convergence in the direction of small gradient. The resulting Levenberg-Marquardt algorithm consists in iteratively solving the following linear system

$$\left(J(\beta_n)^T J(\beta_n) + \lambda \text{diag}(J(\beta_n)^T J(\beta_n))\right) \Delta\beta_n \quad = \quad -J(x)^T r(x) \tag{D.10}$$

and updating

$$\beta_{n+1} = \beta_n + \Delta\beta_n. \tag{D.11}$$

Acronyms

ODE	Ordinary Differential Equation
PDE	Partial Differential Equation
NSCLC	Non-Small-Cell Lung Carcinoma
IF	Immunofluorescence
EPO	Erythropoietin
rHuEPO	Recombinant Human Erythropoietin
MCTS	Multi-Cellular Tumor Spheroid
VEGF	Vascular Endothelial Growth Factor
ECM	Extra-Cellular Matrix
AIF	Arterial Input Function
CA	Contrast Agent
MB	Microbubble
MRI	Magnet Resonance Imaging
CE-MRI	Constrast Enhanced-Magnetic Resonance Imaging
DCE-MRI	Dynamic Constrast Enhanced-Magnetic Resonance Imaging
CT	Computer Tomography
DCE-CT	Dynamic Constrast Enhanced-Computer Tomography
DCE-US	Dynamic Constrast Enhanced-Ultrasonography

MVD	Micro-vessel Density
CSSH	Capillary Shear Stress Homogenization
CFL	Courant-Friedrichs-Lewy

Bibliography

[ABM05] T. Alarcón, H. M. Byrne, and P. K. Maini. A multiple scale model for tumor growth. *Multiscale Model. Simul.*, 3(2):440–475 (electronic), 2005.

[AM02] D. Ambrosi and F. Mollica. On the mechanics of a growing tumor. *Ing. J. Eng. Sci.*, 40(12):1297–1316, 2002.

[BBH+99] Gunnar Brix, Malte L. Bahner, Ulf Hoffmann, Andrea Horvath, and Wolfgang Schreiber. Regional blood flow, capillary permeability, and compartmental volumes: Measurement with dynamic ct - initial experience. *Radiology*, 210:269–276, 1999.

[BH08] Gabriele Bergers and Douglas Hanahan. Modes of resistance to anti-angiogenic therapy. *Nature reviews. Cancer*, 8(8):592–603, August 2008.

[BKL+04] Gunnar Brix, Fabian Kiessling, Robert Lucht, Susanne Darai, Klaus Wasser, Stefan Delorme, and Jürgen Griebel. Microcirculation and microvasculature in breast tumors: Pharmacokinetic analysis of dynamic mr image series. *Magnetic Resonance in Medicine*, 52:420–429, 2004.

[BL79] S. Beucher and C. Lantuejoul. Use of Watersheds in Contour Detection. In *International Workshop on Image Processing: Real-time Edge and Motion Detection/Estimation, Rennes, France.*, September 1979.

[Bow81] Adrian Bowyer. Computing dirichlet tessellations. *The Computer Journal*, 24(2):162–166, 1981.

[BP03] H. Byrne and L. Preziosi. Modelling solid tumour growth using the theory of mixtures. *Mathem. Medicine and Biology*, 20:341 – 366, 2003.

[BR06] K. Bartha and H. Rieger. Vascular network remodeling via vessel cooption, regression and growth in tumors. *J. Theor. Biol.*, page 16, Mar 2006.

[BRJ+09] Markus Basan, Thomas Risler, Jean-François Joanny, Xavier Sastre-Garau, and Jacques Prost. Homeostatic competition drives tumor growth and metastasis nucleation. *HFSP journal*, 3(4):265–72, August 2009.

[BSP+91] Gunnar Brix, Wolfhard Semmler, Rüdiger Port, Lothar R. Schad, Günter Layer, and Walter J. Lorenz. Pharmacokinetic parameters in cns gd-dtpa enhanced mr imaging. *Journal of Computer Assisted Tomography*, 15(4):621–628, 1991.

[Buc11] Peter Buchwald. A local glucose-and oxygen concentration-based insulin secretion model for pancreatic islets. *Theoretical biology & medical modelling*, 8(1):20, January 2011.

[BZKG09] Gunnar Brix, Stefan Zwick, Fabian Kiessling, and Jürgen Griebel. Pharmacokinetic analysis of tissue microcirculation using nested models: Multimodel inference and parameter identifiability. *Med. Phys.*, 36(7):2923–2933, 2009.

[CdB02] S. Van Cruchten and W. Van den Broeck. Morphological and biochemical aspects of apoptosis, oncosis and necrosis. *Anat. Histol. Embryol.*, 31:214–223, 2002.

[CFL28] R. Courant, K. Friedrichs, and H. Lewy. über die partiellen differenzengleichungen der mathematischen physik. *Mathematische Annalen*, 100(1):32–74, 1928.

[Cha96] M.A.J. Chaplain. Avascular growth, angiogenesis and vascular growth in solid tumours: The mathematical modelling of the stages of tumour development. *Mathl. Comput. Modelling*, 23(6):47–87, 1996.

[CM09] V. Capasso and D. Morale. Stochastic modelling of tumour-induced angiogenesis. *J Math Biol*, 58(1-2):219–33, 2009.

[CSS88] J.J. Casciari, S.V. Sotirchos, and R.M. Sutherland. Glucose diffusivity in multicellular tumor spheroids. *Cancer Res.*, 48:3905 – 3909, 1988.

[CSS92a] J J Casciari, S V Sotirchos, and R M Sutherland. Variations in Tumor Cell Growth Rates and Metabolism with Oxygen Concentration, Glucose Concentration, and Extracellular pH. *J. Cell. Physiol.*, 151:386–394, 1992.

BIBLIOGRAPHY

[CSS92b] J.J. Casciari, S.V. Sotirchos, and R.M. Sutherland. Variations in tumor cell growth rates and metabolism with oxygen concentration, glucose concentration, and extracellular ph. *J. Cell. Physiol.*, 151:386–394, 1992.

[CZ83] Alan D. Conger and Marvin C. Ziskin. Growth of mammalian multicellular tumor spheroids. *Cancer Research*, 43:556–560, 1983.

[DH03] D. Drasdo and S. Höhme. Individual-based approaches to birth and death in avascular tumors. *Math. and Comp. Modelling*, 37:1163 – 1175, 2003.

[DH05] D. Drasdo and S. Hoehme. A single-cell based model to tumor growth in-vitro: monolayers and spheroids. *J. Phys. Biol.*, 2:133 – 147, 2005.

[DHB07] D. Drasdo, S. Hoehme, and M. Block. On therole of physics in the growth and pattern formation of multi-cellular systems: What can we learn from individual-cell based models? *J. Stat. Phys*, 128:287–345, 2007.

[DJRC+10] Dirk Drasdo, Nick Jagiella, Ignacio Ramis-Conde, Irene Vignon-Clementel, and William Weens. Modeling steps from benign tumor to invasive cancer: Examples of intrinsically multiscale problems. In Arnaud Chauvière, Luigi Preziosi, and Claude Verdier, editors, *Cell Mechanics - From Single Scale-Based Models to Multi-scale Modeling*. Chapman & Hall/CRC Mathematical & Computational Biology, 2010.

[Dra05] D. Drasdo. Coarse graining in simulated cell populations. *Adv. Complex Syst.*, 8(2 & 3):319–363, 2005.

[DRL+06] Christoph Dehnert, Frank Risse, Sebastian Ley, Tristan A. Kuder, Ralf Buhmann, Michael Puderbach, Elmar Menold, Derliz Mereles, Hans-Ulrich Kauczor, Peter Bärtsch, , and Christian Fink. Magnetic resonance imaging of uneven pulmonary perfusion in hypoxia in humans. *Am J Respir Crit Care Med*, 2006.

[EK11] John M L Ebos and Robert S Kerbel. Antiangiogenic therapy: impact on invasion, disease progression, and metastasis. *Nature reviews. Clinical oncology*, 8(4):210–21, April 2011.

[ELCM+09] John M L Ebos, Christina R Lee, William Cruz-Munoz, Georg A Bjarnason, James G Christensen, and Robert S Kerbel. Accelerated metastasis after short-term treatment with a potent inhibitor of tumor angiogenesis. *Cancer cell*, 15(3):232–9, March 2009.

[ESG+09] Tormod A M Egeland, Trude G Simonsen, Jon-Vidar Gaustad, Kristine Gulliksrud, Christine Ellingsen, and Einar K Rofstad. Dynamic contrast-enhanced magnetic resonance imaging of tumors: preclinical validation of parametric images. *Radiation research*, 172(3):339–47, September 2009.

[FB03] Laure S. Fournier and Robert C. Brasch. The role of blood pool media in the study of tumor pathophysiology. In A. Jackson, David Buckley, and Geoffrey J. M. Parker, editors, *Dynamic contrast-enhanced magnetic resonance imaging in oncology*. Springer-Verlag Berlin and Heidelberg GmbH & Co. K, 2003.

[Fic55a] Adolf Fick. Ueber Diffusion. *Annalen der Physik und Chemie*, 170(1):59–86, 1855.

[Fic55b] Adolph Fick. V. On liquid diffusion. *Philosophical Magazine Series 4*, 10(63):30–39, 1855.

[Fol71] J Folkman. Tumor angiogenesis: therapeutic implications. *The New England journal of medicine*, 285(21):1182–6, November 1971.

[Fre88] J.P. Freyer. Role of necrosis in regulating the growth saturation of multicellular spheroids. *Cancer Res.*, 48:2432 – 2439, 1988.

[FS85] J.P. Freyer and R.M. Sutherland. A reduction in the in situ rates of oxygen and glucose consumption of cells in emt6/ro spheroids during growth. *J. Cell. Physiol.*, 124:516–524, Oct 1985.

[FS86] J.P. Freyer and R.M. Sutherland. Regulation of growth saturation and development of necrosis in emt6/ro multicellular spheroids by the glucose and oxygen supply. *Cancer Res.*, 46:3504–3512, Oct 1986.

[FSJ+91] J P Freyer, P L Schor, K A Jarrett, M Neeman, and L O Sillerud. Cellular energetics measured by phosphorous nuclear magnetic resonance spectroscopy are not correlated with chronic nutrient deficiency in multicellular tumor spheroids. *Cancer research*, 51(15):3831–7, August 1991.

[Fun90] Y.C. Fung. *Biomechanics: Motion, Flow, Stress, and Growth*. Springer-Verlag, New York, 1990.

[FV90] Eric R. Fearon and Bert Vogelstein. A genetic model for colorectal tumorigenesis. *Cell*, 61(5):759–767, June 1990.

BIBLIOGRAPHY

[FZ74] Kitty Fronek and Benjamin W. Zweifach. Pre- and postcapillary resistances in cat mesentery. *Microvascular Research*, 7(3):351 – 361, 1974.

[Geo] Geomodel. Bowyer-watson algorithm. http://images.cnblogs.com/cnblogs_com/renliqq/5.GIF.

[Gil77] D. T. Gillespie. Exact stochastical simulations of coupled chemical reactions. *J. Phys. Chem.*, 81(25):2340–2361, 1977.

[GK01] Ralf Goedde and Haymo Kurz. Structural and biophysical simulation of angiogenesis and vascular remodeling. *Developmental Dynamics*, 220:387–401, 2001.

[GZC+11] Francisco L A F Gomes, Gen Zhang, Felix Carbonell, José A Correa, William A Harris, Benjamin D Simons, and Michel Cayouette. Reconstruction of rat retinal progenitor cell lineages in vitro reveals a surprising degree of stochasticity in cell fate decisions. *Development (Cambridge, England)*, 138(2):227–35, January 2011.

[HK07] Yunlong Huo and Ghassan S. Kassab. A hybrid one-dimensional/womersley model of pulsatile blood flow in the entire coronary arterial tree. *Am J Physiol Heart Circ Physiol*, 292:H2623–H2633, January 2007.

[HMD+10] Franziska Hirschhaeuser, Heike Menne, Claudia Dittfeld, Jonathan West, Wolfgang Mueller-Klieser, and Leoni A Kunz-Schughart. Multicellular tumor spheroids: an underestimated tool is catching up again. *Journal of biotechnology*, 148(1):3–15, July 2010.

[HS52] Magnus R. Hestenes and Eduard Stiefel. Methods of conjugate gradients for solving linear systems. *Journal of Research of the National Bureau of Standards*, 49(6), 1952.

[HW00] Douglas Hanahan and Robert A. Weinberg. The hallmarks of cancer. *Cell*, 100:57–70, January 7 2000.

[HW11] Douglas Hanahan and Robert A. Weinberg. Hallmarks of cancer: The next generation. *Cell*, 144(5):646–674, March 4 2011.

[Jai05] Rakesh K Jain. Normalization of tumor vasculature: an emerging concept in antiangiogenic therapy. *Science (New York, N.Y.)*, 307(5706):58–62, January 2005.

[JB78] Fogh J and Giovanella BC, editors. *The Nude Mouse in Experimental and Clinical Research.*, volume 1. Academic Press, N.Y., 1978.

[JB82] Fogh J and Giovanella BC, editors. *The Nude Mouse in Experimental and Clinical Research.*, volume 2. Academic Press, N.Y., 1982.

[JPGCF05] Y Jiang, J. Pjesivac-Grbovic, C. Cantrell, and JP. Freyer. A multiscale model for avascular tumor growth. *Biophys. J.*, 89(6):3884–3894, 2005.

[Ken48] David G. Kendall. On the role of variable generation time in the development of a stochastic birth process. *Biometrika*, 35(3/4):316–330, Dec. 1948.

[KS97] Haymo Kurz and Konrad Sandau. Modelling of blood vessel development - bifurcation pattern and hemodynamics, optimality and allometry. *Comm Theor Biol*, 4(4):261–291, 1997.

[KSDMKG00] Leoni A. Kunz-Schughart, Joerg Doetsch, Wolfgang Mueller-Klieser, and Karlfried Groebe. Proliferative activity and tumorigenic conversion: impact on cellular metabolism in 3-D culture. *Am J Physiol Cell Physiol*, 278(4):C765–780, April 2000.

[KSO07] Y. Kim, M.A. Stolarska, and H.G. Othmer. A hybrid model for tumor spheroid growth *in vitro*. I. Theoretical development and early results. *Math. Models Methods Appl. Sci.*, 17(suppl.):1773–1798, 2007.

[Lab] Keck Lab. Watershed primer. http://www.wm.edu/as/kecklab/watershedmonitoring/watershedprimer.

[Law72] Charles L. Lawson. Transforming triangulations. *Discrete Mathematics*, 3(4):365–372, 1972.

[Law77] Charles L. Lawson. Software for C^1 surface interpolation. In John R. Rice, editor, *Mathematical Software III*, pages 161–194. Academic Press, NY, 1977.

[LCC+11] Nathalie Lassau, Linda Chami, Mohamed Chebil, Baya Benatsou, Sophie Bidault, Elizabeth Girard, Ghassen Abboud, and Alain Roche. Dynamic contrast-enhanced ultrasonography (DCE-US) and anti-angiogenic treatments. *Discovery medicine*, 11(56):18–24, January 2011.

BIBLIOGRAPHY

[LHBtHR10] G.J.S. Litjens, M. Heisen, J. Buurman, and B.M. ter Haar Romeny. Pharmacokinetic models in clinical practice: what model to use for dce-mri of the breast? In *ISBI'10 Proceedings of the 2010 IEEE international conference on Biomedical imaging: from nano to Macro*, 2010.

[LL07] T. Lecuit and P.-F. Lenne. Cell surface mechanics and the control of cell shape, tissue patterns and morphogenesis. *Nat Rev Mol Cell Biol*, 2007.

[LLK+09] Andreas Lemke, Frederik B. Laun, Miriam Klauß, Thomas J., Dirk Simon, Stefan Delorme, Lothar R. Schad, and Bram Stieltjes. Differentiation of pancreas carcinoma from healthy pancreatic tissue using multiple b-values: Comparison of apparent diffusion coefficient and intravoxel incoherent motion derived parameters. *Investigative Radiology*, 44(12):1–7, Dec. 2009.

[LR06] D.-S Lee and H Rieger. Flow correlated percolation during vascular remodeling in growing tumors. *Phys. Rev. Lett.*, 96(5):4, Feb 2006.

[MAC06] S. R. McDougall, A. R. Anderson, and M. A. Chaplain. Mathematical modelling of dynamic adaptive tumour-induced angiogenesis: Clinical implications and therapeutic targeting strategies. *J Theor Biol*, 241(3):564–89, 2006.

[MK84] W Mueller-Klieser. Method for the determination of oxygen consumption rates and diffusion coefficients in multicellular spheroids. *Biophysical journal*, 46(3):343–8, September 1984.

[MKS82] W F Mueller-Klieser and R M Sutherland. Influence of convection in the growth medium on oxygen tensions in multicellular tumor spheroids. *Cancer research*, 42(1):237–42, January 1982.

[MM] Benedikt Müller and Margareta Müller. Growth experiment of sk-mes-1 tumor spheroids cultivated under four conditions. I:$[G] = 1mM$, $[O_2] = 0.28mM$, II:$[G] = 5mM$, $[O_2] = 0.28mM$, III:$[G] = 25mM$, $[O_2] = 0.28mM$, IV:$[G] = 25mM$, $[O_2] = 0.07mM$. Data and private discussion.

[MMA+09] P. Macklin, S. McDougall, A. R. Anderson, M. A. Chaplain, V. Cristini, and J. Lowengrub. Multiscale modelling and nonlinear simulation of vascular tumour growth. *J Math Biol*, 58(4-5):765–98, 2009.

[MWO04] N. V. Mantzaris, S. Webb, and H. G. Othmer. Mathematical modeling of tumor-induced angiogenesis. *J Math Biol*, 49(2):111–87, 2004.

[OAMB09] M. R. Owen, T. Alarcón, P. K. Maini, and H. M. Byrne. Angiogenesis and vascular remodelling in normal and cancerous tissues. *J Math Biol*, 58(4-5):689–721, 2009.

[PBC+11] Holger Perfahl, Helen M Byrne, Tingan Chen, Veronica Estrella, Tomás Alarcón, Alexei Lapin, Robert A Gatenby, Robert J Gillies, Mark C Lloyd, Philip K Maini, Matthias Reuss, and Markus R Owen. Multiscale modelling of vascular tumour growth in 3D: the roles of domain size and boundary conditions. *PloS one*, 6(4):e14790, January 2011.

[PG08] George F. Pinder and William G. Gray. *Essentials of Multiphase Flow in Porous Media*. Wiley-Interscience, 2008.

[PHL+08] Moritz Palmowski, Jochen Huppert, Gesa Ladewig, Peter Hauff, Michael Reinhardt, Margareta M Mueller, Eva C Woenne, Juergen W Jenne, Mathias Maurer, Guenter W Kauffmann, Wolfhard Semmler, and Fabian Kiessling. Molecular profiling of angiogenesis with targeted ultrasound imaging: early assessment of antiangiogenic therapy effects. *Molecular cancer therapeutics*, 7(1):101–9, January 2008.

[Pow55] E. O. Powell. Some features of the generation times of individual bacteria. *Biometrika*, 42(1-2):16–44, 1955.

[PRM+06] Geoff J.M. Parker, Caleb Roberts, Andrew Macdonald, Giovanni A. Buonaccorsi, Sue Cheung, David L. Buckley, Alan Jackson, Yvonne Watson, Karen Davies, and Gordon C. Jayson. Experimentally-derived functional form for a population-averaged high-temporal-resolution arterial input function for dynamic contrast-enhanced mri. *Magnetic Resonance in Medicine*, 56:993–1000, 2006.

[PS08] A.R. Pries and T.W. Secomb. Blood flow in microvascular networks. In Ronald F. Tuma, Walter N. Duran, and Klaus Ley, editors, *Handbook of Physiology: Microcirculation*, pages 3–36. Academic Press, San Diego, second edition, 2008.

[PSG+94] A. R. Pries, T. W. Secomb, T. Gessner, M. B. Sperandio, J. F. Gross, and P. Gaehtgens. Resistance to blood flow in microvessels in vivo. *Circ. Res.*, 75:904–915, 1994.

[PSOH03] William K. Purves, David Sadava, Gordon H. Orians, and H. Craig Heller, editors. *Life: The Science of Biology*, page 954. W.H.Freeman and Co Ltd, 7th edition, Dec. 2003.

BIBLIOGRAPHY

[PT09] L. Preziosi and A. Tosin. Multiphase modelling of tumour growth and extracellular matrix interaction: Mathematical tools and applications. *J Math Biol*, 58(4-5):625–56, 2009.

[RBH+09] M Radszuweit, M Block, J G Hengstler, E Schöll, and D Drasdo. Comparing the growth kinetics of cell populations in two and three dimensions. *Physical review. E, Statistical, nonlinear, and soft matter physics*, 79(5 Pt 1):051907, May 2009.

[RCCAD09] Ignacio Ramis-Conde, Mark A J Chaplain, Alexander R A Anderson, and Dirk Drasdo. Multi-scale modelling of cancer cell intravasation: the role of cadherins in metastasis. *Physical biology*, 6(1):016008, January 2009.

[RCDCA08] I. Ramis-Conde, D. Drasdo, M. A. J. Chaplain, and A.R.A. Anderson. Modelling the influence of the e-cadherin-β-catenin pathway in cancer cell invasion: a multi-scale approach. *Biophys. J.*, 95:155–165, 2008.

[Rib10] Domenico Ribatti. The inefficacy of antiangiogenic therapies. *Journal of angiogenesis research*, 2(1):27, January 2010.

[RLP+08] Zimei Rong, Eugenia Leitao, Jonathan Popplewell, BurÇak Alp, and Pankaj Vadgama. Needle Enzyme Electrode for Lactate Measurement <emphasis emphasistype="italic">In Vivo</emphasis>. *IEEE Sensors Journal*, 8(1):113–120, January 2008.

[Saa03] Y. Saad. *Iterative methods for sparse linear systems*. 2003.

[SEK+96] Shigeomi Shimizu, Yutaka Eguchi, Wataru Kamiike, Yuko Itoh, Jun ichi Hasegawa, Kazuo Yamabe, Yoshinori Otsuki, Hikaru Matsuda, and Yoshihide Tsujimoto. Induction of apoptosis as well as necrosis by hypoxia and predominant prevention of apoptosis by bcl-2 and bcl-x_l. *Cancer Research*, 56:2161–2166, 1996.

[SGZ+09] Abbas Shirinifard, J Scott Gens, Benjamin L Zaitlen, Nikodem J Popławski, Maciej Swat, and James A Glazier. 3D multi-cell simulation of tumor growth and angiogenesis. *PloS one*, 4(10):e7190, January 2009.

[SMH05] G. Schaller and M. Meyer-Hermann. Multicellular tumor spheroid in an off-lattice voronoi-delaunay cell model. *Phys. Rev. E*, 71(5):16, May 2005.

[TBB+99] Paul S. Tofts, Gunnar Brix, David L. Buckley, Jeffrey L. Evelhoch, Elizabeth Henderson, Michael V. Knopp, Henrik B.W. Larsson, Ting-Yim Lee, Nina A. Mayr, Geoffrey J.M. Parker, Ruediger E. Port, June Taylor, and Robert M. Weisskoff. Estimating kinetic parameters from dynamic contrast-enhanced t1-weighted mri of a diffusable tracer: Standardized quantities and symbols. *Journal of Magnetic Resonance Imaging*, 10:223–232, 1999.

[TC08] Chris H. Takimoto and Emiliano Calvo. Principles of oncologic pharmacotherapy. In Richard Pazdur, Lawrence D. Wagman, Kevin A. Camphausen, and William J. Hoskins, editors, *Cancer Management: A Multidisciplinary Approach*, chapter 3. 11th edition, April 2008.

[TK91] Paul S. Tofts and Allan G. Kermode. Measurement of the blood-brain barrier permeability and leakage space using dynamic mr imaging. 1. fundamental concepts. *Magnetic Resonance in Medicine*, 17:357–367, 1991.

[TKO+09] Baris Turkbey, Hisataka Kobayashi, Mikako Ogawa, Marcelino Bernardo, and Peter L Choyke. Imaging of tumor angiogenesis: functional or targeted? *AJR. American journal of roentgenology*, 193(2):304–13, August 2009.

[vdV92] H. A. van der Vorst. Bi-CGSTAB: A Fast and Smoothly Converging Variant of Bi-CG for the Solution of Nonsymmetric Linear Systems. *SIAM Journal on Scientific and Statistical Computing*, 13(2):631, February 1992.

[VS91] Lee Vincent and Pierre Soille. Watersheds in digital spaces: An efficient algorithm based on immersion simulations. *IEEE PAMI, 1991*, 13(6):583–598, 1991.

[Wat81] David F. Watson. Computing the n-dimensional tessellation with application to voronoi polytopes. *The Computer Journal*, 24(2):167–172, 1981.

[WBR08] M. Welter, K. Bartha, and H. Rieger. Emergent vascular network inhomogeneities and resulting blood flow patterns in a growing tumor. *J Theor Biol*, 250(2):257–80, 2008.

[WDMK90] S Walenta, J Dötsch, and W Mueller-Klieser. ATP concentrations in multicellular tumor spheroids assessed by single photon imaging and quan-

titative bioluminescence. *European journal of cell biology*, 52(2):389–93, August 1990.

[Wei07] R.A. Weinberg. *The Biology of Cancer*. Garland Science, New York and Oxford, 2007.

[WK97] J.P. Ward and J.R. King. Mathematical modelling of avascular-tumor growth. *IMA J. Math. App. Med. Biol.*, 14:39–69, 1997.

[WLFC08] S. M. Wise, J. S. Lowengrub, H. B. Frieboes, and V. Cristini. Three-dimensional multispecies nonlinear tumor growth–i model and numerical method. *J Theor Biol*, 253(3):524–43, 2008.

[WNM+00] J P Wehrle, C E Ng, K A McGovern, N R Aiken, D C Shungu, E M Chance, and J D Glickson. Metabolism of alternative substrates and the bioenergetic status of EMT6 tumor cell spheroids. *NMR in biomedicine*, 13(6):349–60, October 2000.

[WR10] M Welter and H Rieger. Physical determinants of vascular network remodeling during tumor growth. *Eur Phys J E Soft Matter*, 33(2):149–63, 2010.

[WRZ+12] Andreas Max Weng, Christian Oliver Ritter, Sven Zuehlsdorff, Hui Xue, Jens Guehring, Christopher Glielmi, Meinrad Beer, Dietbert Hahn, and Herbert Köstler. Voxelwise analysis of myocardial blood flow from dce-mri data. In *ISMRM 20th Annual Meeting Proceedings*, page 1495, 2012.

[YYR+10] J. Yang, L. X. Yu, M. Y. Rennie, J. G. Sled, and R. M. Henkelman. Comparative structural and hemodynamic analysis of vascular trees. *Am J Physiol Heart Circ Physiol*, 298:H1249–H1259, 2010.